MAGNETOM Flash

Issue Number 80 · 1/2022
ISMRM Edition

siemens-healthineers.com/magnetom-world

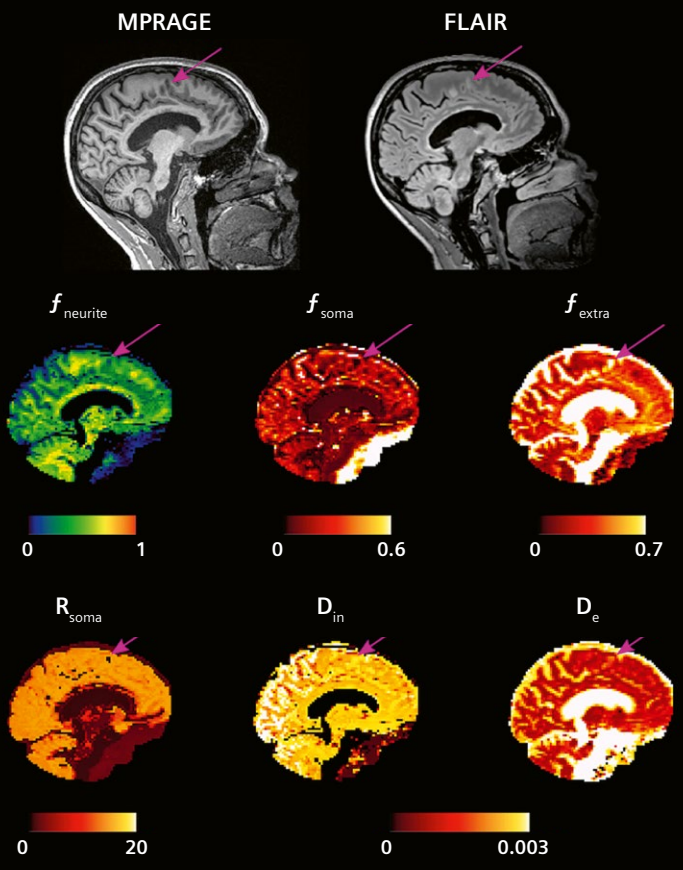

SIEMENS Healthineers

MAGNETOM Free.Star[1] 0.55T, Deep Resolve Gain & Sharp

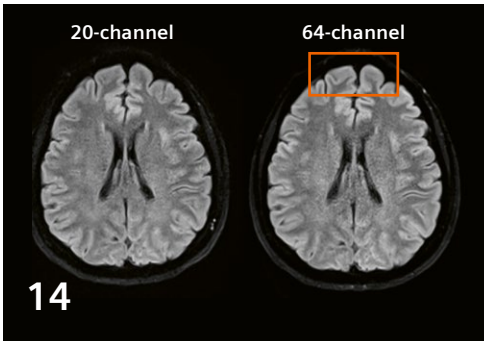

Ultrafast brain imaging with deep-learning multi-shot EPI

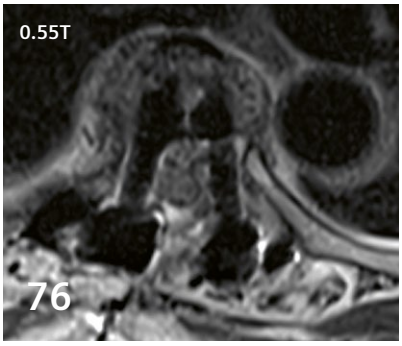

Improved assessment of the postoperative spine

Editorial Comment

Image Gallery

Neurologic Imaging

[1]MAGNETOM Free.Star is under development and is not commercially available. Future availability cannot be guaranteed.
[2]Work in progress. The application is currently under development and is not for sale in the U.S. and in other countries. Its future availability cannot be ensured.

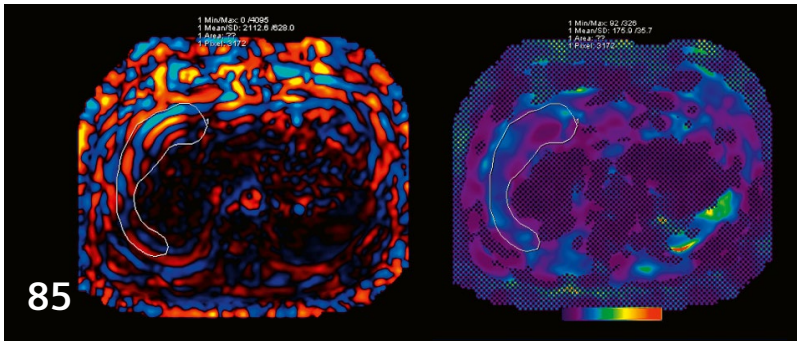

MR Elastography of the liver

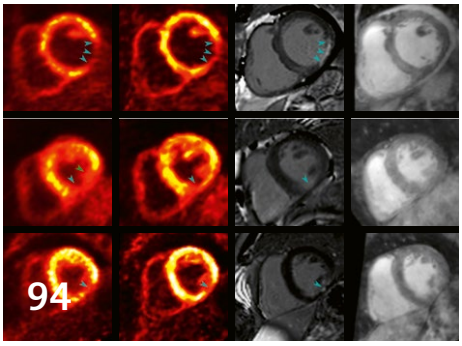

Enhanced myocardial PET-MR imaging

Musculoskeletal Imaging

Spotlight

Abdominal Imaging

Cardiovascular Imaging

Sustainability in Medical Technology

Meet Siemens Healthineers

Professor Daniel Alexander is Director of the Centre for Medical Image Computing (CMIC) and deputy head of the Computer Science Department at University College London (UCL), UK. He leads the Microstructure Imaging Group and the Progression of Neurodegenerative Diseases initiative. Professor Alexander is theme lead for the UCLH Biomedical Research Centre Healthcare Engineering and Imaging theme. He coordinates the Horizon 2020 EuroPOND consortium. His core expertise is in computer science, computational modelling, machine learning, and imaging science.

His first degree was a BA in Mathematics from Oxford, UK completing in 1993. He then studied for MSc and PhD in Computer Science at UCL, completing in 1997. After a post-doc at the University of Pennsylvania, USA, he returned to UCL as a lecturer in 2000 and has been Professor of Imaging Science since 2009.

Dear readers and colleagues,

How exciting is it to be gathering in person as a community again this year for ISMRM in London??? For many of us, the first major gathering of minds for almost three years. I can't wait! My schedule for the week is already delightfully overbooked. And I can feel the buzz building from students attending their first real-life conference (despite being in year 3 of their PhD already!), through to professors who have lost count of how many ISMRMs they have attended ... ahem, mentioning no names ...

I am always fascinated by how developments at the cutting edge of a technology can ultimately define the mainstream. Even when new techniques seem limited to use in only the most highly specialised centres, they are so often essential steps towards advances that ultimately transform research and practice. This year's ISMRM issue of MAGNETOM Flash brings these thoughts to mind through its juxtaposition of cutting-edge advances on high end platforms, e.g. 7T, with realisation of clinical capability on lighter platforms designed for accessibility, e.g. the MAGNETOM Free.Max 0.55T system.

MAGNETOM Flash's focus this time on advanced neuroimaging highlights, as always, advances at the forefront of MRI development and application. Applications in the brain using the latest hardware and software technologies so often drive forward innovations in MRI that propagate to other platforms and applications. We hear about the latest in deep-learning-based EPI for ultra-fast imaging and distortion-free diffusion-weighted imaging from Siemens Healthcare (Clifford et al; Zhou and Liu, respectively). Then three external articles focus on applications in multiple sclerosis. First, how the latest in diffusion MRI can underpin emerging models of disease (Schiavi and Inglese) aiming ultimately to inspire new and effective treatments and interventions. Second, an update on FLAIR Fusion (Bartsch et al.) and how the latest workflow enables robust longitudinal analysis in multiple sclerosis and beyond. Third, thoughts (from Kitzler et al.) on the pathways for translation of computer-assisted MRI assessments in multiple sclerosis to widespread usage in the clinic; thoughts which of course extend to much wider application areas. Attention then switches to epilepsy (Obusez et al.), one of the key demonstrators of how 7T can provide clinical benefit over 3T – blazing the trail for, we hope, a coming of age of 7T over the next decade as a widespread clinical tool. A key element of that maturity of course will be parallel transmit and (Massire, Boulant et al.) provide a welcome breakdown of the latest anatomical sequences available that exploit pTx on the MAGNETOM Terra[1].

Articles by Breit et al. and Sauernheimer in this issue focus on capability of the MAGNETOM Free.Max, highlighting the MR community's recent pursuit of increased accessibility. The former showcases musculoskeletal imaging on this platform, which opens availability to a broader subject base including for example patients with obesity, tattoos, implants, etc. who may find MRI exams unavailable to them on higher field, smaller bore systems. Finally, this issue offers snapshot updates from abdominal imaging, specifically elastography in the liver (Kolipaka et al.), cardiovascular imaging obtaining motion-corrected PET via a PET-MR platform (Munoz, Prieto, et al.), and prospects for sustainability of MR for future generations (von Grätz).

The theme of accessible MRI – devices and analysis techniques that can be deployed to and utilised effectively in low-resource settings and/or are open to wider groups of participants – has come strongly to the fore over the last two pandemic years. Viable portable technology has been a long-standing challenge for the MR community. The convergence of advances in MR hardware and in AI-driven optimised acquisition and reconstruction algorithms have made this a reality. The launch of the Hyperfine Swoop system on the open market is a clear landmark in development. Other systems are close on its heels. Portable systems typically use < 0.1T magnets largely through necessity. However, low-field (< 1T) non-portable systems also offer appeal. They have lower cost of both manufacture and installation, smaller footprint, can accommodate

[1] *For MAGNETOM Terra, pTx technology is included in Research mode (as part of the optional Dual mode) and is not intended for clinical use. Research operation may require observation of national regulations.*

patient groups that cannot be imaged at higher field as mentioned above, can image body parts (e.g. the lungs and other areas with abundant air/tissue interfaces) more effectively than at higher field, and potentially offer different contrasts to higher fields by accessing different relaxation regimes. The launch in 2021 of the MAGNETOM Free.Max is another significant recent landmark, showing the return of mainstream MR manufacturers to these lower field strengths.

So existance proofs show these technologies are viable, and clearly scenarios exist where they offer an advantage. But questions and challenges remain. In what set of clinical scenarios do they offer enough advantage over competing technologies to support an emerging market? Can they compete with, say, ultrasound or X-ray in low-resource settings? Do they offer enough unique capability compared to higher field systems in high resource settings? There is also no doubt that such devices open up compelling research questions. What minimal set of measurements is sufficient to reconstruct a clinically useful image? Will the challenges in sparse image reconstruction drive new frontiers in machine learning? In general, how can advances at the forefront of MRI technology genuinely add value in low-resource settings?

Answers to the last question in particular may come from surprising places. My own experience of working to repurpose state-of-the-art technologies designed for application in high-income countries (HICs) for benefit in lower-and-middle-income countries (LMICs) have been challenging but inspiring, always surprising, sometimes shocking. I have long had a vision of democratising high end imaging tools through machine learning. That vision inspired my work on image quality transfer (IQT); see figures 1 and 2. In 2013 a consortium of UK researchers, led by Derek Jones in Cardiff, UK, obtained funding to work with Siemens Healthineers to install the Connectom[2] scanner in Cardiff. Being part of that team gave me the impetus to develop the first IQT implementation aiming to estimate, given an image from a standard hospital scanner, the image we would have got by transporting the patient to the super-scanner in Cardiff (Fig. 1). Soon afterwards,

[2] *MAGNETOM Connectom is ongoing research. Siemens Healthcare does not intend to commercialize the system.*

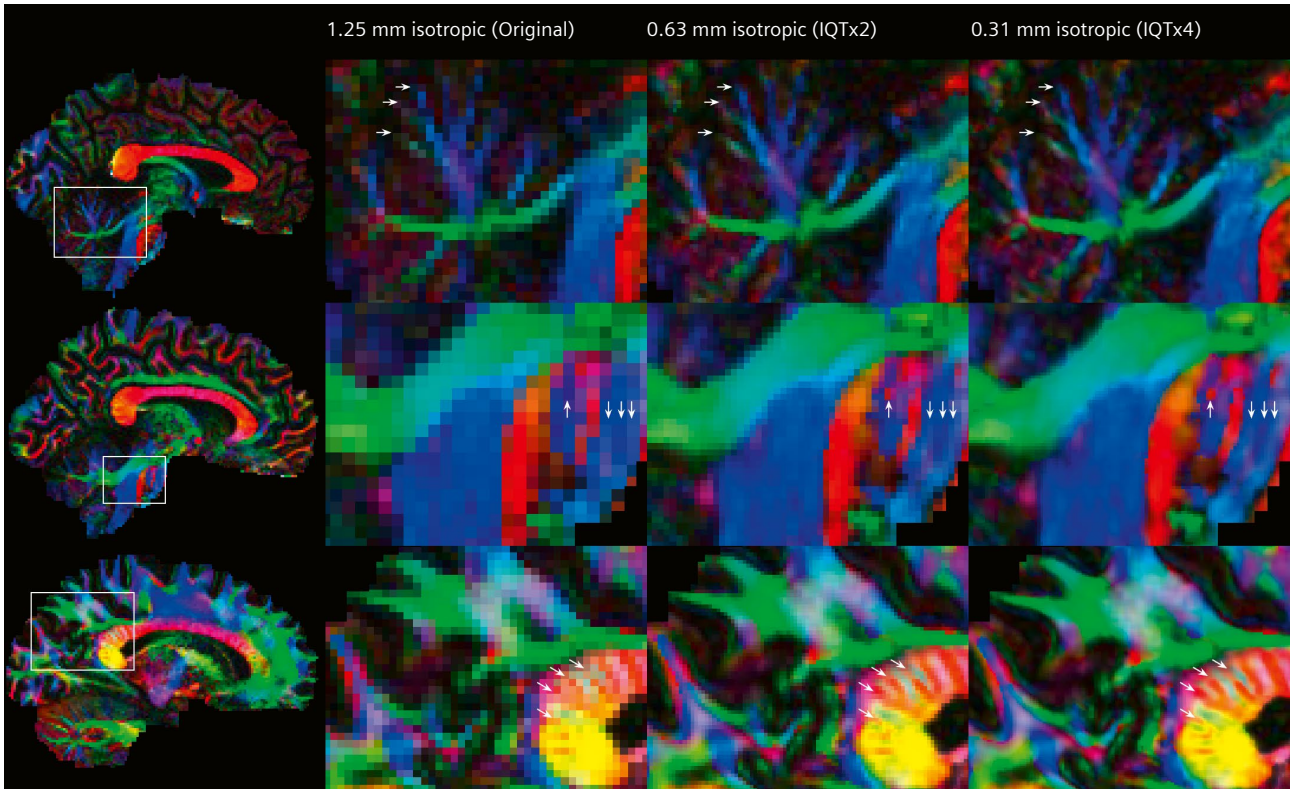

1 Enhanced resolution and contrast from Image Quality Transfer (figure from Alexander et al. Neuroimage 2017). The original implementation (Alexander et al. MICCAI 2014; Neuroimage 2017) used a simple patch-regression approach via random-forest machine-learning. Later implementations, e.g. (Tanno et al. Neuroimage 2021; Iglesias et al. Neuroimage 2021), use deep learning, which improves performance substantially. This initial demonstration aims to estimate specialized diffusion MR images from high gradient systems (MAGNETOM Prisma / Connectom) given an input image from a more standard hospital scanner. It reveals hidden detail and can enhance tractography of small pathways.

I established a collaboration with the University College Hospital in Ibadan, Nigeria with the aim of repurposing the IQT technology to enhance images from low-field MRI scanners, specifically their workhorse 0.36T open permanent-magnet system (Fig. 3), to estimate the image we would have obtained by flying a patient to London and imaging them with a modern 1.5T or 3T machine (Fig. 2 and 4). Their system is typical of LMIC scenarios; the choice is driven by low cost, availability of machine and maintenance, ease of installation, and robustness to frequent failures of power infrastructure. But of course, images from such systems lack the resolution and contrast of standard HIC systems, and that can prevent their usage for clinical decisions such as treatment planning for epilepsy; see figure 4.

Sounds like a great idea? It is! And quite rightly in 2017 the UK government's Global Challenges Research Fund awarded a team of us from UCL and Ibadan funding to develop the idea. But ... I'll leave the detail of the project itself for drinks at ISMRM evening events, and just give a few thoughts on the experience. First, I cannot emphasise enough the absolute necessity of local partners who believe in the project. Basic logistical challenges are impossible without them: recruiting patient cohorts, implementing scanning protocols compatible with local clinical workflows, navigating hospital administration, negotiating transportation, scan time, insurance, etc. etc. etc. But the partnership must run deeper. The idea of parachuting in with a cool machine-learning technology from London and revolutionising local radiology overnight is fantasy. Key application areas to demonstrate the potential and the adaptation of the underlying technology accordingly must be co-created to have a hope of gaining traction as a research initiative let alone translation as a clinical tool. Second, we must strive to understand the context. On first arriving at the hospital in Ibadan to discuss my "cool machine-learning technology from London" I was immediately struck by what a luxury item it is. Can we justify spending time and money on this when the hospital lacks basic capability like modern computers and internet? Those basic capabilities do need addressing, but nevertheless advanced "luxury" projects can help. They inspire forward thinkers to expedite change well beyond what the project envisioned. The most immediate impacts of our IQT-Nigeria project were not directly scientific, but more educational and cultural. They arose for example from getting radiologists in Nigeria and London together to exchange ideas and expertise on image assessment in different scenarios – both sides benefit hugely. We also used our visits to Ibadan to initiate training opportunities for computer science students and staff bringing new computational challenges to an immense pool of local talent and enabling sharing of experiences and ideas between UK and Nigerian computer scientists. The project itself also

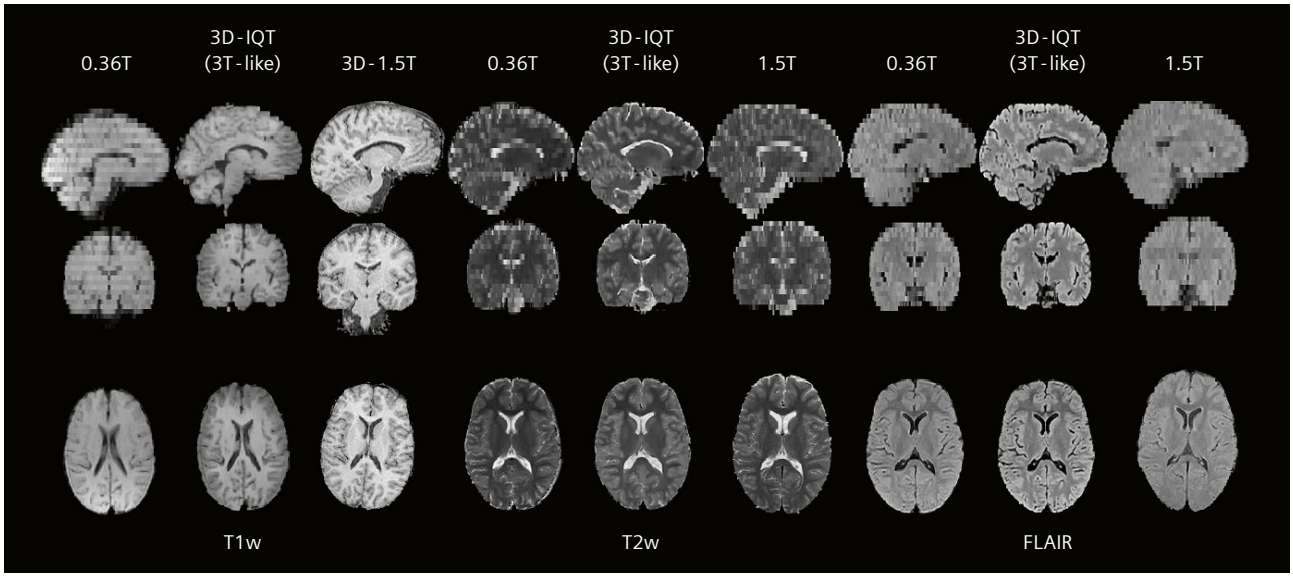

2 Image quality transfer adapted to enhance structural images from a 0.36T scanner in Ibadan, Nigeria, to approximate the image that would have been obtained by imaging the same subject at high field. The operation substantially enhances through-plane resolution and in-plane contrast (Images from Lin et al. MICCAI-MLMIR 2019).

3 The MRI suite and team at University College Hospital Ibadan, Nigeria, including my primary collaborators and friends in Ibadan, Ike Lagunju and Godwin Ogbole, and my wonderful colleague Delmiro Fernandez-Reyes at UCL.

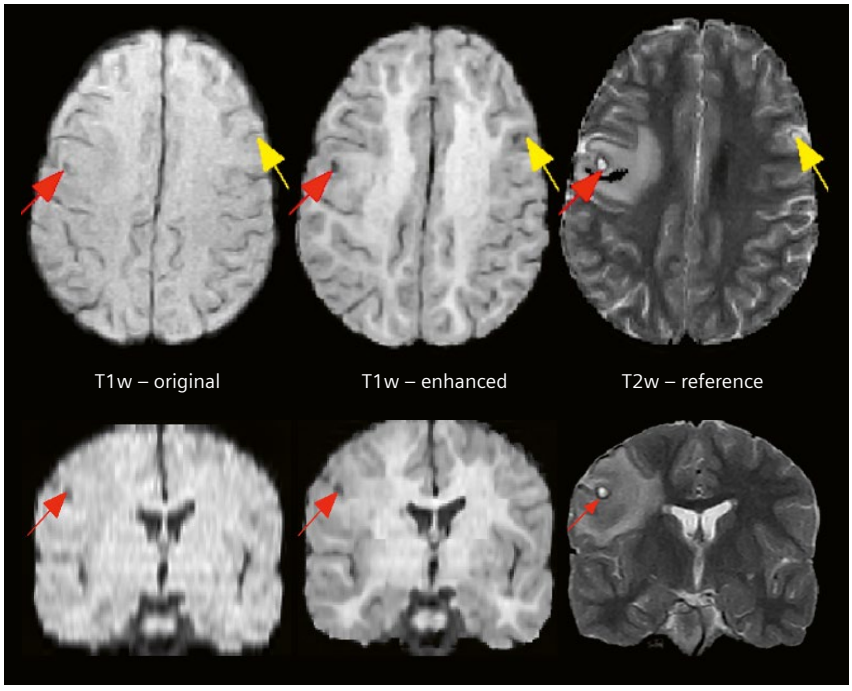

4 A particular case study from the project applying IQT to low-field images from Ibadan. This patient has lesions that are barely visible in the low-field T1-weighted image, but IQT substantially enhances conspicuity (from Lin et al. MICCAI-MLMIR 2019).

directly benefits a relatively small number of paediatric epilepsy patients who received enhanced imaging exams performed. However, the protocols we put in place for the project continue to benefit patients well beyond the initial study. All these activities generate excitement about such collaborations, highlight both the opportunities and the challenges, and give ammunition to arguments for improving basic infrastructure by showcasing the long term possibilities.

Several initiatives are now under way to deploy accessible MRI systems to LMICs around the world, such as the Gates Foundation's UNITY project, led by Steve Williams at King's College London, UK, and elements of the Wellcome Leap 1kD initiative, e.g. the Khula project, led by Kirsty Donald in Cape Town, South Africa. I firmly believe the new generation of low-field/low-power/portable/accessible MRI scanners offer benefit in Africa and LMICs in general, but equally firmly believe we have a way to go in pinning down precisely what those benefits are and how they dovetail with local practice, culture, politics, and beliefs. Early initiatives will teach many lessons that feedback into future devices, analysis tools, logistical solutions, and deployment strategies before we ultimately realise the benefits. Activities like the CAMERA network, see figure 5, which brings together African scientists and practitioners with MR developers and enthusiasts in the rest of the world, are essential to enable the communication we need to embark on this journey. Projects will require us to set aside many of the usual metric-driven markers of scientific success, embrace a substantial serving of chaos, and

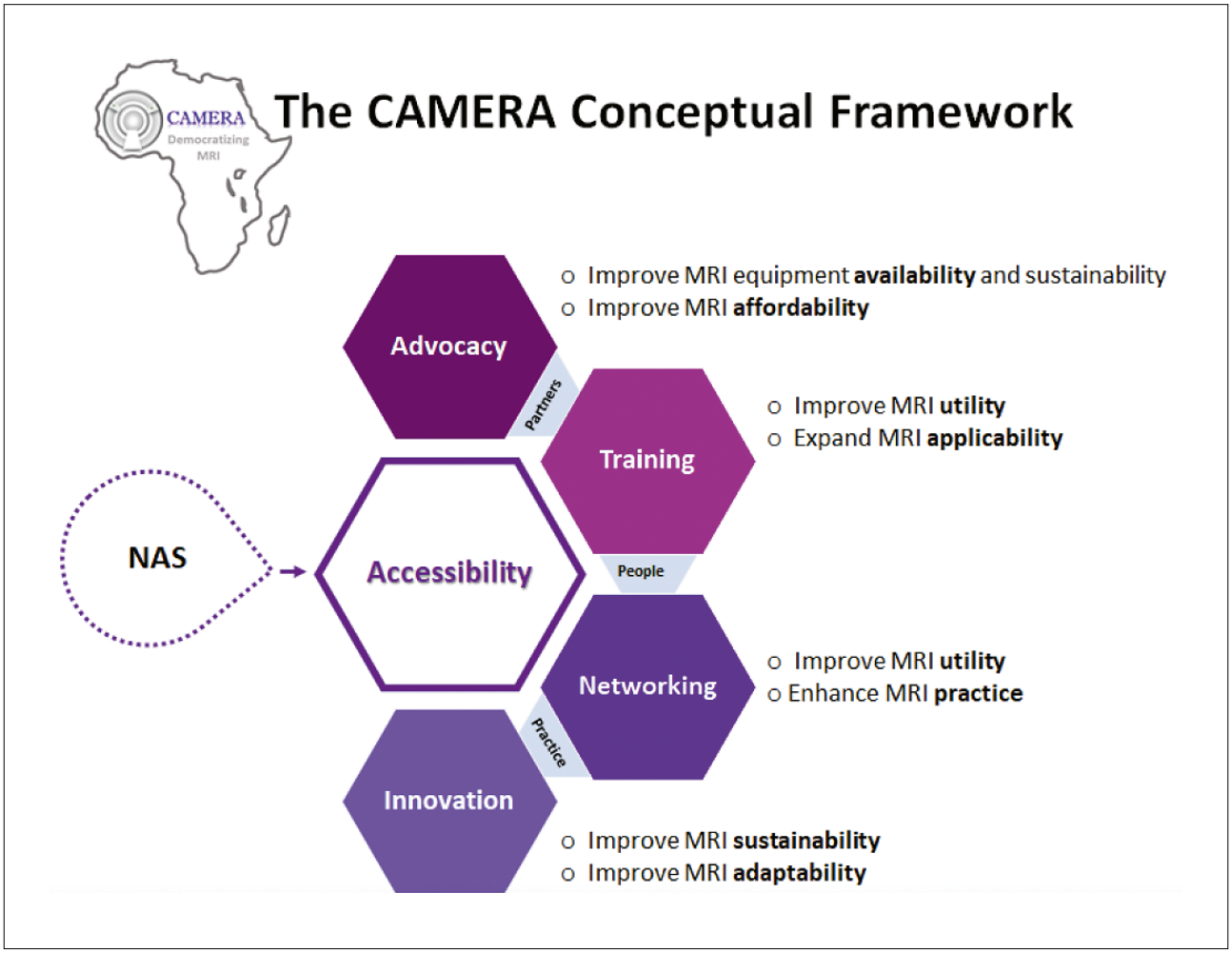

5 The CAMERA (Consortium for Advancement of MRI Education and Research in Africa) network led by the very excellent Udunna Anazodo (McGill). Many thanks to Udunna for generating and sharing the figure.

dedicate time to engage fully with diverse often unfamiliar stakeholders. However, at least in my experience, the rewards are manifold and unexpected. My small IQT-Nigeria project has been one of my favourites over the years. I fully intend to continue the work it started and encourage others to explore similar opportunities.

I hope this issue of MAGNETOM Flash and this year's ISMRM inspire more work at both the cutting edge on high end platforms and in pushing forward accessible MRI, and perhaps most importantly how the two endeavours can inform one another. Looking forward to seeing everyone in London soon!

Danny Alexander

We appreciate your comments.
Please contact us at magnetomworld.team@siemens-healthineers.com

Editorial Board

Review Board

Acquiring sharper images, faster than ever before

Deep reinforcement learning image reconstruction is the next chapter in the digital future of magnetic resonance imaging. With Deep Resolve technologies, Siemens Healthineers applies AI to image acquisition and uses deep learning for accelerated image reconstruction. With a convolutional neural network at its core, it can radically shorten acquisition time without compromising image resolution. We have a solid foundation of state-of-the-art medical technology and curated data from an international network and continue to drive the digitalization of healthcare and improve the patient experience by securely developing AI-powered solutions in MRI.

Targeted denoising and deep learning methods power **Deep Resolve Gain** and **Deep Resolve Sharp** technologies for sharper images acquired in faster scans. Deep Resolve Sharp generates a high-resolution image from low-resolution input. By including raw data in the reconstruction process, clinically robust results are achieved that, in combination with Deep Resolve Gain, outperform classical denoising and interpolation.

Deep Resolve Boost is a raw data-to-image deep learning reconstruction technology that enables high SNR and radically accelerated image acquisition. In combination with Deep Resolve Sharp and SMS it enables faster acquisitions than ever before.

Deep Resolve Swift Brain neuro acquisition combines a multi-shot echo planar imaging (EPI) approach with Deep Learning reconstruction to achieve all relevant contrasts in just one go, enabling a total neuro exam in two minutes.

MAGNETOM Free.Star[1] 0.55T,
T1 SE sag,
resolution 0.4 × 0.4 × 5.0 mm³,
TA 02:38 min

MAGNETOM Free.Star[1] 0.55T,
T2 TSE tra,
Deep Resolve Gain & Sharp,
resolution 0.4 × 0.4 × 5.0 mm³,
TA 02:50 min

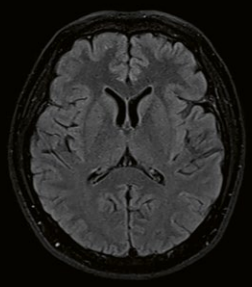

MAGNETOM Free.Star[1] 0.55T,
T2 TSE FLAIR,
Deep Resolve Gain & Sharp,
resolution 0.4 × 0.4 × 5.0 mm³,
TA 04:32 min

7aaaa0195

MAGNETOM Vida 3T,
Deep Resolve Swift Brain,
T1, PAT 3,
resolution 1.0 × 1.0 × 4.5 mm³,
TA 00:21 min

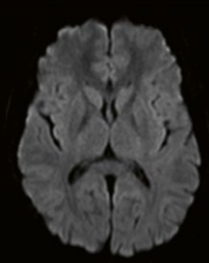

MAGNETOM Vida 3T,
Deep Resolve Swift Brain,
DWI *b*-value 1000 s/mm²,
PAT 2 SMS 2,
resolution 0.7 × 0.7 × 4.0 mm³,
TA 00:21 min

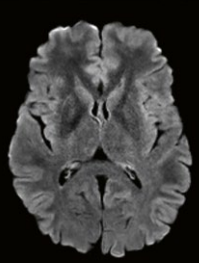

MAGNETOM Vida 3T, Deep
Resolve Swift Brain,
T2 FLAIR, PAT 2,
resolution 0.9 × 0.9 × 4.0 mm³,
TA 00:50 min

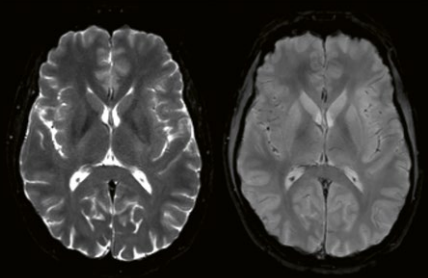

MAGNETOM Vida 3T,
Deep Resolve Swift Brain,
T2 SE + T2*, PAT 2,
resolution 0.9 × 0.9 × 4.0 mm³,
TA 00:25 min

2aaaa2230

[1] *MAGNETOM Free.Star is under development and is not commercially available. Future availability cannot be guaranteed.*

7aaaa0164

MAGNETOM Free.Star[1] 0.55T,
T2 TSE sag,
Deep Resolve Gain & Sharp,
resolution 0.5 x 0.5 x 3.0 mm³,
TA 03:28 min

MAGNETOM Free.Star[1] 0.55T,
T1 TSE sag,
Deep Resolve Gain & Sharp,
resolution 0.5 x 0.5 x 3.0 mm³,
TA 03:50 min

MAGNETOM Free.Star[1] 0.55T,
T2 STIR sag,
Deep Resolve Gain & Sharp,
resolution 0.5 x 0.5 x 3.0 mm³,
TA 03:51 min

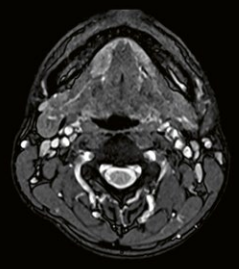

MAGNETOM Free.Star[1] 0.55T,
T2 MEDIC 2D tra,
resolution 0.4 x 0.4 x 3.0 mm³,
TA 04:14 min

7aaaa0259

MAGNETOM Free.Max 0.55T,
PD TSE FatSat cor, PAT 2 SMS 2 Deep Resolve Gain & Sharp, resolution 0.4 × 0.4 × 3.0 mm³, TA 02:55 min. *Courtesy of Radiologische Gemeinschaftspraxis Halle, Germany*

MAGNETOM Free.Max 0.55T, T1 TSE cor,
SMS 2 Deep Resolve Gain & Sharp,
resolution 0.3 × 0.3 × 3.0 mm³, TA 03:19 min.
Courtesy of Radiologische Gemeinschaftspraxis Halle, Germany

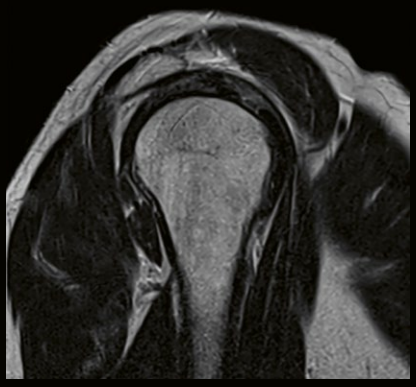

MAGNETOM Free.Max 0.55T, T2 TSE sag,
PAT 2 SMS 2 Deep Resolve Gain & Sharp,
resolution 0.4 × 0.4 × 3.0 mm³, TA 02:34 min.
Courtesy of Radiologische Gemeinschaftspraxis Halle, Germany

2aaaa2260

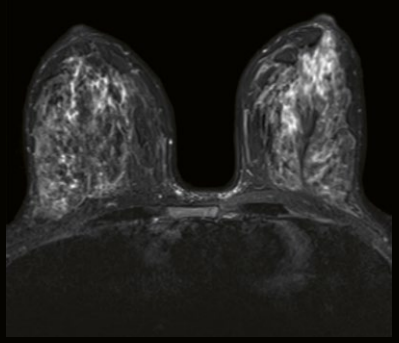

MAGNETOM Vida 3T, T2 STIR TSE, PAT 3,
resolution 0.8 × 0.8 × 4.0 mm³, TA 02:32 min

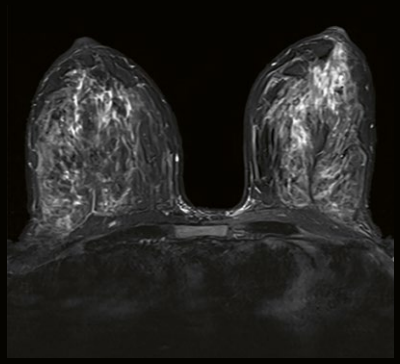

MAGNETOM Vida 3T, T2 STIR TSE,
PAT 4 Deep Resolve Boost & Sharp,
resolution 0.4 × 0.4 × 4.0 mm³, TA 01:21 min

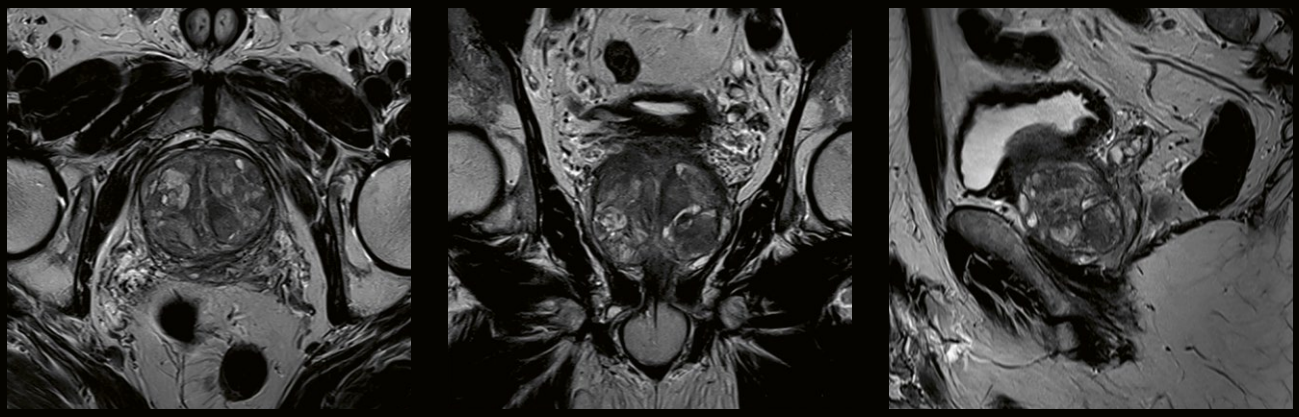

2aaaa2271

MAGNETOM Vida Fit 3T,
T2 TSE tra, PAT 4 Deep Resolve Boost,
resolution 0.3 × 0.3 × 3.0 mm³, TA 00:56 min

MAGNETOM Vida Fit 3T,
T2 TSE cor, PAT 4 Deep Resolve Boost,
resolution 0.3 × 0.3 × 3.0 mm³, TA 00:56 min

MAGNETOM Vida Fit 3T,
T2 TSE sag, PAT 4 Deep Resolve Boost,
resolution 0.3 × 0.3 × 3.0 mm³, TA 00:51 min

2aaaa2270

MAGNETOM Vida 3T,
PD TSE cor, PAT 3 Deep Resolve Boost & Sharp,
resolution 0.1 × 0.1 × 2.0 mm³,
TA 00:40 min

MAGNETOM Vida 3T,
PD TSE FatSat cor, PAT 3 Deep Resolve Boost & Sharp,
resolution 0.2 × 0.2 × 2.0 mm³,
TA 00:37 min

MAGNETOM Vida 3T,
PD TSE tra, PAT 3 SMS 2 Deep Resolve Boost & Sharp,
resolution 0.2 × 0.2 × 2.5 mm³,
TA 00:30 min

MAGNETOM Vida 3T,
PD TSE FatSat tra, PAT 3 SMS 2 Deep Resolve Boost & Sharp,
resolution 0.1 × 0.1 × 2.5 mm³,
TA 00:30 min

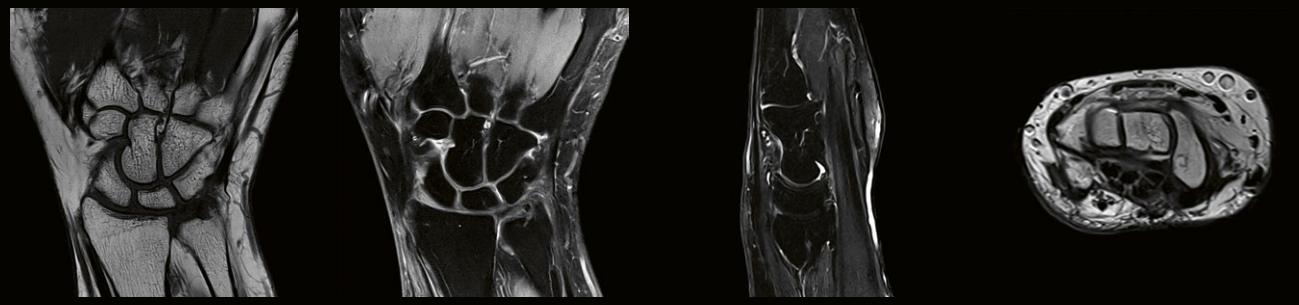

1aaaa4024

MAGNETOM Sola Fit 1.5T,
T1 TSE cor, PAT 4 Deep Resolve Boost & Sharp[2],
resolution 0.1 × 0.1 × 2.0 mm³,
TA 00:45 min

MAGNETOM Sola Fit 1.5T,
PD TSE FatSat cor, PAT 4 Deep Resolve Boost & Sharp[2],
resolution 0.1 × 0.1 × 2.0 mm³,
TA 02:17 min

MAGNETOM Sola Fit 1.5T,
T2 TSE FatSat sag, PAT 4 Deep Resolve Boost & Sharp[2],
resolution 0.2 × 0.2 × 2.0 mm³,
TA 01:44 min

MAGNETOM Sola Fit 1.5T,
T2 TSE tra, PAT 4 Deep Resolve Boost & Sharp[2],
resolution 0.2 × 0.2 × 2.0 mm³,
TA 00:28 min

[2]Work in progress. For MAGNETOM Sola Fit the application is currently under development and is not for sale in the U.S. and in other countries. Its future availability cannot be ensured.

1aaaa4040

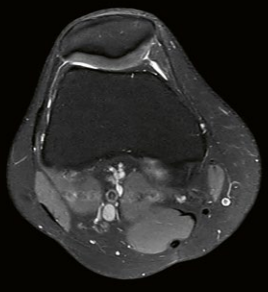

MAGNETOM Sola 1.5T, PD TSE FatSat tra, PAT 2 Deep Resolve Gain & Sharp, resolution 0.2 × 0.2 × 3.0 mm³, TA 01:04 min

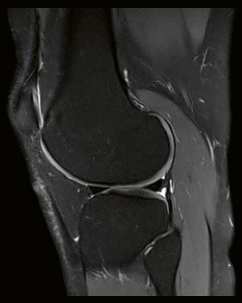

MAGNETOM Sola 1.5T, PD TSE FatSat sag, PAT 2 Deep Resolve Gain & Sharp, resolution 0.3 × 0.3 × 3.0 mm³, TA 02:38 min

MAGNETOM Sola 1.5T, PD TSE FatSat cor, PAT 2 Deep Resolve Gain & Sharp, resolution 0.2 × 0.2 × 3.0 mm³, TA 01:17 min

MAGNETOM Sola 1.5T, T1 TSE cor, PAT 2 Deep Resolve Gain & Sharp, resolution 0.2 × 0.2 × 3.0 mm³, TA 01:30 min

7aaaa0272

MAGNETOM Free.Max 0.55T, T1 TSE sag, PAT 2 SMS 2 Deep Resolve Gain & Sharp, resolution 0.2 × 0.2 × 3.0 mm³, TA 03:43 min

MAGNETOM Free.Max 0.55T, PD TSE FatSat sag, PAT 2 SMS 2 Deep Resolve Gain & Sharp, resolution 0.3 × 0.3 × 3.0 mm³, TA 02:42 min

MAGNETOM Free.Max 0.55T, PD TSE FatSat cor, PAT 2 SMS 2 Deep Resolve Gain & Sharp, resolution 0.3 × 0.3 × 3.0 mm³, TA 02:49 min

7aaaa0272

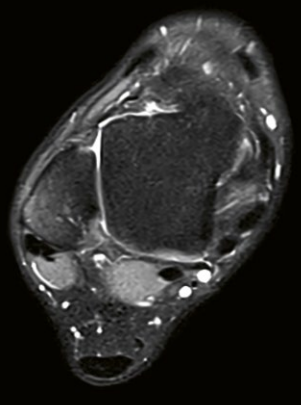

MAGNETOM Free.Max 0.55T, PD TSE FatSat tra, PAT 2 SMS 2 Deep Resolve Gain & Sharp, resolution 0.3 × 0.3 × 3.0 mm³, TA 02:28 min

MAGNETOM Free.Max 0.55T, T2 TSE tra, PAT 2 SMS 2 Deep Resolve Gain & Sharp, resolution 0.2 × 0.2 × 3.0 mm³, TA 01:59 min

Ultrafast Brain Imaging with Deep-Learning Multi-Shot EPI: Technical Implementation

Bryan Clifford[1], John Conklin[2], Susie Y. Huang[2], Thorsten Feiweier[3], Zahra Hosseini[4], Azadeh Tabari[2], Augusto Lio M. Goncalves Filho[2], Serdest Demir[2], Wei-Ching Lo[1], Stephan Kannengiesser[3], Dominik Nickel[3], Min Lang[2], Maria Gabriela Figueiro Longo[2], Michael Lev[2], Pam Schaefer[2], Otto Rapalino[2], Kawin Setsompop[5], Berkin Bilgic[6], Stephen Cauley[6]

[1]Siemens Medical Solutions USA, Boston, MA, USA
[2]Department of Radiology, Massachusetts General Hospital, Boston, MA, USA
[3]Siemens Healthineers, Erlangen, Germany
[4]Siemens Medical Solutions USA, Atlanta, GA, USA
[5]Department of Radiology and Department of Electrical Engineering, Stanford University, Stanford, CA, USA
[6]Department of Radiology, A. A. Martinos Center for Biomedical Imaging, Massachusetts General Hospital, Harvard Medical School, Boston, MA, USA

This work was performed using a prototype that led to the development of the Deep Resolve Swift Brain product.

Introduction

MRI is a crucial tool for the diagnosis and treatment planning of neurological diseases. Compared to CT and ultrasound, however, the underlying physics of the MR imaging process necessitates relatively long acquisition times. This has limited the use of brain MRI in time- or motion-sensitive settings, such as the emergency department, where long or repeated scans can delay urgently needed treatment [1–4].

The integration of parallel imaging (PI) and simultaneous multi-slice (SMS) imaging techniques [5–8] into standard turbo-spin-echo (TSE)-based clinical protocols has allowed for exam times of approximately 10 minutes. Advances in 3D volumetric encoding schemes [9], compressed sensing [10], and deep-learning (DL) reconstruction techniques [11–13] have helped alleviate the geometry-factor (*g*-factor) noise amplification of standard PI and SMS techniques to provide additional acceleration and further reduce exam times. Current application of these techniques to standard TSE-based protocols has lead to exam times of approximately 5 minutes [14–16].

Recently, single-shot echo-planar imaging (ssEPI) has been used to enable ultrafast multi-contrast exams on the order of 1–2 minutes [17, 18]. ssEPI acquisitions acquire all *k*-space lines after a single excitation or "shot" and allow for very rapid scan times, but require longer readout durations and echo times. As such, ssEPI images often suffer from susceptibility-induced geometric distortion as well as signal dropout and pileup artifacts.

To take advantage of the efficiency of EPI while mitigating signal-to-noise (SNR) and susceptibility-induced losses to image quality, we have developed a multi-shot EPI (msEPI)-based prototype[1] that leverages a DL-based image reconstruction to provide high-SNR T1w, T2w, T2*, and T2-FLAIR, complemented by ssEPI diffusion imaging within a 2-minute exam. The prototype's msEPI acquisition acquires readout lines in an interleaved fashion across several shots to achieve shorter echo times and reduce geometric distortion. At the same time, the DL-based image reconstruction produces high-SNR images and limits *g*-factor noise amplification. To provide greater flexibility and robustness to variations in the clinical workflow, the prototype allows each contrast to be acquired individually, in any orientation, and the DL-reconstruction includes a tunable parameter which can be automatically selected to optimize image quality and data fidelity.

In the following sections, we describe the prototype's data acquisition and image reconstruction methods, and provide performance evaluation metrics and preliminary results on clinical data not included during training.

Data acquisition

Prototype sequences were developed for acquiring T1w, T2w, T2*, FLAIR, and diffusion-weighted imaging data. Multi-shot acquisitions with high per-shot undersampling factors were used for all but the DWI sequence, which was

[1]*Work in progress. The application is currently under development and is not for sale in the U.S. and in other countries. Its future availability cannot be ensured.*

acquired using an SMS ssEPI acquisition. T2w and T2* contrasts are obtained before and after the refocusing pulse of the same msEPI scan, which further increases the sampling efficiency. To provide robustness against intra-scan motion and allow for the individual acquisition of any contrast, each scan was preceded by a fast FLASH reference scan [19], which was used to compute coil sensitivity maps, GRAPPA [5], and/or SMS kernels [20]. Additional information on the data acquisition is provided in [21].

Clinical evaluation data were acquired on patients and healthy volunteers using a 20-channel head/neck coil and a 64-channel head coil on 3T systems (MAGNETOM Prisma and Vida, Siemens Healthcare, Erlangen, Germany) with informed written consent and in accordance with local IRB guidelines. Clinical reference data were acquired for comparison immediately before the prototype exam using a standard 10-minute clinical exam. Protocol parameters from both exams are shown in Figure 1.

A deep-learning network was trained using a dataset consisting of more than 26,000 images across T1w, T2w, T2*, and T2-FLAIR contrasts in axial, coronal, and sagittal orientations (Fig. 2). The 2-average data for network training and validation were acquired on a 3T system (MAGNETOM Skyra, Siemens Healthcare, Erlangen, Germany) using a 20-channel head/neck coil.

Deep-learning hybrid image reconstruction

The prototype sequences use a novel image reconstruction algorithm that integrates DL priors into an iterative SENSE [22] reconstruction (Fig. 3). Undersampled data acquired from the scanner are first passed through a standard

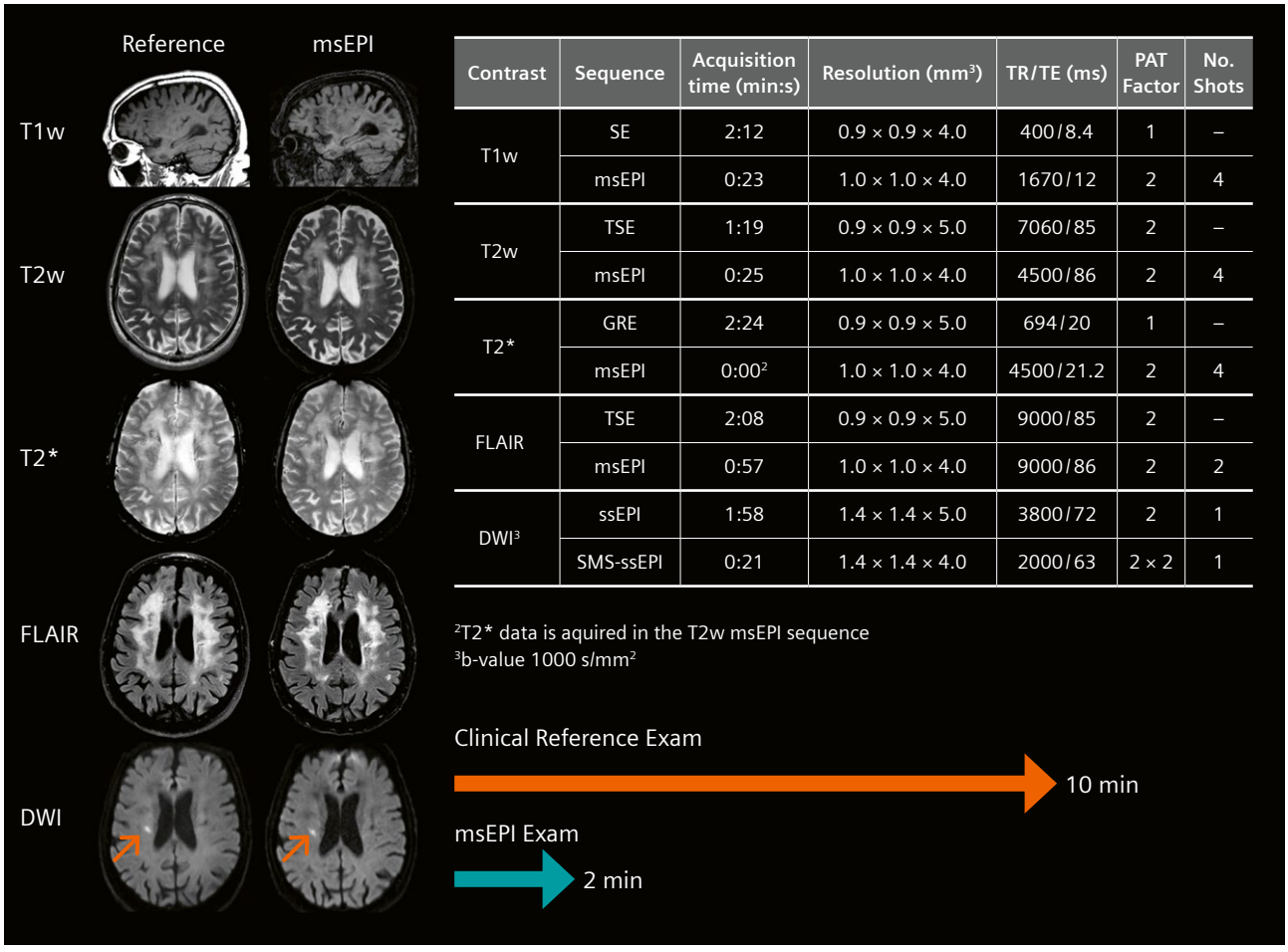

Contrast	Sequence	Acquisition time (min:s)	Resolution (mm³)	TR/TE (ms)	PAT Factor	No. Shots
T1w	SE	2:12	0.9 × 0.9 × 4.0	400/8.4	1	–
	msEPI	0:23	1.0 × 1.0 × 4.0	1670/12	2	4
T2w	TSE	1:19	0.9 × 0.9 × 5.0	7060/85	2	–
	msEPI	0:25	1.0 × 1.0 × 4.0	4500/86	2	4
T2*	GRE	2:24	0.9 × 0.9 × 5.0	694/20	1	–
	msEPI	0:00[2]	1.0 × 1.0 × 4.0	4500/21.2	2	4
FLAIR	TSE	2:08	0.9 × 0.9 × 5.0	9000/85	2	–
	msEPI	0:57	1.0 × 1.0 × 4.0	9000/86	2	2
DWI[3]	ssEPI	1:58	1.4 × 1.4 × 5.0	3800/72	2	1
	SMS-ssEPI	0:21	1.4 × 1.4 × 4.0	2000/63	2 × 2	1

[2]T2* data is aquired in the T2w msEPI sequence
[3]b-value 1000 s/mm²

1 Preliminary clinical results and protocol parameters of the msEPI and clinical reference exam. Images were obtained from a patient not included in the training or validation datasets, with a recent right corona radiata lacunar infarct (DWI images, arrows) and extensive white matter T2-FLAIR hyperintense signal abnormality likely related to cerebral small vessel disease. A graphical representation of the total acquisition times in the clinical reference and msEPI exams is included below the parameter table.

parallel imaging reconstruction, e.g., SENSE, which is used as input to an unrolled gradient-descent network (UGDN) [11]. The UGDN removes residual aliasing artifacts and noise from the initial reconstruction by iteratively passing the image through a deep neural network followed by a data-fidelity increasing operation which incorporates the physics of the acquisition and original measured data. The output of the UGDN, which will have good SNR but may be overly smooth, is then refined in a second iterative SENSE reconstruction, referred to as the DL-SENSE hybrid reconstruction [21].

The DL-SENSE hybrid reconstruction uses the image from the UGDN to regularize an iterative SENSE reconstruction and so generate a high-SNR image with good data fidelity and preservation of fine details. Specifically, the DL-SENSE hybrid reconstruction is a generalization of the methods in [23, 24] and computes the final image by solving the following optimization problem:

$$\min_{\boldsymbol{\rho}} || \boldsymbol{d} - \Omega \mathrm{FC}\boldsymbol{\rho} ||_2^2 + \lambda || \mathrm{WFC}(\boldsymbol{\rho}_{\mathrm{UGDN}} - \boldsymbol{\rho}) ||_2^2$$

where $\boldsymbol{d}$ and $\boldsymbol{\rho}$ are vectors of the measured data and image values, respectively; $\boldsymbol{\rho}_{\mathrm{UGDN}}$ is the output of the UGDN; F and C are the Fourier encoding and coil sensitivity operators; Ω is the *k*-space sampling operator; λ is a tunable denoising parameter; W is a diagonal weighting matrix.

A key feature of the DL-SENSE hybrid reconstruction is its ability to provide explicit control over the way the UGDN influences the final reconstructed image, which allows the same network to be applied to data acquired under novel noise conditions without the need for costly retraining. The user can control the balance between the fidelity of the final image with the measured data (left term in the above optimization problem) and with the output of the UGDN (right term in the above optimization problem) by tuning the denoising parameter λ. Similarly, the weighting matrix W controls the spectral mixing of information from the UGDN image and the measured data. In the current prototype, W was chosen as a sampling operator with the same undersampling factor as Ω but with complementary sample locations. For a given value of λ, this choice of W provided a desirable tradeoff between data fidelity and image quality and helped to focus the UGDN's representational power on unsampled *k*-space regions during training.

Network training and validation

The UGDNs used by the prototype were trained using images from a dataset consisting of more than 26,000 images across all contrasts and orientations (Fig. 2). During training, simulated training examples were generated by retrospectively undersampling high-SNR images, and noise was added to the simulated data to match clinical SNR levels. Separate UGDNs were trained for undersampling (PAT) factors of 2, 3, and 4. Networks were trained to minimize a loss function consisting of a weighted combination of the structural similarity index measure (SSIM) – known to correlate with radiologist quality rating [25, 26] – and the mean absolute error between the reconstructed images and their corresponding ground-truths.

Approximately 6,500 images in the dataset were excluded from training and reserved for validation of the trained networks. Following the same procedure used during training, noisy, undersampled data were generated from these images and reconstructed using the DL-SENSE hybrid scheme. The mean ± SD of the SSIM values between the reconstructed images and their corresponding ground-truth images are shown in Figure 2, sorted by contrast and PAT factor. These results indicate that the proposed method can reliably generate high-quality images, even at higher (≥ 3) acceleration factors.

Automatic selection of the denoising parameter

It can be challenging to select an appropriate denoising parameter given the variability seen in clinical settings. For a given protocol, the denoising parameter can be manually tuned according to radiologist preference; however, the ideal choice can vary with changes to protocol parameters, coil loading, coil selection, etc., which are common in the clinic. The parameter that yields the best results in one scenario may lead to overly smooth or noisy images in another scenario.

This problem was addressed by training a model to automatically select the denoising parameter based on estimated data SNR. The prototype computes the noise level using acquisition-specific noise calibration data and combines this with an estimate of the signal intensity to compute the SNR. A trained model then uses the estimated SNR to predict the denoising parameter preferred by radiologists [27]. This automatic, data-driven adaptation of the denoising parameter makes the prototype robust to changes in protocol parameters and automatically reduces the impact of the DL prior on the reconstruction in higher SNR (or lower PAT factor) scenarios, to maximize data fidelity while preserving image quality.

Figure 4A shows both the GRAPPA and DL-SENSE hybrid reconstructions of T2-FLAIR data (the contrast with lowest SNR) acquired from a healthy volunteer at PAT 2, 3, and 4. The GRAPPA reconstructions show the expected noise amplification with increasing PAT factor, but in the DL-SENSE hybrid reconstruction, the noise levels remain

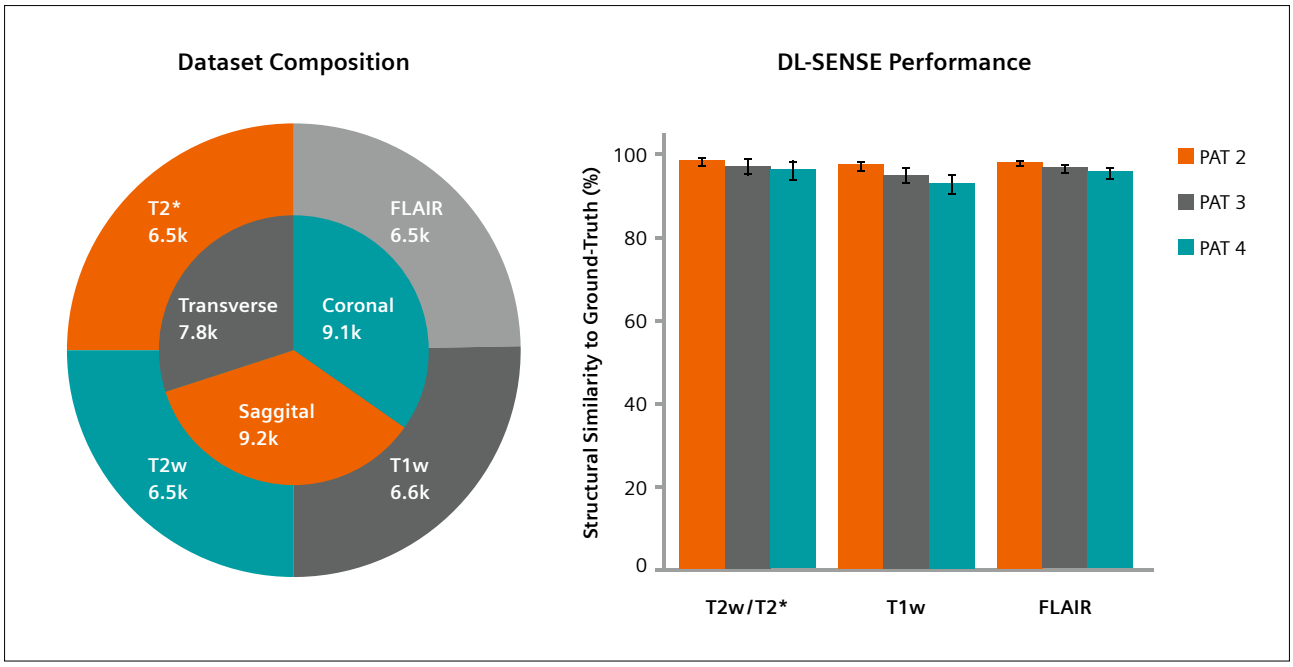

2 Dataset composition and validation results. The dataset consisted of more than 26,000 images and included T1w, T2w, T2*, and T2-FLAIR contrasts as well as coronal, sagittal, and transverse orientations, as shown in the pie chart. The bar chart shows the mean ± SD structural similarity index measure (SSIM) between DL reconstructions and the corresponding ground-truth validation images.

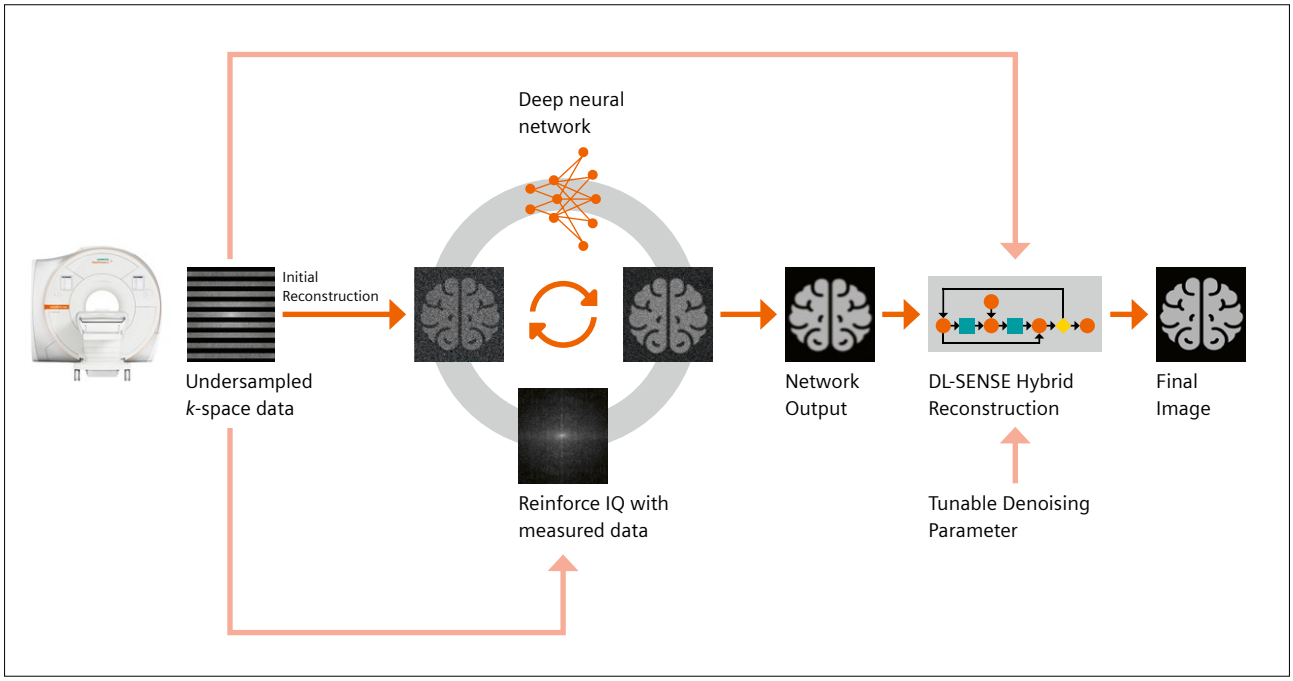

3 Illustration of the proposed reconstruction scheme. An initial SENSE reconstruction is generated from the undersampled *k*-space data and used as input to an unrolled gradient descent network (UGDN). The UGDN repeatedly alternates between deep neural-network denoising and data-fidelity updates to remove noise and residual aliasing while preserving the information in the acquired data. The UGDN output image and the measured data are then used in a regularized DL-SENSE hybrid reconstruction to produce the final image. By incorporating a tunable denoising parameter, the DL-SENSE hybrid reconstruction can be tailored to radiologist preference and also allows the same network to be applied to data acquired under noise conditions not previously seen without retraining.

relatively constant. Examination of representative denoising parameter values (orange markers in Figure 4B) shows that the trained model (orange line in Fig. 4B) automatically adjusts the denoising parameter as the PAT factor increases, using higher values for higher PAT factors. Figure 4B also shows example denoising parameter values from different contrasts and demonstrates how the model uses lower values for higher SNR contrasts (e.g., T2*) as well.

Reconstructions of T2-FLAIR data acquired on the same healthy volunteer using 20- and 64-channel coils are shown in Figure 5. Overall, the SNR of the two images is similar, but in the cortical region, the SNR of the 64-channel image is noticeably higher. These results suggest that the prototype can also adapt to changes in coil selection, allowing users to make the most out of higher density array coils.

Preliminary clinical results

We compared the proposed 2-minute prototype protocol to a standard TSE-based, 10-minute clinical reference protocol on a patient suffering from a recent right corona radiata lacunar infarct (DWI with restricted diffusion, Fig. 1 arrowheads) and extensive patchy and confluent

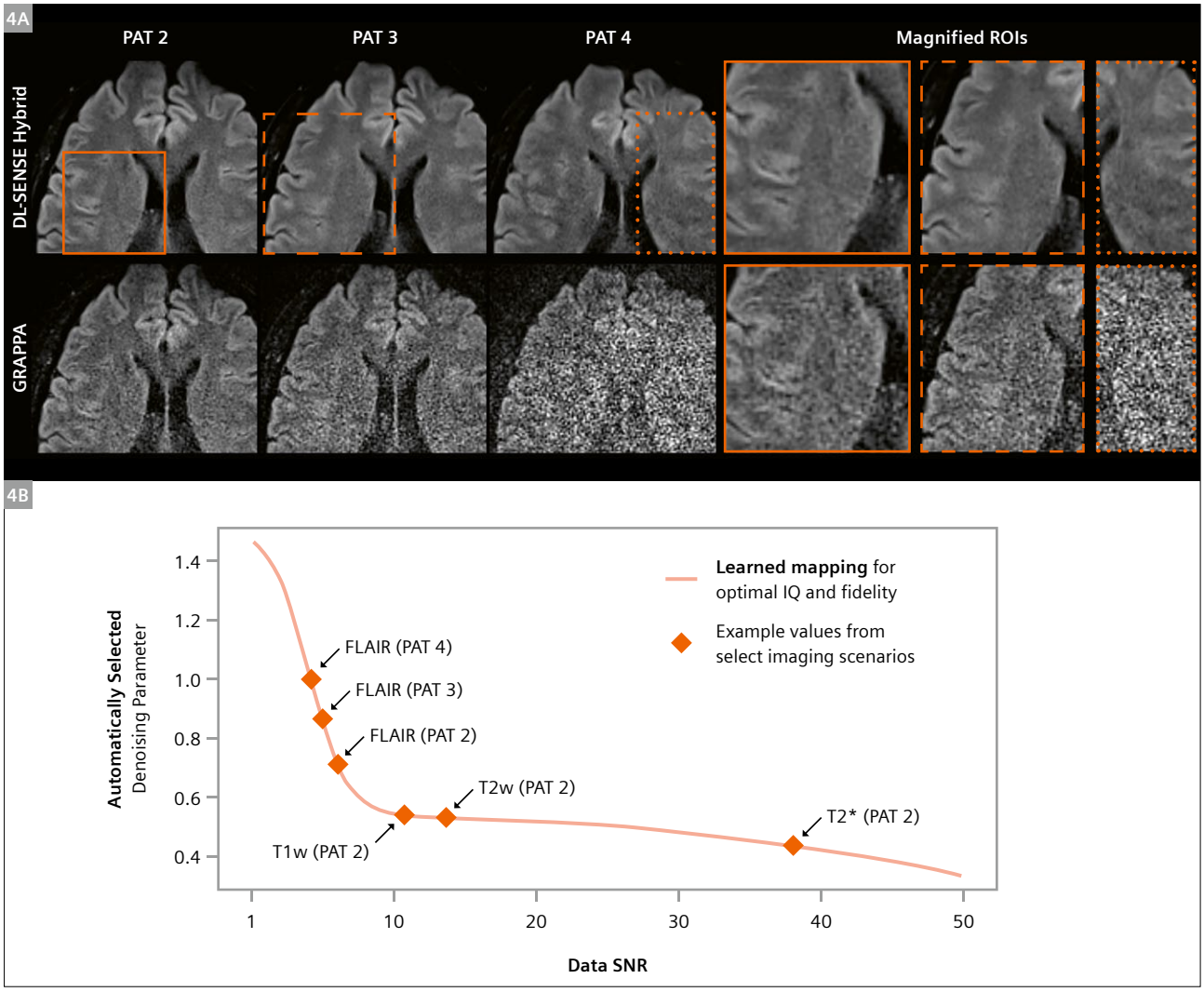

4 Generalization of the DL-SENSE hybrid reconstruction to higher undersampling (PAT) factors and varying SNR levels. **(4A)** Reconstructions of T2-FLAIR data acquired from a healthy volunteer at different PAT factors using the DL-SENSE hybrid reconstruction and GRAPPA. Magnified ROIs displayed on the right show how the proposed DL-SENSE reconstruction automatically adapts the denoising parameter to maintain image quality despite variations in the undersampling factor. **(4B)** The learned mapping between data SNR and optimal denoising parameter (orange line). The mapping was trained to predict parameters chosen by board-certified radiologists. The parameter values for the T2-FLAIR reconstructions in (4A) as well as for representative T1w, T2w, and T2* acquisitions are depicted by orange markers. The trained model tries to provide an optimal balance between image quality and data fidelity; in high-SNR scenarios, the model chooses lower values to maintain image quality while increasing data fidelity.

T2-FLAIR hyperintense white matter signal abnormality likely related to cerebral small vessel disease (T2-FLAIR, Fig. 1). Evaluation of the Figure 1 images by board-certified neuroradiologists indicated that, despite the nearly 5-fold reduction in exam time, the diagnostic quality of the images produced by the prototype was similar to that of the standard 10-minute exam. The white matter signal abnormality as well as the DWI/FLAIR mismatch (indicating a recent infarct) in the infarcted region can be clearly observed in the T2w, T2*, FLAIR, and DWI images from each protocol. Moreover, the gray/white differentiation of the msEPI T1w acquisition is similar to that of the reference SE T1w scan, despite the differences in the respective contrast mechanisms.

Although msEPI T1w images do not optimally depict facial soft tissues, which can be useful in certain diagnostic situations, it is interesting to note that the msEPI T1w images appear to depict the white matter lesions with greater conspicuity than the reference SE acquisition (possibly due to the increased T2* weighting). Regardless, future development will include the evaluation of a GRE-based T1w prototype sequence for the purposes of providing a nearly distortion-free reference, suitable for observing facial soft tissues.

In addition to the results presented here, clinical evaluations of earlier versions of this prototype have also been performed, with similar results [21, 28]. In particular, the report by Tabari et al. [28] provides initial results from a clinical evaluation on a large cohort of inpatients and emergency department patients, which indicate a high degree of interobserver agreement for major diagnostic findings, similar to that of the 5-fold slower clinical reference exam.

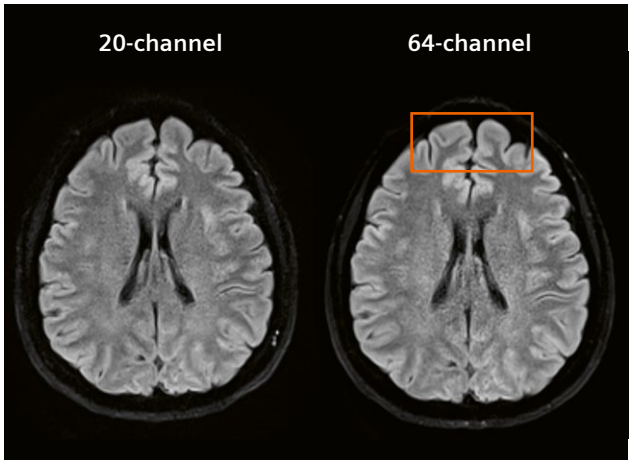

5 T2-FLAIR images acquired at 3T with the msEPI prototype sequence using the 20-channel head/neck coil and the 64-channel head coil from Siemens Healthineers. The msEPI prototype automatically adjusts the denoising level according to the SNR in each acquisition scenario, which makes it robust to variations in coil selection. To take advantage of the increased cortical sensitivity of the 64-channel coil, the prototype automatically reduces the denoising parameter in the DL-SENSE hybrid reconstruction to maximize IQ and data fidelity (see highlighted ROI).

Conclusions

We have developed an ultrafast MRI prototype that integrates a highly efficient msEPI acquisition with DL-based image reconstruction techniques to provide comprehensive brain MR imaging in a 2-minute exam. Although clinical evaluation on large patient cohorts is still ongoing, preliminary results indicate that the prototype can automatically adapt its DL reconstruction to variations in protocol parameters and coil selection to produce T1w, T2w, T2*, T2-FLAIR, and diffusion-weighted imaging with diagnostic quality similar to that of a standard 10-minute TSE-based acquisition.

References

1 Agarwal R, Bergey M, Sonnad S, Butowsky H, Bhargavan M, Bleshman MH. Inpatient CT and MRI utilization: trends in the academic hospital setting. J Am Coll Radiol. 2010;7(12):949–955.
2 Selvarajan SK, Levin DC, Parker L. The Increasing Use of Emergency Department Imaging in the United States: Is It Appropriate? AJR Am J Roentgenol. 2019;213(4):W180–W184.
3 Goyal M, Menon BK, van Zwam WH, Dippel DW, Mitchell PJ, Demchuk AM, et al. Endovascular thrombectomy after large-vessel ischaemic stroke: a meta-analysis of individual patient data from five randomised trials. Lancet. 2016;387(10029):1723–1731.
4 Berkhemer OA, Fransen PS, Beumer D, van den Berg LA, Lingsma HF, Yoo AJ, et al. A randomized trial of intraarterial treatment for acute ischemic stroke. N Engl J Med. 2015;372(1):11–20.
5 Griswold MA, Jakob PM, Heidemann RM, Nittka M, Jellus V, Wang J, et al. Generalized autocalibrating partially parallel acquisitions (GRAPPA). Magn Reson Med. 2002;47(6):1202–1210.
6 Pruessmann KP, Weiger M, Scheidegger MB, Boesiger P. SENSE: Sensitivity encoding for fast MRI. Magn Reson Med. 1999;42(5):952–962.
7 Glover GH. Phase-offset multiplanar (POMP) volume imaging: A new technique. J Magn Reson Imaging. 1991;1(4):457–61.
8 Barth M, Breuer F, Koopmans PJ, Norris DG, Poser BA. Simultaneous multislice (SMS) imaging techniques. Magn Reson Med. 2016;75(1):63–81.
9 Bilgic B, Gagoski BA, Cauley SF, Fan AP, Polimeni JR, Grant PE, et al. Wave-CAIPI for highly accelerated 3D imaging. Magn Reson Med. 2015;73(6):2152–2162.
10 Liang D, Liu B, Wang J, Ying L. Accelerating SENSE using compressed sensing. Magn Reson Med. 2009;62(6):1574–84.
11 Hammernik K, Schlemper J, Qin C, Duan J, Summers RM, Rueckert D. Systematic evaluation of iterative deep neural networks for fast parallel MRI reconstruction with sensitivity-weighted coil combination. Magn Reson Med. 2021;86(4):1859–1872.
12 Schlemper J, Caballero J, Hajnal JV, Price AN, Rueckert D. A Deep Cascade of Convolutional Neural Networks for Dynamic MR Image Reconstruction. IEEE Trans Med Imaging. 2018;37(2):491–503.

13 Aggarwal HK, Mani MP, Jacob M. MoDL: Model Based Deep Learning Architecture for Inverse Problems. IEEE Trans Med Imag. 2019;38(2):394–405.
14 Prakkamakul S, Witzel T, Huang S, Boulter D, Borja MJ, Schaefer P, et al. Ultrafast Brain MRI: Clinical Deployment and Comparison to Conventional Brain MRI at 3T. J Neuroimaging. 2016;26(5):503–510.
15 Recht MP, Zbontar J, Sodickson DK, Knoll F, Yakubova N, Sriram A, et al. Using Deep Learning to Accelerate Knee MRI at 3T: Results of an Interchangeability Study. AJR Am J Roentgenol. 2020;215(6):1421–1429.
16 Gassenmaier S, Afat S, Nickel D, Mostapha M, Herrmann J, Othman AE. Deep learning-accelerated T2-weighted imaging of the prostate: Reduction of acquisition time and improvement of image quality. Eur J Radiol. 2021;137:109600.
17 Skare S, Sprenger T, Norbeck O, Rydén H, Blomberg L, Avventi E, et al. A 1-minute full brain MR exam using a multicontrast EPI sequence. Magn Reson Med. 2018;79(6):3045–3054. doi:10.1002/mrm.26974
18 Delgado AF, Kits A, Bystam J, Kaijser M, Skorpil M, Sprenger T, et al. Diagnostic performance of a new multicontrast one-minute full brain exam (EPIMix) in neuroradiology: A prospective study. J Magn Reson Imaging. 2019;50(6):1824–1833.
19 Wang D, Deshpande V, Li X, Urgurbil K. Siemens Healthcare GmbH, Regents of the University of Minnesota, assignee. Multiband Slice Accelerated Imaging With Balanced Slice-Selective Gradients. United States patent 9,989,610. June 5, 2018.
20 Cauley SF, Polimeni JR, Bhat H, Wald LL, Setsompop K. Interslice leakage artifact reduction technique for simultaneous multislice acquisitions. Magn Reson Med. 2014;72(1):93–102.
21 Clifford B, Conklin J, Huang SY, Feiweier T, Hosseini Z, Goncalves Filho ALM, et al. An artificial intelligence-accelerated 2-minute multi-shot echo planar imaging protocol for comprehensive high-quality clinical brain imaging. Magn Reson Med. 2022;87(5):2453–2463. Epub 2021 December 31.
22 Pruessmann KP, Weiger M, Börnert P, Boesiger P. Advances in sensitivity encoding with arbitrary k-space trajectories. Magn Reson Med. 2001;46(4):638–651.
23 Hyun CM, Kim HP, Lee SM, Lee S, Seo JK. Deep learning for undersampled MRI reconstruction. Phys Med Biol. 2018;63(13):135007.
24 Wang S, Su Z, Ying L, Peng X, Zhu S, Liang F, et al. ACCELERATING MAGNETIC RESONANCE IMAGING VIA DEEP LEARNING. In: Proc IEEE Int Symp Biomed Imaging. 2016;2016:514–517.
25 Mason A, Rioux J, Clarke SE, Costa A, Schmidt M, Keough V, et al. Comparison of Objective Image Quality Metrics to Expert Radiologists' Scoring of Diagnostic Quality of MR Images. IEEE Trans Med Imaging. 2020;39(4):1064–1072.
26 Muckley MJ, Riemenschneider B, Radmanesh A, Kim S, Jeong G, Ko J, et al. Results of the 2020 fastMRI Challenge for Machine Learning MR Image Reconstruction. IEEE Trans Med Imaging. 2021;40(9):2306–2317.
27 Hosseini Z, Feiweier T, Conklin J, et al. A data-driven method for automatic regularization selection in a hybrid DL-SENSE reconstruction. In: Proc. Intl. Soc. Magn. Reson. Med. 2022:0206.
28 Tabari A, Clifford B, Goncalves Filho ALM, Hosseini Z, Feiweier T, Lo WC, et al. Ultrafast Brain Imaging with Deep Learning Multi-Shot EPI: Preliminary Clinical Evaluation. MAGNETOM Flash. 2021;79(2):66–70.

Contact

Bryan Clifford, Ph.D.
Siemens Medical Solutions USA
149 13th St, Suite 2301
Boston, MA 02129
USA
Bryan.Clifford@siemens-healthineers.com

→ Don't miss the clinical aspects of Deep Resolve Swift Brain

John Conklin, Azadeh Tabari, et al. (Massachusetts General Hospital, Boston, MA, USA)

"Ultrafast Brain Imaging with Deep Learning Multi-Shot EPI: Preliminary Clinical Evaluation"

The article is available at www.magnetomworld.siemens-healthineers.com/clinical-corner/case-studies/deep-resolve-swift-brain

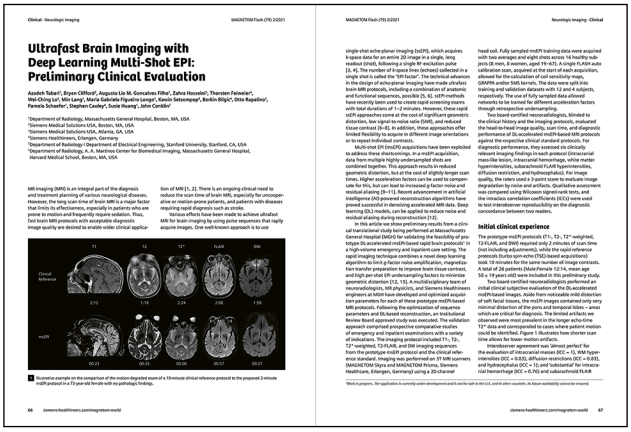

Clinical · Neurologic Imaging MAGNETOM Flash (79) 2/2021

Ultrafast Brain Imaging with Deep Learning Multi-Shot EPI: Preliminary Clinical Evaluation

Azadeh Tabari[1], Bryan Clifford[2], Augusto Lio M. Goncalves Filho[1], Zahra Hosseini[3], Thorsten Feiweier[4], Wei-Ching Lo[5], Min Lang[1], Maria Gabriela Figueiro Longo[6], Kevin Setsompop[5], Berkin Bilgic[5], Otto Rapalino[1], Pamela Schaefer[1], Stephen Cauley[5], Susie Huang[2], John Conklin[1]

[1]Department of Radiology, Massachusetts General Hospital, Boston, MA, USA
[2]Siemens Medical Solutions USA, Boston, MA, USA
[3]Siemens Medical Solutions USA, Atlanta, GA, USA
[4]Siemens Healthineers, Erlangen, Germany
[5]Department of Radiology | Department of Electrical Engineering, Stanford University, Stanford, CA, USA
[6]Department of Radiology, A. A. Martinos Center for Biomedical Imaging, Massachusetts General Hospital, Harvard Medical School, Boston, MA, USA

MR imaging (MRI) is an integral part of the diagnosis and treatment planning of various neurological diseases. However, the long scan time of brain MRI is a major factor that limits its effectiveness, especially in patients who are prone to motion and frequently require sedation. Thus, fast brain MRI protocols with acceptable diagnostic image quality are desired to enable wider clinical application of MRI [1, 2]. There is an ongoing clinical need to reduce the scan time of brain MRI, especially for uncooperative or motion-prone patients, and patients with diseases requiring rapid diagnosis such as stroke.

Various efforts have been made to achieve ultrafast MRI for brain imaging by using acive sequences that rapidly acquire images. One well-known approach is to use

Illustrative example on the comparison of the motion-degraded exam of a 10-minute clinical reference protocol to the proposed 2-minute mSPI protocol in a 73-year-old female with no pathologic findings.

MAGNETOM Flash (79) 2/2021 Neurologic Imaging · Clinical

single-shot echo-planar imaging (ssEPI), which acquires k-space data for an entire 2D image in a single, long readout (shot), following a single RF excitation pulse [3, 4]. The number of k-space lines (echoes) collected in a single shot is called the "EPI factor". The technical advances in the design of echo-planar imaging have made ultrafast brain MRI protocols, including a combination of anatomic and functional sequences, possible [5, 6]. ssEPI methods have recently been used to create rapid screening exams with total durations of 1–2 minutes. However, these rapid ssEPI approaches come at the cost of significant geometric distortion, low signal-to-noise ratio (SNR), and poor tissue contrast [6–8]. In addition, these approaches offer limited flexibility to acquire in different image orientations or to repeat individual contrasts.

Multi-shot EPI (msEPI) acquisitions have been exploited to address these shortcomings. In a msEPI acquisition, data from multiple highly-undersampled shots are combined together. This approach results in reduced geometric distortion, but at the cost of slightly longer scan times. Higher acceleration factors can be used to compensate for this, but can lead to increased g-factor noise and residual aliasing [9]. Recently, artificial intelligence (AI)-powered reconstruction algorithms have proved successful in denoising accelerated MRI data. Deep learning (DL) models, can be applied to reduce noise and residual aliasing during reconstruction [1,2].

In this article we show preliminary results from a clinical translational study being performed at Massachusetts General Hospital (MGH) for validating the feasibility of prototype DL-accelerated msEPI-based rapid brain protocols[1] in a high-volume emergency and inpatient care setting. The rapid imaging technique combines a novel deep learning algorithm to limit g-factor noise amplification, magnetization preparation to improve brain tissue contrast, and high-bandwidth acquisitions to reduce susceptibility geometric distortion [10, 11]. A multidisciplinary team of neuroradiologists, MR physicists, and Siemens Healthineers engineers at MGH have developed and optimized acquisition parameters for each of these prototype msEPI-based MRI protocols. Following the optimization of sequence parameters and DL-based reconstruction, an Institutional Review Board-approved study was executed. The validation approach comprised prospective comparative studies of emergency and inpatient examinations with a variety of indications. The imaging protocol included T1-, T2-, T2*-weighted, FLAIR, and DWI sequences acquired from the prototype msEPI protocol and the clinical reference standard. Imaging was performed on 3T MRI scanners (MAGNETOM Skyra and MAGNETOM Prisma, Siemens Healthcare, Erlangen, Germany) using a 20-channel head coil. Fully sampled msEPI training data were acquired with two averages and eight shots across 16 healthy subjects (8 men, 8 women, aged 19–67). A single FLAIR auto calibration scan, acquired at the start of each acquisition, allowed for the calculation of coil sensitivity maps, GRAPPA, and/or SWI kernels. The data were split into training and validation datasets with 12 and 4 subjects, respectively. The use of fully sampled data allowed networks to be trained for different acceleration factors through retrospective undersampling.

Two board-certified neuroradiologists, blinded to the clinical history and the imaging protocols, evaluated the head-to-head image quality, scan time, and diagnostic performance of DL-accelerated msEPI-based MRI protocols against the respective clinical standard protocols. For diagnostic performance, they assessed six clinically relevant imaging findings in each protocol (intracranial mass-like lesion, intracranial hemorrhage, white matter hyperintensities, subarachnoid FLAIR hyperintensities, diffusion restriction, and hydrocephalus). For image quality, the raters used a 3-point scale to evaluate image degradation by noise and artifacts. Qualitative assessment of image sharpness, artifacts, and ssEPI tests, and the interclass correlation coefficients (ICCs) were used to test interobserver reproducibility on the diagnostic concordance between two readers.

Initial clinical experience

The prototype msEPI protocols (T1-, T2-, T2*-weighted, T2-FLAIR, and DWI) required only 2 minutes of scan time (not including adjustments), while the rapid reference protocols (turbo spin-echo (TSE)-based acquisitions) took 10 minutes for the same clinical diagnostic protocols. A total of 50 patients (30 adult, mean age 52.1 ± 17.8 years; 20 pediatric, mean age 10.2 ± 5.1 years) were included in this study.

Two board-certified neuroradiologists performed an initial clinical subjective evaluation of the DL-accelerated msEPI-based images. Aside from noticeable mid-dissection of soft facial tissues, the msEPI images contained only very minimal distortion of the pons and temporal lobes – areas which are critical for diagnosis. The limited artifacts we observed were most prevalent in the longer echo-time T2* data and corresponded to cases where patient motion could be identified. Figure 1 illustrates how shorter scan time allows for lower motion artifacts.

The msEPI protocols were considered perfect for the evaluation of intracranial masses (ICC = 1), WM hyperintensities (ICC = 0.83), diffusion restrictions (ICC = 0.83), and hydrocephalus (ICC = 1) and 'substantial' for intracranial hemorrhage (ICC = 0.76) and subarachnoid FLAIR

*Work in progress. The application is currently under development and is not for sale in the U.S. and in other countries. Its future availability cannot be ensured.

MR Fingerprinting Development Kit

for Tailored Research Applications

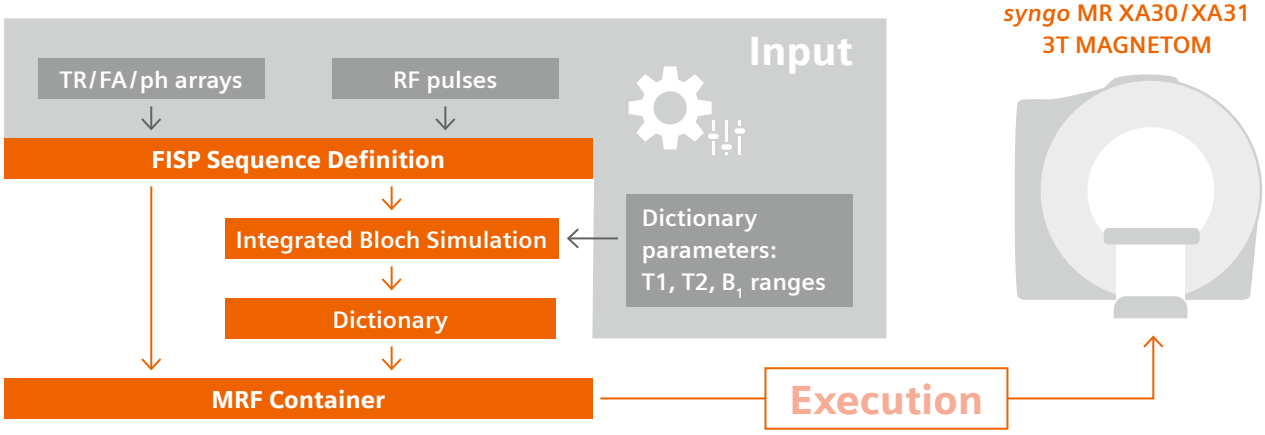

The MR Fingerprinting Development Kit[1] takes files describing the input parameters T1, T2, RF- flip angles and pulse phases. This input generates a customized MR Fingerprinting[1] sequence. The input also serves as the basis for a Bloch simulation, which creates a MR Fingerprinting dictionary unique to its input parameters.

In a final step, the new MR Fingerprinting sequence and its unique dictionary are bundled in the so-called MR Fingerprinting container. This container can be transferred and executed on a qualified MAGNETOM 3T scanner from Siemens Healthineers[2] with a valid MR Fingerprinting license.

The sequence generation, the Bloch simulation, and the creation of the MR Fingerprinting container are performed by running a Windows command line tool[3] provided with the MR Fingerprinting Development Kit.

The MR Fingerprinting Development Kit is available for download to all users of MR Fingerprinting at **www.magnetomworld.siemens-healthineers.com/hot-topics/mr-fingerprinting/mrf-developer-kit**

This unique MRF Development Kit empowers you to tailor the research application to your needs.

[1]The product / feature is not for sale in the U.S. Its future availability cannot be guaranteed.
[2]syngo MR XA30: MAGNETOM Prisma, MAGNETOM Prisma Fit, MAGNETOM Skyra; syngo MR XA31: MAGNETOM Vida
[3]The user needs to install the MR Fingerprinting Development Kit on a standalone Windows 10 PC. Installation on the host computer is not possible.

SIEMENS Healthineers

Distortion-free Diffusion-weighted Imaging Based on a TGSE BLADE Sequence: Technique and Clinical Application

Kun Zhou, Ph.D.; Wei Liu, Ph.D.

Siemens Shenzhen Magnetic Resonance Ltd., Shenzhen, China

Introduction

Diffusion-weighted imaging (DWI) is a powerful tool for probing tissue microstructures by measuring the Brownian motion of water molecules. It has been widely used for diagnosing a broad spectrum of pathologies. Single shot echo planar imaging (ssEPI) is the most commonly used sequence for DWI, due to its high data acquisition rate and low sensitivity to bulk motion and physiological movement. However, this technique often suffers from geometric distortion caused by susceptibility change at tissue interfaces, and image blurring caused by signal decay in the long acquisition window.

In the ssEPI sequence, the time between sampling points in phase encoding (PE) direction is relatively long, so the phase caused by static B_0 inhomogeneity accumulates, leading to geometric distortion [1]. Two variants of multishot techniques – interleaved EPI (iEPI) and readout segmented EPI (rsEPI) – can be applied to mitigate image distortion by reducing effective echo spacing. iEPI accelerates the *k*-space traversal by interleaving EPI trajectories along the PE direction [2], while rsEPI divides the full *k*-space into multiple segments along the readout direction [3]. However, significant residual problems still exist where strong B_0 inhomogeneities are present, such as in the inner ear, skull base, orbit, and sinuses. This is particularly true at higher field strengths since susceptibility artifacts increase along with the field strength.

To further reduce geometric distortion, DWI can also be carried out by turbo spin echo (TSE) sequences, which are free of phase error accumulation. These techniques fall into two categories: single-shot and multishot. Half-Fourier acquisition single shot turbo spin echo (HASTE) DWI belongs to the first category and has been used for cholesteatoma detection at 1.5T for many years [4]. It was recently rolled out to 3T because of the excellent lesion conspicuity [5]. HASTE DWI has some limitations: e.g., because a different diffusion encoding scheme is applied, the contrast is different from other DWI techniques. It is also more prone to blurring due to the relatively long echo train.

To overcome those limitations, multi-shot DWI sequences are introduced. However, shot-to-shot variations introduced by motion during the diffusion encoding gradients can impact image quality. Thus special acquisition strategies like BLADE are usually the method of choice, as the *k*-space center region in each shot can be used to correct these variations [6].

However, the application of TSE-BLADE-based DWI is limited due to its relatively long scan time, high specific

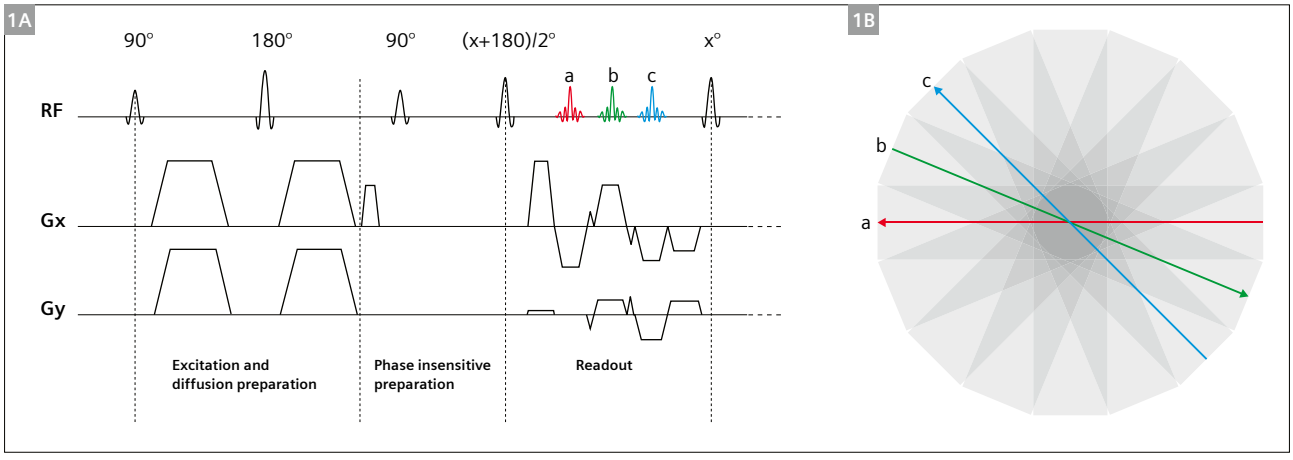

1 Sequence diagram and *k*-space filling order with EPI factor = 3. Note that only one echo spacing is shown.

absorption rate (SAR), and issues caused by violation of Carr-Purcell-Meiboom-Gill (CPMG) conditions. Several techniques have been developed to address these challenges. For example, a phase cycling method can be used to stabilize the echo train by reducing the interference coming from the non-CPMG components [7]. However, this scheme requires that the flip angles of refocusing pulses are as close to 180° as possible. Therefore, SAR is still high, especially at high fields, and B_1 field variation may result in unstable image quality. The turbo gradient spin echo (TGSE, or GRASE) technique, which generates and acquires gradient echoes and spin echoes via EPI-like bipolar gradients, can speed up the acquisition and reduce SAR accordingly. The gradient echoes and spin echoes sampled in one shot can be placed in one blade [8, 9] or distributed in different blades [10, 11]. In any case, the EPI factor should be kept in a moderate range to avoid off-resonance effects.

To provide a distortion-free DWI sequence that has high image quality and reasonable measurement time, the TGSE BLADE-based DWI sequence (TGSE BLADE DWI) was developed and rolled out to the 3T systems MAGNETOM Vida and MAGNETOM Lumina with software version *syngo* MR XA50A. This sequence is based on the TGSE sequence and acquires *k*-space with a BLADE trajectory [12]. A phase-insensitive preparation method [13] is used to handle the non-CPMG problem. Besides the TGSE readout technique, Simultaneous Multi-Slice (SMS) and the integrated parallel acquisition technique (iPAT) are applied to further reduce the measurement time [14].

Method

Diffusion encoding and phase-insensitive preparation

In diffusion imaging, physiological fluctuation and even tiny amounts of motion during the application of diffusion-sensitizing gradients introduce spatially varying and unknown phases to the spins in the transversal plane. If TSE-based sequences are used to sample the signals, the CPMG condition is not fulfilled and hence the echo amplitudes in the echo train attenuate rapidly. This results in image artifacts, e.g., severe inhomogeneity and signal loss in regions affected by the motion.

To address this problem, a phase-insensitive preparation module is applied between the diffusion preparation and the following refocusing pulses as shown in the sequence diagram in Figure 1.

EPI readout

To accelerate the conventional BLADE sequence, EPI-like readout gradients and blips are played out on both readout and phase encoding directions, producing radial-like *k*-space lines which are placed into separate blades, as shown in Figure 1. The readout is repeated throughout the whole echo train, producing all *k*-space lines for each blade. These blades cover *k*-space completely.

SMS and iPAT

SMS and iPAT is implemented to speed up the acquisition. To reduce the *g*-factor penalty, blipped-controlled aliasing [15] is used.

The time to acquire the necessary SMS calibration data is kept to a minimum by applying a quick separate TSE-based reference scan for the first blade. For other blades, the calibration data are interpolated from the acquired data.

This reference scan is also compatible with in-plane GRAPPA. In-plane GRAPPA makes it possible to acquire a wider blade, which can speed up the acquisition and can increase the robustness against motion.

Results of internal volunteer test

Figure 2 shows images of b = 0 s/mm², 1000 s/mm², and an ADC acquired with the TGSE BLADE DWI sequence on a MAGNETOM Vida with a 20-channel head-neck coil. With the application of SMS, in-plane GRAPPA, and TGSE readout, distortion-free diffusion-weighted images covering the whole brain can be acquired in a reasonable time.

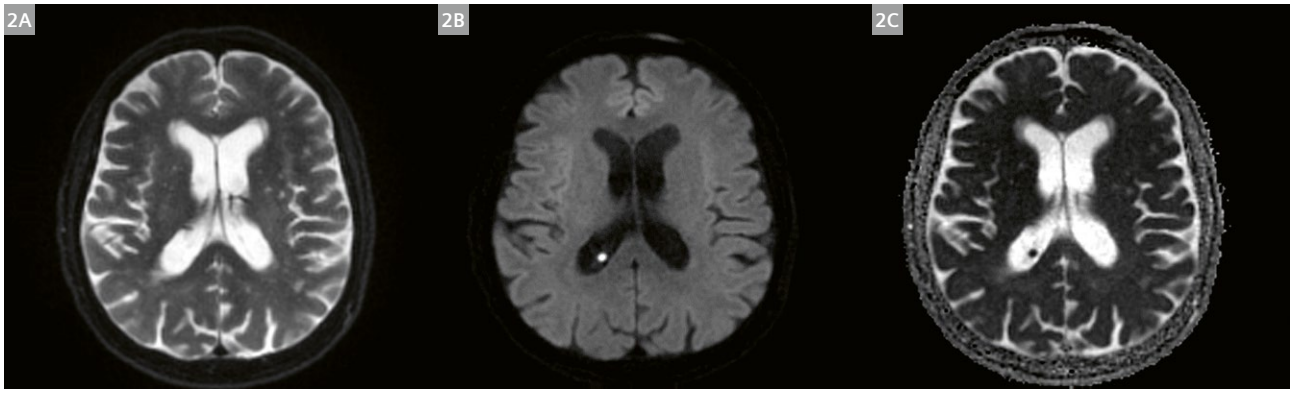

2 b = 0 s/mm², 1000 s/mm², and ADC from the TGSE BLADE diffusion sequence with a PE acceleration of 2 and a slice acceleration factor of 2. Other parameters are TE = 55 ms, TR = 4000 ms, FOV = 220 × 220 mm², matrix size = 176 × 176, and TA= 3:12 min.

Figure 3 shows a comparison between RESOLVE DWI and TGSE BLADE DWI of b = 1000 s/mm^2. Residual geometric distortions and signal pile-ups (arrows) are seen in the RESOLVE diffusion images and are less noticeable in the BLADE diffusion images.

Clinical applications

The application of EPI-based DWI is well established for many body regions. However, its ability to diagnose lesions could be compromised in regions with strong local susceptibility variations caused by magnetic field inhomogeneities. Several studies on the performance of TGSE BLADE DWI in these challenging regions were performed during the evaluation phase of this sequence, indicating that this sequence could be a promising solution for those challenging regions [16–20].

Cholesteatoma

Cholesteatoma is a benign, gradually expanding, and destructive epithelial lesion of the temporal bone that results in the erosion of adjacent bony structures and can lead to various complications [5].

Although CT imaging has traditionally been the method of choice, MRI with DWI is becoming more and more important in the evaluation of cholesteatoma, due to its superior soft tissue contrast. To evaluate the performance of RESOLVE and TGSE BLADE in this application, Sheng et al. performed a study to compare image quality qualitatively and quantitatively between TSGE BLADE and RESOLVE on a MAGNETOM Prisma with a 64-channel head-neck coil [16]. 42 patients with surgically confirmed cholesteatoma in the middle ear were enrolled in this study.

The results indicate that TGSE BLADE DWI significantly improved the image quality of cholesteatoma imaging by reducing B_0 inhomogeneity related artifacts and blurring. The authors found that TGSE BLADE DWI is more valuable than RESOLVE DWI for diagnosing small (2 mm) cholesteatoma lesions. As shown in Figure 4, axial TGSE BLADE DWI could completely and clearly show a small lesion (1.9 mm in width) located in the left tympanic cavity with less geometric distortion than was observed using RESOLVE DWI.

Although the study also found that the signal-to-noise ratio (SNR) of TGSE BLADE DWI is lower than RESOLVE, this is anticipated because the same acquisition time is used while the SNR efficiency of TGSE BLADE DWI is lower, since it has to compensate for the non-CMPG condition.

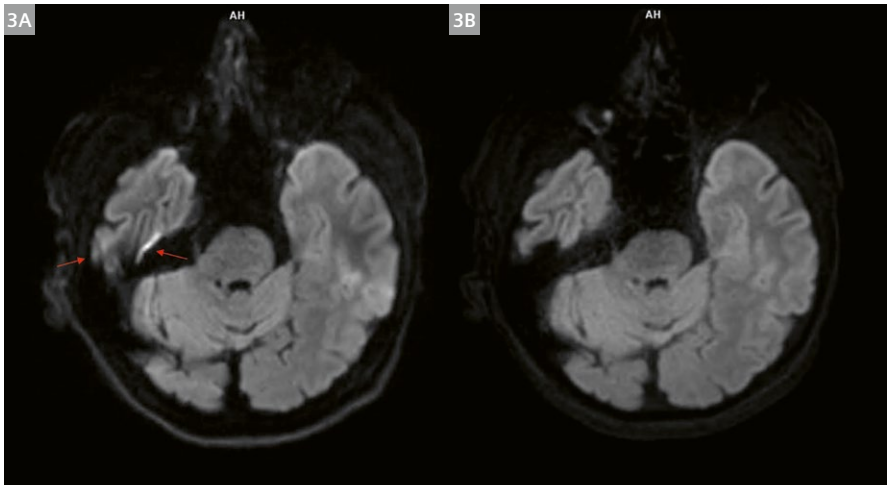

3 Example of the b = 1000 s/mm^2 trace-weighted images acquired with a product RESOLVE sequence **(3A)** and TGSE BLADE diffusion sequence **(3B)** at 3T.
Common parameters:
Matrix = 160 × 160,
FOV 220 × 220 mm^2,
slice thickness = 4 mm,
in-plane Grappa factor = 2.
RESOLVE: TR = 5240 ms,
TE = 58 ms, TA = 1:57 min;
TGSE BLADE: TR = 5500 ms,
TE = 44 ms, TA = 3:50 min.

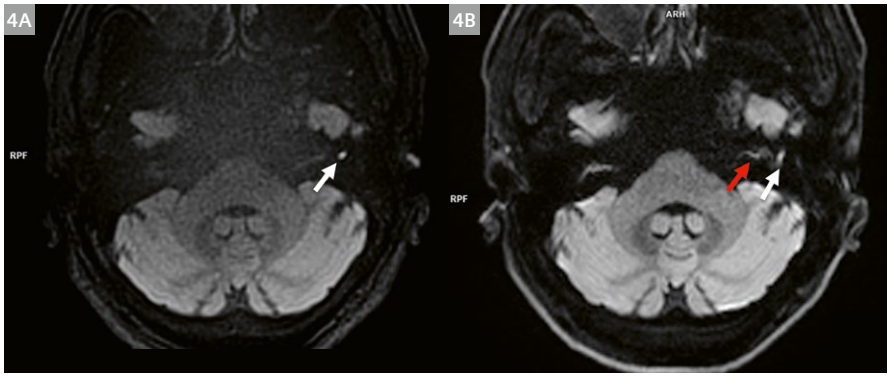

4 A 44-year-old male with a small cholesteatoma (1.9 mm width) in the left tympanic cavity (white arrow). **(4A)** Axial TGSE BLADE DWI (b = 1000 s/mm^2) clearly shows a markedly high signal intensity for the small cholesteatoma (white arrows) without artifacts. **(4B)** Axial RESOLVE DWI (b = 1000 s/mm^2) shows the high signal intensity of a small lesion (white arrow) with light geometric distortion, and the bilateral middle ear mastoid process with a few artifacts (red arrow).

Orbital tumor

DWI is also an essential MR sequence for diagnosing orbital diseases. Geometric fidelity is important for depicting small lesions in orbital DWI. Moreover, accurately characterizing the extent of invasion of orbital tumors is essential for clinical treatment planning or even prognosis of the orbital tumors.

Fu et al. performed a study that qualitatively and quantitatively compared the image quality and diagnostic performance of TGSE BLADE DWI and RESOLVE on a MAGNETOM Skyra with a 20-channel head-neck coil [17]. 43 patients with suspected orbital tumors were enrolled in this study.

TGSE BLADE DWI significantly outperformed RESOLVE on scores for geometric distortions, susceptibility artifacts, lesion conspicuity, and overall image quality. Three cases are shown in Figure 5.

Pediatric

In a preliminary study of 53 patients (10.4 ± 7.9 years), Hu et al. compared the diagnostic image quality of TGSE BLADE DWI versus ssEPI DWI in pediatric patients* on a

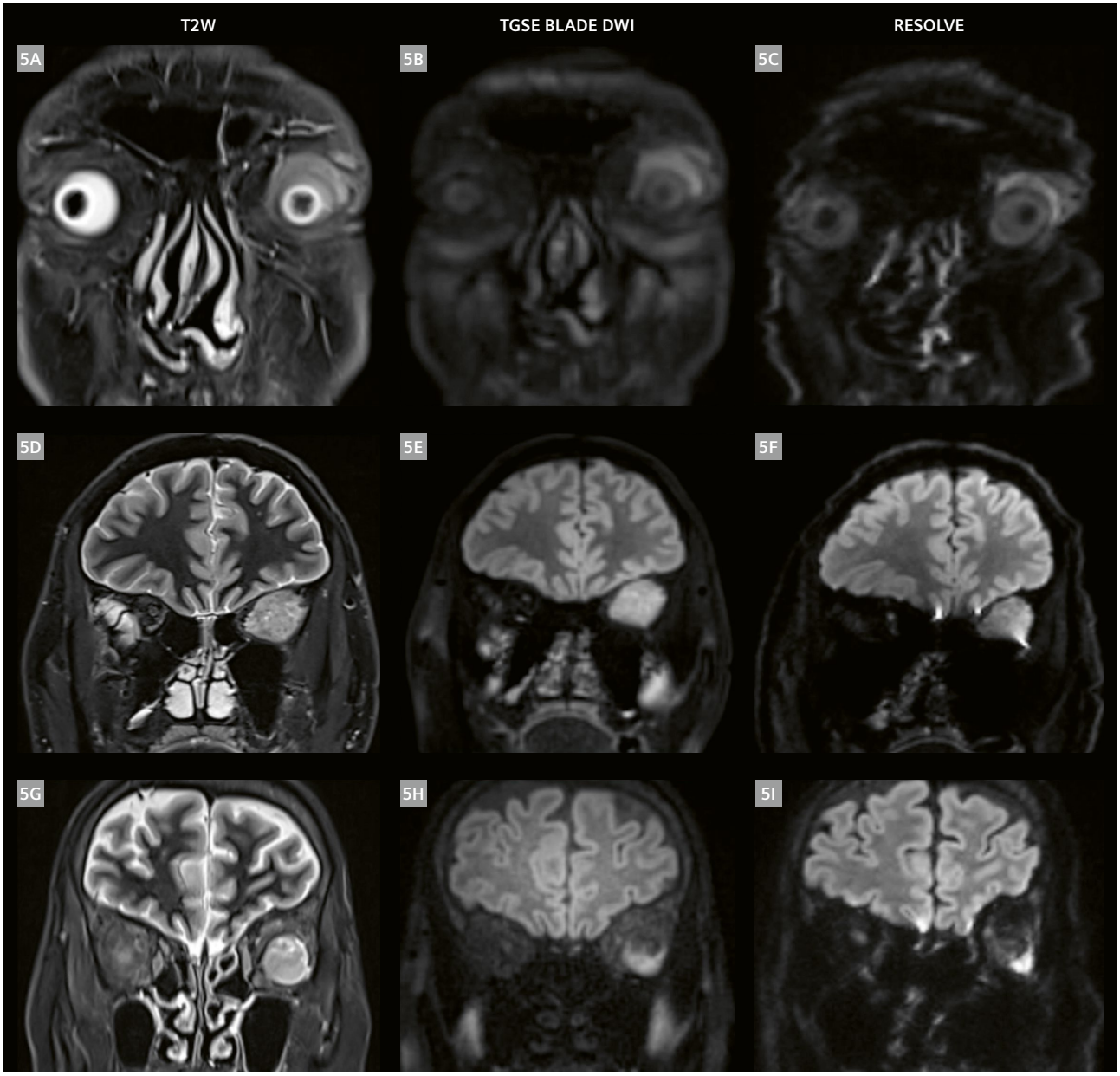

5 Coronal T2-weighted images **(5A, D, G)**, TGSE BLADE DWI b = 1000 s/mm² images **(5B, E, H)**, and RESOLVE b = 1000 s/mm² images **(5C, F, I)**. Patient 1 (5A–C), 62-year-old male, left orbital lymphoma; Patient 2 (5D–F), 50-year-old male, left orbital fibroma; Patient 3 (5G–I), 61-year-old female, left orbital hemangioma.

MAGNETOM Prisma with a 20-channel head-neck coil or a 64-channel head-neck coil [18]. The results show the feasibility of TGSE BLADE DWI in pediatric patients and children at 3T. Since there are fewer geometric distortions and signal pile-ups, it could be a viable first-choice alternative for ssEPI DWI in areas around air–tissue interfaces or in the presence of shunts/orthodontia.

Figure 6 shows a representative example from a 5-year-old boy with a right frontal lobe craniotomy for epileptic focus resection. Distortion and pile-ups can be seen in the ssEPI data in the anterior part of the resected area (solid arrows), but are not visible in the TGSE BLADE image. ADC maps highlight postsurgical contusion tissue along the resection margins and within the extra-axial spaces (hollow arrow). The TGSE BLADE ADC map (6D) appears less grainy centrally than the ssEPI ADC map (6C, square highlighted region).

Figure 7 shows an example from a 10-year-old girl with braces. TGSE BLADE images demonstrate reduced susceptibility-related artifacts compared to ssEPI.

Sinonasal lesions

Application of EPI-based DWI has been limited in the sinonasal regions, which contain many bone and air-tissue interfaces.

Geng et al. investigated the feasibility of TGSE BLADE DWI for assessing sinonasal lesions and compared the quality of TGSE BLADE with RESOLVE both qualitatively and quantitatively [19]. The study included 36 patients and was performed on a MAGNETOM Prisma with a 64-channel head-neck coil. The results show that TGSE BLADE can produce better image quality than RESOLVE in sinonasal lesions by reducing susceptibility artifacts and geometric distortion.

**MR scanning has not been established as safe for imaging fetuses and infants less than two years of age. The responsible physician must evaluate the benefits of the MR examination compared to those of other imaging procedures.*

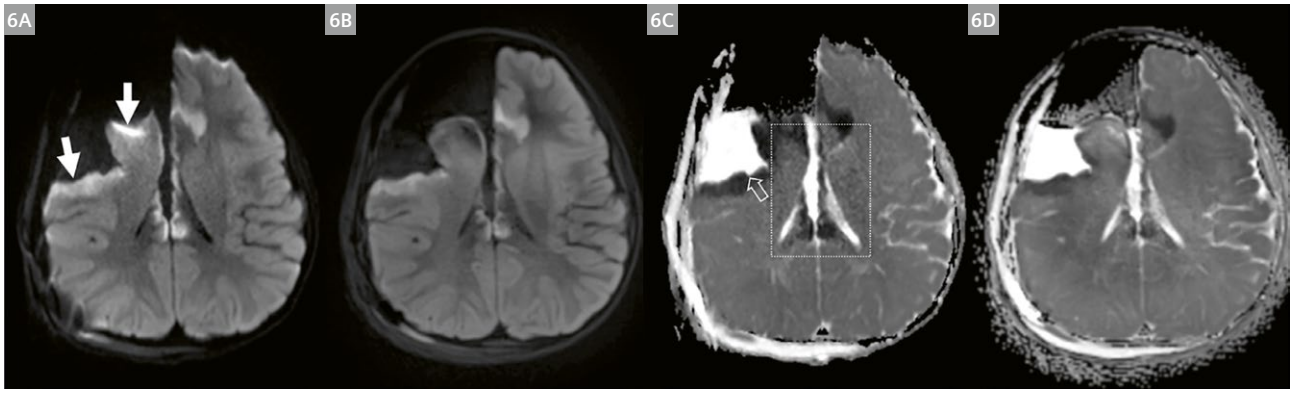

6 Images from a 5-year-old boy with right frontal lobe craniotomy for epileptic focus resection. DWI trace-weighted images and ADC maps are shown for ssEPI **(6A, C)** and TGSE BLADE **(6B, D)**.

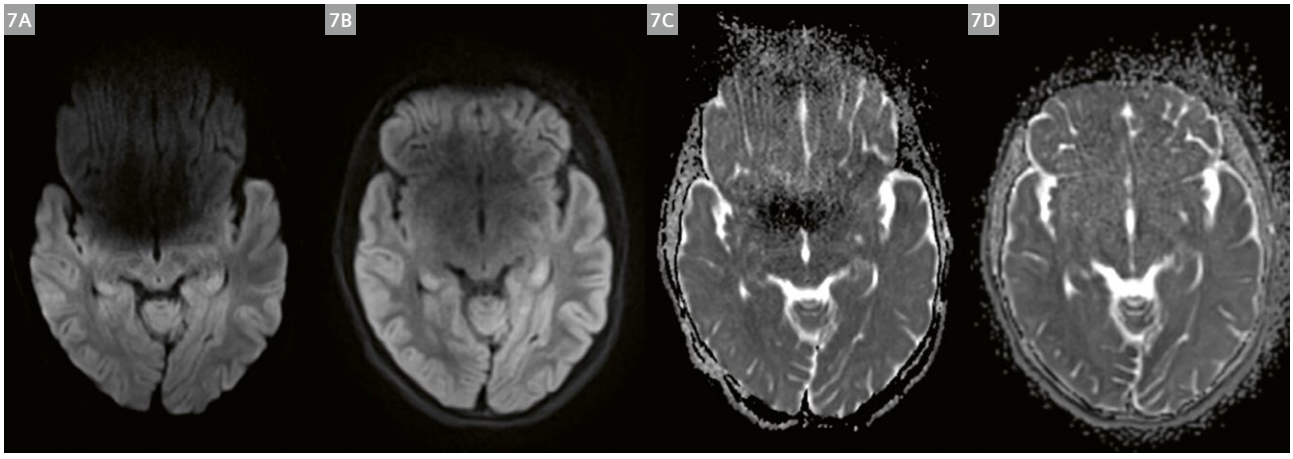

7 Images from a 10-year-old girl with braces. DWI trace-weighted images and ADC maps shown for ssEPI **(7A, C)** and TGSE BLADE **(7B, D)**.

Figure 8 shows an example of a 73-year-old woman with a schwannoma. The RESOLVE images have increased artifacts and distortion at the edge of the lesion (arrow), while TGSE BLADE has fewer artifacts.

Cerebellopontine angle tumors

The cerebellopontine angle (CPA) is the area bound by the pons and anterior aspect of the cerebellum medially, the petrous temporal bone laterally, and the tentorium superiorly. The complex anatomical structures of CPA pose a unique challenge to EPI-based DWI.

Fu et al. compared the clinical utility of TGSE BLADE DWI with RESOLVE DWI and ssEPI DWI for visualizing anatomical structures of CPA and depicting CPA tumors [20]. Eight volunteers and 36 patients with CPA tumors were enrolled. The results show that, compared with RESOLVE and ssEPI, TGSE BLADE minimized geometric distortions and ghosting artifacts and demonstrated an improved ability for depicting CPA tumors with better lesion conspicuity.

Figure 9 shows the images from a 50-year-old female patient with an acoustic neuroma located in the left internal auditory canal (IAC). Compared with the lesion depicted by the T2W image and contrast-enhanced T1W image (long white arrows, 9A, B), the lesion was visualized clearly in the trace-weighted image from TGSE BLADE DWI and ADC map without geometric distortion (long white arrows, 9C, D). Moderate and severe distortion can be observed on RESOLVE and ssEPI images (9E–H), respectively (long red arrows), which impacted demonstration of this small lesion. Moreover, signal pile-ups (short arrows) in the bone-air interfaces in TGSE BLADE were absent (9C), but were present both in RESOLVE (9E) and ssEPI (9G). The visualization of anatomical structures (triangular arrows) in TGSE BLADE (9C) was superior to RESOLVE (9E) and ssEPI (9G).

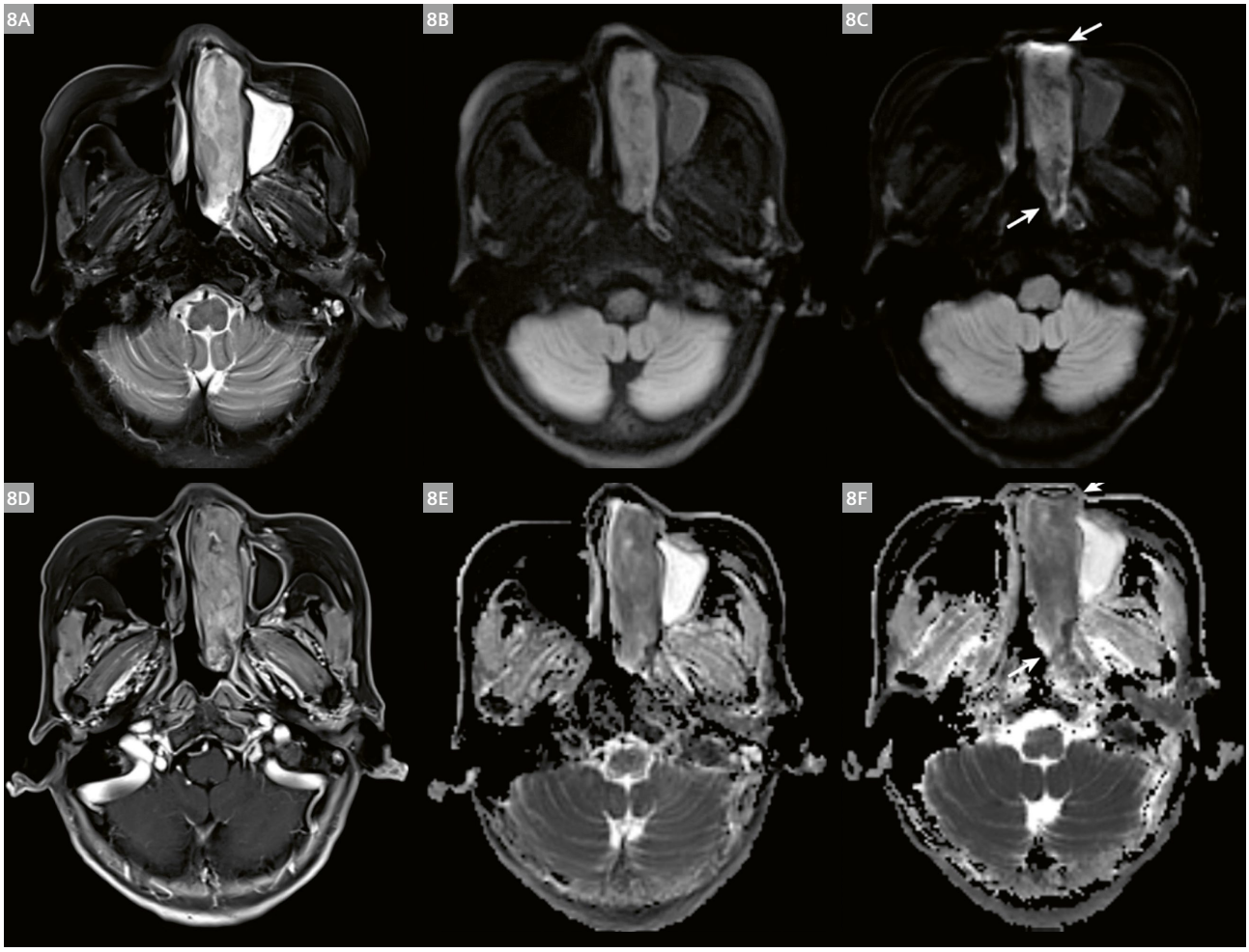

8 A schwannoma in a 73-year-old woman. **(8A)**: Axial T2W imaging, **(8D)**: contrast-enhanced T1W imaging, **(8B, E)**: TGSE BLADE, and **(8C, F)**: RESOLVE showed a mass that mainly involved the left nasal cavity. The image quality of (8B) TGSE BLADE b = 1000 s/mm² and (8E) ADC maps was significantly higher than that of (8C) RESOLVE b = 1000s/mm² and (8F) ADC maps.

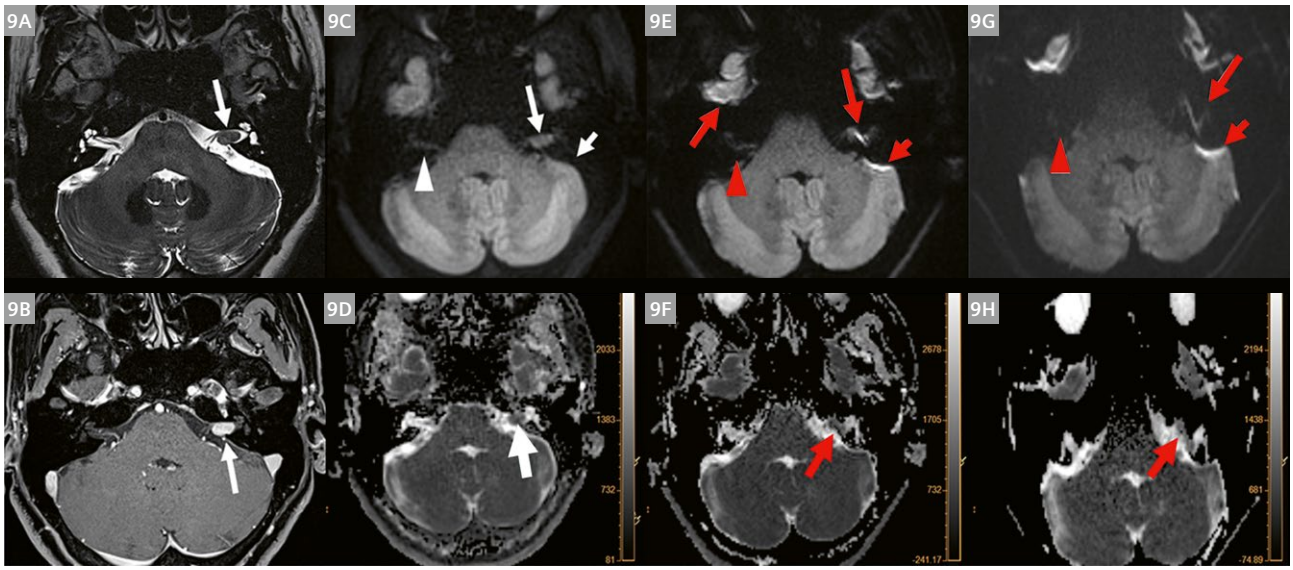

9 A 50-year-old female with an acoustic neuroma located in the left internal auditory canal (IAC). **(9A)** T2W image; **(9B)** contrast-enhanced T1W image; **(9C, E, G)** trace-weighted images of b = 1000 s/mm² of TGSE BLADE, RESOLVE and ssEPI; **(9D, F, H)** the corresponding ADC images.

Discussion

EPI-based sequences remain the clinical workhorse and default method for DWI in many applications. However, their image quality could be compromised and the feasibility of diagnosis could be challenged in regions or situations where strong B_0 inhomogeneities are present.

The TGSE BLADE DWI sequence samples a train of spin echoes and gradient echoes, and can generate distortion-free DWI images. Several studies have compared the image quality and diagnostic performance of TGSE BLADE DWI and EPI-based DWI, e.g. for cholesteatoma, orbital tumors, sinonasal lesions, and cerebellopontine angle tumors. The results show that TGSE BLADE DWI yields superior diagnostic quality to EPI-based methods in these challenging applications.

However, TGSE BLADE DWI sequences also have some limitations.

While the SNR efficiency of TGSE BLADE Diffusion is lower than that of EPI-based DWI sequences, because it has to compensate for the non-CPMG-condition, acceleration techniques like SMS and iPAT can reduce the additional scan time needed to achieve similar SNR.

The scan time can also be influenced by changing the EPI factor, but can also impact T2* and off-resonance effects. A factor of 3 to 5 is recommended as a good compromise between speed and undesired effects.

Conclusion

TGSE BLADE DWI is not sensitive to B_0 inhomogeneities while keeping a reasonable scan time. It is therefore a promising alternative to EPI DWI for detecting pathologies in regions with strong B_0 inhomogeneities.

Acknowledgments

We would like to thank all the institutions and individuals who evaluated this sequence and provided valuable feedback.

We are also grateful to all the collaborating scientists for their support and key observations: Benjamin Schmitt, Fu Cai Xia, Zhang Zhong Shuai, Jin Ning, Guo Yi Hao, Tobias Kober, Frederik Testud, Peter Kollasch, Vicky Sherwood, Pedro Itriago Leon, Gerald R. Moran, Yuta Urushibata, and Shani Ben-Amitay.

Thank you to Alto Stemmer, Thorsten Feiweier, Dominik Paul, and George W. Ferguson for the important discussions regarding the early development and productization of this sequence.

And thank you to Heiko Meyer and Weng De He for supporting this project.

References

1 Jezzard P, Balaban RS. Correction for geometric distortion in echo planar images from B_0 field variations. Magn Reson Med. 1995;34(1):65–73.
2 Chen NK, Guidon A, Chang HC, Song AW. A robust multi-shot scan strategy for high-resolution diffusion weighted MRI enabled by multiplexed sensitivity-encoding (MUSE). Neuroimage. 2013 15;72:41–7.
3 Porter DA, Heidemann RM. High resolution diffusion-weighted imaging using readout-segmented echo-planar imaging, parallel imaging and a two-dimensional navigator-based reacquisition. Magn Reson Med. 2009;62(2):468–75.
4 De Foer B, Vercruysse JP, Pilet B, Michiels J, Vertriest R, Pouillon M, et al. Single-shot, turbo spin-echo, diffusion-weighted imaging versus spin-echo-planar, diffusion-weighted imaging in the detection of acquired middle ear cholesteatoma. AJNR Am J Neuroradiol. 2006;27(7):1480–2.
5 Troalen T, Pellerin A, Bertrand D, Michelot Y, Svensson J, Testud F. HASTE diffusion-weighted imaging at 3 Tesla: evaluation of non-EPI diffusion for the detection of cholesteatomas. MAGNETOM Flash. 2021;79(2):83–88.
6 Pipe JG, Farthing VG, Forbes KP. Multishot diffusion-weighted FSE using PROPELLER MRI. Magn Reson Med. 2002;47(1):42–52. Erratum in: Magn Reson Med 2002;47(3):621.
7 Le Roux P. Non-CPMG Fast Spin Echo with full signal. J Magn Reson. 2002;155(2):278–92.
8 Lee CY, Li Z, Pipe JG, Debbins JP. Turboprop+: enhanced Turboprop diffusion-weighted imaging with a new phase correction. Magn Reson Med. 2013;70(2):497–503.
9 Pipe JG, Zwart N. Turboprop: improved PROPELLER imaging. Magn Reson Med. 2006;55(2):380–5.
10 Srinivasan G, Rangwala N, Zhou XJ. Steer-PROP: a GRASE-PROPELLER sequence with interecho steering gradient pulses. Magn Reson Med. 2018;79(5):2533–2541.
11 Li Z, Pipe JG, Lee CY, Debbins JP, Karis JP, Huo D. X-PROP: a fast and robust diffusion-weighted propeller technique. Magn Reson Med. 2011;66(2):341–7.
12 Zhou K, Liu W, Cheng S. Non-CPMG PROPELLER diffusion imaging: comparison of phase insensitive preparation with split acquisition. Proc Int Soc Magn Reson Med. 2018;26:5320.
13 Alsop DC. Phase insensitive preparation of single-shot RARE: application to diffusion imaging in humans. Magn Reson Med. 1997;38(4):527–33.
14 Zhou K, Liu W, Dong F, Cheng S. Slice-GRAPPA calibration using pre-scan data and application to simultaneous multi-slice PROPELLER. Proc Int Soc Magn Reson Med. 2017;25:3842.
15 Setsompop K, Gagoski BA, Polimeni JR, Witzel T, Wedeen VJ, Wald LL. Blipped-controlled aliasing in parallel imaging for simultaneous multislice echo planar imaging with reduced *g*-factor penalty. Magn Reson Med. 2012;67(5):1210–24.
16 Sheng Y, Hong R, Sha Y, Zhang Z, Zhou K, Fu C. Performance of TGSE BLADE DWI compared with RESOLVE DWI in the diagnosis of cholesteatoma. BMC Med Imaging. 2020;20(1):40.
17 Fu Q, Kong XC, Liu DX, Zhou K, Guo YH, Lei ZQ, et al. Turbo Gradient and Spin Echo PROPELLER-Diffusion Weighted Imaging for Orbital Tumors: A Comparative Study With Readout-Segmented Echo-Planar Imaging. Front Neurosci. 2021;15:755327.
18 Hu HH, McAllister AS, Jin N, Lubeley LJ, Selvaraj B, Smith M, et al. Comparison of 2D BLADE Turbo Gradient- and Spin-Echo and 2D Spin-Echo Echo-Planar Diffusion-Weighted Brain MRI at 3 T: Preliminary Experience in Children. Acad Radiol. 2019;26(12):1597–1604.
19 Geng Y, Shi Y, Chen W, Tang Z, Zhang Z, Zhou K, et al. BLADE turbo gradient- and spin-echo in the assessment of sinonasal lesions: a comprehensive comparison of image quality in readout-segmented echo-planar imaging. Acta Radiol. 2021:2841851211041820. Epub ahead of print.
20 Fu Q, Kong XC, Liu DX, Zhou K, Guo YH, Wang MF, et al. Clinical comparison of single-shot EPI, readout-segmented EPI and TGSE-BLADE for diffusion-weighted imaging of cerebellopontine angle tumors on 3 tesla. Magn Reson Imaging. 2021;84:76–83.3.

Contact

Kun Zhou, Ph.D.
Siemens Shenzhen Magnetic Resonance Ltd.
Hi-Tech Industrial Park
518057 Shenzhen
China
kun.zhou@siemens-healthineers.com

Wei Liu, Ph.D.
Siemens Shenzhen Magnetic Resonance Ltd.
Hi-Tech Industrial Park
518057 Shenzhen
China
weiwlliu@siemens-healthineers.com

Advanced Diffusion MRI in Neurological Diseases: The Multiple Sclerosis Model

Simona Schiavi, Ph.D.[1]; Matilde Inglese, M.D., Ph.D.[1,2]

[1]Department of Neuroscience, Rehabilitation, Ophthalmology, Genetics, Maternal and Child Health (DINOGMI), University of Genoa, Italy
[2]IRCCS Ospedale Policlinico San Martino, Genoa, Italy

Introduction

Multiple sclerosis (MS) is a chronic inflammatory demyelinating and neurodegenerative disease of the central nervous system and the most common cause of non-traumatic disability in young and middle-aged adults [1]. Pathologically, MS is characterized by areas of demyelinated plaques scattered throughout the central nervous system with a predilection for optic nerves, the spinal cord, periventricular white matter (WM), the corpus callosum, and cortical and sub-cortical grey matter (GM). MS lesions reveal a great heterogeneity with respect to the presence and extent of inflammation, demyelination, axonal injury, gliosis, and remyelination. Similar pathological features have been described, albeit to a lesser extent, in normal-appearing (NA) brain tissues: both white (NAWM) and grey matter (NAGM) [1]. Conventional MRI (including T2-weighted, pre- and post-contrast T1-weighted scans) has had a huge impact on MS by enabling earlier diagnosis, and by providing surrogate markers for monitoring response to current disease-modifying treatments and upcoming experimental agents. Despite its increasing role in the clinical management and scientific investigation of MS, conventional MRI is limited by low pathological specificity and low sensitivity to diffuse damage in NAWM and NAGM. In addition, conventional MRI shows only limited associations with clinical status.

Diffusion MRI (dMRI) is a powerful quantitative technique that probes information on the movement of water molecules within brain tissues [2] and can thus provide markers of different types of microstructural alterations. Since its introduction and with the establishment of multishell sequences, many microstructural models and signal representations have been proposed [3–5] and applied to study how different neurological diseases affect the integrity of brain tissues. The sensitivity of dMRI to the microscopic motion of water molecules allows to use this technique also to recover the principal directions of diffusion, which can be assumed to coincide with that of the underlying white matter fibers. This forms the basis for diffusion tractography [6], a method able to produce three-dimensional reconstructions of the major white matter pathways, thereby offering a reasonable representation of anatomy. Recently, the possibility to reconstruct WM connections using diffusion tractography has been combined with network analysis and graph theory to form connectomics, a branch of science aimed at mapping all neural connections within the central nervous system, i.e., the brain connectome [7].

Here we summarize some applications of dMRI in the context of MS and illustrate some real-life acquisitions using MAGNETOM MRI scanners from Siemens Healthcare (3T and 7T).

Lesions and normal-appearing white matter microstructure

MS was among the first neurological diseases to be investigated with dMRI. Indeed, ever since the introduction of diffusion tensor imaging (DTI), the scalar indices derived from the tensor, such as the axial, radial, and mean diffusivity (AD, RD, and MD, respectively), which quantify the magnitude of principal, radial, and average diffusion within a voxel, and the fractional anisotropy (FA), which measures the directionality of diffusion, have been applied to study MS alone or compare its microstructural alterations with those caused by other neurological pathologies [8–11]. DTI has proven to be a valuable tool for investigating the variety of pathological features of T2-visible lesions. Increased MD and RD, and decreased FA are always more pronounced in lesions than in NAWM; however, their values are highly heterogeneous, indicating the variable degrees of tissue damage occurring within MS lesions [9]. Examples of DTI indices obtained with a 3T MAGNETOM Prisma scanner (Siemens Healthcare, Erlangen, Germany) in a patient with MS are shown in Figure 1. These results are consistent with increased water content, loss of myelin and axons, and the presence of gliosis. More interestingly,

abnormal DTI parameter values are typically found in the NAWM of patients relative to age-matched healthy controls, consistent with subtle but widespread damage known to occur in MS. These initial findings have contributed to the knowledge that white matter damage is widespread in MS, even in the early phases, although they did not provide a clear definition of the substrate underpinning these abnormalities [8–12].

Although DTI has been proven to have good sensitivity to disease changes over time, it has low pathological specificity, which does not allow to discriminate between the different pathological processes underlying MS pathogenesis [13]. To overcome these issues, multishell dMRI sequences and many multicompartment microstructural models and signal representations have been proposed [3–5]. Two very popular examples that can be obtained using a clinically feasible two-shell sequence are the Neurite Orientation Dispersion and Density Imaging (NODDI) [14] model and the multicompartment Spherical Mean Technique (SMT) [15] model, both of which have also been proven to be sensitive to MS [16]. Briefly, NODDI distinguishes between three microstructural environments: intracellular (or intra-axonal), extracellular (or extra-axonal), and cerebrospinal fluid compartments. All these compartments have fixed diffusivities (with a relationship between the external axial and radial diffusivities), and geometrical assumptions that affect diffusion in a unique way, resulting in three separate dMRI signals. Similarly, the multicompartment SMT estimates microscopic features specific to the intra- and extra-neurite compartments in the WM. The use of the spherical mean average in the fitting allows minimization of the confounding effects derived from axonal fiber crossings, curving, and orientation dispersion. Moreover, compared to NODDI, although it can only indirectly capture the potential presence of free water, it does not fix any values for the intra- and extra-neurite axial diffusivities, allowing to estimate them from the measured signal. In Figure 2 we show the microstructural maps of NODDI and SMT estimated on the same subject using the same multishell dMRI sequence. An example of using these two microstructural models in MS can be found in [17], where the authors

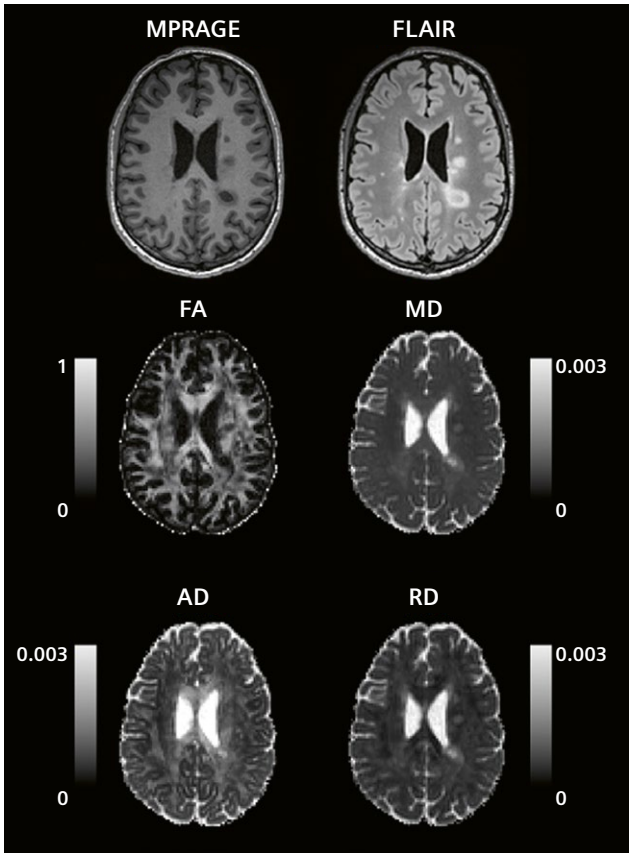

1 DTI microstructural metrics extracted for one patient affected by MS. On the top row, we show MPRAGE and FLAIR axial views in which T1 and T2 lesions are clearly visible. Below, we show fractional anisotropy (FA), mean, axial, and radial diffusivities (MD, AD, RD) in approximately the same position. Diffusivities are reported in mm^2/s.

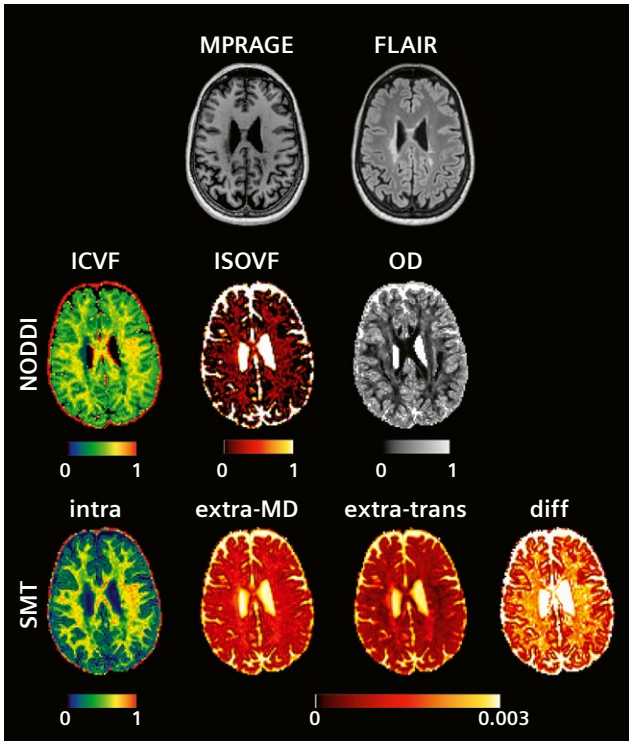

2 Microstructural maps derived from NODDI and SMT models on the same MS patient. The top row shows axial views of FLAIR and MPRAGE sequences in which T2 and T1 lesions are visible. The middle row shows axial views of intra-axonal and isotropic signal fractions (ICVF and ISOVF) and the orientation dispersion index (OD) derived from NODDI. The bottom row shows axial views of intra-axonal signal fraction (intra), extra- mean and transversal diffusivities (extra-MD and extra-trans) and axial diffusivity (diff) derived from SMT. Diffusivities are reported in mm^2/s.
ICVF: Intracellular volume fraction, ISOVF: Isotropic volume fraction

used a MAGNETOM Prisma 3T scanner to acquire a multi-shell diffusion (TR / TE / resolution = 4.5 s / 75 ms / 1.8 × 1.8 × 1.8 mm^3 isotropic with b-values 0 / 700 / 1000 / 2000 / 3000 s/mm^2 with 12 / 6 / 20 / 45 / 66 measurements, respectively, per shell) and a non-diffusion weighted acquisition with 12 measurements of b-value 0 s/mm^2 with reversed phase encoding to quantify the axonal damage among different lesion types, in NAWM, and across MS clinical subtypes and healthy controls (HCs). Comparing diffusion metrics reflecting axonal integrity with MRI-derived myelin maps, the authors found that myelin and axonal pathology in MS is extensive in both lesions and normal-appearing tissue; certain types of lesions exhibit more damage to myelin and axons than others; and myelin and axonal pathology in lesions is related to disability in patients with clinical deficits and global measures of neuroaxonal damage.

Another multicompartment model that was proposed to resolve multiple tensor-like populations of water that may arise not only in healthy tissue but also from axonal injury, inflammation, and demyelination is Diffusion Basis Spectrum Imaging (DBSI) [18, 19]. Briefly, DBSI models diffusion as a combination of multiple discrete anisotropic tensors and a spectrum of isotropic diffusion tensors. The discrete anisotropic tensors are intended to represent myelinated and unmyelinated axons oriented in varying directions. The isotropic tensors, then, represent the integration of multiple pools of water, typically separated into the restricted spectrum which may reflect cellularity. The non-restricted isotropic diffusion spectrum reflects extracellular edema and cerebrospinal fluid. Thus, in DBSI, the diffusion signal is modeled as a summation of many diffusion tensors and an integration of free water with varying diffusivities. DBSI involves complex signal fitting of many free variables. By applying this model, in each voxel we obtain measures of fiber fraction (reflecting fiber density), non-restricted fraction (reflecting tissue destruction), restricted fraction (reflecting cellularity), axial and radial diffusivities (DBSI AD and DBSI RD, reflecting fiber integrity and demyelination), and fractional anisotropy (DBSI FA, reflecting intact fiber integrity). This model can be used to perform non-invasive quantification of inflammation, axonal, and myelin injury in MS. An example can be found in [20], where a MAGNETOM 7T scanner (Siemens Healthcare, Erlangen, Germany) was used with a 32-channel head coil to acquire a diffusion-weighted spin-echo imaging sequence with a 99-encoding-directions scheme selected as prescribed in DBSI of the human brain [21] (acquired with both anterior-posterior and posterior-anterior phase encoding directions) and maximum b-value = 2000 s/mm^2 (TR / TE: 4000 / 62 ms, resolution 2 × 2 × 2 mm^3) to compare the microstructural differences of different lesions and NAWM in MS patients and HCs.

The results obtained in that study confirmed the role of DBSI-derived metrics in the characterization of lesions and NAWM tissue at different stages of the disease. This also demonstrated the metrics' clinical relevance, suggesting that DBSI is a promising tool for investigating MS pathophysiology and monitoring disease progression and treatment response. Moreover, this type of protocol can be easily adapted to 3T scanners.

Finally, another clinically feasible example is Diffusion Kurtosis Imaging (DKI) [22]. DKI can be obtained using a standard spin-echo EPI sequence with two shells at b = 1000 s/mm^2 and b = 2000 s/mm^2, and multiple gradient directions in addition to at least one b = 0 s/mm^2 image. This type of acquisition makes it possible to model tissue microstructure using a white matter tract integrity (WMTI) model to quantify in each voxel the intra- (D_{axon}) and extra-axonal diffusivities (both radial and axial; De_{radial} and De_{axial}, respectively), the axonal water fraction (AWF), and the tortuosity of the extra-axonal space. In contrast to all the previously mentioned models, the

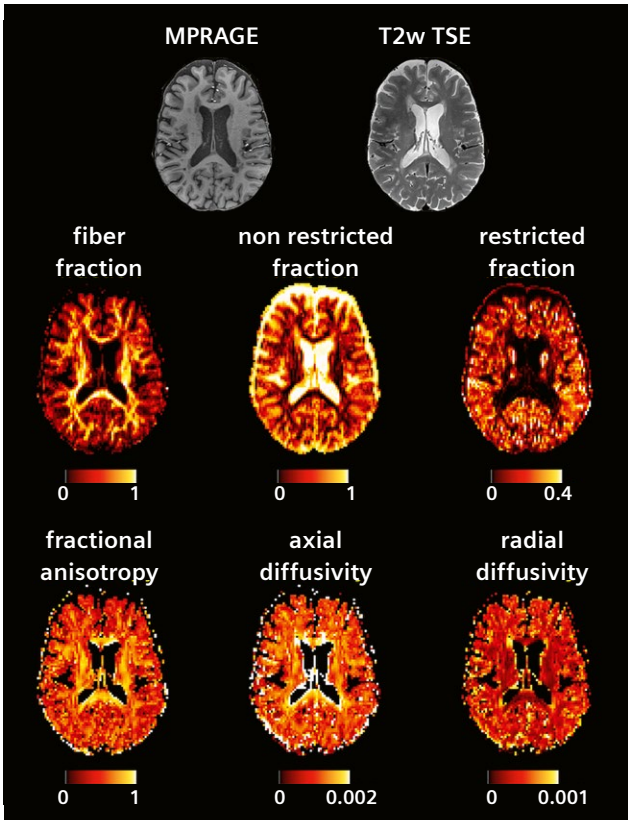

3 Microstructural map metrics estimated using the DBSI model for one MS patient. The top row shows axial views of MPRAGE and T2 sequences in which T1 and T2 lesions are visible. The other rows show all the DBSI microstructural metrics obtained in approximately the same position in diffusion space. Diffusivities are reported in mm^2/s.

assumptions involved in WMTI mean that it cannot be used to characterize lesions. However, it is very sensitive to NAWM alterations. In [23], the authors used a MAGNETOM Trio, A Tim System MRI scanner (Siemens Healthcare, Erlangen, Germany) to acquire a twice-refocused spin-echo EPI sequence for DKI with b-values of 1000 and 2000 s/mm^2 and 30 directions each (repeated twice), in addition to 11 b = 0 s/mm^2 images (TR/TE: 3700/96 ms, FOV 222 × 222 mm^2, matrix 82 × 82, 28 axial 2.7 mm thick slices) to compare 32 relapsing-remitting patients and 19 age- and sex-matched healthy controls (HC) in terms of WMTI metrics. The authors showed that WMTI metrics were sensitive to changes in the NAWM of MS patients and related to different clinical scores, which suggests that they provide a more pathologically specific, clinically meaningful, and practical complement to standard DTI-derived metrics.

Lesions and normal-appearing grey matter microstructure

Although results on WM lesions and NAWM microstructural alterations have been proven to be highly correlated with clinical deficit, the chronic inflammatory process in MS also involves the cortical and deep GM. Thus, the possible effect of the presence of both WM and GM lesions/alteration must be considered when determining their role in causing clinical deficit [24]. However, although some of the previously mentioned dMRI models (DTI, DKI, NODDI, and SMT) have also been applied to capture tissue modifications in GM caused by MS [9, 11, 12], they are based on assumptions that are specific to WM. When applied to study GM, the results must be interpreted with particular care. Very recently, the Soma And Neurite Density Imaging (SANDI) [25] model has been proposed to noninvasively estimate MRI indices of apparent neurite and soma density in the brain. This model assumes that soma (neuronal and glial cell bodies) and neurites (axons, dendrites, and glial processes) can be approximated as two non-exchanging compartments, modelled as a sphere of certain size and cylinders of zero radius ("sticks"), respectively. Under these assumptions, it is possible to recover the neurite, soma, and extracellular signal fractions ($f_{neurite}$, f_{soma}, and f_{extra}), apparent soma radius (R_{soma}) and the intra-neurite and extra-cellular diffusivities (D_{in} and D_e, respectively). Although this model requires multishell dMRI acquisitions including b-values that are at least six times higher than those used in clinical practice, a recent work [26] demonstrated that measures of f_{soma}, $f_{neurite}$, and R_{soma} from SANDI were highly reliable across multiple GM regions using images acquired on a Connectom scanner[1] (based on a MAGNETOM Skyra 3T system, Siemens Healthcare, Erlangen, Germany) with maximum b-value = 6000 s/mm^2. We have recently proposed a 10-minute protocol based on a spin-echo EPI sequence [27–29] for multishell dMRI acquisition on a 3T MAGNETOM Prisma equipped with a 64-channel receive coil with the following parameters: TR/TE = 2600/80 ms, resolution 2 × 2 × 2 mm^3, GRAPPA 2, SMS factor 4, with b-values 0/500/1000/2000/3000/4000/6000 s/mm^2 with 15/6/32/40/40/40/40 measurements per shell in anterior-posterior phase encoding, as well as one b-value = 0 s/mm^2 with reversed phase encoding. Using this sequence, we showed that we could reliably assess GM and WM microstructures according to the SANDI model on a clinical scanner. Moreover, we showed the potential clinical impact of simultaneously studying GM and WM, by demonstrating the sensitivity to GM microstructural changes due to lesions (Fig. 4) and the potential discrimination of lesions that appear to have similar contrast in FLAIR and MPRAGE but are actually different in their microstructure.

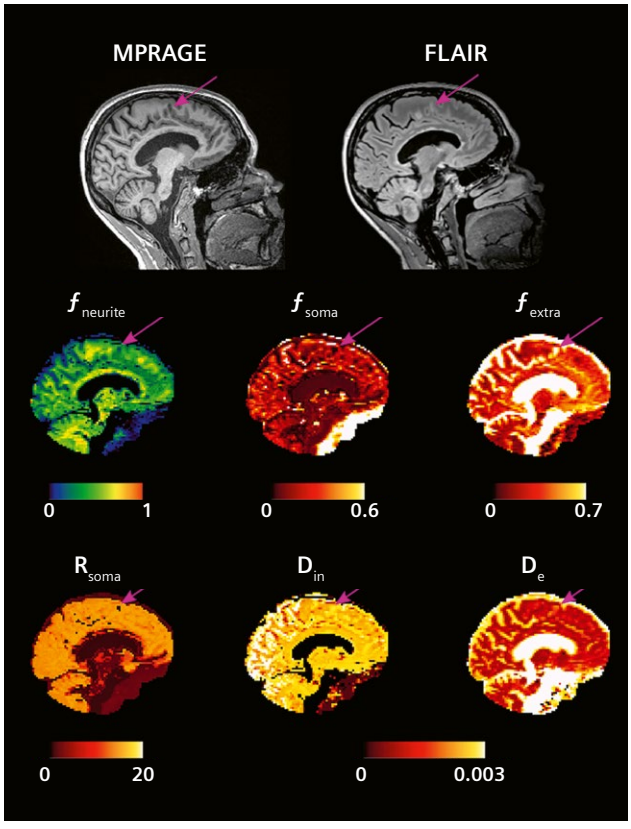

4 Microstructural metrics estimated using the SANDI model for one MS patient. The top row reports sagittal views of MPRAGE and FLAIR, with the purple arrows indicating the location of a GM lesion. Below, we show approximately the same sagittal views of neurite, soma, and extra-cellular signal fractions ($f_{neurite}$, f_{soma}, and f_{extra}), average soma radius (R_{soma}), as well as intra- and extra-neurite diffusivities (D_{in}, D_e). In correspondence to the lesion, we observe a decrease in $f_{neurite}$, f_{soma}, and R_{soma}, and an increase in f_{extra} and De. Diffusivities are reported in mm^2/s, R_{soma} in µm.

[1] *MAGNETOM Connectom is ongoing research. Siemens Healthcare does not intend to commercialize the system.*

Tractography and structural connectivity

Beyond microstructural estimation, dMRI also allows to estimate the principal trajectories followed by the axons in the brain and thus investigate structural connectivity (Fig. 5). Recent developments in the tractography algorithm have allowed users to perform tract reconstruction in the presence of WM lesions using the most common multishell acquisitions [30]. These advancements have permitted the study of potential disconnections caused by MS, not only via indirect quantification of fiber loss expressed as area, volume, thickness, or average voxel-wise microstructural damage of specific regions of interest, but also by using subject-specific bundle reconstructions. Using tractography, we can then either segment specific tracts of interest and study only their properties (number of reconstructed streamlines, average of microstructural parameters from dMRI, and/or other quantitative sequences, volumes, etc.) or analyze global structural connectivity disruptions via graph theory [7]. Examples of this can be found in [31, 32, and 33], where the same data from a multishell dMRI sequence performed on a 3T MAGNETOM Prisma scanner were used to

1. investigate different degrees of disconnection for each portion of the corpus callosum via streamline density;
2. characterize sensory motor alterations in MS patients versus HCs via graph theory applied to quantitative connectomes obtained via microstructure-informed tractography;
3. classify MS patients by applying a robust feature selection procedure to quantitative structural connectomes.

Moreover, in all these studies, when comparing dMRI-derived features with clinical scales, strong relationships were identified. This indicates that these types of analyse are useful for understanding the mechanisms underlying the manifestation of disability in MS.

Another example can be found in [34], where researchers used data from the same multishell dMRI sequence performed on the 3T MAGNETOM Prisma scanner in [17] to investigate differences in global network metrics among MS patients and HCs and their sensitivity, and the sensitivity to MS of diffusion-based microstructural maps used to build the connectomes were assessed via correlation with clinical scores. Results indicated that graph metrics extracted from connectomes weighted by intra-axonal microstructural components were most sensitive to MS pathology and most related to clinical disability. In contrast, measures of network segregation extracted from the connectomes weighted by maps describing extracellular diffusivity were most related to serum concentration of neurofilament light chain.

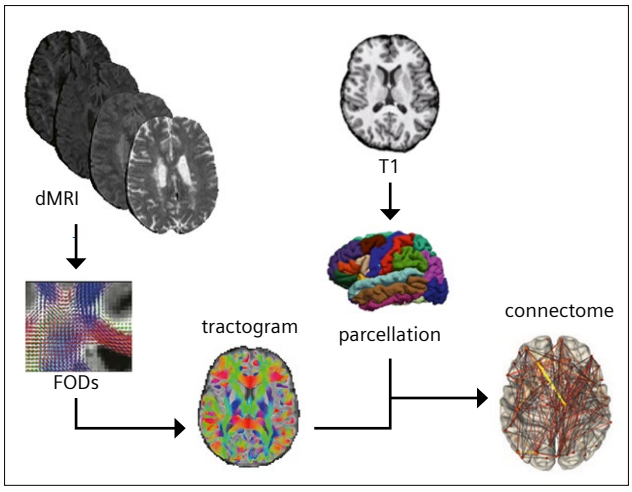

5 Example of a structural connectivity pipeline. Starting from multishell dMRI data, fiber orientation distribution (FOD) functions are estimated to reconstruct the major pathways, followed by the axons in the brain (streamlines), to create the tractogram. Using T1 images, the grey matter is parcellated to obtain regions of interests that, when combined with the tractogram, create the connectome: A graph representing all the connections found in the brain and their strengths.

Conclusions

DiffusionMRI can play an essential role in better understanding the pathophysiology of MS and in monitoring the disease course and, possibly, response to treatments. Here we provided examples of the research applications and the potential clinical impact of this technique that has not been fully exploited to date. The use of multishell sequences coupled with advanced microstructural models and quantitative tractography might really help to investigate multiple sclerosis pathophysiology and monitor structural connectivity changes.

References

1 Inglese M, Petracca M. MRI in multiple sclerosis: Clinical and research update. Curr Opin Neurol. 2018;31(3):249–255.
2 Basser PJ, Mattiello J, LeBihan D. MR diffusion tensor spectroscopy and imaging. Biophys J. 1994;66(1):259–267.
3 Novikov DS, Kiselev VG, Jespersen SN. On modeling. Magn Reson Med. 2018;79(6):3172–3193.
4 Alexander DC, Dyrby TB, Nilsson M, Zhang H. Imaging brain microstructure with diffusion MRI: practicality and applications. NMR Biomed. 2019;32(4):e3841.
5 Jelescu IO, Budde MD. Design and Validation of Diffusion MRI Models of White Matter. Front Phys. 2017;28:61. Epub 2017 Nov 28.
6 Basser PJ, Pajevic S, Pierpaoli C, Duda J, Aldroubi A. In vivo fiber tractography using DT-MRI data. Magn Reson Med. 2000;44(4):625–632.

7 Zhang F, Daducci A, He Y, Schiavi S, Seguin C, Smith RE, et al. Quantitative mapping of the brain's structural connectivity using diffusion MRI tractography: A review. Neuroimage. 2022;249:118870.
8 Cercignani M, Lannucci G, Filippi M. Diffusion-weighted imaging in multiple sclerosis. Ital J Neurol Sci. 1999;20(5 Suppl):S246–249.
9 Inglese M, Bester M. Diffusion imaging in multiple sclerosis: Research and clinical implications. NMR Biomed. 2010;23(7):865–872.
10 Filippi M, Cercignani M, Inglese M, Horsfield MA, Comi G. Diffusion tensor magnetic resonance imaging in multiple sclerosis. Neurology. 2001;56(3):304–311.
11 Hygino da Cruz LC, Batista RR, Domingues RC, Barkhof F. Diffusion magnetic resonance imaging in multiple sclerosis. Neuroimaging Clin N Am. 2011;21(1)71–88, vii-viii.
12 Cercignani M, Gandini Wheeler-Kingshott C. From micro- to macro-structures in multiple sclerosis: what is the added value of diffusion imaging. NMR Biomed. 2019;32(4):e3888.
13 Pagani E, Bammer R, Horsfield MA, Rovaris M, Gass A, Ciccarelli O, et al. Diffusion MR imaging in multiple sclerosis: technical aspects and challenges. AJNR Am J Neuroradiol. 2007;28(3):411–420.
14 Zhang H, Schneider T, Wheeler-Kingshott CA, Alexander DC. NODDI: Practical in vivo neurite orientation dispersion and density imaging of the human brain. Neuroimage. 2012;61(4):1000–1016.
15 Kaden E, Kelm ND, Carson RP, Does MD, Alexander DC. Multi-compartment microscopic diffusion imaging. Neuroimage. 2016;139:346–359.
16 Lakhani DA, Schilling KG, Xu J, Bagnato F. Advanced Multicompartment Diffusion MRI Models and Their Application in Multiple Sclerosis. AJNR Am J Neuroradiol. 2020;41(5):751–757.
17 Rahmanzadeh R, Lu PJ, Barakovic M, Weigel M, Maggi P, Nguyen TD, et al. Myelin and axon pathology in multiple sclerosis assessed by myelin water and multi-shell diffusion imaging. Brain. 2021;144(6):1684–1696.
18 Wang X, Cusick MF, Wang Y, Sun P, Libbey JE, Trinkaus K, et al. Diffusion basis spectrum imaging detects and distinguishes coexisting subclinical inflammation, demyelination and axonal injury in experimental autoimmune encephalomyelitis mice. NMR Biomed. 2014;27(7):843–852.
19 Chiang CW, Wang Y, Sun P, Lin TH, Trinkaus K, Cross AH, et al. Quantifying white matter tract diffusion parameters in the presence of increased extra-fiber cellularity and vasogenic edema. Neuroimage. 2014;101:310–319.
20 Schiavi S, Petracca M, Sun P, Fleysher L, Cocozza S, El Mendili MM, et al. Non-invasive quantification of inflammation, axonal and myelin injury in multiple sclerosis. Brain. 2021;144(1):213–223.
21 Wang Y, Wang Q, Haldar JP, Yeh FC, Xie M, Sun P, et al. Quantification of increased cellularity during inflammatory demyelination. Brain. 2011;134(Pt 12):3590–3601.
22 Jensen JH, Helpern JA, Ramani A, Lu H, Kaczynski K. Diffusional kurtosis imaging: The quantification of non-gaussian water diffusion by means of magnetic resonance imaging. Magn Reson Med. 2005;53(6):1432–1440.
23 de Kouchkovsky I, Fieremans E, Fleysher L, Herbert J, Grossman RI, Inglese M. Quantification of normal-appearing white matter tract integrity in multiple sclerosis: a diffusion kurtosis imaging study. J Neurol. 2016;263(6):1146–1155.
24 Todea RA, Lu PJ, Fartaria MJ, Bonnier G, Du Pasquier R, Krueger G, et al. Evolution of Cortical and White Matter Lesion Load in Early-Stage Multiple Sclerosis: Correlation With Neuroaxonal Damage and Clinical Changes. Front Neurol. 2020;11:973.
25 Palombo M, Ianus A, Guerreri M, Nunes D, Alexander DC, Shemesh N, et al. SANDI: A compartment-based model for non-invasive apparent soma and neurite imaging by diffusion MRI. Neuroimage. 2020;215:116835.
26 Genc S, Chamberland M, Koller K, Tax CMW, Zhang H, Palombo M, et al. Repeatability of soma and neurite metrics in cortical and subcortical grey matter. bioRxiv. 2020.
27 Xu J, Moeller S, Auerbach EJ, Strupp J, Smith SM, Feinberg DA, et al. Evaluation of slice accelerations using multiband echo planar imaging at 3 T. Neuroimage. 2013; 83:991–1001.
28 Feinberg DA, Moeller S, Smith SM, Auerbach E, Ramanna S, Gunther M, et al. Multiplexed echo planar imaging for sub-second whole brain FMRI and fast diffusion imaging. PLoS One. 2010;5(12):e15710.
29 Moeller S, Yacoub E, Olman CA, Auerbach E, Strupp J, Harel N, et al. Multiband multislice GE-EPI at 7 tesla, with 16-fold acceleration using partial parallel imaging with application to high spatial and temporal whole-brain FMRI. Magn Reson Med. 2010;63(5):1144–1153.
30 Lipp I, Parker GD, Tallantyre EC, Goodall A, Grama S, Patitucci E, et al. Tractography in the presence of multiple sclerosis lesions. Neuroimage. 2019:116471.
31 Petracca M, Schiavi S, Battocchio M, El Mendili MM, Fleysher L, Daducci A, et al. Streamline density and lesion volume reveal a postero–anterior gradient of corpus callosum damage in multiple sclerosis. Eur J Neurol. 2020;27(6):1076–1082.
32 Schiavi S, Petracca M, Battocchio M, El Mendili MM, Paduri S, Fleysher L, et al. Sensory-motor network topology in multiple sclerosis: Structural connectivity analysis accounting for intrinsic density discrepancy. Hum Brain Mapp. 2020 ;41(11):2951–2963.
33 Schiavi S, Azzari A, Mensi A, et al. Classification of multiple sclerosis patients based on structural disconnection: a robust feature selection approach. J Neuroimaging. 2022.
34 Bosticardo S, Schiavi S, Schaedelin S, Lu PJ, Barakovic M, Weigel M, et al. Microstructure-Weighted Connectomics in Multiple Sclerosis. Brain Connect. 2021;12(1):6–17.

Contact

Professor Matilde Inglese, M.D., Ph.D.
University of Genoa, DINOGMI
Largo Paolo Daneo 3
16134, Genoa
Italy
m.inglese@unige.it

Update on FLAIR Fusion in Multiple Sclerosis Follow-up and Beyond: An Indispensable Tool in Clinical Routine

Andreas Bartsch, M.D.[1]; Thomas Illigen[2]

[1]Radiologie Bamberg, Germany
[2]Siemens Healthineers, Erlangen, Germany

This is an update on the article "FLAIR Fusion in Multiple Sclerosis Follow-Up: An Indispensable Tool in Clinical Routine" by Stéphane Cantin and Emeline Lamain (Groupe Clinique du Mail, Grenoble, France), and Thomas Troalen and Melisa Bakir (Siemens Healthineers, Saint-Denis, France) that was published in MAGNETOM Flash (69) 3/2017.

Background

Modern radiologists face the challenge of managing a rising number of examinations (which, with more focus on 3D imaging and multiplanar reconstructions, themselves include an increasing number of images) without compromising the quality of their reports. *syngo*.via offers solutions to meet this challenge.

Radiologie Bamberg is a German radiological practice with a focus on neuroradiology and inflammatory CNS diseases like multiple sclerosis (MS), in particular. Its MR scanner primarily used to address the related clinical-radiological challenges is a 64-channel 3T MAGNETOM Skyra, now running on Numaris X with software version *syngo* MR XA30. Established core brain MR recordings for monitoring MS are a sagittal 3D FLAIR at 1 mm isotropic resolution or sagittal and axial 2D FLAIR at 3 mm slice thickness and submillimeter in-plane resolution.

For follow-up studies and comparisons, we generally recommend and use the AutoAlign functionality, since it is very beneficial for recording subsequent studies in good initial alignment, especially if anisotropic 2D recordings are used.

Follow-up of MS patients primarily consists of comparing current and prior examinations. The European Collaborative Research Network Magnetic Resonance Imaging in Multiple Sclerosis (MAGNIMS), has – together with the Consortium of Multiple Sclerosis Centers (CMSC) and the North American Imaging in Multiple Sclerosis Cooperative (NAIMS) – just recently published consensus recommendations on the use of MRI in MS [1], both for establishing the diagnosis and specifically for longitudinal follow-ups and monitoring the effectiveness and safety of treatment. To support detection of new MS- or treatment-related progressive multifocal leukoencephalopathy (PML) lesions, *syngo*.via can be used.

Inspired by the article "FLAIR Fusion in Multiple Sclerosis Follow-Up" by Stéphane Cantin, Thomas Troalen, Emeline Lamain, and Melisa Bakir published in MAGNETOM Flash 69 [2], we introduce further modifications, improvements and simplifications to the workflow and extend it to other applications, such as the detection of T2-progress in gliomas.

Goals

Using the previously described MPR/MPR overlay and the parathyroid-blue Color look-up table (LUT) recommended by Cantin et al. we were able to replicate their identification of new lesions. Yet, our goal and purpose for further development and improved *syngo*.via application was

1. to fully meet and comply with the new 2021 MAGNIMS-CMSC-NAIMS recommendations, which emphasize the clinical utility of co-registration, fusion, and subtraction techniques, especially if T2 lesion load is high and to increase the sensitivity for detecting new T2 lesions [1] (Panel 4, p. 10 and Appendix p. 7);
2. to provide a visualization of the registration quality between successive scans (prior and current) for QA/QC purposes; and
3. to enable the (neuro)radiologist to clearly differentiate between
   a) new or progressive lesions;
   b) unchanged lesions ("no evidence of disease activity" = NEDA according to radiological criteria);
   c) potentially decreasing lesions,

not only in MS, based on the information we can extract from the MR images.

Method

Evaluation of intramodal registration quality, see above, is essential for QA/QC in serial assessments because even at the same scanner and coil, using the same software and sequences, image co-registration/fusion is never perfect. In theory, intra-individual image registration upon follow-up is an affine problem requiring six (three translations and three rotations, "rigid-body co-registration") or seven (+ global scaling) degrees of freedom (DoF). However, gradient nonlinearities and image distortions pose challenges for this model and may lead to suboptimal results after image registration. Naturally, registration accuracy tends to be more limited for anisotropic 2D than isotropic 3D recordings, but 3D pulse sequences are more vulnerable to image intensity variations across the acquired volume. Notably, the quality of image registration between current and prior scans will influence both the sensitivity and specificity for detecting changes in lesion load or volume. Sufficient image registration accuracy is currently one of the main obstacles limiting the technological availability and widespread use of serial subtraction scans for MS follow-up, treatment, and pharmacovigilance safety monitoring as recommended by the 2021 MAGNIMS-CMSC-NAIMS consensus. Another main challenge is, due to the non-quantitative nature of standard scans, to achieve a common image intensity scaling to a best denominator between previous and follow-up scans.

We relinquished the use of color overlays as proposed by Cantin et al. and instead use an inverted grayscale. Numaris X software now provides *syngo*.via functionalities also on the scanner. One benefit is the automated grayscale adaption with no need for individual windowing using the MPR/MPR overlay, especially with the images from the prior examination being displayed at inverted grayscale on top of the current scans. The idea behind this approach was to

a) highlight new lesions,
b) obscure those that did not change in comparison and
c) obtain opposed contrast to a) for areas that decreased in size.

The latter and QA/QC evaluation of the image registration quality is not sufficiently feasible using color volume overlays.

Workflow

To establish our new workflow on *syngo*.via or directly on the scanner in View&GO, you need to simultaneously load the current and prior examinations. This can be achieved automatically with *syngo*.via using the prefetch functionality.

We would recommend a 2 x 3 layout to display the images in axial and sagittal orientations. Depending on your examination strategy and/or monitor settings, other layouts might be more expedient.

As a next step, an MPR/MPR overlay is created as described by Cantin et al.

For the reasons detailed above, we do not use the parathyroid-blue Color LUT. Instead, we recommend using the inverted grayscale overlay, which effectively yields an intensity-normalized subtraction between the current and

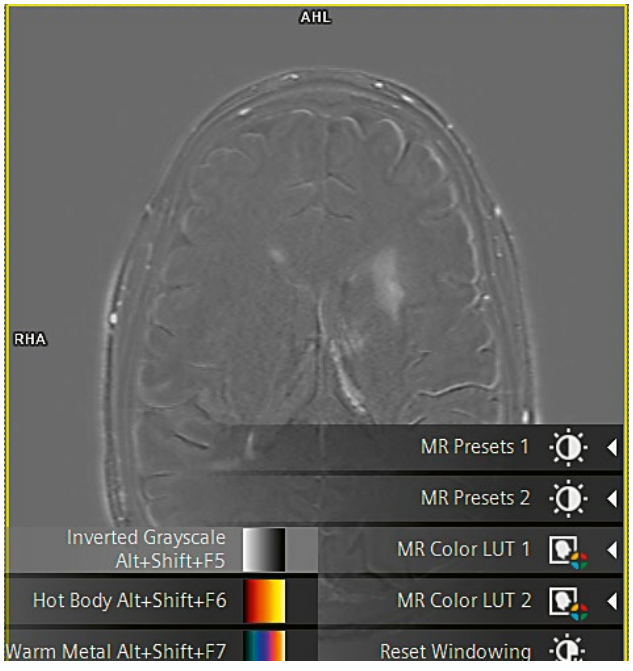

1 Assigning the MR Color LUT 1 Inverted Grayscale.

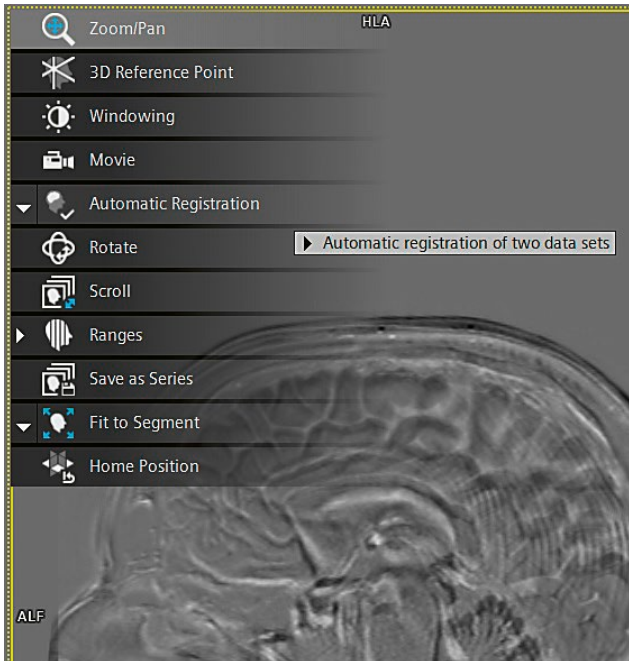

2 Top-left menu with Automatic Registration tool.

prior examination. Please note that Color LUT 1 will be used for the second loaded dataset; usually this will be the prior examination (Fig. 1).

It is essential to co-register the datasets. The Automatic Registration tool can be used for this next step.

The automatic registration is applied for all datasets simultaneously, so axial and sagittal images will be coregistered together just with one click.

Automatic registration will only work if both the current as well as prior exam have either been distortion corrected or not. We recommend 2D distortion correction per default. However, if this was disabled for one of the exams it can be reset in syngo.via for the other to generate a new series to match the two for registration.

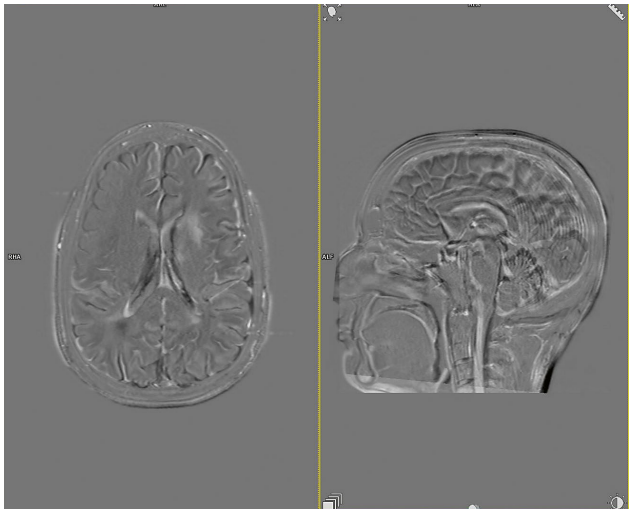

3 Axial and sagittal MPR/MPR inverted grayscale overlays before co-registration.*
** Although the initial overlay is reasonable, due to AutoAligned acquisitions, it should be further improved.*

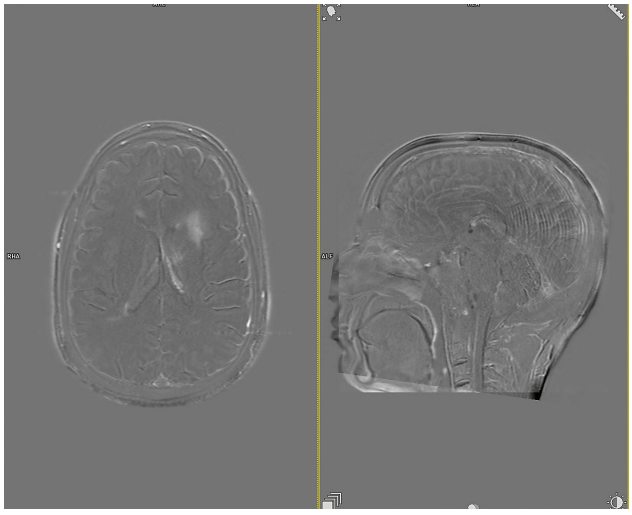

4 Axial and sagittal MPR/MPR inverted grayscale overlays after automatic registration.*
** Better (though not perfect) alignment between the current and prior scans becomes obvious at the outer and inner (ventricular) brain edges.*

If the automatic registration should not meet the expectations, there is still the opportunity to perform a visual alignment or manual registration of the two datasets (Fig. 5).

The proposed layout now offers, at rapid and convenient glance, a fast and easy comparison and reliable appraisal of lesions according to our primary goals a) to c) (see above).

The arrows and arrowheads in Figure 6 mark new FLAIR-hyperintense lesions in the current dataset as compared to the previous examination. The MPR/MPR overlay of our workflow properly highlights those lesions as white hyperintense areas at high contrast.

The red arrow in Figure 7 depicts an unchanged lesion in the current as compared with the previous examination. It is "zeroed out" in the MPR/MPR overlay, confirming that there is no radiological evidence of disease activity with regards to this particular lesion.

The following slice from another case in Figure 8 shows the conceivable lesion behavior of new or enlarging, unchanged, and decreasing lesions all in one image.

On the slice from the current data, the red arrow indicates an unchanged lesion which is "zeroed out" in the overlay subtraction (right), while the pink arrow reveals a new, expanding lesion juxtacortical to the insular cortex. The green arrow on the slice of the prior examination shows a lesion that was decreasing in the current compared with prior examination and which is visualized hypointense (black) on the MPR/MPR overlay.

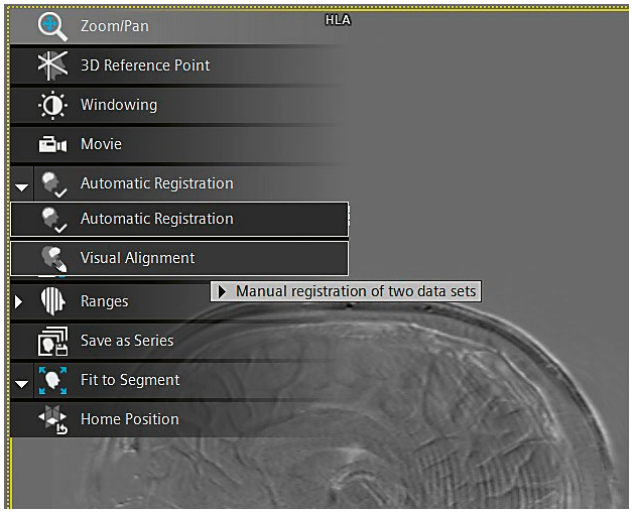

5 Top-left menu with Visual Alignment tool.*
** In our experience, a visual alignment was never necessary; automatic registration is recommended.*

Registration accuracy is best judged on the outer and inner (ventricular) brain edges. Here, misalignments will show up as hyper- and/or hypointense bands, respectively, in subtraction images. Such misalignments also affect the appearance of lesions in the overlay images and can, if not judiciously accounted for, lead to false-positive and false-negative detections. Compared to color overlays, our use of an inverted grayscale in a 2 x 3 layout substantially facilitates the recognition of such registration errors and thereby enhances both sensitivity and specificity.

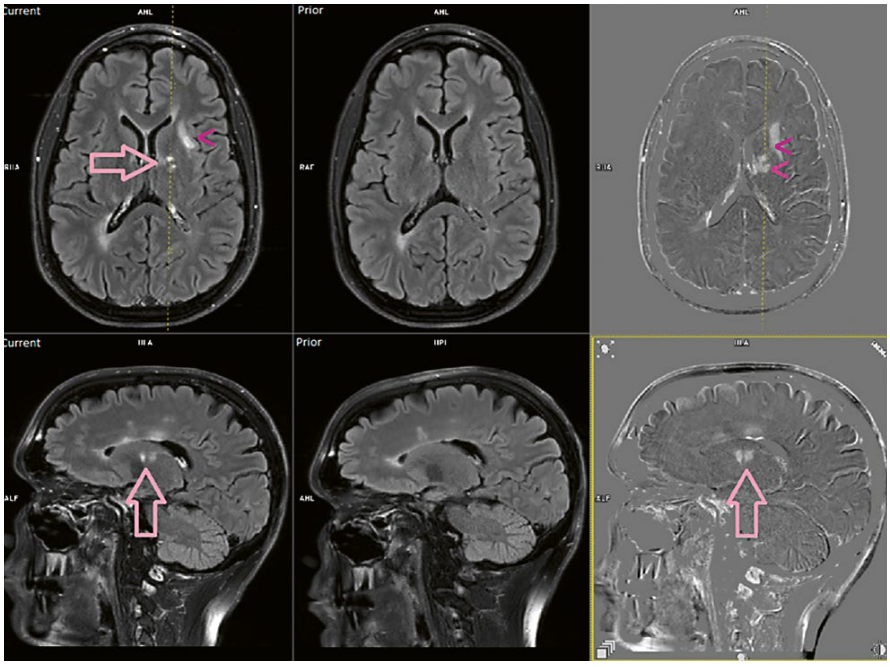

6 Detection of new lesions upon MS follow-up according to our workflow.*
** Note that for the current but not prior examination, gadolinium agent has been applied IV before the FLAIR acquisitions to prolong the delay to improve contrast enhancement as per the latest MAGNIMS 2021 recommendations. Therefore, there is positive contrast in the overlay subtraction images on the right in the choroid plexus.*

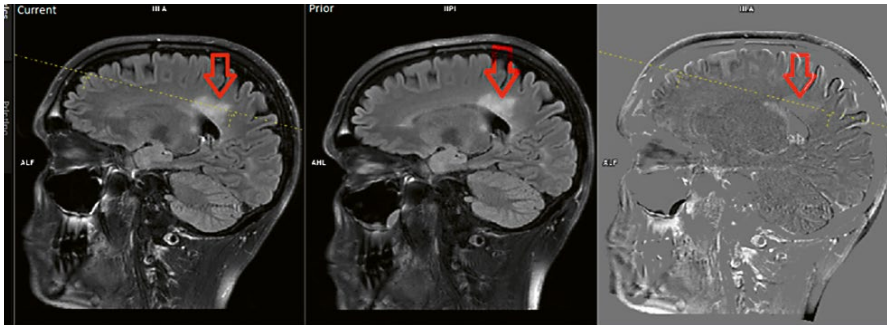

7 Concealing unchanged lesions upon MS follow-up in our workflow.*
** Also note the regression of mucosal swelling in the maxillary sinus in the current as compared to the prior exam, which therefore shows up hypointense in the overlay subtraction image on the right.*

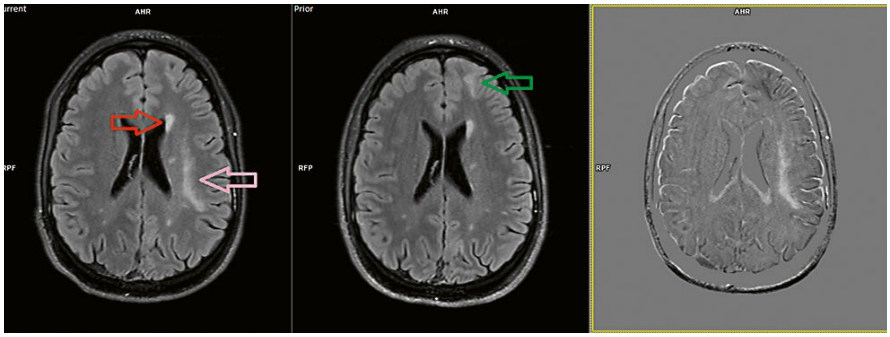

8 New (pink arrow), unchanged (red arrow), and decreasing (green arrow) lesions in a patient positive for the John Cunningham polyomavirus (JCV) with MS who developed an inflammatory PML after his 81st natalizumab infusion. Unchanged lesions are "zeroed out" in the MPR/MPR overlay, while new or enlarging lesions appear hyperintense, and regressive lesions hypointense. This is the desired behavior.*
** Slight misalignments between the current and prior scans appear as hyper/hypointense bands at brain edges and allow to assess the quality of image registration.*

In theory, optimal alignment of prior and follow-up scans would involve an unbiased, robust, inverse consistent co-registration into a mid-space between both images (in order to apply the same amount of interpolation to both) that iteratively deweights areas of high variance (i.e., differences/changes) between the two time points [3–5]. However, in our experience automatic registration of current and prior exams using MPR/MPR with inverted grayscale overlay works quite well if the same scanner and sequence were used for follow-up.

For 3D sequences recorded at 3T, particular care is required to avoid variable image intensity biases in the serial scans. If image alignment is sufficiently accurate according to visual QA/QC judgement, new lesions well below the 3 mm scale (reference size according to QBK-RL 2020 [6]) can be detected, in our experience even at the 1 mm scale.

Conclusion

In summary, our new proposed workflow enables the user to rapidly perform image co-registration, fusion, and intensity-normalized inverted grayscale overlay of serial scans that allows for good quality control and visualizes differences in lesion load/volume (i.e., numerical and in lesion extent) at opposite contrast while "zeroing out" unchanged

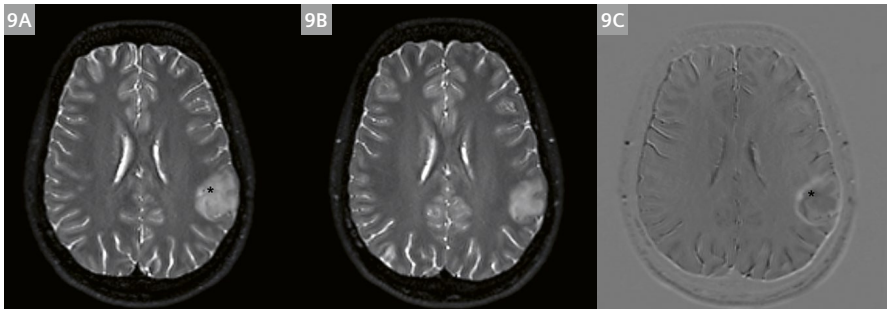

9 Detection of long-term T2 progression in a left supramarginal oligodendroglioma using co-registered 1 mm isotropic fat-saturated 3D T2 SPACE scan subtraction.
(9A) Current exam (March 2021).
(9B) Prior exam, not yet registered to (9A) but displaying approximately the same location at the tumor level, dating back 44 months (June 2017; and prior to stereotactic biopsy).
(9C) T2 scan subtraction using co-registered and inverted grayscale overlay of (9B) on (9A).

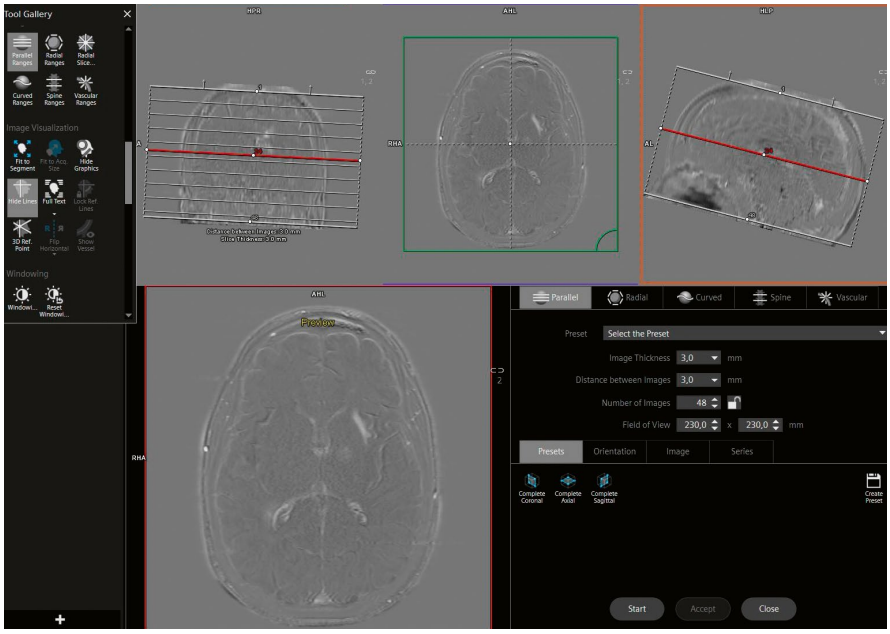

10 Axial reconstruction using the Parallel Ranges tool.

lesions as in subtraction images. This meets the recently published MAGNIMS-CMSC-NAIMS 2021 consensus recommendations on the clinical utility of co-registration, fusion, and subtraction techniques for monitoring disease activity, treatment response, and treatment safety in MS, especially if T2 lesion load is high, and to increase the sensitivity for detecting new T2 lesions [1].

According to in-house experience during the past year, our workflow may lead to several MS lesion detections which would have otherwise, due to high lesion load of the patient or, similarly, high work load of the reporting radiologist, been missed.

Furthermore, the technique can equally be applied to monitor T2 progress and treatment responses in intra-axial brain tumors, such as gliomas. In Figure 9 long-term, crescent-shaped T2 progression of the primary brain tumor became apparent comparing (Fig. 9A) and (Fig. 9B) and is accurately visualized in (Fig. 9C). Previously, it was missed on the short-term comparison of successive scans. The tiny dot (*) of a hypointense signal loss in the medial aspect of the tumor is due to a microbleed from the biopsy and also detectable on (Fig. 9C). The main tumor bed comes out slightly hypointense (i.e., with negative overlay values) due to discrete changes of the signal characteristics of the oligodendroglioma.

Additionally, any on a suitable given sequence/contrast hyper- (or even hypo-) intense lesion can be longitudinally monitored by our method (e.g., epidermoid cysts on diffusion or arachnoid cysts on T2/FLAIR) and, at least in theory, even the development of brain atrophy (which will present as “misregistration bands”; see OA/QC of registration accuracy in the Workflow section above). Global (and local) atrophy development is generally considered to reflect a neurodegenerative component of MS [7] but its assessment is not part of the current MAGNIMS 2021 recommendations [1].

For documentation and storage, the created MPR/MPR overlays can easily be reconstructed and saved in a separate series using the Parallel Ranges functionality (Fig. 10). To avoid interpolation artifacts, we recommend to reconstruct the subtraction overlays at no less than 2 mm slice thickness (we routinely use 3 mm). These subtraction series (“delta maps” or “change maps”) are then exported to the institution’s PACS.

The overlay subtractions generated by our workflow are – aside from pure radiological disease, treatment, and safety monitoring itself – well suited to present the detected changes to the patient in an intuitive manner that is easy to understand in order to argue for treatment options, to obtain informed consent, and to potentially improve compliance with the suggested management during further personalized care.

Acknowledgment

We are very grateful for the long-standing collaboration, support, and regular suggestions and requests for improvements provided by Dr. Boris-Alexander Kallmann, M.D., from the Multiple Sclerosis Center Bamberg (MSZB).

References

1 Wattjes MP, Ciccarelli O, Reich DS, Banwell B, de Stefano N, Enzinger C, et al. 2021 MAGNIMS-CMSC-NAIMS consensus recommendations on the use of MRI in patients with multiple sclerosis. Lancet Neurol. 2021;20(8):653–670.
2 Cantin S, Troalen T, Lamain E, Bakir M. FLAIR Fusion In Multiple Sclerosis Follow-Up. MAGNETOM Flash. 2017;69(3):100–103. Available from https://www.magnetomworld.siemens-healthineers.com/clinical-corner/application-tips/flair-fusion-in-multiple-sclerosis-follow-up.html
3 Reuter M, Rosas HD, Fischl B. Highly accurate inverse consistent registration: a robust approach. Neuroimage. 2010;53(4):1181–1196.
4 Reuter M, Schmansky NJ, Rosas HD, Fischl B. Within-subject template estimation for unbiased longitudinal image analysis. Neuroimage. 2012;61(4):1402–1418.
5 Reuter M, Gerstner ER, Rapalino O, Batchelor TT, Rosen B, Fischl B. Impact of MRI head placement on glioma response assessment. J Neurooncol. 2014;118(1):123–129.
6 Richtlinie des Gemeinsamen Bundesausschusses über Kriterien zur Qualitätsbeurteilung in der Kernspintomographie nach § 135b Absatz 2 SGB V [Internet]. Berlin, Germany: Gemeinsamer Bundesausschuss [cited February 10, 2022]. Available from: https://www.g-ba.de/downloads/62-492-2036/QBK-RL_2019-10-17_iK_2020-01-01.pdf
7 De Stefano N, Stromillo ML, Giorgio A, Bartolozzi ML, Battaglini M, Baldini M, et al. Establishing pathological cut-offs of brain atrophy rates in multiple sclerosis. J Neurol Neurosurg Psychiatry.2015;0:1–7.

Contact

PD Dr. med Andreas Bartsch, M.D.
Radiologie Bamberg
Heinrichsdamm 6
96047 Bamberg
Germany
bartsch@radvisory.net

Thomas Illigen
SHS EMEA CWE DI MR
Karlheinz-Kaske-Str. 2
91052 Erlangen
Germany
thomas.illigen@siemens-healthineers.com

Translation of Computer-Assisted MRI Assessments of Multiple Sclerosis to Clinical Care

Hagen H Kitzler[1]; Paul Kuntke[1]; Caroline Köhler[1]; Jennifer Linn[1]; Maria-Laura Blefari[2]; Sara Makaretz[2]; Adrian Tsang[2]; Till Hülnhagen[3]; Jonathan A Disselhorst[3]; Rodrigo Perea[2]; Ricardo A. Corredor-Jerez[3]; Punith B Venkategowda[4]; Sowmya Devdas[4]; Tjalf Ziemssen[5]; Elizabeth Fisher[2]; Tobias Kober[3]; on behalf of the MS PATHS* Investigators

*Multiple Sclerosis Partners Advancing Technology and Health Solutions

[1]Institute of Diagnostic and Interventional Neuroradiology, University Hospital Carl Gustav Carus, Technische Universität Dresden, Germany
[2]Biogen Digital Health, Biogen, Cambridge, MA, USA
[3]Advanced Clinical Imaging Technology, Siemens Healthineers, Lausanne, Switzerland
[4]Siemens Healthcare Pvt. Ltd., Bangalore, India
[5]Multiple Sclerosis Center, Center of Clinical Neuroscience, Department of Neurology, University Hospital Carl Gustav Carus, Technische Universität Dresden, Germany

MSPie served as a prototype platform to optimize and validate the performance of parts of the AI-Rad Companion Brain MR product solution.

Key points

- Standardized volumetric MRI follow-up protocols
- Fully automatic MRI data routing
- Immediate volumetric MRI analysis
- Computer-assisted monitoring
- Approval/rejection of results and report generation

Background

The Multiple Sclerosis Partners Advancing Technology and Health Solutions (MS PATHS; https://www.mspaths.com) is a Biogen-sponsored network that aims to standardize and quantify clinical, radiological, and biomarker assessments of MS in routine clinical practice, with the ultimate goals of enabling personalized medicine and large-scale real-world research. For the imaging assessments, the intention is to provide highly precise, automated quantification of disease-specific volumetric changes of both MS lesions and normalized brain volume. Mainly sub-clinical in nature, these MRI changes over time can provide important information on disease severity and response to disease modifying therapies [1].

In 2009, the concept of an MS treatment target termed, "no evidence of disease activity" (NEDA) arose from a retrospective analysis of clinical trial data [2], with the original definition consisting of no relapses, no disability progression, and no MRI-based disease activity markers, i.e., no gadolinium enhancing lesions or new or enlarging T2 lesions. Subsequently, further

Parameter	3D FLAIR MS-P	3D T1 MS-P
Brain coverage	Full	Full
Acquired pre-contrast	Pre-contrast	Pre-contrast
Orientation	Sagittal	Sagittal
MR acquisition type	3D	3D
Repetition time (ms)	5000	2300
Echo time (ms)	392–394	2.96–2.98
Inversion time (ms)	1800	900
Flip angle (deg)	120	9
Read FOV (mm)	256	256
Phase FOV (mm)	240	240
Percent FOV (%)	93.8	93.8
No. phase encoding steps	221	239
Phase encoding direction	A >> P	A >> P
Slice thickness (mm)	1	1
Pixel spacing (mm)	1 × 1	1 × 1
Pixel bandwidth (Hz/Px)	780	240

Table 1: The standardized MS PATHS acquisition protocol. This MRI protocol was implemented on available 3T scanners from Siemens Healthineers within all participating MS PATHS centers allowing optimal regional monitoring and inter-institutional comparison.

development of the NEDA definition led to the incorporation of the annualized rate of brain volume loss [3]. Based on recent imaging protocol and monitoring recommendations [4, 5], standardized imaging data acquisition forms the basis towards individual precision medicine monitoring in MS when supplemented by computer-aided evaluation technology.

The concept of new or enlarging T2 lesions (NET2L) as a marker of MS inflammatory activity is based on the understanding that the vast majority of gadolinium-enhancing lesions evolve into permanent T2 lesions. In addition, the growth of chronic inflammatory active lesions is yet another recognized marker of disease activity. The occurrence of NET2L in MS under treatment is considered evidence of therapy insufficiency or even failure [3].

The gradual loss of brain volume over lifetime represents a physiological process termed atrophy. Brain atrophy however intensifies and accelerates in MS, constituting the accumulative result of tissue destruction [6]. Therefore, (1) the cross-sectional comparison of individual brain volume measures with age-matched control groups and (2) the determination of the brain atrophy rate over defined intervals are measurable determinants of non-physiological brain atrophy. To normalize overall brain volume measures, brain tissue volume is typically normalized using the individually stable intracranial volume. The resulting ratio is called brain parenchymal fraction (BPF) and thus allows inter-individual comparison [7]. Although disease-modifying therapies attenuate brain volume loss in MS [8], the use of brain atrophy as a clinical marker of disease progression in individual patients is still subject of debate [9].

To realize the goals of reliable, quantitative MRI metrics in the MS PATHS network, Biogen initiated a collaboration with Siemens Healthineers to jointly develop the MS PATHS image evaluation (MSPie) software.[1] This *syngo*.via Frontier-based prototype enabled optimization and validation of the employed algorithms within the clinical workflow in a close collaboration between the University Hospital Dresden, other MS PATHS partners, Biogen and Siemens Healthineers. To this end, the prototype has an interactive user interface and means to correct the results. The final product which will be available within the AI-Rad Companion Brain MR suite incorporates the learnings which were gained from MSPie and is a fully automatic, non-interactive solution. Here, we present the results of our initial experience with translating this development to the point of care.

[1] *Work in progress. The application is currently under development and is not for sale in the U.S. and in other countries. Its future availability cannot be ensured.*

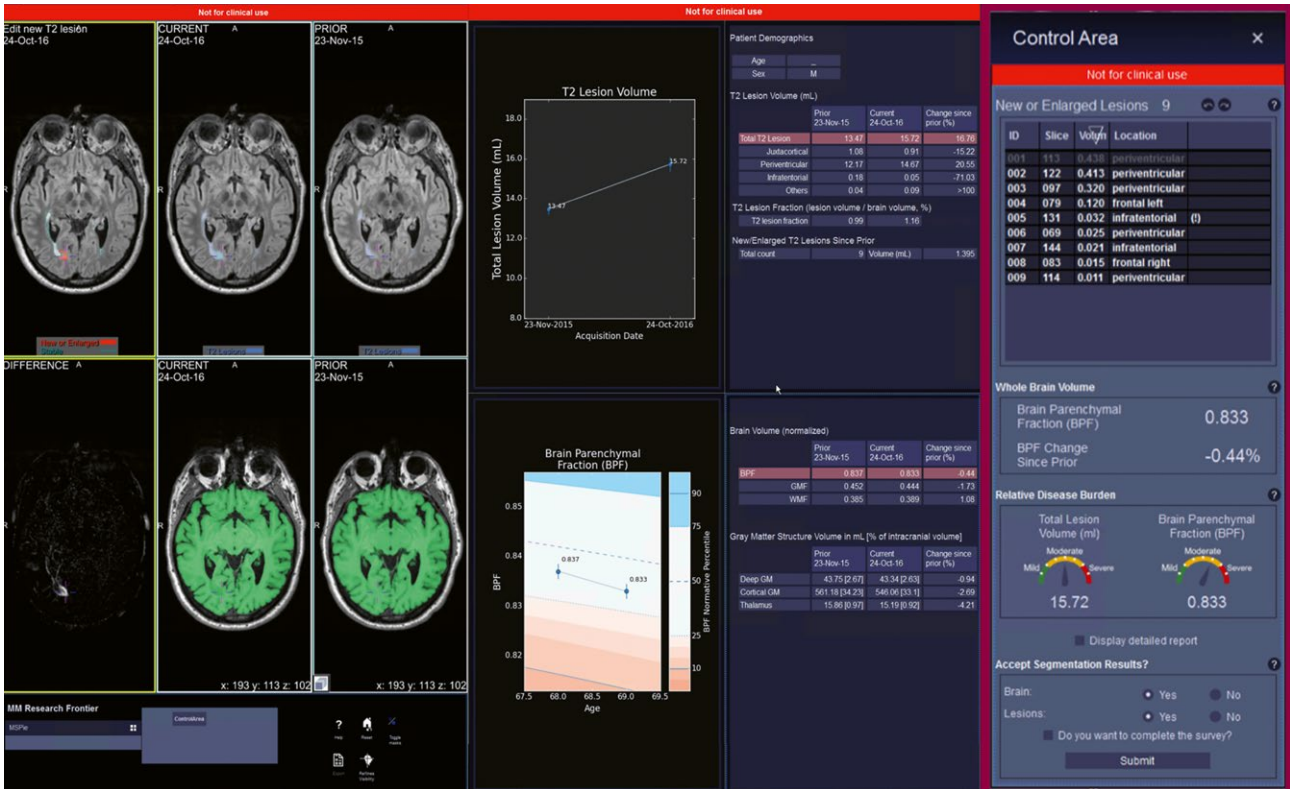

1 The graphical user interface provides a full screen presentation of segmentation and comparison results combined with a collection of numerical and graphical evaluations and a separate articulated control area for interactive lesion editing. Reformats can be adapted to coronal or sagittal viewing habits.

Methods

Standardized follow-up brain MRI acquisition

The use of MRI to measure MS disease activity and progression required minimal adjustments in primary data acquisition to ensure high sensitivity to changes over time [10]. The MS PATHS network therefore agreed to harmonize their institutional scanner protocols across all 3T MRI scanners from Siemens Healthineers at participating centers.

Core sequences are a 3D fluid-suppressed T2 contrast (FLAIR SPACE; "3D FLAIR MS-P") and a 3D T1 contrast (MPRAGE; "3D T1 MS-P") for detection of changes in T2 lesion burden and brain volume (for protocol details, see Table 1).

These two contrasts are taken as input for generating the imaging biomarkers (most importantly NET2L and BPF change) needed for the assessment. The lesion segmentation is a novel, fully automated prototype software, which showed good robustness and detection performance both cross-sectionally and longitudinally since it also takes partial volume effect into account [11–13].

During the development of MSPie, the BPF calculation was highly optimized in order to be able to robustly measure smallest volume changes, as the average rate of brain atrophy in MS is only about 0.5%/year.

The *syngo*.via Frontier setup is configured to allow an automated routing of the sequences described in Table 1 to *syngo*.via which then retrieves the prior MRI (if available) from the PACS and sends it to MSPie. The images are immediately analyzed and results are available approximately 10 minutes after the acquisition without any user interaction. They can then be viewed and evaluated in a graphical user interface (GUI) which was specifically designed for the application in the MS PATHS centers. The experiences gathered during its design and optimization in the clinical testing workflow were incorporated into the reports which are output by the product solution.

The MSPie GUI consists of two panels and a separate control area (Fig. 1). The main page provides the processed prior and current standardized "3D FLAIR MS-P" and "3D T1 MS-P" images overlaid with T2 lesions (blue) and whole brain parenchyma segmentations (green), respectively. A grey scale difference map presents highlighted changes over time accompanied by a color-coded map, where new or enlarging T2 lesions are marked differently (red) from stable lesions (blue). NET2L volume, total T2 lesion volume, T2 lesion volume fraction per total brain volume as well as the sub-volumes of juxtacortical, periventricular, infratentorial, and remaining other lesion types are provided together with their percentage change since the prior MRI.

2 The automatically generated report contains all the quantitative metrics displayed in the user interface. Subdivided into T2 lesion metrics and morphometry, i.e., volume measurements, the aim was to create an overview to inform referring neurologists of processing and evaluation results. Supplementary information documents technical constraints and quality impairments.

Brain volume is provided as BPF, alongside with the segmented grey matter (GM) and white matter (WM) fractions and their percent change. Additionally, volume fractions of cortical and deep GM and of the thalamus are generated.

The separated control area allows the evaluating neuroradiologist to edit the detected NET2L separately, i.e., NET2L can be removed from the results or added in case they were missed. In the latter case, a single click on the missed lesion is sufficient to activate a local segmentation, thus no manual segmentation needs to be conducted. In addition, both qualitative dials describing total lesion volume and BPF severity are provided based on a comparison with MS patients collected within the MS PATHS network.

All results are included in the report (see Fig. 2) to inform on the quantitative analysis. The report is created only after completion of the interactive review and, if the results are accepted by the neuroradiologist, it is sent to the PACS to accompany MSPie annotated lesion and brain masks.

Results

MSPie deployment into the MS radiology workflow

At our institution, we established an exploratory workflow to evaluate the integration of such a solution in our routine work while it was made sure that the standard radiological reading was not affected. The integration required minor adaptation of the institutional radiology workflow for follow-up MRI evaluation. For comparison with the MSPie results, the 3D FLAIR and T1 sequences were simultaneously reviewed in at least two perpendicular reformats in conventional setup. Furthermore, registered T2 and proton density acquisitions of the institutional protocol allowed infratentorial constraints of the 3D FLAIR-based lesion segmentation to be overcome. Reading using the MSPie prototype was arranged to follow conventional visual evaluation to avoid over-reliance on technical processing.

Since the MSPie evaluation was an additional procedure step of the application it initially prolonged the workflow. Whereas getting used to the MSPie handling compensated and subsequently even increased evaluation speed, some delay persisted in conjunction with institutional information technology performance restrictions. With growing confidence in the algorithm performance, we anticipate that evaluations can considerably accelerate today's routine reading.

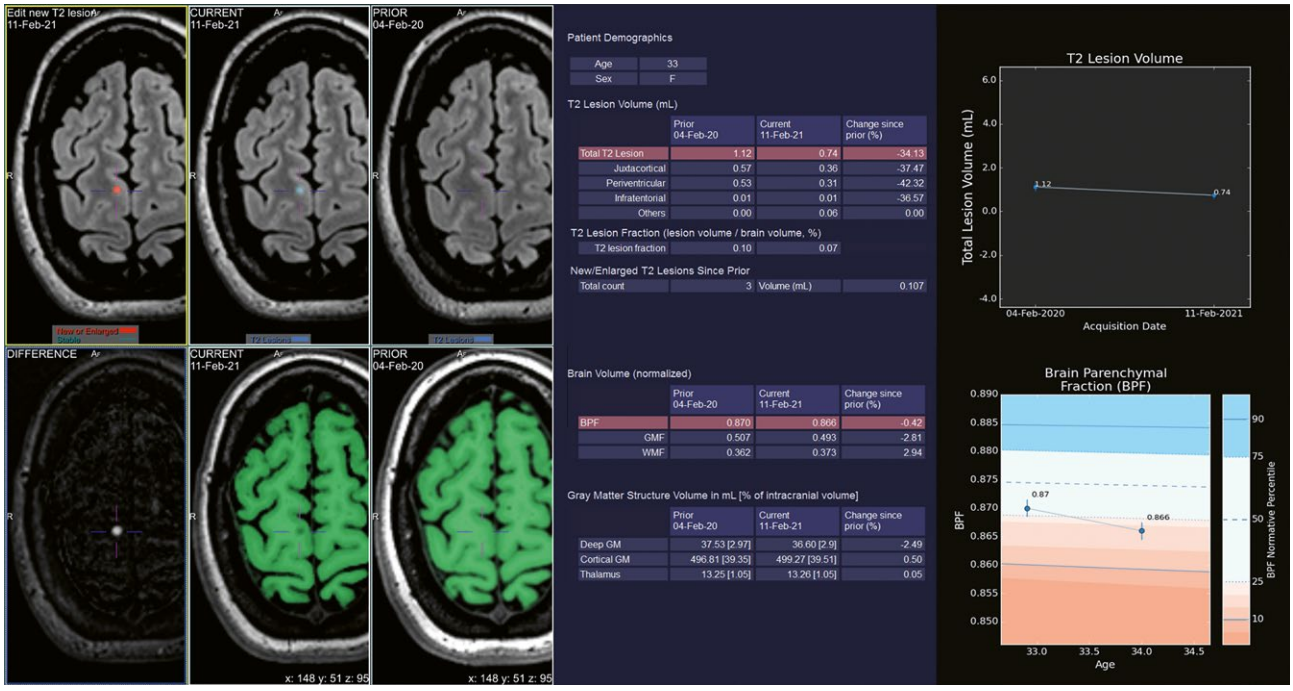

3 Within the standardized annual follow-up examination of this example MS patient a new juxtacortical T2 lesion appeared in the right frontal location (crosshairs), visible in the difference map and classified as NET2L (red) in the upper left segment used for lesion editing. In this segment, lesions can be deleted or added if necessary (see Fig. 4).

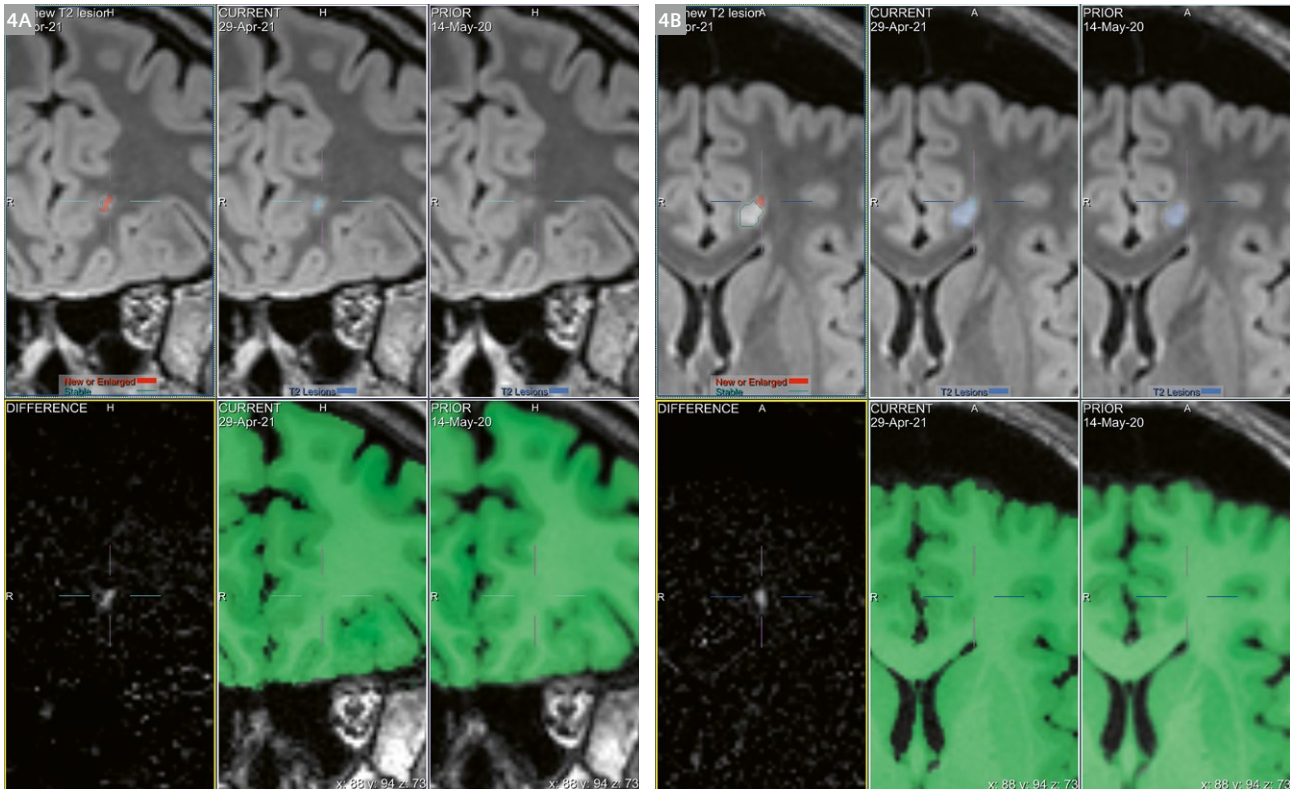

4 Two example patients with lesion growth of different geometry in standardized follow-up examination. The volume increase can be quaquaversal, i.e., resulting in a volume inflation in all directions **(4A)**, but more often regional outgrowth can be detected **(4B)**, resulting in an annex exceeding the prior lesion boundary.

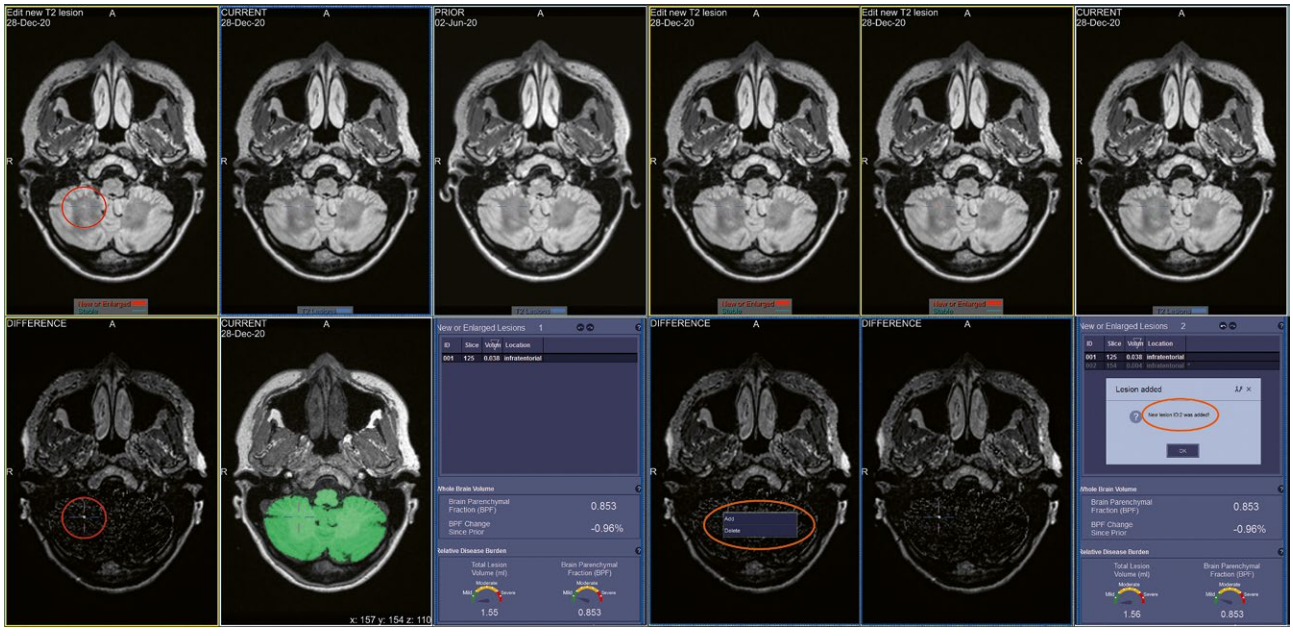

5 The MSPie prototype allows corrections to the automatically detected new or enlarging lesions. The difference map visualizes highlighted changes that occurred between the two time points (red circle; left half of the panel). Missed NET2L can be selected by an interactive window (orange ellipse) to add it to the NET2L segmentation.

Automated detection of new or enlarging T2 lesions

The detection of NET2L represents the essential task of the MRI evaluation in MS neuroradiology. Optimal MRI acquisition quality is thereby crucial to enable high precision of visual inspection. However, in MS patients with high lesion load, or with very small lesion size, juxtacortical lesions, or new lesions located adjacent to pre-existing lesions, visual detection can be challenging. Computer-assisted detection ensures high precision of the evaluating neuroradiologist even in difficult cases.

The software immediately provides all detected lesion differences with a clear visualization of stable lesions and NET2L volumes using well-distinguishable color-coding. Upon completion of conventional visual evaluation, it allowed checking for completeness, i.e., the review of perceived NET2L and other changes. This double-pass approach likely increases diagnostic certainty.

Besides newly forming lesions, lesion growth is also common in MS. Detection of enlarging lesions represents the more difficult task for the evaluating neuroradiologist since growth can be subtle, of complex geometry or ill-defined margins, and the surrounding diffusely abnormal WM might obscure the lesion formation and size change. However, lesion growth provides an important marker of subclinical inflammatory activity. The detection rate of enlarging lesions using conventional visual evaluation is therefore relatively low in comparison to new T2 lesions.

As with any image analysis software, automated lesion segmentation and change detection are subject to error. The interactive review of MSPie results was therefore deemed a significant feature when the prototype was in its planning stages. Thus, within MSPie, lesions missed (false negatives) and falsely detected NET2L (false positives) can be added or deleted using single mouse clicks in the GUI prior to being stored in the PACS or patient medical record (see Fig. 5). The generated corrections were consecutively used to optimise the final, non-interactive product solution.

Upon finalization of the editing process and completed PACS archiving, all results are summarized in an embedded report (see Fig. 2).

Brain volume assessment

In later adulthood, continuous decrease of brain volume is observed in normal aging. In MS, brain volume loss, or brain atrophy, begins at disease onset and progresses at an accelerated rate compared to healthy controls throughout the disease course. Within MS PATHS, normative values for the BPF were established, which allow volumetric changes exceeding normal brain aging to be detected.

In the prototype software, the BPF is automatically calculated and plotted against an age-matched healthy control subgroup which indicates age-specific percentiles. This already allowed visual perception and immediate age-appropriate and age-inappropriate classification for a single time point (see Fig. 6).

Further details of brain parenchyma volumes are provided, i.e., the normalized GM and WM volume fraction, as well as the compartmental volumes of cortical, deep and thalamic GM, including their shares in overall brain tissue volume.

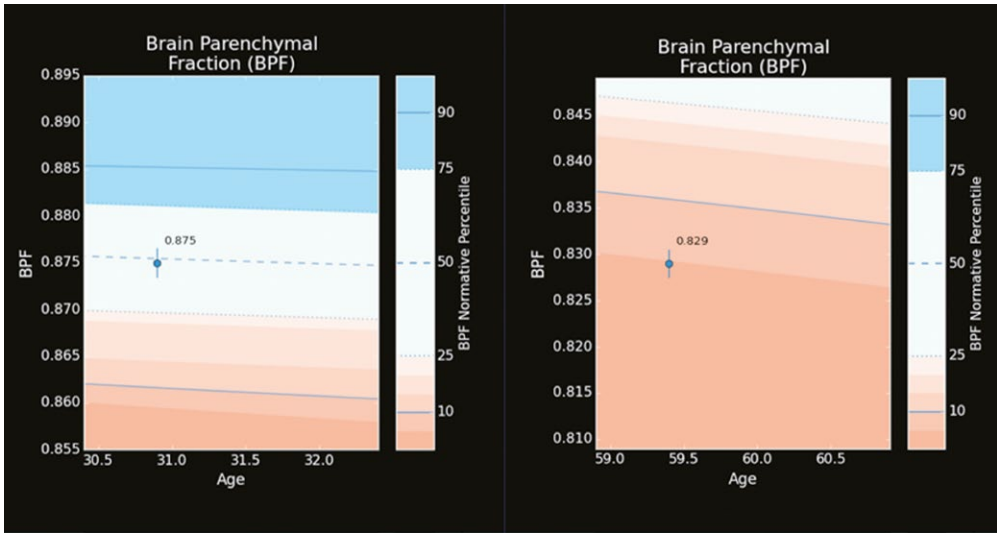

6 Cross-sectional evaluation to classify age-appropriateness of brain tissue volume for a given examination age using BPF percentiles. For quick reference the color-coded percentile score is displayed beside each plot for contextualization. Whereas the left case showed an age-appropriate BPF of 0.875 at the age of approx. 31 years, the right case clearly demonstrated an age-inappropriate BPF of 0.829 at the age of 59 years.

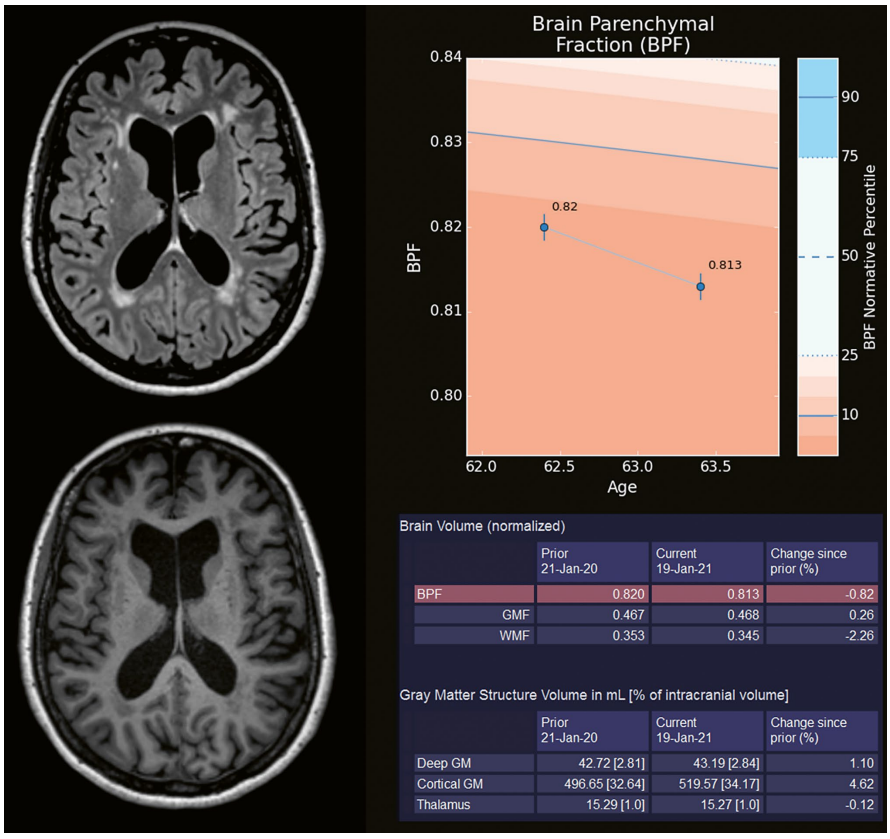

7 The natural course of MS is characterized by an accelerated loss of brain parenchyma resulting in age-inappropriate brain volume denominated as atrophy. The transition from age-appropriate to age-inappropriate normalized brain parenchyma volumes (BPF) is depicted in Figure 2. In the example on the left, BPF was already age-inappropriate at the prior MRI and further decreased by 0.82% in the annual follow-up, illustrating an explicitly increased acceleration of brain volume loss over time. The example FLAIR and T1 reformats below corpus callosum level visually demonstrated a predominant WM loss numerically confirmed by a relative 2.26% decrease.

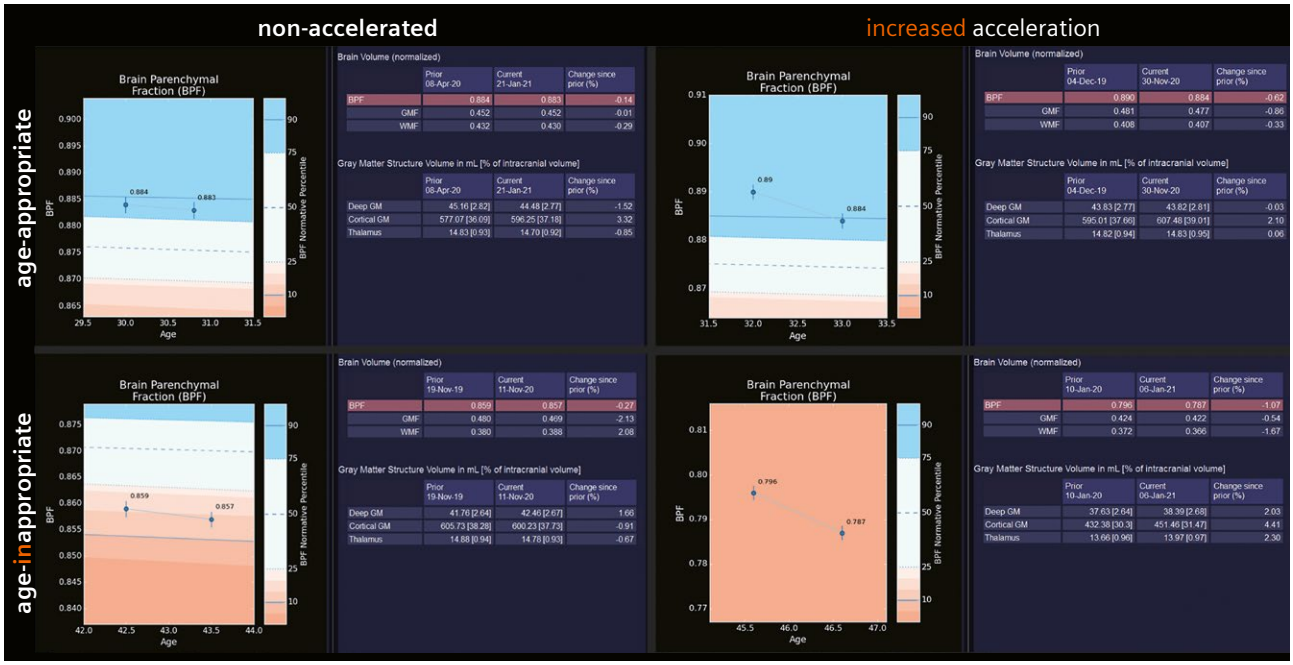

8 A classification in categories attempt of MS brain volume conditions and slopes of parenchymal volume loss.

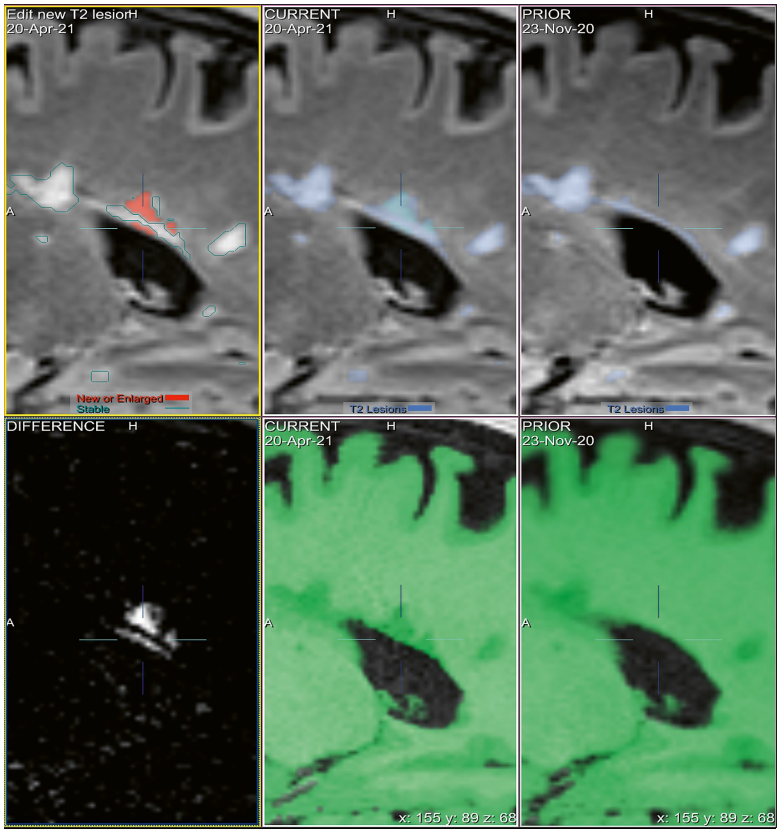

9 Multifocal growths of a stable periventricular lesion resembling three different NET2Ls selected by the prototype but effectively being separate growth zones of the same lesion.

Assessment of annual normalized brain volume change
To determine brain atrophy at the point of care in individual MS patients, the combined assessment of current state and rate of change is necessary. Based on the approach seen in Figure 8, four different descriptive classifications can be distinguished:

1. Age-appropriate and non-accelerated,
2. Age-inappropriate and non-accelerated,
3. Age-appropriate and increased acceleration, and
4. Age-inappropriate and increased acceleration, of BPF and BPF annual change, respectively.

It should be noted that the normative data for the BPF change over time are generated from single-time point assessments; it is thus assumed that the resulting rate of change describes healthy brain aging accurately on a group level.

Perils and pitfalls

The evaluation of the well-defined new T2 lesion segmentation results did not represent a problem. A couple of conditions, however, require careful interpretation of computer assisted tools for MS.

First, new MSPie users had to become acquainted with assessing lesion growth, especially in confluent lesions. If lesion/conglomerate growth was multifocal, as is shown in an illustrative case in Figure 9, NET2L segmentation resulted in multiple separated growth areas, i.e., erroneously classified growing lesions. Hence, the NET2L number was artificially increased. More sophisticated editing is currently being discussed to mitigate this issue in future software versions.

The change of a stable lesion location between two consecutive scans due to temporary displacement led to anomalous segmentation. Since only growth but not shrinkage was detected, this resulted into erroneously classified lesion growth (Fig. 10).

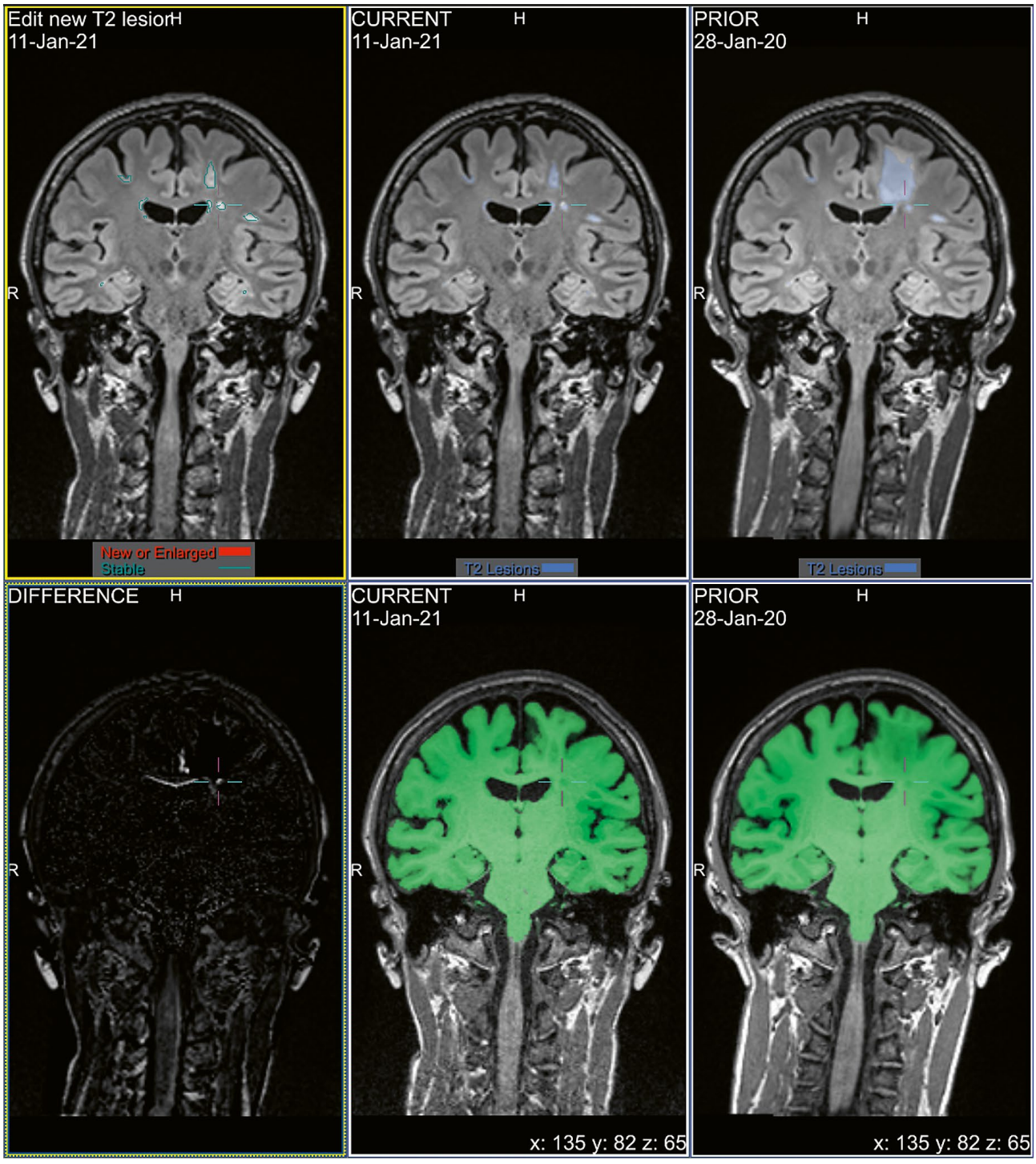

10 Due to a left frontal hyperacute lesion with perifocal edema and swelling, an adjacent lesion (crosshairs) was displaced in the prior scan. When edema and space occupation are resolved in the current scan this lesion held a slightly different position (note the shift within the cross hairs). As a result, a difference due to the lesion position change was detected during follow-up of this, in fact, unchanged lesion.

11 A case of long-standing Baló's sclerosis with clinical progression. No new or growing lesions were found, but there was an annualized 1.87% BPF change. Since the absolute T2 lesion volume decreases, such extreme atrophy may result in concomitant total apparent lesion volume reduction.

The quantification of the T2 lesion burden and brain tissue loss may also not be independent from each other, since in severe atrophy, an apparent overall T2 lesion volume reduction may emerge, as observed in Figure 11. However, this issue might be expected in severe and predominant WM atrophy only, but may be overcome by correction.

Finally, co-morbid diseases in MS patients may complicate both conventional and computer-assisted image evaluation. The cause of possible confusion is the limited specificity of the T2 signal and lesions. Stroke residues, brain tumors, and post-traumatic gliosis (see example in Fig. 12) may resemble lesions detected by the prototype. To prevent erroneous inclusion, the respective patients need to be evaluated with caution to exclude all non-MS pathology in computer-assisted segmentation.

Discussion

MSPie provides automatic data routing, longitudinal processing, and visualization of the results, as well as report generation, integrated into the neuroradiologist's workflow. The immediate, automated analysis represents the most important development for efficient translation, since results are ready for evaluation promptly after the acquisition. Retrieving results directly after scanning will allow the integration into standard radiological reporting that immediately follows. For the evaluating neuroradiologist it can increase reading speed for most MS cases.

The integration of quantitative cross-sectional and follow-up information on imaging MS pathology, including NET2L and brain atrophy rates, in so-called subclinical disease activity monitoring after definite clinical diagnosis and under treatment, fulfills an increasing demand for translation of highly specific volumetric assessments to routine reading by treating MS neurologists [3, 6].

To achieve precise volumetric measurements and especially reliable assessments of their change over time, the standardization of imaging data acquisition is mandatory [14]. This was recently reiterated in recommendations on the use of MRI in patients with MS, with a particular focus on follow-up MRI protocols in established disease and under immune-modulating treatment [5].

Based on our preliminary experience, this software can provide distinct benefits for MS image evaluation precision and reliability. In MS cases with extensive MRI pathology, visual evaluation can be laborious and prone to neurora-

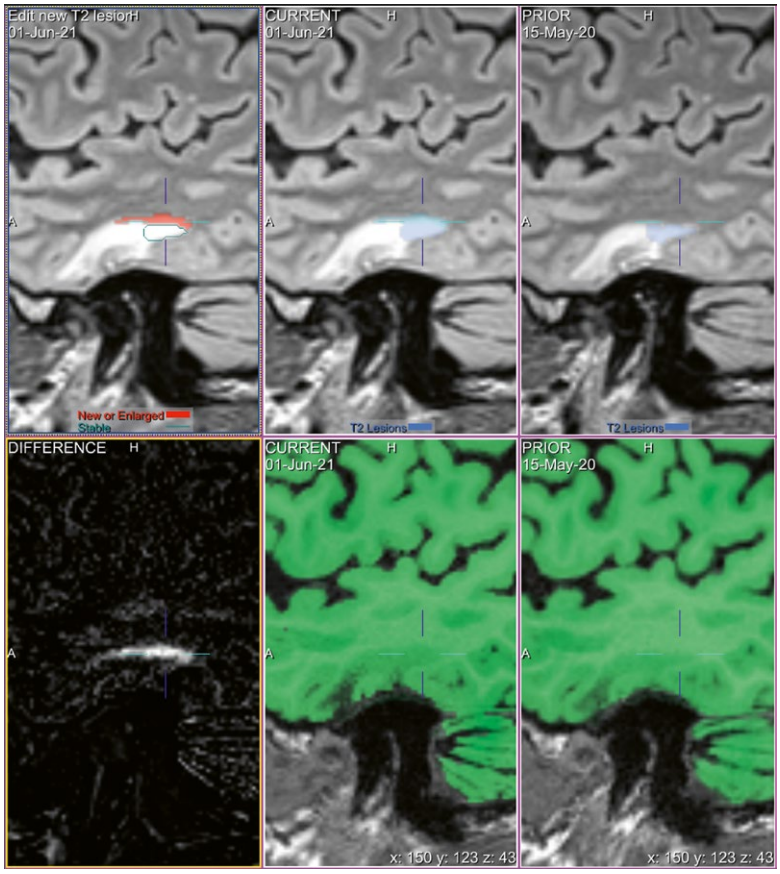

12 Post-traumatic temporal gliosis in an MS patient analyzed with the software prototype. The residue of a contusion resembles a T2 signal similar to an MS lesion and therefore was partly segmented. Progressing within the observation period, the prototype even detected lesion growth. However, this lesion needed to be excluded from the analysis.

diological misjudgment. Here, MSPie may ensure precision for follow-up MRI reading.

In particular, the MS imaging feature of subtle T2 lesion growth has likely been missed by conventional visual evaluation without computer aid. Hence, the importance of precision increase in clinical follow-up is obvious. However, this also identifies the need of common definitions of variants of MS lesion growth which are so far not incorporated into the neuroradiological repertoire of disease-related changes in MS [15].

The longitudinal quantification of brain tissue volume in MS allows the observation of increased rate of brain volume loss, exceeding the age-dependent acceleration. So far, conventional neuroradiology has been unable to quantify this characteristic feature of MS pathology in routine assessment. Thus, the precise determination of accelerated atrophy rates here appears to be the greatest translational advancement achieved.

However, the still incomplete clinical definition of MS imaging surrogates of subclinical disease activity and their clinical meaning [16, 17] presents neuroradiologists with a situation where precise characteristic alterations are provided at the diagnostic point of care that are still subject of debate in clinical MS neurology [18, 19].

Conclusions

Automated quantification of MS imaging metrics has long been a challenge, and the lack of standardization and highly precise techniques hindered its translation into clinical care. Insufficient MRI data quality, resolution, and limited reproducibility further impeded such application at the diagnostic point of care.

In combination with a perpetual standardized MR imaging protocol, the prototype may enable robust and fully integrated assessment of MS cases. While the neuroradiologist must remain vigilant with respect to machine-generated results, the software proves to support advanced clinical care and could serve the high information demand in MS neurology.

References

1 Mowry EM, Bermel RA, Williams JR, Benzinger TLS, de Moor C, Fisher E, Hersh CM, Hyland MH, Izbudak I, Jones SE, Kieseier BC, Kitzler HH, et al. Harnessing Real-World Data to Inform Decision-Making: Multiple Sclerosis Partners Advancing Technology and Health Solutions (MS PATHS). Front Neurol. 2020 Aug 7;11:632.

2 Havrdova E, Galetta S, Hutchinson M, Stefoski D, Bates D, Polman CH, O'Connor PW, Giovannoni G, Phillips JT, Lublin FD, Pace A, Kim R, Hyde R. Effect of natalizumab on clinical and radiological disease activity in multiple sclerosis: a retrospective analysis of the Natalizumab Safety and Efficacy in Relapsing-Remitting Multiple Sclerosis (AFFIRM) study. Lancet Neurol. 2009 Mar;8(3):254-60.

3 Kappos L, De Stefano N, Freedman MS, Cree BA, Radue EW, Sprenger T, Sormani MP, Smith T, Häring DA, Piani Meier D, Tomic D. Inclusion of brain volume loss in a revised measure of 'no evidence of disease activity' (NEDA-4) in relapsing-remitting multiple sclerosis. Mult Scler. 2016 Sep;22(10):1297-305.

4 Sastre-Garriga J, Pareto D, Battaglini M, Rocca MA, Ciccarelli O, Enzinger C, Wuerfel J, Sormani MP, Barkhof F, Yousry TA, De Stefano N, Tintoré M, et al.; MAGNIMS study group. MAGNIMS consensus recommendations on the use of brain and spinal cord atrophy measures in clinical practice. Nat Rev Neurol. 2020 Mar;16(3):171-182.

5 Wattjes MP, Ciccarelli O, Reich DS, Banwell B, de Stefano N, Enzinger C, Fazekas F, et al.; Magnetic Resonance Imaging in Multiple Sclerosis study group; Consortium of Multiple Sclerosis Centres; North American Imaging in Multiple Sclerosis Cooperative MRI guidelines working group. 2021 MAGNIMS-CMSC-NAIMS consensus recommendations on the use of MRI in patients with multiple sclerosis. Lancet Neurol. 2021 Aug;20(8):653-670.

6 Giovannoni G, Butzkueven H, Dhib-Jalbut S, Hobart J, Kobelt G, Pepper G, Sormani MP, Thalheim C, Traboulsee A, Vollmer T. Brain health: time matters in multiple sclerosis. Mult Scler Relat Disord. 2016 Sep;9 Suppl 1:S5-S48.

7 Rudick RA, Fisher E, Lee JC, Simon J, Jacobs L. Use of the brain parenchymal fraction to measure whole brain atrophy in relapsing-remitting MS. Multiple Sclerosis Collaborative Research Group. Neurology. 1999 Nov 10;53(8):1698-704.

8 Tsivgoulis G, Katsanos AH, Grigoriadis N, Hadjigeorgiou GM, Heliopoulos I, Papathanasopoulos P, Dardiotis E, Kilidireas C, Voumvourakis K. The efect of disease-modifying therapies on brain atrophy in patients with clinically isolated syndrome: a systematic review and meta-analysis. Ther Adv Neurol Disord. 2015;8(5):193–202.

9 Andravizou A, Dardiotis E, Artemiadis A, Sokratous M, Siokas V, Tsouris Z, Aloizou AM, Nikolaidis I, Bakirtzis C, Tsivgoulis G, Deretzi G, Grigoriadis N, Bogdanos DP, Hadjigeorgiou GM. Brain atrophy in multiple sclerosis: mechanisms, clinical relevance and treatment options. Auto Immun Highlights. 2019 Aug 10;10(1):7.

10 Simon JH, Li D, Traboulsee A, Coyle PK, Arnold DL, Barkhof F, Frank JA, Grossman R, Paty DW, Radue EW, Wolinsky JS. Standardized MR imaging protocol for multiple sclerosis: Consortium of MS Centers consensus guidelines. AJNR Am J Neuroradiol. 2006 Feb;27(2):455-61.

11 Fartaria MJ, Bonnier G, Roche A, Kober T, Meuli R, Rotzinger D, Frackowiak R, Schluep M, Du Pasquier R, Thiran JP, Krueger G, Bach Cuadra M, Granziera C. Automated detection of white matter and cortical lesions in early stages of multiple sclerosis. J Magn Reson Imaging. 2016 Jun;43(6):1445-54.

12 Fartaria MJ, Todea A, Kober T, O'brien K, Krueger G, Meuli R, Granziera C, Roche A, Bach Cuadra M. Partial volume-aware assessment of multiple sclerosis lesions. Neuroimage Clin. 2018 Feb 28;18:245-253.

13 Fartaria MJ, Kober T, Granziera C, Bach Cuadra M. Longitudinal analysis of white matter and cortical lesions in multiple sclerosis. Neuroimage Clin. 2019;23:101938.

14 Suthiphosuwan, Suradech & Kim, David & Bharatha, Aditya & Oh, Jiwon. (2017). Imaging Markers for Monitoring Disease Activity in Multiple Sclerosis. Curr Treat Options Neurol. 2017 May;19(5):18.

15 Köhler C, Wahl H, Ziemssen T, Linn J, Kitzler HH. Exploring individual multiple sclerosis lesion volume change over time: Development of an algorithm for the analyses of longitudinal quantitative MRI measures. Neuroimage Clin. 2019;21:101623.

16 Lublin FD. Disease activity free status in MS. Mult Scler Relat Disord. 2012 Jan;1(1):6-7.

17 Hegen H, Bsteh G, Berger T. 'No evidence of disease activity' – is it an appropriate surrogate in multiple sclerosis? Eur J Neurol. 2018 Sep;25(9):1107-e101.

18 Monschein T, Salhofer-Polanyi S, Altmann P, Zrzavy T, Dal-Bianco A, Bsteh G, Rommer P, Berger T, Leutmezer F. Should I stop or should I go on? Disease modifying therapy after the first clinical episode of multiple sclerosis. J Neurol. 2021 Apr;268(4):1247-1253.

19 Mayssam EN, Eid C, Khoury SJ, Hannoun S. No evidence of disease activity: Is it an aspirational therapeutic goal in multiple sclerosis? Multiple sclerosis and related disorders. 2020;40:101935.

Contact

Dr. Hagen H. Kitzler, M.D.
Institute of Diagnostic and Interventional Neuroradiology
Universitätsklinikum Carl Gustav Carus an der Technischen Universität Dresden
Fetscherstrasse 74
01307 Dresden
Germany
Tel.: +49 (0)351 458-18331
Hagen.Kitzler@ukdd.de

Comparison of Clinical 7T vs 3T MRI for Epilepsy: A Photo Essay

Emmanuel C. Obusez, M.D.; Doksu Moon, M.D.; Paul Ruggieri, M.D.; Irene Wang, Ph.D.; Stephen E. Jones, M.D., Ph.D.

Section of Neuroradiology, Department of Radiology, Imaging Institute, Cleveland Clinic, Cleveland, OH, USA

Introduction

Patients with drug-resistant epilepsy have a poor quality of life, high hospitalization costs, and high hospital readmission rates [1–3]. Surgery is highly effective for the management of drug-resistant seizures in such cases [4, 5]; however, surgical outcomes are dependent on accurate imaging identification of the epileptogenic pathology [6–9], and approximately 20% to 40% of focal epilepsy lesions are not identified on lower-field 3T or 1.5T magnetic resonance imaging (MRI) [10, 11]. Although gross lesions such as tumors, developmental abnormalities, trauma, infarctions, and infections can be clearly identified as the cause of seizures on imaging studies, many smaller or subtle lesions are not easily detected or characterized on lower-field imaging. These lesions therefore present a diagnostic challenge during the preoperative evaluation of patients with epilepsy.

Although 7T MRI was initially developed as a research tool, the U.S. clearance of this modality in 2017 rapidly led to its use in clinical settings, with studies showing improved detection of epileptogenic lesions not seen on lower-field imaging studies, in addition to improved characterization and delineation of the extent of such lesions [12]. The higher field strength of 7T accounts for a substantial gain in signal when compared with lower-field imaging, permitting higher spatial resolution and enhanced tissue contrast of the gray-white matter junction and thus allowing for improved accuracy in the identification of epileptogenic pathology. 7T MRI may therefore help to identify patients with drug-resistant seizures who may be candidates for epilepsy surgery. In this article, we present a photo essay of cases illustrating the added value of 7T neuroimaging in the evaluation of patients with epilepsy who are being assessed as potential candidates for surgery.

MRI technique

The 7T MR images included in this article were acquired at our institution with a 7T whole-body MR clinical scanner (MAGNETOM Terra; Siemens Healthcare, Erlangen, Germany) using a 1Tx/32Rx head coil (Nova Medical, Inc., Wilmington, MA, USA). Patients excluded and not scanned on 7T MR scanners were those with an inability to remain motionless while in the MR machine, those with implants not yet validated to be safe on 7T scanners, and those with claustrophobia. The 7T MAGNETOM Terra scan parameters are listed in Table 1. Comparative lower-field images were acquired at our institution with a 3T whole-body scanner (MAGNETOM Skyra, Verio, Trio, or Vida; Siemens Healthcare, Erlangen, Germany) using a 20-channel phased-array head/neck coil or a 32-channel phased-array coil; or with a 1.5T whole-body scanner (MAGNETOM Symphony, Aera, Avanto, or Espree; Siemens Healthcare, Erlangen, Germany) using conventional phased-array coils. There are differences in the scan parameters for the various types of 3T and 1.5T MRI scanners; Table 2 and Table 3 list the basic scan protocols for epilepsy on 3T and 1.5T scanners, respectively.

Sequence	TR/TE (ms)	FOV (mm^2)	Slice thickness (mm)	In-plane resolution (mm^2)	TI1/TI2 (ms)	Band-width (Hz/pixel)	Scan time (min)	FA
Coronal and axial 2D T2 FLAIR	9000/68	80	1.5	0.3 × 0.3	2599	284	6.20	130°
Sagittal T1 MPRAGE	3000/2.5	160	0.71	0.71 × 0.71	1050	340	5.56	9°
Sagittal T1 MP2RAGE	4540/2.9	150	0.71	0.71 × 0.71	1040/3200	200	7.13	4°
Coronal T2*-weighted GRE	5000/90	80	1.5	0.2 × 0.2		233	6.12	100°
Axial 3D SW	22/15	240	1.2	0.2 × 0.2		140	5.17	15°

Table 1: **7T MAGNETOM Terra sequence parameters**
FA, flip angle; FOV, field of view; TE, echo time; TI, inversion time; TR, repetition time

Sequence	TR/TE1/TE2 (ms)	FOV (mm^2)	Slice thick-ness (mm)	Matrix
Coronal T2 FLAIR	7800/128	168*180	3	320 × 180
Axial T2 FLAIR	8640/136	166*190	3	320 × 204
Coronal T2	3000/104	166*179	3	416 × 269
Coronal MPRAGE	2300/2.84	210	1.2	192 × 192
Sagittal MPRAGE	2300/2.84	256	1	192 × 192
Axial SWI	27/20	2.5	2.5	256 × 256

Table 2: **3T sequence parameters**
FOV, field of view; TE, echo time; TR, repetition time

Sequence	TR/TE1/TE2 (ms)	FOV (mm^2)	Slice thick-ness (mm)	Matrix
Coronal T2 FLAIR	8360/111	170	4	320 x 320
Axial T2 FLAIR	8360/117	201	4	224 × 192
Coronal T2	9.8/4.76	256	1	256 × 256
Coronal MPRAGE	11/4.92	230	1.25	224 × 256
Sagittal MPRAGE	1800/3.12	256	1	256 × 256
Axial SWI	49/40	220	3	224 × 204

Table 3: **1.5T sequence parameters**
FOV, field of view; TE, echo time; TR, repetition time

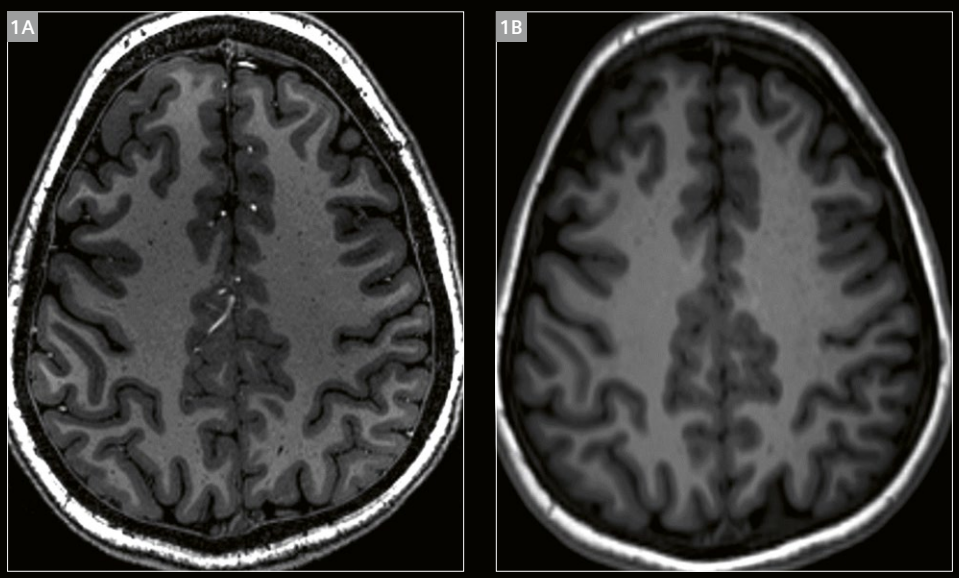

1 Comparative images, co-registered in the same patient, showing generalized increased tissue contrast at the gray-white matter junction with 7T imaging. Images from an axial 7T MAGNETOM Terra MPRAGE 0.71-mm isotropic scan **(1A)** and an axial 3T MAGNETOM Vida MPRAGE 1-mm isotropic scan **(1B)** are shown. In our experience, the clear delineation of the gray-white matter junction aids in better detection of focal cortical dysplasia (FCD) in patients with epilepsy.

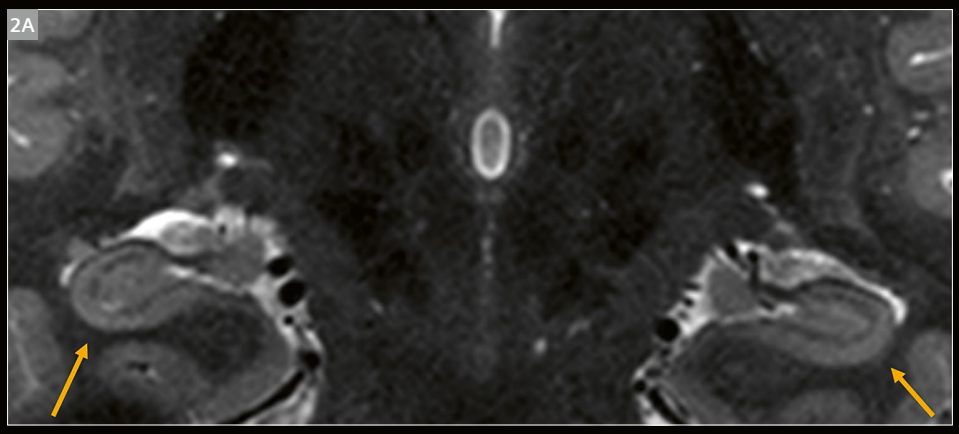

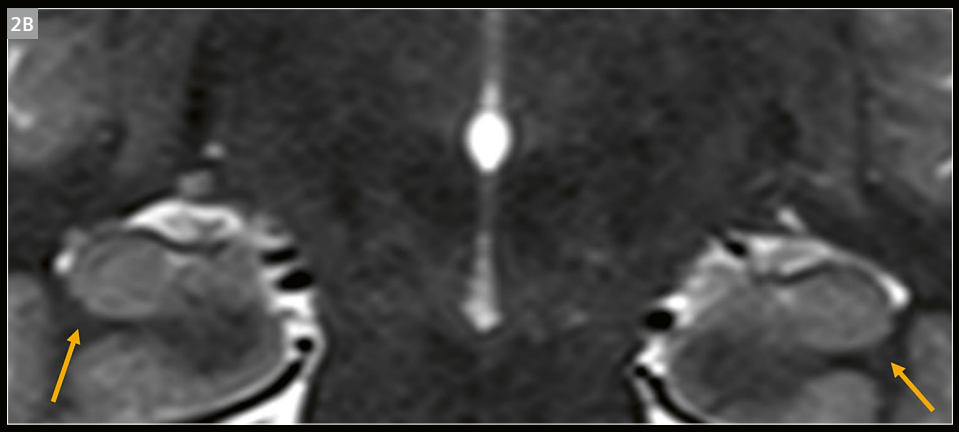

2 Improved detail of hippocampal structures with 7T imaging. Coronal 7T MAGNETOM Terra T2*-weighted imaging **(2A)** and co-registered coronal 3T MAGNETOM Vida T2 imaging **(2B)** of the same patient showing normal hippocampal anatomy. This comparison illustrates the improved delineation of the margins of both hippocampal formations and dentate gyri (arrows) at 7T due to the higher tissue contrast and spatial resolution.

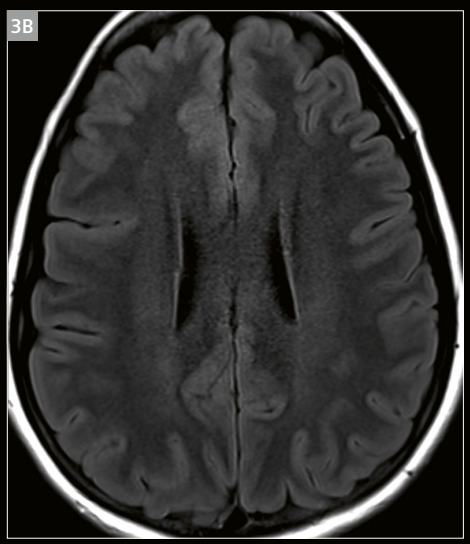

3 Comparative FLAIR images, co-registered in the same patient, for evaluating the gray-white matter junction. Images from an axial 7T MAGNETOM Terra FLAIR 1-mm slice thickness scan **(3A)** and an axial 3T MAGNETOM Vida FLAIR 3-mm slice thickness scan **(3B)** show little apparent clinical benefit in evaluating the margins of the gray-white matter junction with 7T even with the apparently higher signal-to-noise ratio and thinner slice thickness of the 7T FLAIR sequence.

Case 1

A 24-year-old man with epilepsy onset at age 20 presented to our institution with drug-resistant epilepsy. The results of all previous imaging studies (all performed at 3T or lower field strength) were normal. Electroencephalogram (EEG) demonstrated seizure activity in the left hemisphere. Axial **(4A)** and coronal **(4C)** 7T T1 MP2RAGE images demonstrate an FCD, which manifests as blurring of the gray-white matter junction in the right parietal lobe (yellow arrows). In retrospect, the lesion can also be seen on 3T T1 MPRAGE images **(4B, 4D)**. Although the lesion is clearly more conspicuous on the 7T T1 MP2RAGE images than on the 3T T1 MPRAGE images, it can be argued that it is no more evident on a 7T FLAIR image **(4E)** than on a 3T FLAIR image **(4F)** (where the FCD is barely visible and only appreciated with a priori knowledge). We have found this to be the case for most of our patients with FCD: the FCDs are most conspicuous on 7T T1 MP2RAGE sequences.

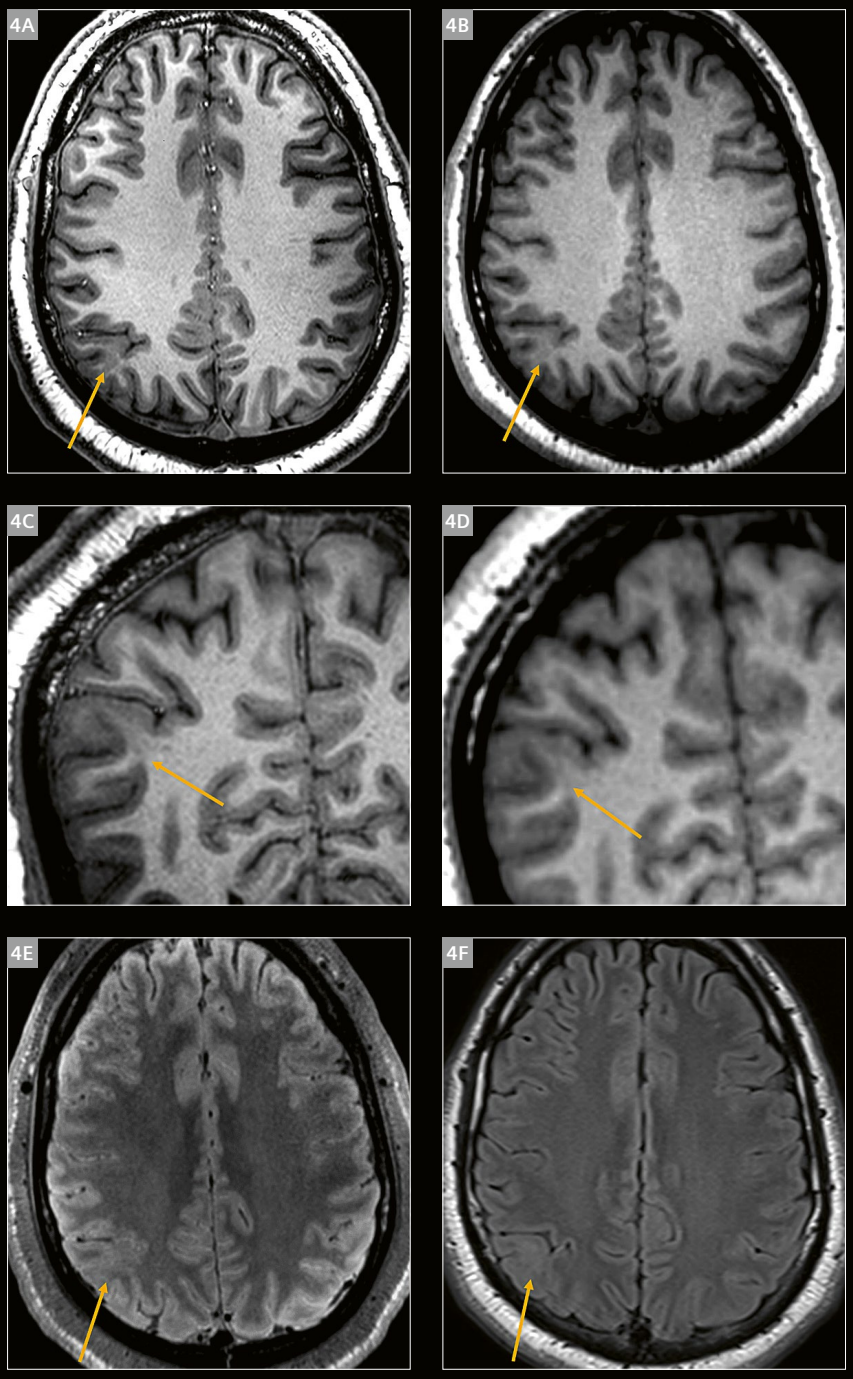

Case 2

A 34-year-old woman with drug-resistant epilepsy and recurrent generalized tonic-clonic seizures since age 12. Previous MR studies had demonstrated heterotopic gray matter. At our institution, the patient was initially evaluated with 1.5T MRI; however, it was decided that further evaluation with 7T MRI without intervening 3T MRI would be most expedient and cost efficient to further delineate any lesions. Coronal 1.5T T1 MPRAGE image **(5A)** shows periventricular heterotopic gray matter (red arrows) lateral to the hippocampal formation (yellow arrows). Coronal 7T T1 MP2RAGE image **(5B)** shows additional areas of heterotopia (red arrows) not evident on 1.5T and more obvious dysplastic appearance of the left hippocampal body (yellow arrows). This case clearly illustrates the greater tissue contrast of gray-white matter at 7T compared to 1.5T. The findings were evident on the initial 1.5T scan but were better delineated on the 7T scan, with the 7T scan providing improved characterization and delineation of extent of the lesions.

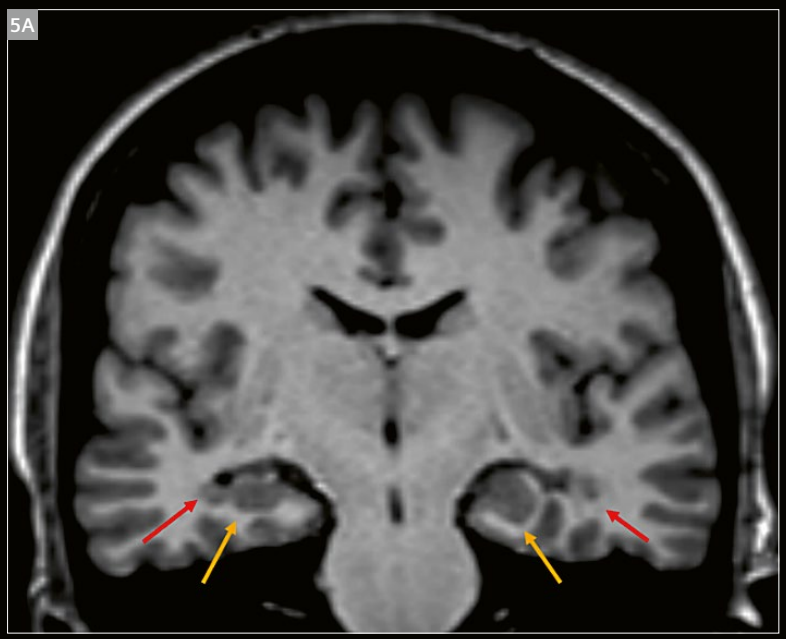

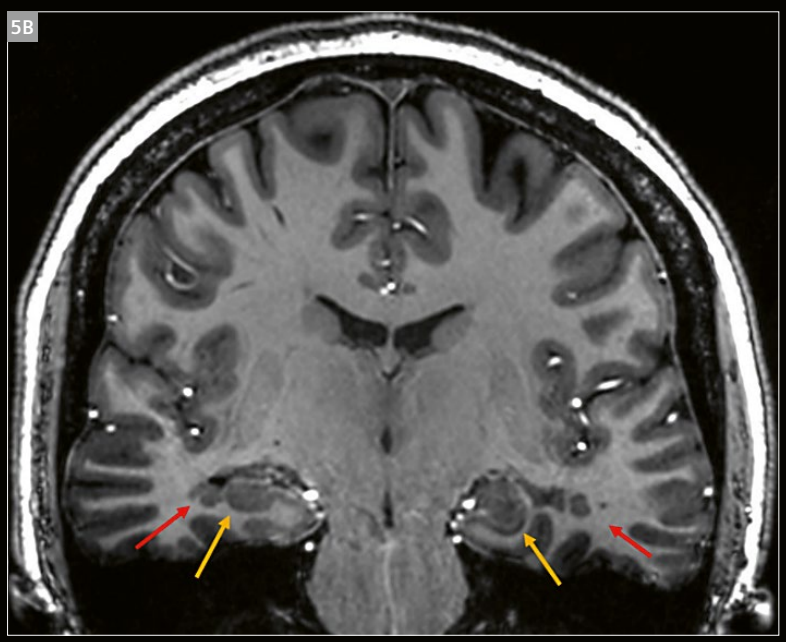

Case 3

Images from the same patient shown in Case 2. Magnified axial 1.5T T1 MPRAGE **(6A)** and axial 7T T1 MP2RAGE **(6B)** images show heterotopic gray matter in the left occipital periventricular white matter extending posteriorly (yellow arrows). The 1.5T MR image **(6A)** is not definitive but raises a question regarding how far posteriorly the heterotopic gray matter extends. This question is answered on the axial **(6B)** and coronal **(6D)** 7T T1 MP2RAGE images, which clearly show at least a small amount of heterotopic gray matter extending to and involving the overlying cortex (red arrows).

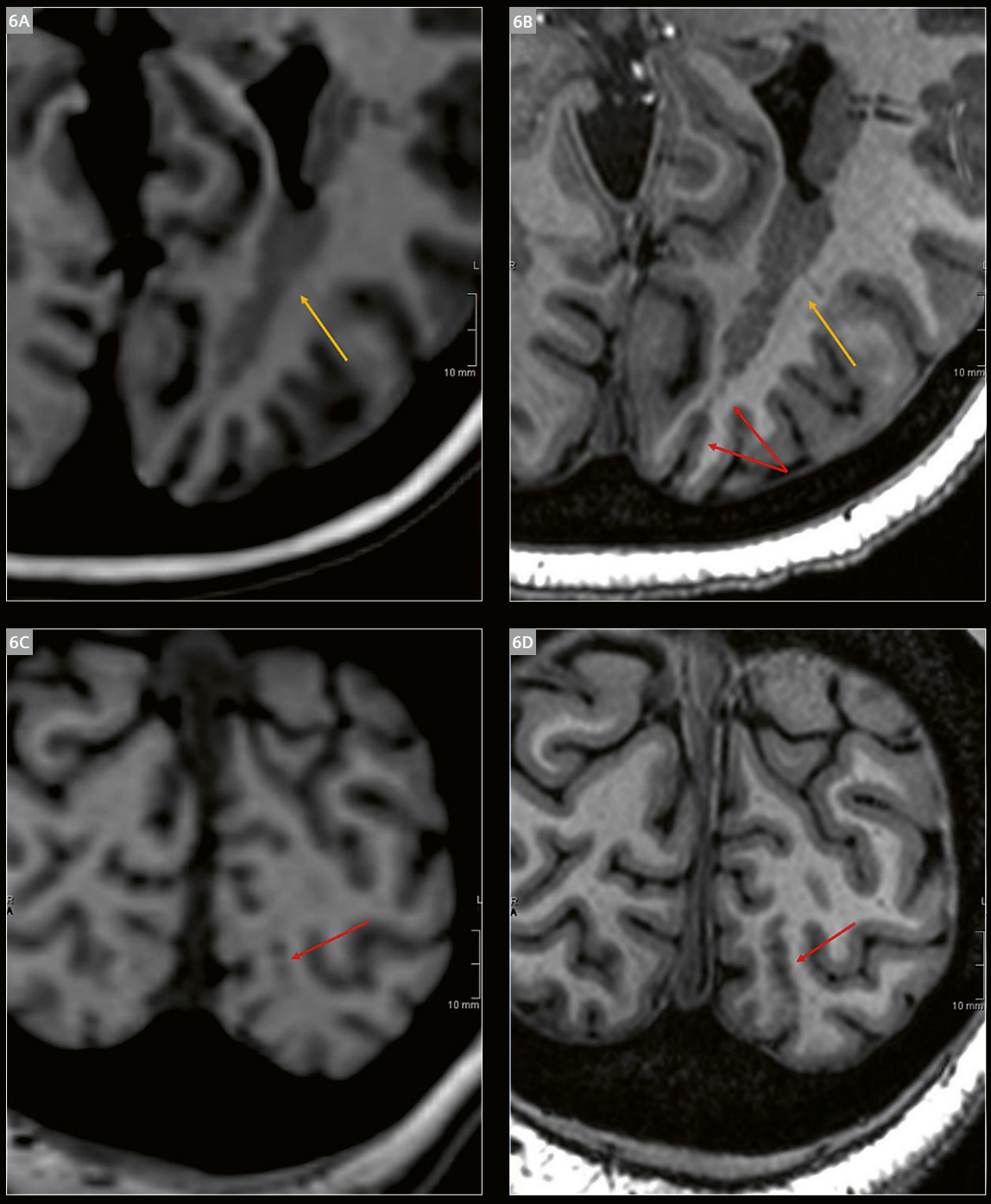

Case 4

A 39-year-old man with a history of cerebral palsy and motor developmental delays who had experienced his first seizure at age 29. The patient had been evaluated at an outside hospital for seizures and was diagnosed with left hemispheric schizencephaly. At our institution, 7T MRI was performed to delineate the extent of the abnormality. Coronal 7T T1 MPRAGE **(7A)** and axial T1 MPRAGE **(7B)** images clearly show the left hemisphere schizencephaly, as well as additional abnormal cortex in the right frontal lobe, which had not been appreciated on the outside hospital lower-field MR images (red arrow). In addition, further evaluation of the sagittal 7T T1 MPRAGE images **(7C, 7D)** shows the extent of the polymicrogyria associated with the left hemispheric schizencephaly, which clearly extends to the left superior, middle, and inferior temporal gyri (red arrows). Further evaluation on coronal and axial 7T T1 MPRAGE images **(7E, 7F)** show abnormal cortex, likely polymicrogyria, involving the dorsal aspects of the orbitofrontal gyri (yellow ovals). This case illustrates the advantage of the increased tissue contrast of 7T.

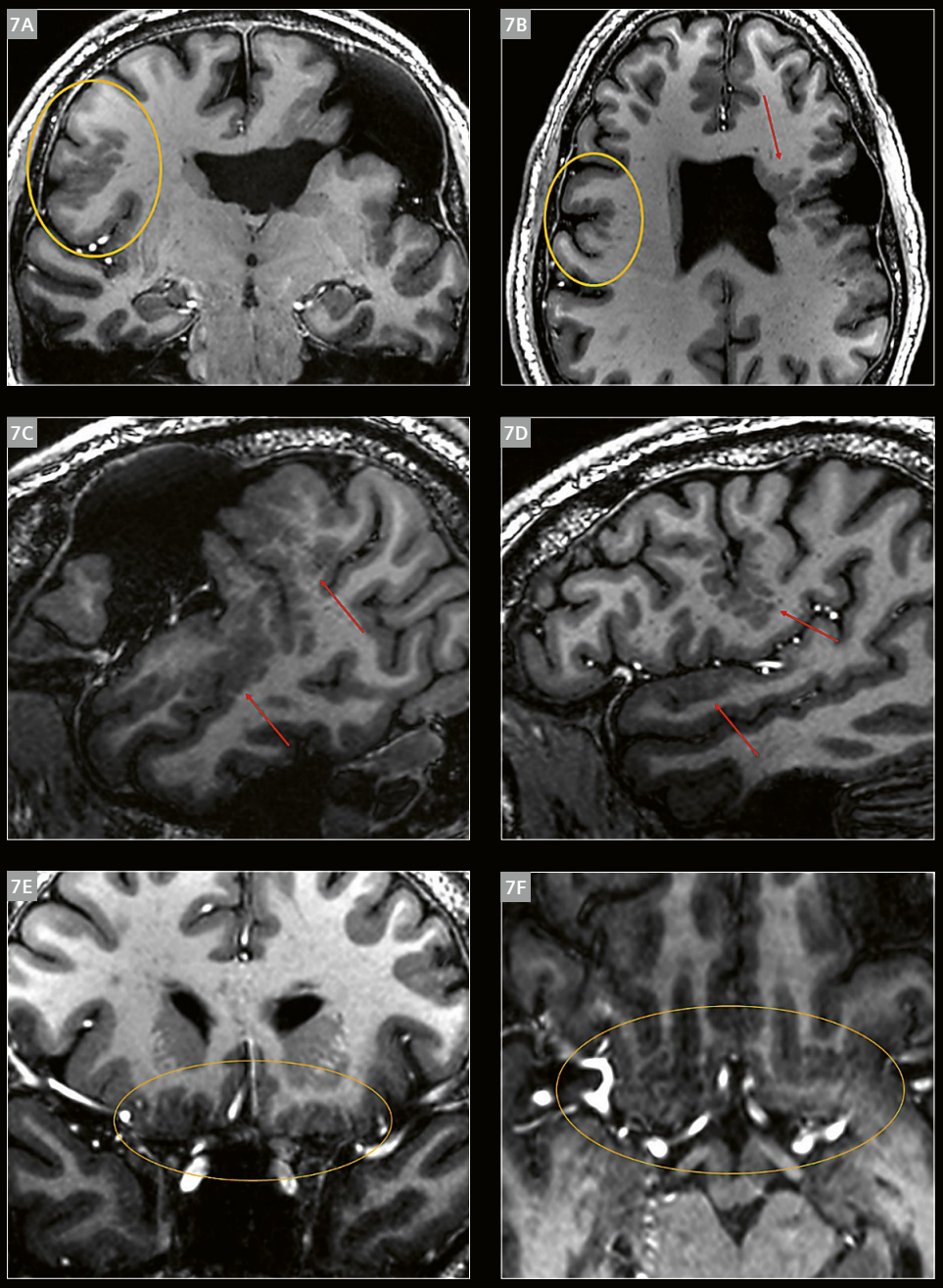

Case 5

A 21-year-old woman with medically intractable epilepsy and worsening seizures. Evaluation with 7T MRI demonstrated a left frontal type II FCD. Coronal **(8A, 8B)** and sagittal **(8D)** 7T T1 MP2RAGE images show subtle focal blurring of the gray-white matter junction of the left superior frontal sulcus and a subtle thin linear hypointensity (transmantle sign) emanating from the lesion and extending to the frontal horn of the left lateral ventricle (yellow ovals). The lesion was not identified on coronal **(8C)** or sagittal **(8E)** 3T T1 MPRAGE images. The lesion was ablated with laser interstitial thermal therapy, and the seizures immediately resolved. A sagittal 3T T1 MPRAGE image **(8F)** shows the postablation zone encompassing the lesion (red arrow).

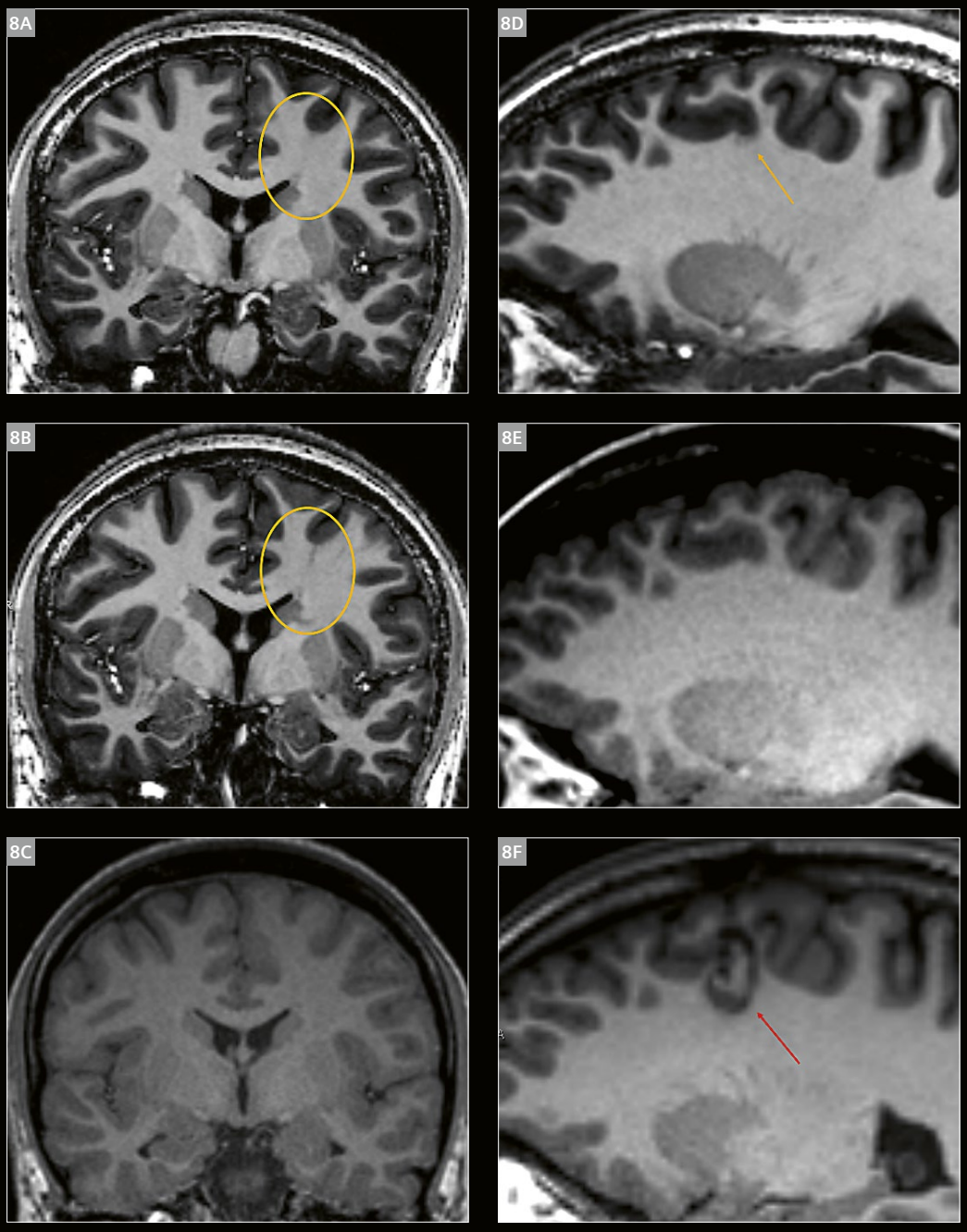

Case 6

An 8-year-old boy was experiencing weekly small drug-resistant seizures while falling asleep. An axial 7T T1 MPRAGE image **(9A)** demonstrates increased conspicuity of blurring of the gray-white matter junction in the right superior frontal gyrus when compared to the blurring on a 3T MPRAGE image (yellow arrows) **(9B)**. The lesion was initially identified on an axial 3T FLAIR image as a focus of increased hyperintensity at the subcortical white matter/juxtacortical region **(9D)**. 7T imaging clarified the presence of the FCD which was consistent with EEG findings. The patient underwent right frontal lesionectomy and has been seizure-free since surgery. This case illustrates a limitation of using 2D images, as this type of lesion is best appreciated while actively scrolling. The case also shows the 7T FLAIR image **(9C)** as a counterexample to 7T MPRAGE image **(9A)**, which the 7T FLAIR did not help much in this case.

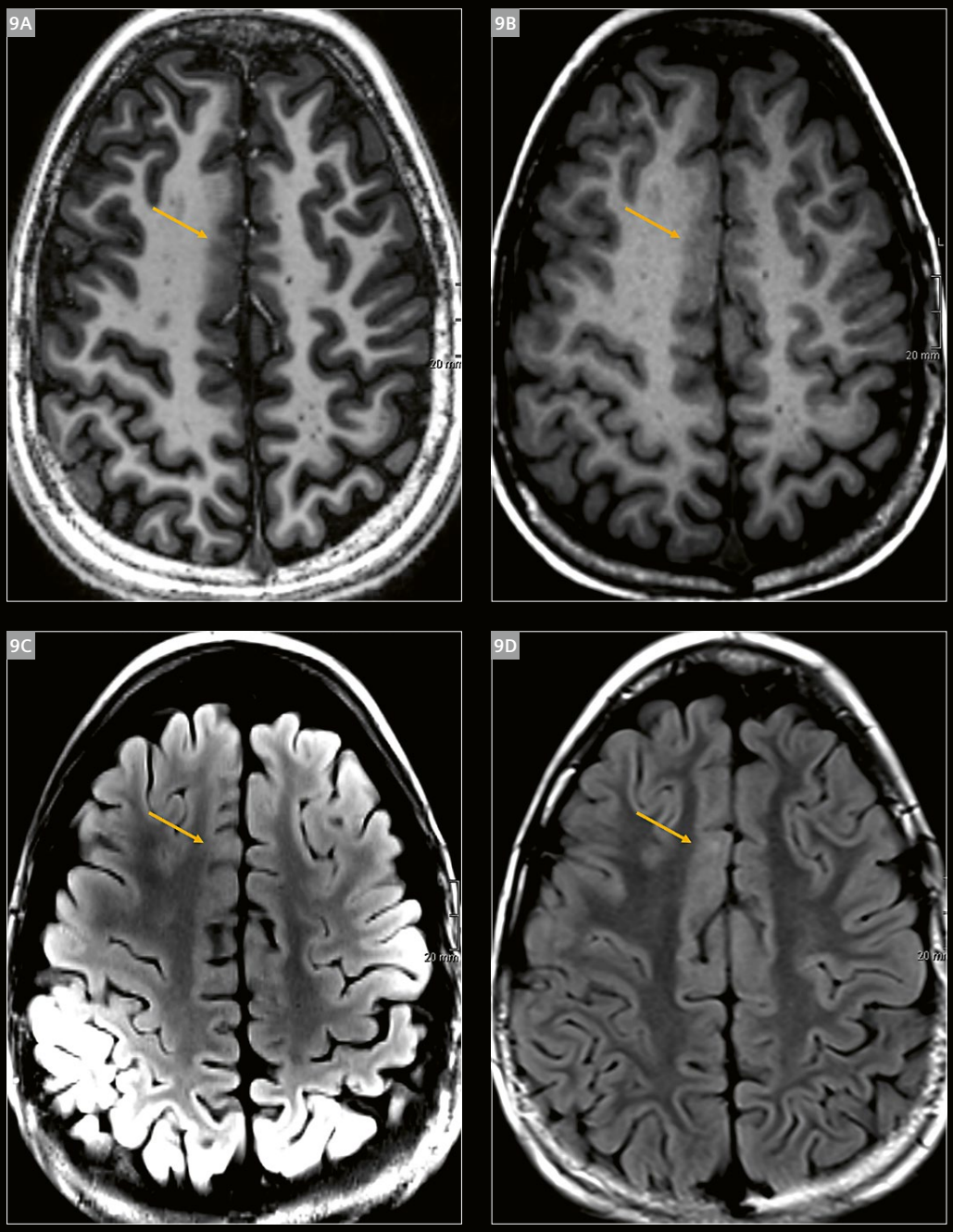

Discussion

This article provides comparative images illustrating the potential advantages of 7T imaging versus 3T and 1.5T imaging for the evaluation of patients with epilepsy. These advantages are derived from the higher magnet strength at 7T, which provides higher signal-to-noise ratio at the same voxel size. This increased signal can alternatively be used to obtain higher in-plane resolution and smaller slice thickness, thus leading to less effect from partial volume averaging. We include images of normal anatomy to emphasize the clear delineation of the gray-white matter junction and clearer anatomical detail of the hippocampal formations at 7T. We also provide specific examples of cases of polymicrogyria, FCD, schizencephaly, and gray matter heterotopia to emphasize the increased conspicuity and characterization of these lesions at 7T. These examples emphasize how the increased tissue contrast at the gray-white matter junction on 7T MPRAGE and MP2RAGE imaging provides increased visibility of polymicrogyria, hetero-topia, and FCDs. As noted in these cases, we infrequently see a lesion at 7T that was not present entirely at lower field strengths; rather, the lesion was usually present at lower field strengths but was not detected by the radiologist in a standard clinical setting because of its lower conspicuity. An exception was the type II FCD lesion with the transmantle sign in Case 5, in which the lesion was not apparent on 3T imaging but was clearly visible on 7T imaging. One may argue that a potential effect of increased conspicuity at 7T could be helping less experienced radiologists or radiologists in a high-volume clinical practice to detect subtle epileptogenic lesions that they would have otherwise missed on lower-field images.

Several studies in recent years have provided data regarding the advantages of 7T MRI. In a study of 67 patients with epilepsy, Wang et al. [13], found that the added value of 7T was the detection of subtle extratemporal epilepsies, specifically FCDs. The authors also demonstrated that patients with lesions detected at 7T were more likely to undergo surgery and have a seizure-free outcome. Similarly, in a study of 19 patients with epilepsy, Burbick et al. [14], showed that 7T MRI detected new lesions in more than one-third of patients whose previous 3T MR studies revealed no lesions. In addition, 7T was able to exclude suspected lesions in one-third of patients, and lesions were better characterized at 7T than at 3T [14]. In a meta-analysis that included 467 patients with epilepsy, 7T MRI had a detection rate of 65% versus 22% for lower-field 3T and 1.5T imaging [12]. In contrast to these studies that scientifically investigated the utility of 7T imaging in data-driven analyses, the current article simply provides illustrative examples showing how 7T MRI affected surgical management decisions.

Our current 7T clinical protocol was developed to augment our lower-field protocols and was designed predominantly for patients with medically intractable epilepsy with a high clinical suspicion for malformations of cortical development and other subtle epileptogenic lesions. The protocol was not designed to screen for patients with acute new-onset seizures or to follow-up patients with seizures who have already undergone MRI screening. Rather, this protocol was designed to provide higher resolution and higher contrast resolution to improve the detection of subtle neocortical nodularity and thickening associated with gray matter heterotopia and to detect blurring of the gray-white matter junction and transmantle abnormalities associated with FCD. In addition, our 7T protocol includes the use of T2*-weighted sequences to evaluate the hippocampal anatomy for loss of normal architecture, increased signal, and atrophy associated with mesial temporal sclerosis.

There are limitations to using a photo essay to compare 7T and lower-field images. One limitation is the lower qualitative assessment of lesions viewed in this format compared with the complete evaluation of lesions that is possible using DICOM, where one is able scroll through the images. An example of this is shown in Figure 9, where scrolling up and down the images gives a better appreciation for the lesion than assessing the 2D images we have provided.

A general limitation of 7T imaging for epilepsy evaluation is the variation in signal loss/susceptibility effects in the inferior frontal lobes, posterior fossa, and temporal lobes due to local B_0 inhomogeneity and RF transmit B_1 inhomogeneity caused by skull-based bone and air; these effects are greatly reduced at 3T/1.5T. This limitation may hinder the evaluation of epileptogenic lesions such as temporal encephaloceles in these regions. To counter this problem, we have, with variable success, used dielectric pads at our institution to reduce these artifacts [16]. However, this technique has been used in research cases only, as the use of these "pads" is not released for the U.S.. Another general limitation of 7T imaging that we have observed is that spatial resolution and tissue contrast on T2 FLAIR imaging are not substantially improved and do not provide added benefit for the evaluation of epileptogenic lesions when compared with lower-field imaging, as shown here in Case 1 and Case 6. This is in contrast to conventional lower-field imaging, in which FLAIR and T2-weighted images are primarily used to evaluate the blurring of the gray-white matter junction that results from an FCD. Small T2-weighted differences at the gray-white matter junction at 7T are likely due to specific absorption rate limits imposed by U.S. regulations, which limit the long TE possible at 3T.

Conclusion

This photo essay shows that 7T MRI may provide increased conspicuity of subtle lesions at 7T that are much less conspicuous at lower field strengths in patients with epilepsy. These diagnostic advantages can substantially alter patient care.

References

1 Begley CE, Durgin TL. The direct cost of epilepsy in the United States: A systematic review of estimates. Epilepsia. 2015 Sep;56(9):1376-87. doi: 10.1111/epi.13084. Epub 2015 Jul 27. Review. PubMed PMID: 26216617.

2 Berto P. Quality of life in patients with epilepsy and impact of treatments. Pharmacoeconomics. 2002;20(15):1039-59. doi: 10.2165/00019053-200220150-00002. Review. PubMed PMID: 12456200.

3 Blank LJ, Crispo JAG, Thibault DP, Davis KA, Litt B, Willis AW. Readmission after seizure discharge in a nationally representative sample. Neurology. 2018 Dec 21;. doi: 10.1212/WNL.0000000000006746. [Epub ahead of print] PubMed PMID: 30578373; PubMed Central PMCID: PMC6369906.

4 Jobst BC, Cascino GD. Resective epilepsy surgery for drug-resistant focal epilepsy: a review. JAMA. 2015 Jan 20;313(3):285-93. doi: 10.1001/jama.2014.17426. Review. PubMed PMID: 25602999.

5 Engel J Jr, Wiebe S, French J, Sperling M, Williamson P, Spencer D, Gumnit R, Zahn C, Westbrook E, Enos B. Practice parameter: temporal lobe and localized neocortical resections for epilepsy. Epilepsia. 2003 Jun;44(6):741-51. doi: 10.1046/j.1528-1157.2003.48202.x. Review. PubMed PMID: 12790886.

6 Jones AL, Cascino GD. Evidence on Use of Neuroimaging for Surgical Treatment of Temporal Lobe Epilepsy: A Systematic Review. JAMA Neurol. 2016 Apr;73(4):464-70. doi: 10.1001/jamaneurol.2015.4996. Review. PubMed PMID: 26926529.

7 McIntosh AM, Averill CA, Kalnins RM, Mitchell LA, Fabinyi GC, Jackson GD, Berkovic SF. Long-term seizure outcome and risk factors for recurrence after extratemporal epilepsy surgery. Epilepsia. 2012 Jun;53(6):970-8. doi: 10.1111/j.1528-1167.2012.03430.x. Epub 2012 Mar 14. PubMed PMID: 22417071.

8 Berkovic SF, McIntosh AM, Kalnins RM, Jackson GD, Fabinyi GC, Brazenor GA, Bladin PF, Hopper JL. Preoperative MRI predicts outcome of temporal lobectomy: an actuarial analysis. Neurology. 1995 Jul;45(7):1358-63. doi: 10.1212/wnl.45.7.1358. PubMed PMID: 7617198.

9 Muhlhofer W, Tan YL, Mueller SG, Knowlton R. MRI-negative temporal lobe epilepsy-What do we know?. Epilepsia. 2017 May;58(5):727-742. doi: 10.1111/epi.13699. Epub 2017 Mar 7. Review. PubMed PMID: 28266710.

10 Nguyen DK, Rochette E, Leroux JM, Beaudoin G, Cossette P, Lassonde M, Guilbert F. Value of 3.0 T MR imaging in refractory partial epilepsy and negative 1.5 T MRI. Seizure. 2010 Oct;19(8):475-8. doi: 10.1016/j.seizure.2010.07.002. Epub 2010 Jul 29. PubMed PMID: 20673641.

11 Winston GP, Micallef C, Kendell BE, Bartlett PA, Williams EJ, Burdett JL, Duncan JS. The value of repeat neuroimaging for epilepsy at a tertiary referral centre: 16 years of experience. Epilepsy Res. 2013 Aug;105(3):349-55. doi: 10.1016/j.eplepsyres.2013.02.022. Epub 2013 Mar 26. PubMed PMID: 23538269; PubMed Central PMCID: PMC3888924.

12 Park JE, Cheong EN, Jung DE, Shim WH, Lee JS. Utility of 7 Tesla Magnetic Resonance Imaging in Patients With Epilepsy: A Systematic Review and Meta-Analysis. Front Neurol. 2021;12:621936. doi: 10.3389/fneur.2021.621936. eCollection 2021. PubMed PMID: 33815251; PubMed Central PMCID: PMC8017213.

13 Wang I, Oh S, Blümcke I, Coras R, Krishnan B, Kim S, McBride A, Grinenko O, Lin Y, Overmyer M, Aung TT, Lowe M, Larvie M, Alexopoulos AV, Bingaman W, Gonzalez-Martinez JA, Najm I, Jones SE. Value of 7T MRI and post-processing in patients with nonlesional 3T MRI undergoing epilepsy presurgical evaluation. Epilepsia. 2020 Nov;61(11):2509-2520. doi: 10.1111/epi.16682. Epub 2020 Sep 19. PubMed PMID: 32949471; PubMed Central PMCID: PMC7722133.

14 Bubrick EJ, Gholipour T, Hibert M, Cosgrove GR, Stufflebeam SM, Young GS. 7T versus 3T MRI in the presurgical evaluation of patients with drug-resistant epilepsy. J Neuroimaging. 2021 Dec 29;. doi: 10.1111/jon.12958. [Epub ahead of print] PubMed PMID: 34964194.

15 Obusez EC, Lowe M, Oh SH, Wang I, Jennifer Bullen, Ruggieri P, Hill V, Lockwood D, Emch T, Moon D, Loy G, Lee J, Kiczek M, Manoj Massand, Statsevych V, Stultz T, Jones SE. 7T MR of intracranial pathology: Preliminary observations and comparisons to 3T and 1.5T. Neuroimage. 2018 Mar;168:459-476. doi: 10.1016/j.neuroimage.2016.11.030. Epub 2016 Nov 30. PubMed PMID: 27915116.

Contact

Emmanuel Obusez, M.D.
Assistant Professor of Radiology
Cleveland Clinic Lerner College of Medicine
9500 Euclid Ave., L10
Cleveland, OH 44195
USA
Tel.: +1 216 410 5775
OBUSEZE@ccf.org

PASTEUR: Package of Anatomical Sequences Using Parallel Transmission Universal Pulses Now Available for MAGNETOM Terra

Aurélien Massire, Ph.D.[1]; Franck Mauconduit, Ph.D.[2]; Vincent Gras, Ph.D.[2]; Marc Lapert, Ph.D.[1]; Mathieu Naudin, Ph.D.[3,4,5]; Rémy Guillevin, M.D., Ph.D.[3,4,5]; Alexandre Vignaud, Ph.D.[2]; Nicolas Boulant, Ph.D.[2]

[1]Siemens Healthineers, Saint-Denis, France
[2]Université Paris-Saclay, CEA, CNRS, BAOBAB, NeuroSpin, Gif-sur-Yvette, France
[3]CHU Poitiers, France
[4]LRCOM I3M, University and University Hospital of Poitiers, France
[5]Laboratory of Applied Mathematics, UMR CNRS 7348, University of Poitiers, France

Introduction

In MRI, ultra-high-field (UHF) strengths (≥ 7T) provide a higher signal-to-noise ratio, enabling increased spatial resolution and/or reduced acquisition time as compared to lower-field MR systems [1–3]. As more and more patients have been scanned with UHF systems over the last decade, 7T MRI has markedly demonstrated its added value for diagnosing and characterizing two key diseases of the central nervous system: multiple sclerosis (MS) and focal epilepsy [4, 5]. With MS, 7T structural MRI successfully detects smaller and earlier lesions in both white matter (WM) and gray matter (GM), and provides improved characterization of lesion localization, formation, and resulting damage [4]. As for epilepsy, 7T structural MRI successfully increases the diagnosis success rate in patients with drug-resistant focal onset epilepsy for whom lesions could not be found using lower-field MR systems [5].

However, certain anatomies can be more challenging to acquire with UHF MRI, especially when examining larger volumes. This is due to destructive field interferences that can lead to spatial inhomogeneity in the radiofrequency (RF) excitation profile. In the head, the cerebellum and the temporal lobes can be affected by such inhomogeneities [6].

The use of parallel transmission (pTx) technology with an array of transmit coil elements has proven to be very efficient in addressing these challenges [7]. With pTx, the amplitudes and phases of the RF pulses transmitted by the channels of the coil array are independently modulated in time to homogenize the excitation profile over the volume of interest, provided the actual transmit RF field (B_1^+) and static field offset (ΔB_0) distributions are known. For non-selective excitations used in 3D anatomical MR sequences,

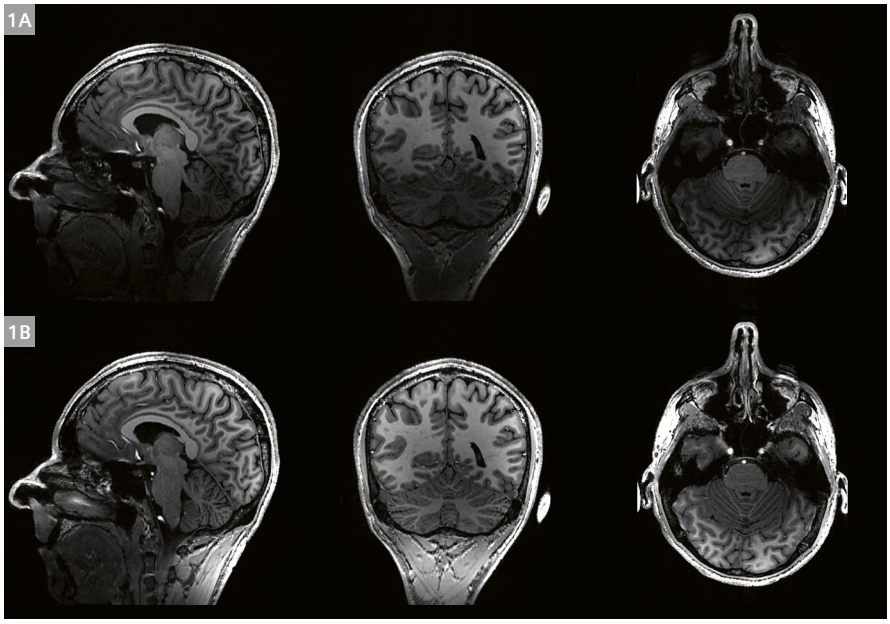

1 T1-weighted MPRAGE (Magnetization-Prepared Rapid Acquisition Gradient-Echo) sequence
(1A) Proposed MPRAGE protocol in standard non-pTx excitation. **(1B)** Same protocol with Universal Pulses (GRAPE RF pulses were used for magnetization inversion and excitation). Note how GM/WM contrast is specifically improved in the cerebellum and temporal lobes with UP imaging. The sequence SAR is lower using UPs than non-pTx excitation, since the inversion UP is less energetic than the conventional adiabatic RF pulse.

various parametrization approaches, such as k_T-points [8] or GRAPE [9, 10], have been proposed to design optimized RF and magnetic field gradient waveforms. The design of such subject-tailored RF pulses results in very homogeneous RF excitation profiles, but this is at the cost of the extra scan time required to map the patient field distributions and to design the RF pulses. It also demands specific expertise from the MR user [11, 12].

Alternate methods for a subject-tailored approach can avoid systematic measurement of the RF and static field distributions for each subject and subsequent RF pulse computation. Recently, an original approach that uses "Universal Pulses" (UP) for calibration-free pTx neuroimaging was developed by CEA NeuroSpin [13–15]. To ensure universality, the RF pulses of the PASTEUR package [16] were designed offline using a database of B_1^+ and ΔB_0 brain distributions experimentally acquired from a representative cohort and using state-of-the art optimization algorithms. Several key 3D MR sequences providing anatomical imaging were reprogrammed to host these UPs. The PASTEUR workflow is therefore completely transparent to the 7T radiographer, who can focus on the MR exam with no time penalty or need for advanced sequence parametrization.

In this work, the PASTEUR package, originally designed for the investigational MAGNETOM 7T, was brought to the latest generation of the 7T MR system from Siemens Healthineers: MAGNETOM Terra[1]. To demonstrate the power and versatility of UPs for neuroimaging, the PASTEUR package was deployed in the clinical environment of Poitiers University Hospital (CHU Poitiers) in France. The image quality achieved using conventional non-pTx excitation (i.e., circularly polarized (CP) mode) brain imaging was compared with that from PASTEUR UP brain imaging for MPRAGE, MP2RAGE, FLASH, and SPACE sequences performed on healthy volunteers.

Theory

To design the non-selective RF pulses of the PASTEUR package, two different *k*-space parametrizations were chosen according to the desired properties of the pulses: k_T-points [8] and GRAPE [9]. Briefly, k_T-points consist of multiple rectangular RF sub-pulses interleaved with gradient blips. The resulting degrees of freedom are therefore amplitude, phase, and the *k*-space position of each RF sub-pulse. The GRAPE pulses are made of simultaneously applied RF and gradient waveforms that vary at every time step. The additional degrees of freedom enable shorter GRAPE pulses compared to the k_T-points.

The MR sequences considered here require diverse RF pulses to influence spin magnetization, and each type has specific properties (e.g., small flip angle (FA), large FA, refocusing, inversion). Nevertheless, the general problem with FA homogenization is relatively similar and related to the pTx MR system, which is equipped with N_c transmitters. It usually involves optimizing the N_c RF complex temporal shapes and the G_X-G_Y-G_Z gradient temporal shapes (defining the locations in *k*-space during transmission) so as to minimize the deviation of the resulting FA map from the desired nominal value (as prescribed in the MR protocol).

For one subject, this problem is often (but not always) written as a magnitude least-squares (MLS) problem [17]. To generalize the concept of simultaneous FA homogenization over multiple subjects and thereby promote universality, the optimal RF / gradient shapes that minimize the root mean square error over N_s subjects are sought [13]. In the case of the PASTEUR package, the database consisted of 20 brain field distributions (male and female Caucasian healthy adult volunteers, age range: between 20 and 50 years old), acquired using MAGNETOM 7T MR systems equipped with 8Tx/32Rx Nova brain coils at CEA NeuroSpin (n = 10) and DZNE Bonn (n = 10). Due to evolutions in MAGNETOM Terra hardware and software, several modifications were made to UPs originally designed for MAGNETOM 7T, in order to update the original RF pulses (details and illustration of these "travelling pulses" are provided in [18]). Lastly, as designed RF pulses must respect hardware and safety limits for all patients [19], a set of explicit constraints on SAR and power per channel should be added [13–16]. For the PASTEUR package currently available for MAGNETOM Terra, the default RF power limits set by Siemens Healthineers were enforced. Design examples of UPs included in the PASTEUR package using GRAPE and k_T-point parametrizations are illustrated in Figure 2.

MR imaging

Data were acquired at CHU Poitiers on a 7T MR system[1] (MAGNETOM Terra, Siemens Healthcare, Erlangen, Germany) equipped with an 8Tx/32Rx transmit/receive coil (Nova Medical, Wilmington, MA, USA). The MR protocol, which consisted of 3D non-selective anatomical sequences, was approved by the local ethics committee. Informed consent was obtained for each subject prior to the MR examination. Exclusion criteria followed the GUFI recommendations [20].

[1] *For MAGNETOM Terra, pTx technology is included in Research mode (as part of the optional Dual mode) and is not intended for clinical use. Research operation may require observation of national regulations.*

MR sequences supported by the PASTEUR package are MPRAGE [21], MP2RAGE [22], FLAWS [23], FLASH, and SPACE [24], with several magnetization preparations (dark fluid, DIR). The main sequence parameters used at CHU Poitiers are summarized in the table below. Specific sequence information and additional observations are provided, along with images acquired from several healthy volunteers (Figs. 1, 3–9).

Results

High image quality over the whole brain was obtained for all MR sequences and imaging contrasts when UPs were activated (Figs. 1, 3–9). Where applicable (Figs. 1, 4, 7–9), image quality was significantly improved when compared to conventional non-pTx excitation (i.e., CP: circularly polarized mode). It should be noted that no additional image filters were used to reduce signal bias or to smooth images. Improvements were particularly visually striking in the cerebellum and the temporal lobes, notably on SPACE-based imaging. This is already a well-known phenomenon since the 3D SPACE sequence uses multiple refocusing RF pulses to maintain magnetization along a long echo train. Errors in FA profiles are additive, ultimately creating signal voids within the brain. Regarding sequence-specific absorption rate (SAR), SPACE protocols were usually close to the Level 1 limit. Nevertheless, all MR sequences could be run on millimetric or sub-millimetric spatial isotropic resolution. UP SAR is usually higher than standard rectangular RF pulses, but significantly lower than adiabatic RF pulses. As a result, sequence SAR was sometimes lower when using UPs than with conventional non-pTx excitation (for instance, in MPRAGE or DIR). The radiographers encountered no additional time penalties caused by pTx during the MR exams.

MR sequences	MPRAGE	MPRAGE HR	MP2RAGE	FLAWS	T2* FLASH	T2 SPACE	Dark Fluid $T2_p$ SPACE	DIR SPACE
TA (min)	4:59	9:54	12:20	9:40	5:12	6:00	7:12	7:06
TR (ms)	2600	3000	5000	5000	22	9000	9000	8000
TE (ms)	2.48	3.84	2.06	1.6	16	383	270	320
TI (ms)	1100	1200	740/2430	620/1430	–	–	2300	3500/650
FA (°)	5	6	5/4	4/8	15	T_2 var	T_2 var	T_2 var
FOV (mm^2)	224x224	224x224	230x230	230x230	224x224	230x230	230x230	240x240
Matrix size	320x320	448x448	384x384	288x288	448x376	288x288	288x288	240x240
Resolution (mm^3)	0.7 iso	0.5 iso	0.6 iso	0.8 iso	0.5 iso	0.8 iso	0.8 iso	1.0 iso
Number of partitions	256	320	288	208	320	240	240	192
Parallel imaging technique	GRAPPA	GRAPPA	GRAPPA	GRAPPA	GRAPPA	CAIPIRINHA	CAIPIRINHA	GRAPPA
Parallel imaging factor	3	3	3	3	2x2	3x3	3x3	3x3
Partial Fourier	7/8 (phase)	7/8 (slice)	7/8 (slice)	6/8 (slice)	6/8	allowed	allowed	allowed
Number of averages	1	1	1	1	1	1	1	2
Turbo Factor	256	280	252	156	–	218	180	180
Bandwidth (Hz/px)	210	220	350	500	200	827	599	401

Table 1: The main sequence parameters used at CHU Poitiers.

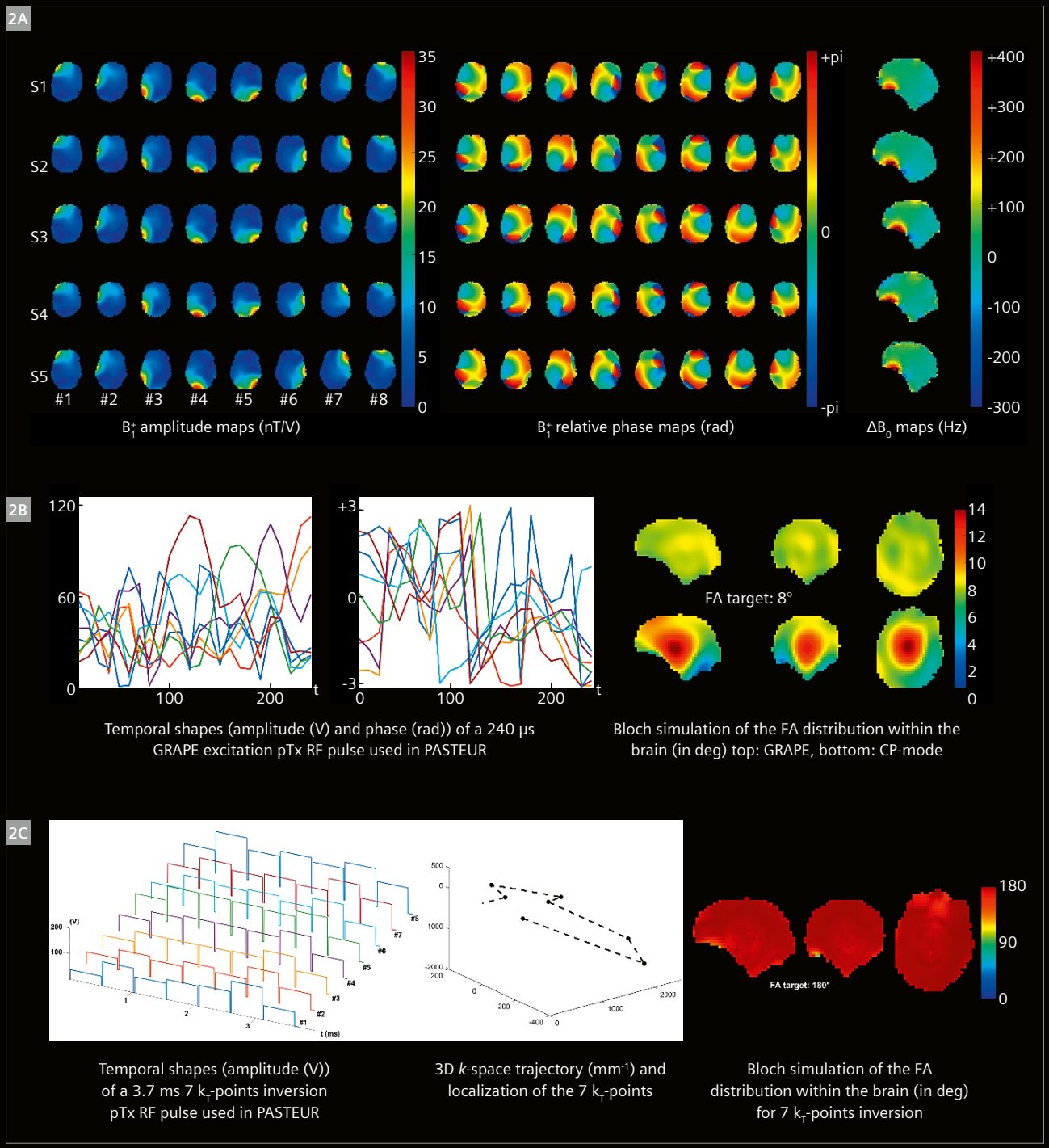

Temporal shapes (amplitude (V) and phase (rad)) of a 240 µs GRAPE excitation pTx RF pulse used in PASTEUR

Bloch simulation of the FA distribution within the brain (in deg) top: GRAPE, bottom: CP-mode

Temporal shapes (amplitude (V)) of a 3.7 ms 7 k_T-points inversion pTx RF pulse used in PASTEUR

3D *k*-space trajectory (mm^{-1}) and localization of the 7 k_T-points

Bloch simulation of the FA distribution within the brain (in deg) for 7 k_T-points inversion

2 Design examples of Universal Pulses of the PASTEUR package using GRAPE and K_T-points

(2A) Extract of the database of brain B_1^+ and ΔB_0 distributions (n = 5 subjects) experimentally acquired on a representative cohort. Measured B_1^+ maps amplitude (nT/V) and relative phase (rad) are displayed in axial view at isocenter. Images are sorted by subjects from top to bottom and by channel indexes from left to right. Measured ΔB_0 offset maps (Hz) are displayed in sagittal view at isocenter. Qualitatively, the B_1^+ maps reveal a high degree of similarity across subjects, with typical spatial correlations of about 0.95 throughout channels. Additional technical details on the database construction can be found in [13].

(2B) Example of excitation UP RF temporal shapes designed with the GRAPE algorithm (different color indicates different transmit channel), along with the corresponding FA distribution in the brain simulated with Bloch equations (results from non-pTx excitation – circularly polarized mode – are also provided below to demonstrate the expected improvement).

(2C) Example of inversion Universal Pulses RF temporal shapes and *k*-space trajectory designed with k_T-points, along with the corresponding FA distribution in the brain simulated with Bloch equations.

3 **High-resolution T1-weighted MPRAGE imaging using PASTEUR package**
Representative zoomed images in all orientations (sagittal, transverse, coronal) of a 500 µm isotropic spatial resolution MPRAGE sequence acquired in 10 minutes with Universal Pulses. Note the very high image quality over the whole brain, which could be further improved using image filters to mitigate the reception field bias.

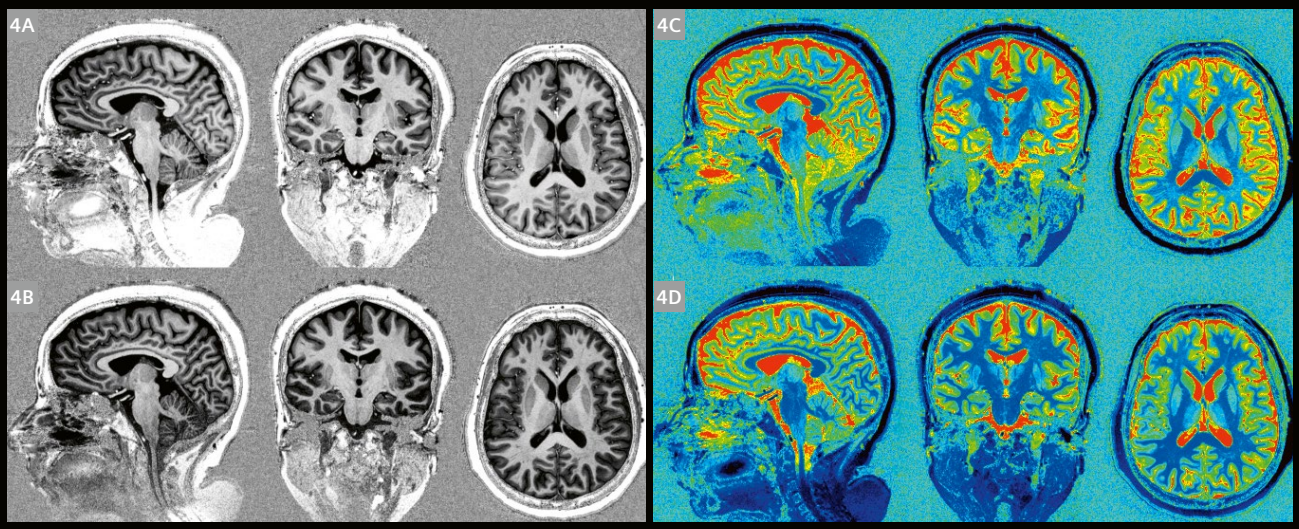

4 **T1-weighted MP2RAGE (Magnetization-Prepared 2 Rapid Acquisition Gradient-Echoes) sequence**
(4A) Uniform (UNI) images obtained with the proposed MP2RAGE protocol in standard non-pTx excitation. Note that MP2RAGE UNI images are inherently corrected for reception bias field, so the resulting signal inhomogeneity only comes from B_1^+ excitation bias. **(4B)** UNI images obtained with the same protocol using Universal Pulses. Signal homogeneity within the brain is improved (see, for instance, the signal homogeneity of the cortex). **(4C)** Associated quantitative T1 map (in ms) in colormap obtained with non-pTx excitation imaging. **(4D)** Associated T1 map obtained with UPs. The improvement in excitation homogenization significantly improves the accuracy of T1 measurement, as T1 values are computed with Bloch equation integration, notably in the WM and in the cortex.

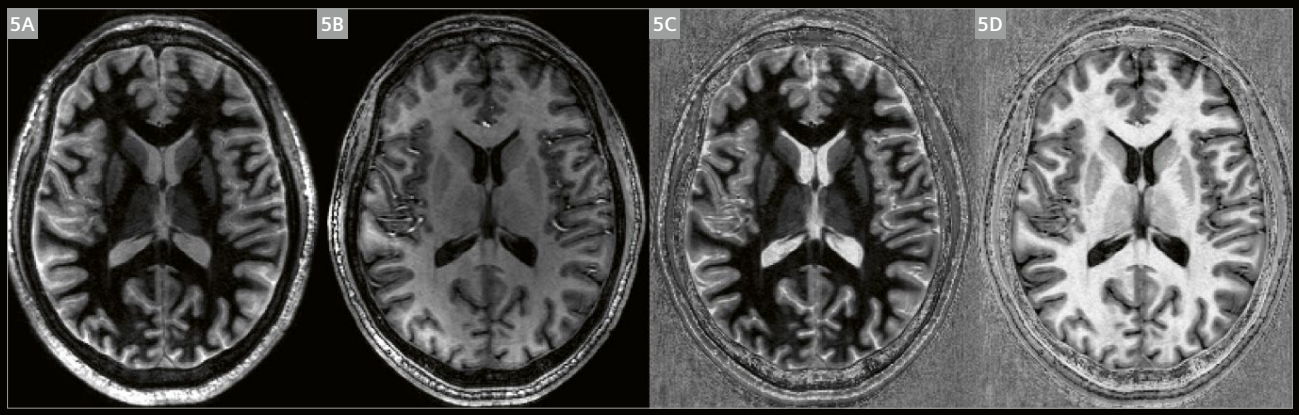

5 **T1-weighted FLAWS (FLuid And White matter Suppression) sequence**
Proposed protocol with Universal Pulses. **(5A)** Inversion 1 volume (equivalent to fast gray matter acquisition T1 inversion recovery, FGATIR), **(5B)** Inversion 2 volume (equivalent to MPRAGE), **(5C)** synthetic high contrast (HC), and **(5D)** synthetic high contrast opposite (HCO). Note that synthetic contrasts were computed offline. These synthetic contrasts are relevant for deep brain structure and/or cortex visualization, though they do amplify image noise [23].

6 **T2*-weighted FLASH sequence (6A)** Proposed GRE protocol with Universal Pulses. **(6B)** Associated minimum-intensity projection (minIP), with 4 mm slice thickness. Note the high image quality, including in the lower part of the brain. This type of protocol could be used for quantitative susceptibility mapping (QSM).

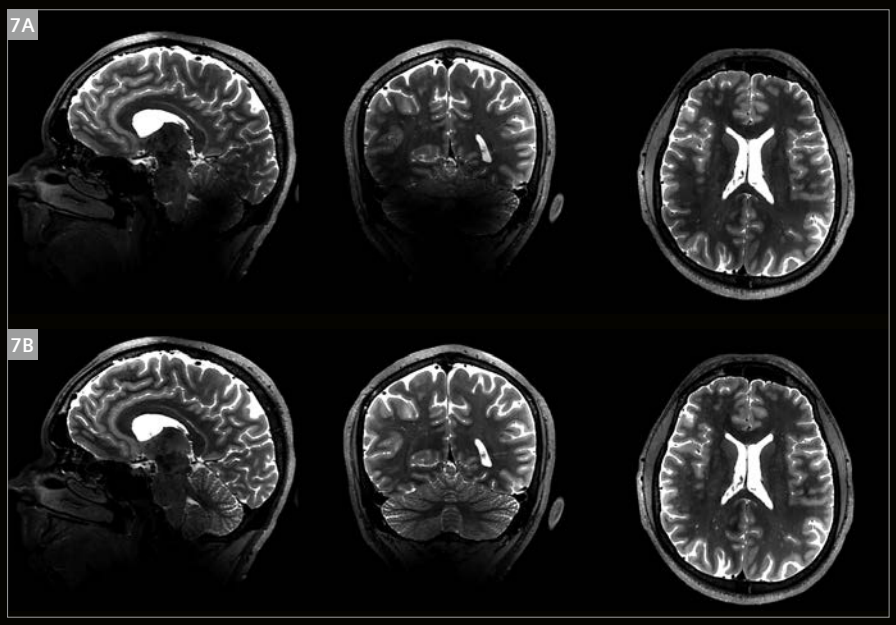

7 **T2-weighted SPACE (Sampling Perfection with Application optimized Contrasts using different flip angle Evolution) sequence (7A)** Proposed protocol in standard non-pTx excitation. **(7B)** Same protocol with Universal Pulses. The 3D SPACE sequence generates one T2-weighted volume. The chosen refocusing train option was T2 var (with target T1: 1400 ms, target T2: 50 ms). The improvement in excitation and refocusing homogenization significantly enhances signal homogeneity, notably in the cerebellum and temporal lobes.

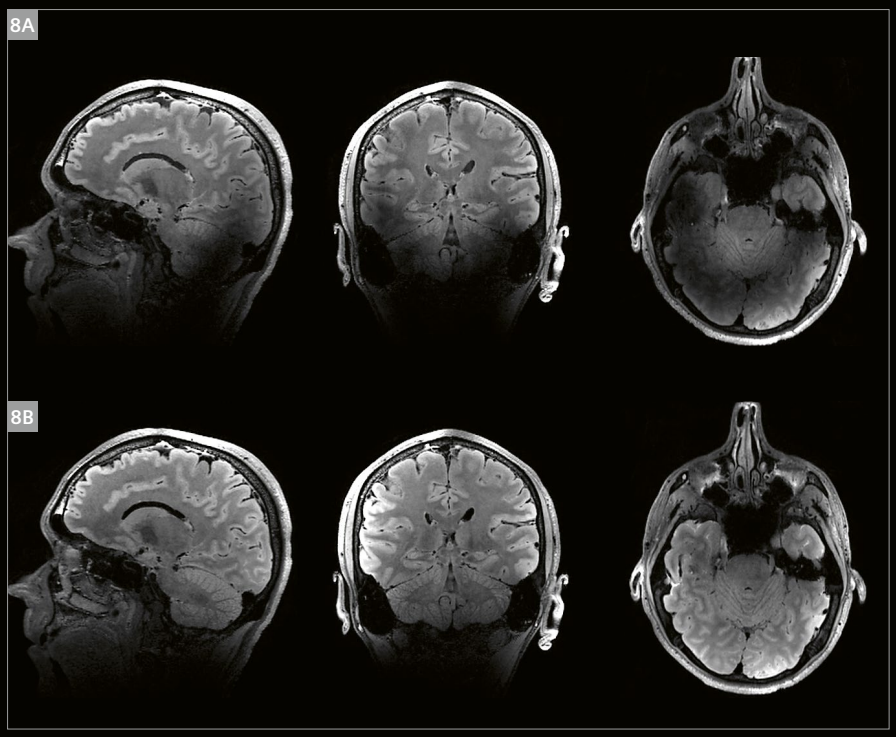

8 Dark fluid T2-weighted SPACE sequence with T2 magnetization preparation
(8A) Proposed protocol in standard non-pTx excitation. **(8B)** Same protocol with Universal Pulses. This sequence generates one T2-weighted volume with suppressed cerebrospinal fluid (CSF) signal. The preparation consisted of a 90°-τ-180°-τ-90° module (τ = 50 ms) to achieve an effective inversion of the CSF signal and a saturation in the brain tissues. This module is described in detail in [25]. The chosen refocusing train option was T2 var (with target T1: 1400 ms, target T2: 50 ms). The multiple improvements in preparation, excitation, and refocusing RF pulses results in an efficient signal restoration in the cerebellum and temporal lobes.

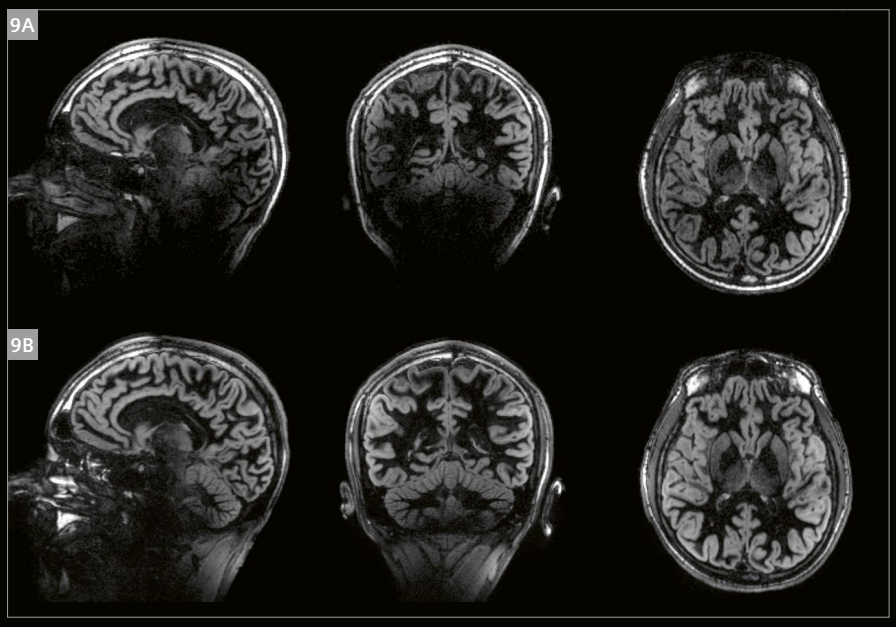

9 Double Inversion Recovery (DIR) SPACE sequence
(9A) Proposed protocol in non-pTx excitation. **(9B)** Same protocol with Universal Pulses. The 3D SPACE sequence generates one T2-weighted volume with both WM- and CSF-suppressed signals. The chosen refocusing train option was T2 var (with target T1: 1400 ms, target T2: 50 ms). The sequence SAR is lower with UP than with standard non-pTx excitation, since the inversion GRAPE pulses are less energetic than the standard adiabatic RF pulses. The multiple improvements in preparation, excitation, and refocusing RF pulses significantly enhances signal homogeneity and achieves efficient signal restoration in the cerebellum.

Discussion

In this work, the PASTEUR package was successfully deployed in a clinical site equipped with a MAGNETOM Terra and with no previous expertise in pTx or RF pulse design. The easy-to-use package allowed the team to acquire high-quality, high-resolution, whole-brain 3D structural images from several healthy volunteers, with various clinically relevant MR contrasts and at strictly zero workflow penalty. The results were very favorably received by the local radiologists, who concluded that typical UHF image artifacts were "gone for good".

The Universal Pulses presented here rely on a representative field database acquired in advance, and designed offline once by MR experts using thorough optimization approaches (since the offline computation time is irrelevant, increased pulse-design performance was achieved). UPs are thus valid for a given field strength (7T), body part (head), patient position (headfirst supine), and pTx RF coil. Assuming a certain degree of similarity in the B_1^+ and ΔB_0 maps among the population, UPs could be successfully applied to new patients without personalized field map measurements and RF pulse calculations. The PASTEUR package therefore makes the use of the underlying pTx hardware completely transparent to the operator.

While earlier work showed that increasing the size of the database improves UP robustness, the pulses' universality appears to converge rather quickly with the number of subjects [13]. Nevertheless, the idea of introducing database subgroups based, for instance, on gender, age, body mass index, or disease condition should be investigated in the future. Additional improvements could be made to further improve the universality, based on either of the following:

1. the latest machine-learning approaches to categorize the patients (Smart Pulse) [26];
2. fast subject- and exam-specific calibration using standardized UPs (SUPs) [27];
3. a combination of UPs with fast, tailored approaches (FOCUS) [28].

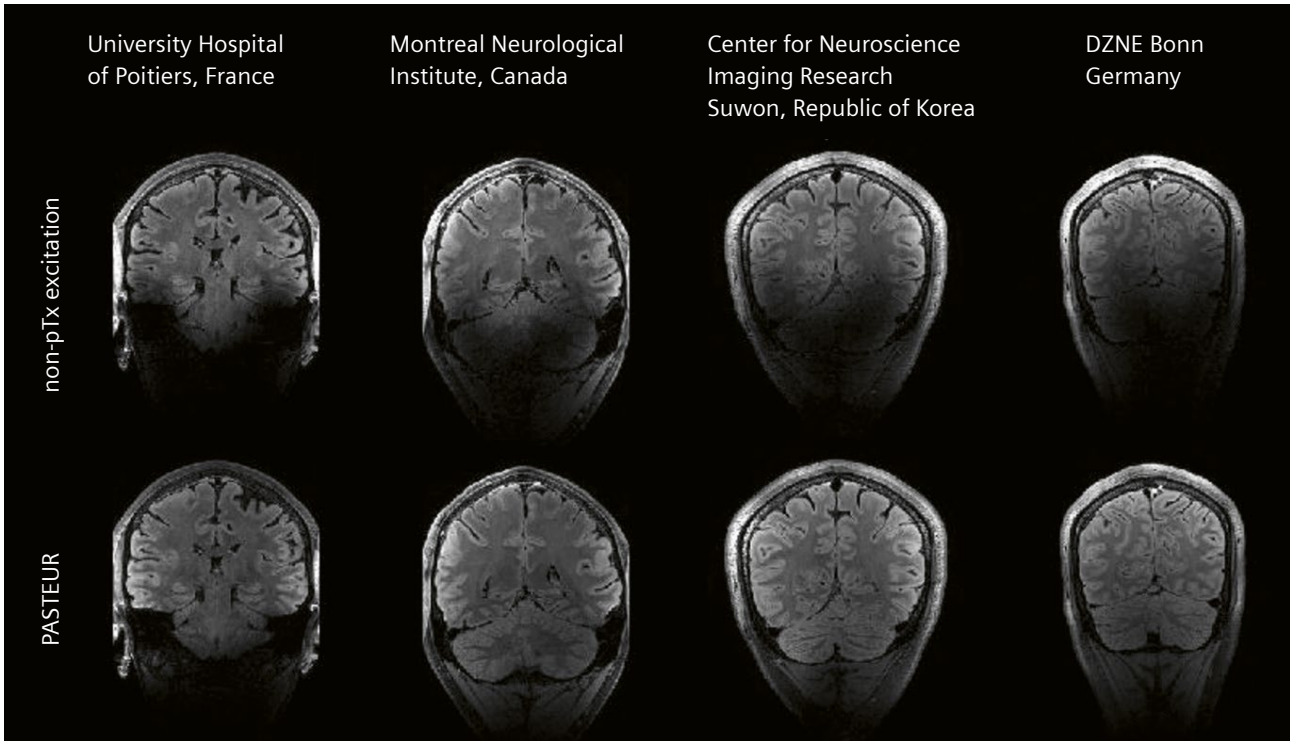

10 **Dark fluid T2-weighted SPACE imaging with PASTEUR in four testing sites**
Comparisons of standard non-pTx excitation and PASTEUR images from several research centers equipped with MAGENTOM Terra and MAGENTOM 7T^{Plus} systems (Figure adapted from [18]), illustrating the universality and reliability of UPs. From left to right: University Hospital of Poitiers in France; Montreal Neurological Institute in Canada; Center for Neuroscience Imaging Research in Suwon, Republic of Korea; and German Center for Neurodegenerative Diseases (DZNE) in Bonn, Germany.

Lastly, UP advantages were soundly demonstrated for brain imaging [9, 13–16, 25], yet other organs could likely also benefit from this approach, accounting for increased anatomical variability [29].

As already stated, image quality of the whole brain was always significantly improved with UPs compared to standard non-pTx excitation, in all considered imaging contrasts. Occasionally, small image artifacts remained in UP imaging. These hyper-signal artifacts arise from very localized and strong off-resonance effects, which have more variability among individuals (see also Figure 2). This is a known limitation of UPs, and radiologists should be aware of it. Note that the proposed imaging protocols could likely be improved, especially to reduce acquisition time. For instance, the latest acceleration techniques, such as compressed sensing, were not yet available for MPRAGE and MP2RAGE [30].

Additional MR sequences and supported features are planned for the PASTEUR package in the future: Several non-selective 3D MR sequences could be added, an important milestone would be the ability to excite arbitrary slabs with UPs [31], and 2D imaging should also be addressed while still maintaining the universality of the approach [32]. Importantly, all PASTEUR developments will be deployed to operate on the Iseult MAGNETOM 11.7T MRI system [33] recently installed at CEA NeuroSpin, a world-leading R&D collaboration between CEA and Siemens Healthineers.

The PASTEUR package is currently available for the 7T MAGNETOM Terra on the C2P platform[2] from Siemens Healthineers. At the time of writing, the PASTEUR package has already been distributed to 15 sites around the world (Fig. 10). Its adoption by the UHF community could help pave the way for pTx integration in clinical workflows.

Acknowledgments

This project received funding from the European Union's Horizon 2020 research and innovation program under Grant Agreement No 885876 (AROMA project). The authors would like to thank Iulius Dragonu, Carole Guillevin, Rene Gumbrecht, Robin Heidemann, Patrick Liebig, and Eberhard Pracht for their support. The authors are also grateful to Ilana Leppert, Christine Lucas Tardif, Sugil Kim, Kamil Uludag, and Tony Stöcker for providing PASTEUR images from their respective institutions.

[2]Access to the C2P platform from Siemens Healthineers is possible for collaboration partners who have signed the associated IDEA agreement. Please contact your local collaboration manager for more information.

References

1 Trattnig S, Bogner W, Gruber S, Szomolanyi P, Juras V, Robinson S, et al. Clinical applications at ultrahigh field (7 T). Where does it make the difference? NMR Biomed. 2016;29(9):1316–34.
2 Kraff O, Fischer A, Nagel AM, Mönninghoff C, Ladd ME. MRI at 7 tesla and above: Demonstrated and potential capabilities. J Magn Reson Imaging. 2015;41(1):13–33.
3 Van der Zwaag W, Schäfer A, Marques JP, Turner R, Trampel R. Recent applications of UHF-MRI in the study of human brain function and structure: a review. NMR Biomed. 2016;29(9):1274–88.
4 Bruschi N, Boffa G, Inglese M. Ultra-high-field 7-T MRI in multiple sclerosis and other demyelinating diseases: from pathology to clinical practice. Eur Radiol Exp. 2020;4(1):59.
5 Opheim G, van der Kolk A, Markenroth Bloch K, Colon AJ, Davis KA, Henry TR, et al. 7T Epilepsy Task Force Consensus Recommendations on the Use of 7T MRI in Clinical Practice. Neurology. 2021;96(7):327–341.
6 Van de Moortele PF, Akgun C, Adriany G, Moeller S, Ritter J, Collins CM, et al. B(1) destructive interferences and spatial phase patterns at 7 T with a head transceiver array coil. Magn Reson Med. 2005;54(6):1503–18.
7 Padormo F, Beqiri A, Hajnal JV, Malik SJ. Parallel transmission for ultrahigh-field imaging. NMR Biomed. 2016;29(9):1145–61.
8 Cloos MA, Boulant N, Luong M, Ferrand G, Giacomini E, Le Bihan D, et al. kT-points: short three-dimensional tailored RF pulses for flip-angle homogenization over an extended volume. Magn Reson Med. 2012;67(1):72–80.
9 Van Damme L, Mauconduit F, Chambrion T, Boulant N, Gras V. Universal nonselective excitation and refocusing pulses with improved robustness to off-resonance for Magnetic Resonance Imaging at 7 Tesla with parallel transmission. Magn Reson Med. 2021;85(2):678–693.
10 Khaneja N, Reiss T, Kehlet C, Schulte-Herbrüggen T, Glaser SJ. Optimal control of coupled spin dynamics: design of NMR pulse sequences by gradient ascent algorithms. J Magn Reson. 2005;172(2):296–305.
11 Massire A, Vignaud A, Robert B, Le Bihan D, Boulant N, Amadon A. Parallel-transmission-enabled three-dimensional T2 -weighted imaging of the human brain at 7 Tesla. Magn Reson Med. 2015;73(6):2195–203.
12 Cloos MA, Boulant N, Luong M, Ferrand G, Giacomini E, Hang MF, et al. Parallel-transmission-enabled magnetization-prepared rapid gradient-echo T1-weighted imaging of the human brain at 7 T. Neuroimage. 2012;62(3):2140–50.
13 Gras V, Vignaud A, Amadon A, Bihan D, Boulant N. Universal pulses: A new concept for calibration-free parallel transmission. Magn Reson Med. 2017;77(2):635–643.
14 Gras V, Mauconduit F, Vignaud A, Amadon A, Le Bihan D, Stöcker T, et al. Design of universal parallel-transmit refocusing kT -point pulses and application to 3D T2 -weighted imaging at 7T. Magn Reson Med. 2018;80(1):53–65.
15 Gras V, Boland M, Vignaud A, Ferrand G, Amadon A, Mauconduit F, et al. Homogeneous non-selective and slice-selective parallel-transmit excitations at 7 Tesla with universal pulses: A validation study on two commercial RF coils. PLoS One. 2017;12(8): e0183562.
16 Gras V, Mauconduit F, Vignaud A, Le Ster C, Leroi L, Amadon A, et al. PASTeUR: Package of Anatomical Sequences using parallel Transmission UniveRsal kT-point pulses. In: Proceedings of the 27th Annual Meeting of ISMRM. Montréal, QC, Canada. 2019; p. 4626.

17 Idrobo AH, Weiss P, Massire A, Amadon A, Boulant N. On variant strategies to solve the magnitude least squares optimization problem in parallel transmission pulse design and under strict SAR and power constraints.
IEEE Trans Med Imaging. 2014;33(3):739–748.
18 Mauconduit F, Massire A, Gras V, et al. Traveling pulses visit 7T Terra sites: Getting ready for Parallel Transmission in routine use.
Submitted to ISMRM 2022. London, United Kingdom.
2022; p. 2488.
19 International Electrotechnical Commission. Medical electrical equipment - Part 2–33: Particular requirements for the basic safety and essential performance of magnetic resonance equipment for medical diagnosis. 3rd ed. Geneva. 2010;603:2–33.
20 German Ultrahigh Field Imaging (GUFI). Approval of subjects for measurements at ultra-high-field MRI [Internet]. Germany [cited August 12, 2021]. Available from:
https://mr-gufi.de/index.php/en/documents.
21 Mugler III JP, Brookeman JR. Three-dimensional magnetization-prepared rapid gradient-echo imaging (3D MP RAGE).
Magn Reson Med. 1990;15(1):152–7.
22 Marques JP, Kober T, Krueger G, van der Zwaag W, Van de Moortele P-F, Gruetter R. MP2RAGE, a self bias-field corrected sequence for improved segmentation and T1-mapping at high field.
Neuroimage. 2010;49(2):1271–81.
23 Beaumont J, Gambarota G, Saint-Jalmes H, Acosta O, Ferré JC, Raniga P, et al. High-resolution multi-T1 -weighted contrast and T1 mapping with low B1>+ sensitivity using the fluid and white matter suppression (FLAWS) sequence at 7T.
Magn Reson Med. 2021;85(3):1364–1378.
24 Mugler III JP. Optimized three-dimensional fast-spin-echo MRI.
J Magn Reson Imaging. 2014;39(4):745–67.
25 Gras V, Pracht ED, Mauconduit F, Le Bihan D, Stöcker T, Boulant N. Robust nonadiabatic T2 preparation using universal parallel-transmit kT-point pulses for 3D FLAIR imaging at 7 T.
Magn Reson Med. 2019;81(5):3202–3208.
26 Tomi-Tricot R, Gras V, Thirion B, Mauconduit F, Boulant N, Cherkaoui H, et al. SmartPulse, a machine learning approach for calibration-free dynamic RF shimming: Preliminary study in a clinical environment. Magn Reson Med. 2019;82(6):2016–2031.
27 Le Ster C, Mauconduit F, Massire A, Boulant N, Gras V. Standardized Universal Pulse: a fast RF calibration approach to improve flip angle accuracy in parallel transmission.
Magn Reson Med. 2022; 10.1002/mrm.29180
28 Herrler J, Liebig P, Gumbrecht R, Ritter D, Schmitter S, Maier A, et al. Fast online-customized (FOCUS) parallel transmission pulses: A combination of universal pulses and individual optimization.
Magn Reson Med. 2021;85(6):3140–3153.
29 Aigner C Stefan, Dietrich S, Schaeffter T, Schmitter S. Calibration-free pTx of the human heart at 7T via 3D universal pulses.
In: Proceedings of the 29th Annual Meeting of ISMRM.
Online conference. 2021; p. 777.
30 Mussard E, Hilbert T, Forman C, Meuli R, Thiran J-P, Kober T. Accelerated MP2RAGE imaging using Cartesian phyllotaxis readout and compressed sensing reconstruction.
Magn Reson Med. 2020;84(4):1881–1894.
31 Jamil R, Mauconduit F, Gras V, Boulant N. General gradient delay correction method in bipolar multispoke RF pulses using trim blips.
Magn Reson Med. 2021;85(2):1004–1012.
32 Gras V, Poser BA, Wu X, Tomi-Tricot R, Boulant N. Optimizing BOLD sensitivity in the 7T Human Connectome Project resting-state fMRI protocol using plug-and-play parallel transmission.
Neuroimage. 2019;195:1–10.
33 Le Bihan D, Schild T. Human brain MRI at 500 MHz, scientific perspectives and technological challenges.
Supercond Sci Technol. 2017;30(3):033003.

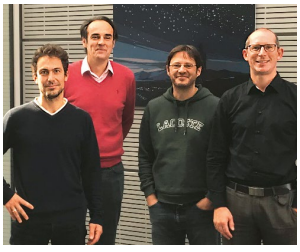

Contact

The METRIC team (from left to right: Vincent Gras, Alexandre Vignaud, Nicolas Boulant, Franck Mauconduit)
Université Paris-Saclay, CEA, CNRS, BAOBAB, NeuroSpin
91191, Gif-Sur-Yvette
France
nicolas.boulant@cea.fr
franck.mauconduit@cea.fr
https://joliot.cea.fr/drf/joliot/recherche/neurospin

Aurélien Massire, Ph.D.
MR Clinical Scientist
Siemens Healthcare SAS
40 Avenue des Fruitiers
93210, Saint Denis
France
aurelien.massire@siemens-healthineers.com

Improving the Assessment of the Postoperative Spine with 0.55T MRI: A Case Report

Hanns-Christian Breit, M.D.; Jan Vosshenrich, M.D.; Thilo Rusche, M.D.; Michael Bach, Ph.D.; Dorothee Harder, M.D.

Department of Radiology, University Hospital Basel, University of Basel, Switzerland

Introduction

Acute and chronic back pain are common complaints and a major burden for healthcare systems worldwide [1]. With aging populations, the number of patients requiring spinal decompression or stabilization surgery related to trauma or degenerative changes is rising. As a result, the number of patients with spinal metal implants[1] requiring follow-up imaging is also increasing [2, 3]. Since magnetic resonance imaging (MRI) is the gold standard for spinal imaging in most practices, growing numbers of metal implants are creating diagnostic limitations caused by inevitable susceptibility artifacts. Besides the continual improvements in metal artifact reduction techniques for the assessment of the postoperative spine over the last few decades, another promising approach for increasing diagnostic accuracy of MRI is the use of low-field systems [4]. While 1.5T and 3T MRI systems currently dominate clinical routine, low-field MRI systems are experiencing a renaissance after their initial use in the 1980s and 1990s. In particular, innovations in coil design, gradient systems, and image reconstruction techniques offer new opportunities for the use of low-field MRI systems in patients with metal implants [5].

This case report aims to highlight the potential of a newly commercially available 0.55T low-field MRI system in postoperative spinal imaging, compared to MRI systems operating at field strengths of 1.5T and 3T. It is based on our recent experiences with a 76-year-old female patient with multiple prior spinal stabilization surgeries.

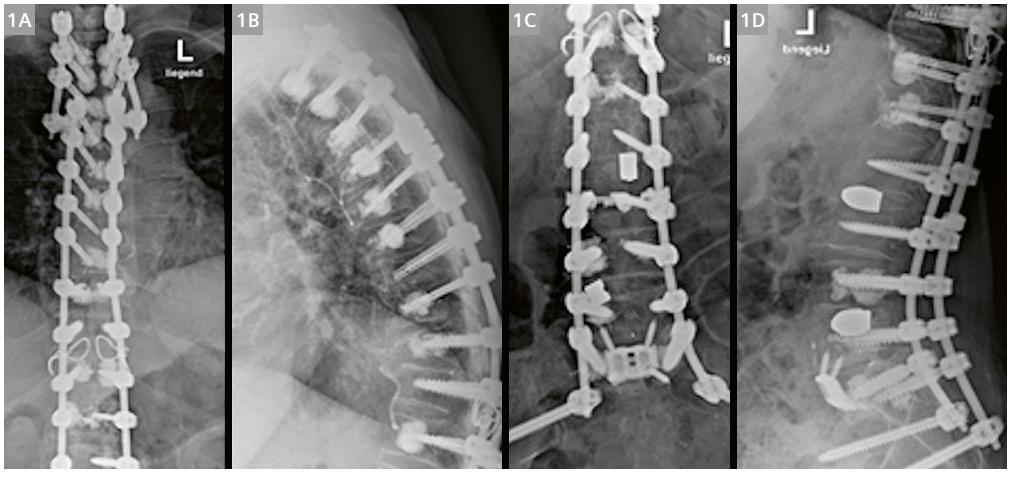

1 AP **(1A, 1C)** and lateral **(1B, 1D)** radiographs of a 76-year-old female patient following lumbopelvic fusion and posterior spondylodesis up to the T2 level.

[1]*The MRI restrictions (if any) of the metal implant must be considered prior to patient undergoing MRI exam. MR imaging of patients with metallic implants brings specific risks. However, certain implants are approved by the governing regulatory bodies to be MR conditionally safe. For such implants, the previously mentioned warning may not be applicable. Please contact the implant manufacturer for the specific conditional information. The conditions for MR safety are the responsibility of the implant manufacturer, not of Siemens Healthineers.*

Case presentation

Imaging was performed within the scope of a prospective study that was approved by the local ethics committee (BASEC 2021-00166). Written informed consent was obtained.

A 76-year-old female patient was referred to our hospital for a progressive paraparesis of the lower extremities after posterior decompression and stabilization surgery of the thoracic spine had been performed at another institution.

The patient history comprises multiple prior spinal surgeries. Initial single-level lumbar fusion of the L5–S1 segment was performed more than ten years ago. In October 2019, loosening of the pedicle screws in S1 as a result of pseudarthrosis made it necessary to perform anterior lumbar interbody fusion of the L5–S1 segment, and corrective posterior spondylodesis and lumbopelvic fusion. Progressive degeneration of the adjacent motion segments required extension of the posterior spondylodesis with cement-augmented pedicle screws up to the T5 level in September 2021. This was followed in October 2021 by a further posterior decompression and revision of the spondylodesis with extension up to the T2 level due to an acute T4 compression fracture with resulting spinal canal stenosis. The extent of the posterior instrumentation is shown in Figure 1. The aforementioned progressive paraparesis developed after the latter surgery, and the patient was ultimately transferred to our institution for further treatment. After initial clinical assessment, the spine surgery team ordered an MR examination of the whole spine to rule out a compressive postoperative spinal hematoma.

Imaging

Given the patient's symptoms, the resulting potential indication for urgent spinal decompression surgery, and the lack of availability of a 1.5T MRI system at the time of presentation, initial imaging was performed on a 3T MRI scanner (MAGNETOM Skyra, Siemens Healthcare GmbH, Erlangen, Germany). Even though metal artifact reduction sequences were used during the examination, the severity of the susceptibility artifacts caused by the posterior instrumentation prevented assessment of the spinal canal. To rule out or confirm a postoperative compressive spinal hematoma, an additional MR examination of the whole spine was performed at 1.5T (MAGNETOM Avanto Fit, Siemens Healthcare GmbH, Erlangen, Germany). Metal artifact reduction sequences were again used to reduce artifact severity. However, the MR examination had to be stopped following the acquisition of the sagittal T1- and T2-weighted sequences, as the patient reported unbearable back pain whilst lying down. An image review by musculoskeletal radiologists and a discussion with the spine surgery team resulted in agreement that a final diagnosis could not be made with sufficient certainty, even though the ability to assess the spinal canal had improved on the 1.5T MRI system. In particular, the exact craniocaudal extent of the suspected postoperative hematoma, which would affect the surgical approach, could not be determined on the available sequences. It was therefore decided to repeat the MR examination with sufficient analgesia and take advantage of the newly installed low-field 0.55T MRI system (MAGNETOM Free.Max, Siemens Shenzhen Magnetic Resonance Ltd., Shenzhen, China). The examination at 0.55T was completed according to protocol (Table 1).

Sequence	B0 Field [T]	FOV [mm²]	Matrix	TR [ms]	TE [ms]	Bandwidth [Hz/px]	TA [min:s]
T1 TSE sag	0.55	320 × 320	288 × 216	602	16	299	03:54
T2 TSE tra	0.55	200 × 200	192 × 144	4830	94	299	04:25
T2 TSE sag	0.55	320 × 320	320 × 240	3500	96	120	03:23
T1 TSE sag	0.55	320 × 320	320 × 224	454	13	130	02:28
T2 TSE Dixon cor	1.5	300 × 300	256 × 205	5200	92	455	04:04
T2 TSE sag	1.5	320 × 320	448 × 358	4400	102	505	04:10
T1 TSE sag	1.5	320 × 320	448 × 358	470	7.7	505	04:02
T2 TSE Dixon sag	3	340 × 340	448 × 314	5000	88	250	03:05
FLAIR sag	3	340 × 340	448 × 403	2000	29	260	03:20
T2 TSE tra	3	190 × 190	256 × 179	3000	100	500	03:06

Table 1: Sequences and associated parameters at 0.55T, 1.5T, and 3T. FOV = field of view

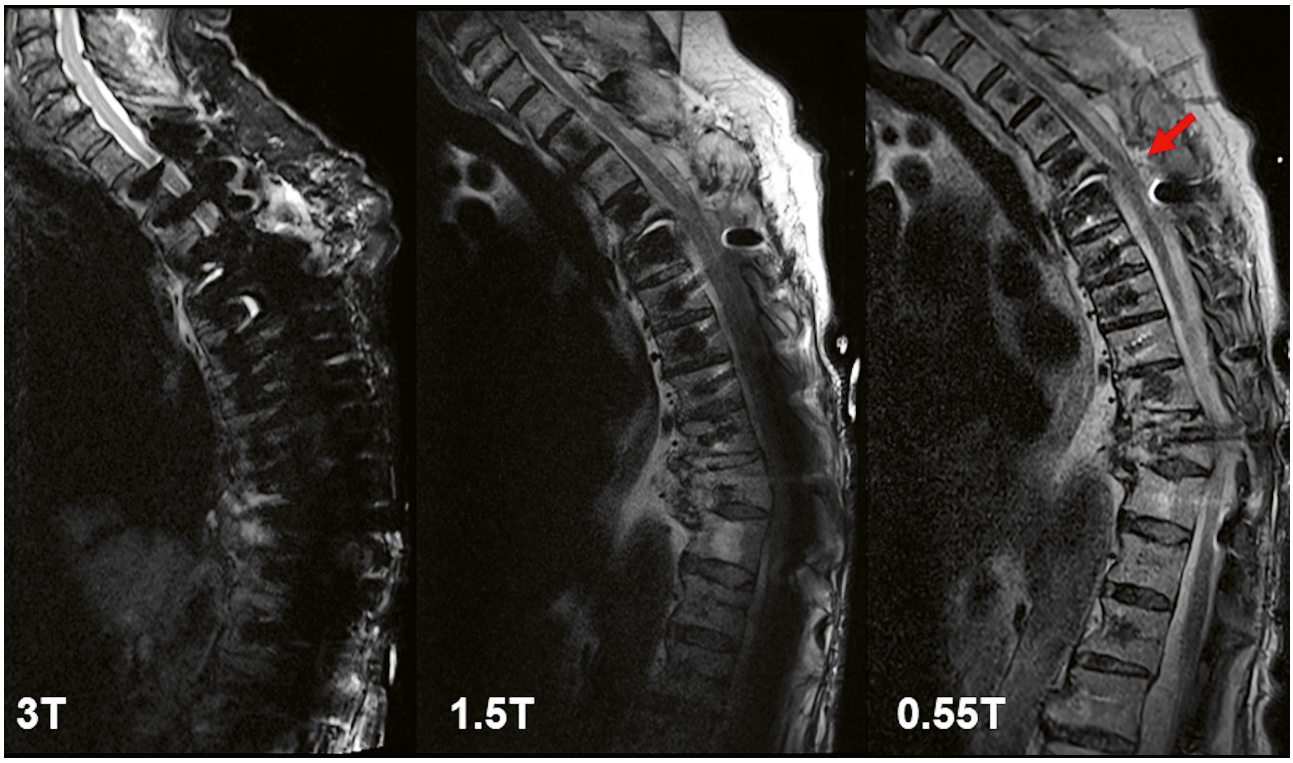

2 Sagittal T2-weighted metal artifact reduction sequences at 3T, 1.5T, and 0.55T. Note the decrease in susceptibility artifacts and substantially improved visibility of the spinal canal at 0.55T, with demarcation of a high-grade spinal stenosis at the T4/5 level caused by a compressive postoperative spinal hematoma (red arrow).

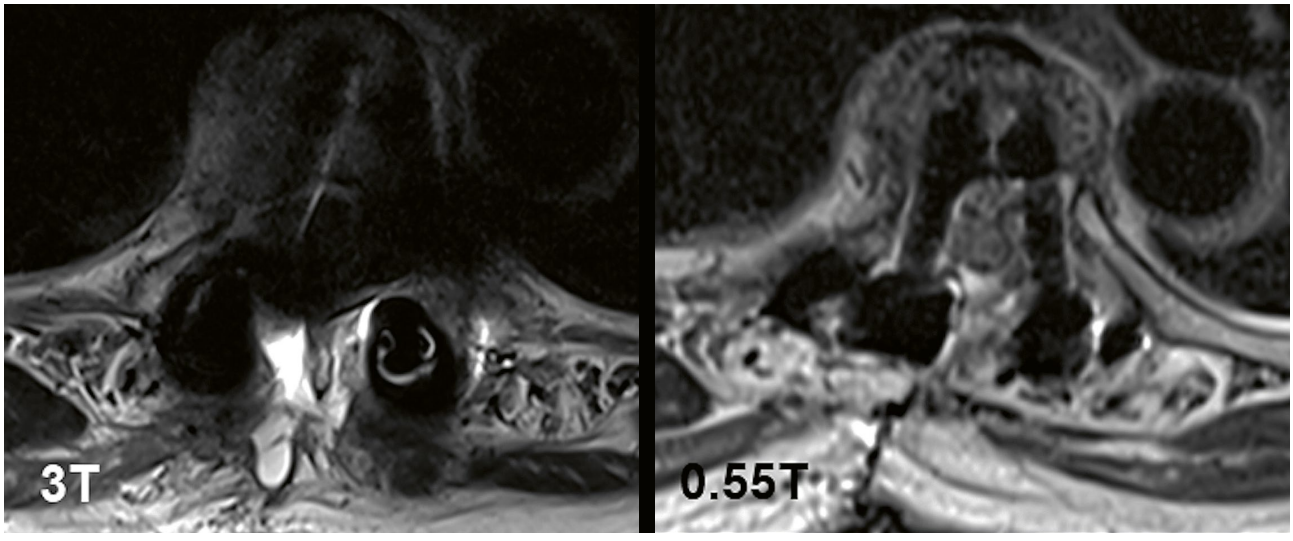

3 Axial T2-weighted metal artifact reduction sequences at 3T and 0.55T. High-grade spinal canal stenosis at the T4 level is clearly depicted at 0.55T, while the assessment of the spinal canal is not possible at 3T.

Diagnosis

With the substantially improved ability to assess the spinal canal on sagittal and axial T2-weighted images acquired using the low-field 0.55T MRI system, a postoperative compressive subdural hematoma extending from T4 to T5, and resulting in high-grade spinal canal stenosis without myelopathy, could be identified (Fig. 2). Even though a potential spinal hematoma might have been suspected on the sagittal T2-weighted images acquired at 1.5T, diagnostic confidence would have been low as spinal canal assessment was limited at this location. In particular, the craniocaudal extent of the subdural hematoma along two thoracic vertebrae was not visible on either 1.5T or 3T images, due to extensive susceptibility artifacts from the posterior instrumentation. Also, the degree of narrowing in the spinal canal and spinal cord deformation could only be determined on the axial T2-weighted images acquired at 0.55T (Fig. 3). The additional low-field MRI of the spine therefore provided crucial information to the referring spine surgeons with regards to their surgical approach for this patient.

Discussion

The correlation between field strength and metal artifact severity in MR imaging is well known and has been demonstrated both in phantom experiments and clinical studies [6, 7]. In addition to numerous existing and continually refined metal artifact reduction techniques, the introduction of a novel generation of low-field MRI systems operating at 0.55T may be considered as providing a new approach for improving image quality and diagnostic opportunities in patients with metal implants, especially following spinal instrumentation [5, 8, 9]. Particularly in an era of aging populations with accompanying increases in the prevalence of metal implants in multiple countries worldwide, these new approaches may overcome the current challenges of imaging this patient clientele on traditional 1.5T or 3T MRI systems. To the best of our knowledge, however, no studies have been performed to establish whether the reduction in metal artifact severity automatically translates into improved diagnostic performance or systematically affects patient management. This requires systematic investigation of large patient collectives.

This case report from our daily routine may provide a basis for future investigations, as the findings further underline the potential of modern low-field MRI systems in cases where diagnostic limits are reached when using well-established 1.5T and 3T MRI systems.

References

1 Wenig CM, Schmidt CO, Kohlmann T, Schweikert B. Costs of back pain in Germany. Eur J Pain. 2009;13(3):280–6.
2 Rajaee SS, Kanim LEA, Bae HW. National trends in revision spinal fusion in the USA: patient characteristics and complications. Bone Joint J. 2014;96-B(6):807–16.
3 Pfuntner A, Wier LM, Stocks C. Most frequent procedures performed in U.S. hospitals, 2011: statistical brief #165. 2013 Oct. I n: Healthcare Cost and Utilization Project (HCUP) Statistical Briefs [Internet]. Rockville (MD): Agency for Healthcare Research and Quality (US); 2006 Feb–. Available from: https://www.ncbi.nlm.nih.gov/books/NBK174682/
4 Stradiotti P, Curti A, Castellazzi G, Zerbi A. Metal-related artifacts in instrumented spine. Techniques for reducing artifacts in CT and MRI: state of the art. Eur Spine J. 2009;18(Suppl 1):102–108.
5 Runge VM, Heverhagen JT. Advocating the Development of Next-Generation, Advanced-Design Low-Field Magnetic Resonance Systems. Invest Radiol. 2020;55(12):747–753.
6 Olsrud J, Lätt J, Brockstedt S, Romner B, Björkman-Burtscher IM. Magnetic resonance imaging artifacts caused by aneurysm clips and shunt valves: dependence on field strength (1.5 and 3 T) and imaging parameters. J Magn Reson Imaging. 2005;22(3):433–7.
7 Liebl H, Heilmeier U, Lee S, Nardo L, Patsch J, Schuppert C, et al. In vitro assessment of knee MRI in the presence of metal implants comparing MAVRIC-SL and conventional fast spin echo sequences at 1.5 and 3 T field strength. J Magn Reson Imaging. 2015;41(5):1291–9.
8 Campbell-Washburn AE, Ramasawmy R, Restivo MC, Bhattacharya I, Basar B, Herzka DA, et al. Opportunities in interventional and diagnostic imaging by using high-performance low-field-strength MRI. Radiology. 2019;293(2):384–393.
9 Basar B, Sonmez M, Yildirim DK, Paul R, Herzka DA, Kocaturk O, et al. Susceptibility artifacts from metallic markers and cardiac catheterization devices on a high-performance 0.55 T MRI system. Magn Reson Imaging. 2021;77:14–20.

Contact

Hanns-Christian Breit, M.D.
University Hospital Basel
Department of Radiology
Spitalstrasse 21
4031 Basel
Switzerland
Tel.: +41 61 328 56 33
hanns-christian.breit@usb.ch

Our Connected Scanner is a Smart Deal: You Care for Your Patients, We Stay Connected to Care for Your MAGNETOM Free.Max

Julia Sauernheimer

Global Service Business Manager for MRI, Siemens Healthineers, Erlangen, Germany

We are breaking the accessibility barriers thanks to our new scanner design with its light weight, excellent diagnostic image quality, improved remote connection support, and greater sustainability. Almost everything has already been said about MAGNETOM Free.Max, but not quite everything. That's why, today, we are making it about service, and our disruptively innovative approach to how we deliver service. In other words: Why our connected scanner approach is the final touch for your new scanner.

New service features for more MRI affordability and availability

Since day one of the design and development of MAGNETOM Free.Max, our Siemens Healthineers Customer Services (CS) teams have been on board, creating a fitting new service concept. We have worked continuously on numerous cutting-edge innovations, starting with the development and engineering of the scanner itself (1), moving on to handover training (2) and operations (3). With service in mind, our connected scanner approach accompanies you each step of the way, while reducing the total life cycle cost, and increasing the uptime of MAGNETOM Free.Max. These two keywords, life cycle cost and uptime, ultimately lead us to the topic of remote accessibility, and to the system's service portal. This feature is crucial for troubleshooting current issues and trending parameters to predict future failures, all with one goal in mind: Improving operation.

Development & Engineering

DryCool technology

Just like previous MRI scanners from Siemens Healthineers, MAGNETOM Free.Max also uses a superconducting magnet to create the main magnetic field. But, and this is an important but: The magnet and the water cooling design

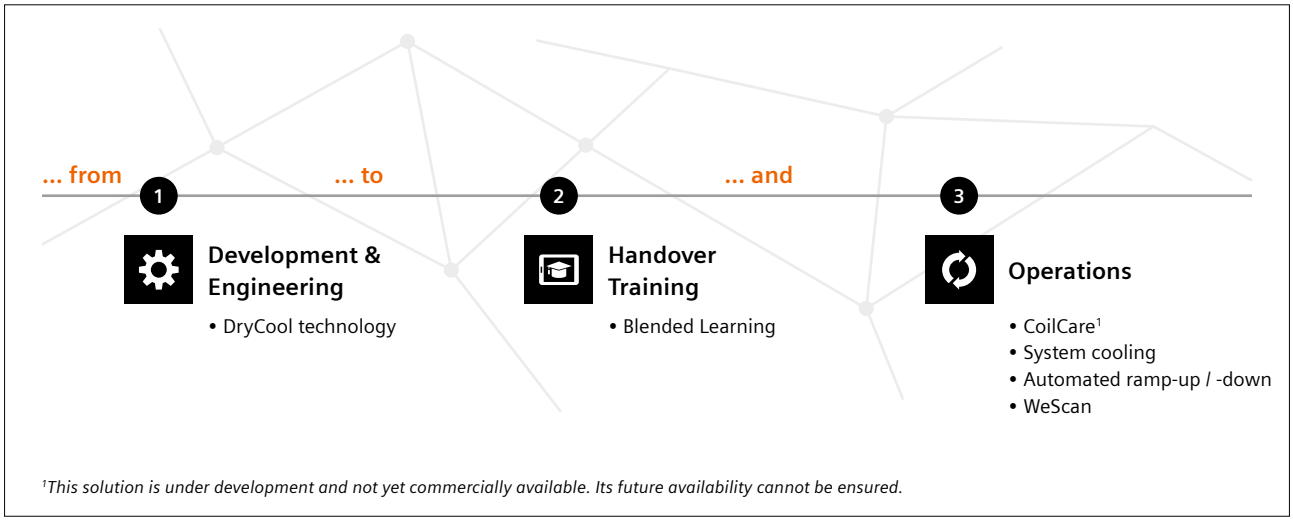

1 Our new Service concept accompanies each step of the entire equipment life cycle.

have been significantly changed, impacting the way it is serviced throughout its life cycle. Instead of having the coils inside a large helium vessel containing up to 1,500 L of liquid helium (He), they are cooled by conduction to a small helium pot that only contains 0.7 L of liquid He – which means an enormous 99.95% reduction.

The big advantage now is that you only need helium gas to fill the system and no longer depend on liquid helium, which is excellent news for geographical regions where supply of helium is limited. Once the helium refrigeration system is turned on, it cools and condenses the helium gas into liquid. Further, the system is equipped with a buffer tank that stores helium gas, which occurs during the ramp-down of the magnet, for instance. Designed as a self-contained system, all helium remains in a closed cycle and is reused to cool down the magnet again. And last but not least, no quench pipe is needed, which simplifies the site requirements significantly.

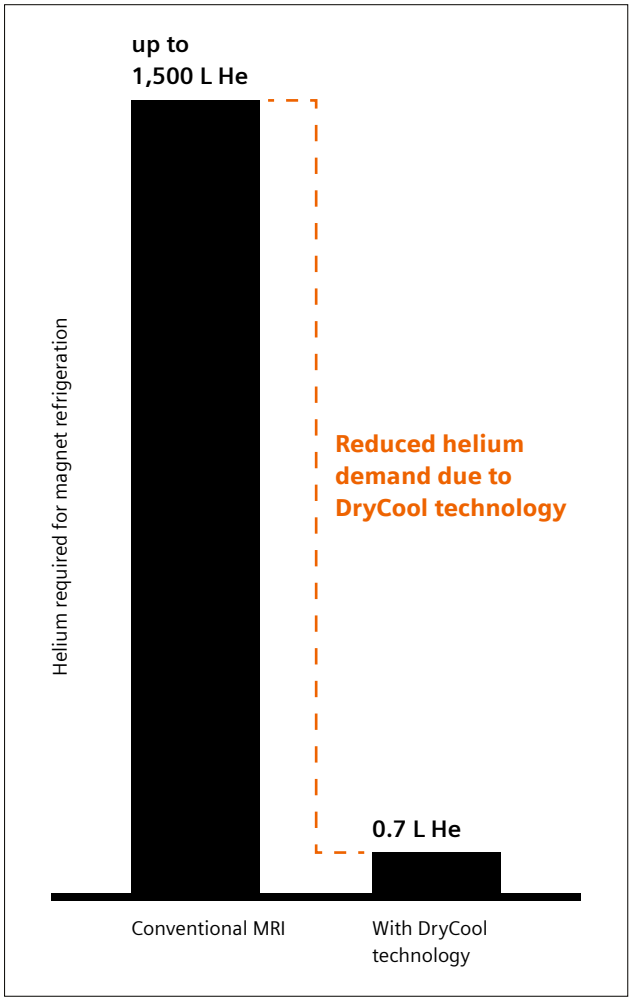

2 MAGNETOM Free.Max DryCool technology allows you to run your MRI system with just a small fraction of the standard volume of helium – 99.95% less than conventional MRI scanners.

Handover Training

Blended Learning

When it comes to handover training, we support you with an optimal mix of online training formats and onsite hands-on experience, especially designed for MAGNETOM Free.Max. On the one hand, our digital training portfolio is complemented by our online education experience, PEPconnect, which enables basic learning on user interfaces (UI), workflows, postprocessing, and more. On the other hand, our new SmartSimulator performs cloud-based simulation training for software applications and workflows. Therefore, you are given access to a simulator that allows your staff to practice in a safe environment, on a simulator that replicates the same system used in your clinical routine.

The big advantage is that you benefit from practical, highly flexible, and interactive training without the time-consuming interference in the daily routine of your scanner and without compromising on quality [1]. The most suitable content, level of detail, and duration is defined by your individual needs. Training can be started in tandem with the installation, and operations can smoothly begin directly after the handover of the scanner.

Benefits of Blended Learning:

- Access the training material earlier, even before the system delivery
- Learn more flexibly, at the time, location, and pace that suits you best
- Pre-onsite steps, performed via PEPconnect and SmartSimulator, provide you with an early insight into a wide range of topics, available for various levels of experience and interests
- Additional clarification of topics that require more detailed explanation
- Getting the best out of the onsite training and maximizing focus
- Continuous education during the entire life cycle of the system

We do not leave after training is finished. We always stay by your side while you're working with your MAGNETOM Free.Max, accompanying your journey with remote monitoring and companion services.

"I think the simulator was excellent, and it was good to get some hands on practice. […] I think a blended approach to learning is good to ensure that all learning styles are catered for. After the training we received I did feel well prepared for the on-site applications training."

Liz Loele, Clinical Lead MRI, Cobalt Health, UK[3]

Operations

CoilCare[1]
Tried and tested for MRI with our Guardian Program we predict possible failure through proactive, real-time, AI-based analysis, monitoring all critical components to increase your MRI uptime. With CoilCare, we now dive even deeper: Connected to your scanner day and night, seamlessly integrating into your daily clinical routine, we monitor and oversee your entire scanner system – from the magnet to crucial system parameters, including temperature and pressure, the cooling chain, and even your local receiver coils. For the latter, we also use machine learning and neural networks-based algorithms, to constantly monitor their performance and quality, identifying any event before it occurs. You can just sit back and rely on our technology and services, take care of your patients, and achieve excellent and reliable image quality and clinical results. Used with MAGNETOM Free.Max, CoilCare allows even more precise detection of errors by continuously monitoring 50 trend parameters[2].

[1] *This solution is under development and not yet commercially available. Its future availability cannot be ensured.*
[2] *50 trend parameters including temperature, voltage, water pressure, and humidity of subcomponents, e.g., magnet, patient table, cooling system, gradient component, or GPA gradient power amplifier.*
[3] *The statements by customers of Siemens Healthineers described herein are based on results that were achieved in the customer's unique setting. Since there is no "typical" hospital and many variables exist (e.g., hospital size, case mix, level of IT adoption) there can be no guarantee that other customers will achieve the same results.*

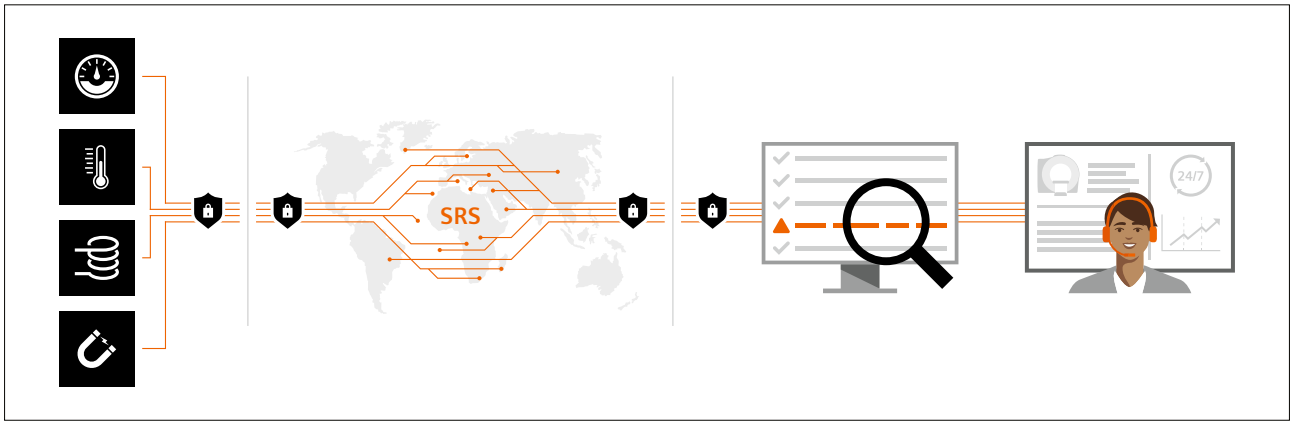

3 We have developed different service features that keep the critical components of your MAGNETOM Free.Max running smoothly over their entire life cycle.

Benefits of CoilCare:

- Machine learning and neural networks-based algorithms
- Monitoring and analysis of local coils performed several times a day
- Enables reliable usage of scanning system without downtime
- Self-learning and intelligent system

System cooling

Redesigned, making the cooling chain even more effective. This is exactly what we did with the cooling system needed for MRI components such as power amplifiers, compressors, and gradient coils. We now offer an indoor unit which combines the cabinet's air conditioning and water separator functions. A 50 L expansion vessel is fitted to compensate for unavoidable water leaks in the cooling system, such as those through bearings. An optional set of two outdoor units can be fitted to provide cooling for the indoor unit. The advantage of this is that the indoor unit is then independent of the customer's water-cooling circuit. And thanks to this new solution, our Customer Service team can now oversee and monitor the entire cooling chain. In the event of any incidents, we react fast, are solution oriented, and fix errors before they occur. This is of utmost importance for any MRI scanner, but especially for MAGNETOM Free.Max, and it helps improve system availability [2].

Automated ramp down / ramp up

To support trouble-free operations when you are working with your MAGNETOM Free.Max in your daily routine we have developed an integrated power supply and control enabling automated ramping of the magnet. First, in the event of loss of refrigeration – e.g., due to a power outage – which can, in the worst case, lead to the magnet warming up and quenching, the system starts an automated ramp-down 30 minutes after a refrigeration event is detected. This ramp-down takes 20 minutes and prevents the magnet from experiencing a strong heat load. As soon as the refrigeration is reinstated, the system checks remotely that temperatures and other parameters are stable, before automatically ramping up the magnet again. In a nutshell: No user or service engineer action is needed to initiate the process, as MAGNETOM Free.Max performs the ramp-down and ramp-up automatically.

WeScan[4] Remote Scanning

Many MRI users are currently experiencing a shortage of technologists, making it increasingly difficult for many radiology departments to cover peak periods and non-core hours, such as late night, and weekend shifts. At the same time, staff stress levels are on the rise, which can lead to high staff turnover and quality fluctuations, jeopardizing economic success and reproducibility of high-quality

[4] *WeScan is compatible with most scanners from Siemens Healthineers.*

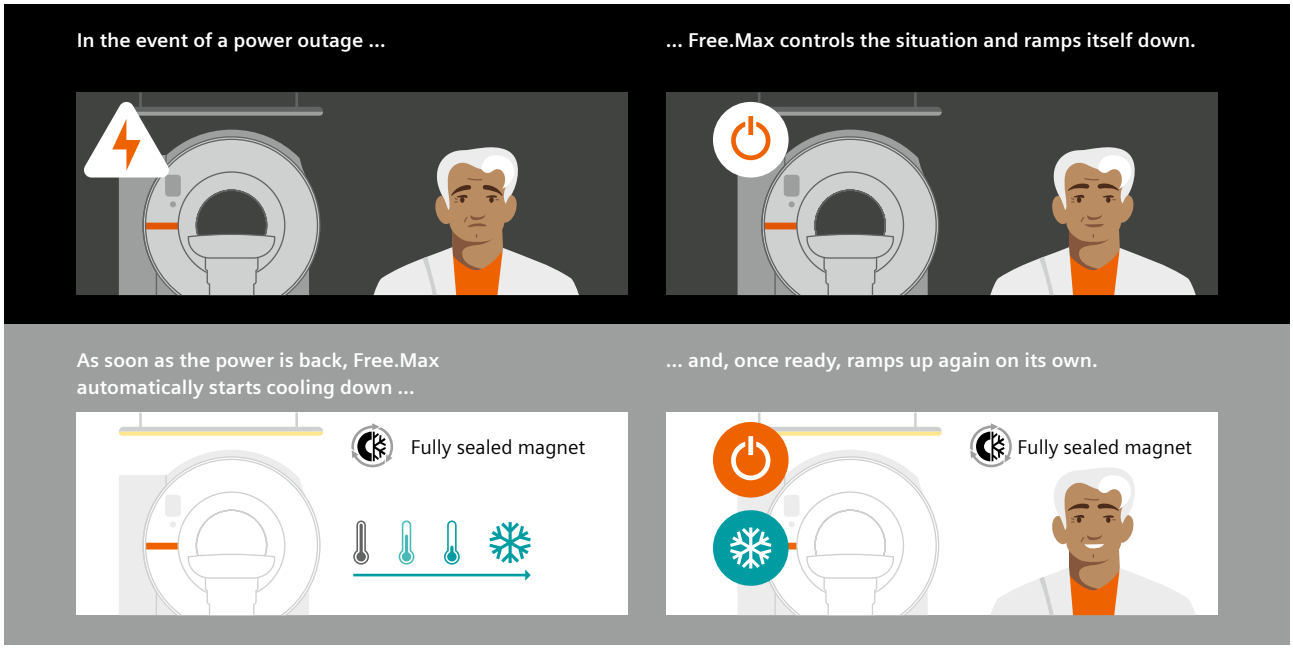

4 Always on the safe side: Intelligent automated ramp-down feature acts faster and smarter than any human could in the event of loss of refrigeration.

"With WeScan, we can compensate for staff shortages in a targeted manner and can therefore continue to offer our entire spectrum of MRI examinations at our two sites. Especially in the event of staff changes, as this allows for real planning, security, and flexibility for our technologists and patients."

Norbert Wilke, M.D., Radiological Center, Höchstadt/Aisch and Nuremberg, Germany[3]

outcomes. This is why we have developed WeScan: A remote scanning service for MRI systems, also designed to enable serviceability in remote locations. Qualified technologists either offer your onsite staff remote support with scanning tasks or perform the scan themselves. The system is remotely controlled using *syngo* Virtual Cockpit and Smart Remote Services (SRS)[5]. To sum up: While your staff focuses on the patient onsite, you can request MRI scan support from a qualified remote MRI technologist.

Benefits of WeScan Remote Scanning:

- Easy staff scheduling
- Flexible access to the expertise of remote MRI technologists thanks to remote scanning technology
- Reliable quality
- Higher revenue thanks to the potential to extend services without additional staff

We are by your side whenever you need us, with a smart combination of personal and digital support

We help safeguard your investment: MAGNETOM Free.Max is connected to Siemens Healthineers to deliver the best performance in a smart way. First, the connectivity enables simulations of the workflow – such as initial training – even before the scanner is handed over. In the next step, during operations, the connectivity enables solution-oriented monitoring of all critical components, while software updates improve the performance and security of your equipment – all to maximize your equipment uptime. And the icing on top of the cake: With our Advance Plan service agreement, you benefit from our continuous, digitally driven, long-term software update and upgrade service and computing hardware replacements that keep your MAGNETOM Free.Max cybersecure,[6] protecting your patients' data. Our Advance Plans also enable you to benefit from easy access to clinical and digital innovations, keeping users at the forefront of developments.

More convenient, faster, less expensive

We connect to your world to make service easy. Digitalizing healthcare allows us to be right by your side 24/7, making sure your equipment and knowledge are up to date and clinical processes optimized – so you can focus on what really matters: your patients.

References

1 Kasap C. Utilizing Blended Learning for Customer Support During the COVID-19 Pandemic: An Experience from the UK and Ireland. MAGNETOM Flash (77) 2/2020: 68-77.
2 Biber S. MAGNETOM Free.Max: Keeping a Hot System Cool. MAGNETOM Flash (79) 2/2021: 95-98.

Contact

Julia Sauernheimer
Siemens Healthineers
CS CRM BM
Hartmannstr. 16
91052 Erlangen
Germany
Tel.: +49 (1525) 4593954
julia.sauernheimer@siemens-healthineers.com

www.siemens-healthineers.com/services/customer-services

[5] *Smart Remote Services (SRS) is the fast, secure, and powerful data link that connects your medical equipment to our experts, who provide proactive and interactive services that speed up their running operations. To reduce onsite time and improve remote capabilities, Siemens Healthineers Smart Remote Services (SRS) connectivity should be established from day one to increase uptime and reduce service efforts.*

[6] *Cybersecurity updates are available for latest system software versions.*

The products/features and/or service offerings (here mentioned) are not commercially available in all countries and are only available for selected CT and MRI modalities. If the services are not marketed in countries due to regulatory or other reasons, the service offering cannot be guaranteed. Please contact your local Siemens Healthineers organization for further details.

Prerequisites: stable SRS connection with adequate bandwidth.

Magnetic Resonance Elastography of the Liver: Best Practices

Manjunathan Nanjappa, Ph.D.[1]; Bradley Bolster, Ph.D.[2]; Ning Jin, Ph.D.[2]; Stephan Kannengießer, Ph.D.[3]; Robert Sellers, RT(R)(MR)(CT)[2]; Arunark Kolipaka, Ph.D., FAHA, FSCMR[1]

[1]The Ohio State University, Columbus, OH, USA
[2]Siemens Healthineers, US MR R&D Collaborations, Malvern, PA, USA
[3]Siemens Healthineers, MR DL ONCO, Erlangen, Germany

Introduction

Liver is the largest solid internal organ of the human body. It performs a wide range of functions including aiding digestion, storing energy, removing metabolic waste and microorganisms from the circulatory system, and producing blood-clotting components. The liver can repair, regenerate and/or regrow itself to maintain its structure and functions, yet certain health conditions can overwhelm these capabilities leading to the progression of liver disease [1]. Alcohol abuse, obesity, and chronic illness can lead to excessive accumulation of extracellular matrix proteins including collagen. This results in diminished blood flow and the subsequent build-up of scar tissue in the liver known as liver fibrosis [2].

Liver fibrosis in its initial and moderate stages causes no clinical symptoms by itself and can often be missed by routine blood tests or by medical imaging examinations. Fibrosis can be treated and reversed on early detection; however, if this condition is left untreated for a long time, it may lead to a severe condition called cirrhosis. Once cirrhosis has developed, clinical symptoms and their associated problems may begin to appear, and eventually liver damage becomes permanent and irreversible [3]. Therefore, early detection of liver fibrosis plays an important role in treatment and disease management.

Traditionally, liver fibrosis is diagnosed and staged by percutaneous liver biopsy, an invasive technique. Lately, non-invasive methodologies such as blood serum tests and medical imaging techniques have emerged as an alternative to biopsy. However, serum tests such as APRI, FIB-4, and other commercial assays have proven less accurate than the imaging modalities [4] such as ultrasound (US) elastography and magnetic resonance elastography (MRE) for staging fibrosis. Several studies comparing MR- and US-based elastography techniques concluded that the MRE has been shown to exceed all other diagnostic methods in terms of accuracy, sensitivity, specificity, and organ coverage [5].

Magnetic Resonance Elastography

MRE is a non-invasive technique to estimate the stiffness of soft tissues. Given the non-invasive nature and accuracy of diagnostic results, in recent years MRE has become a standard clinical tool to stage liver fibrosis on both 1.5T and 3T scanners [6]. MRE can be acquired with or without contrast agent on board [8], meaning it can be performed at any point in a standard clinical examination, depending on site preference.

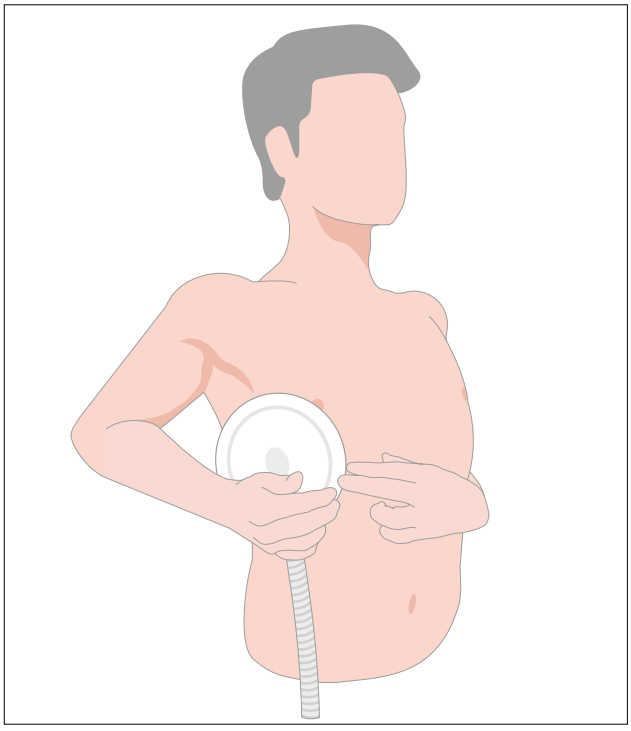

1 Illustration of the passive driver placement for liver MRE imaging. The entire flat surface of the drive should be in contact with the subject's upper abdomen at the fifth intercostal space and lateral to the mid-clavicular line.

The liver MRE technique can be separated into four elements as described below.

1. Inducing shear wave motion into the liver using an external mechanical driver
2. Acquiring wave images of the liver via motion encoding and phase-contrast imaging
3. Reconstructing stiffness maps from the wave images using an inversion algorithm
4. Reporting average stiffness values in ROIs identified in the liver stiffness maps as having good wave quality and no artifacts

Liver MRE has been described in a QIBA profile [10], which also gives practical guidance for performing MRE and interpreting the results. Conformance to this profile supports the claim that a change in measured hepatic stiffness of at least 19% is considered to be real with 95% confidence.

This article reviews the essentials of MRE and provides best practice for its routine clinical usage. To clinicians, the MRE technique offers the special benefit that all major MR manufacturers adopted the same standard solution, hardware and inversion algorithm, and high reproducibility has been demonstrated [6]. This uniformity makes the interpretation of diagnostic results much easier, especially in centers where multiple platforms are used. However, some image acquisition sequences and workflow options may differ, so in the following, the focus will be on the Siemens Healthineers platform.

The most commonly used and commercially available solution (Resoundant Inc, Rochester, MN, USA) induces continuous single frequency mechanical shear wave motion in the liver using a special hardware complement to the MR system that consists of an active driver (frequency generator) and a passive driver (plastic drum), and a standardized inversion algorithm implementation [17].

Insert 1: Best practice workflow

Pay attention to the following workflow elements to improve chances of performing a high quality MRE exam.

1. Inspect the hardware regularly for any damage to the passive driver diaphragm, or air leakage in the tubing system.

2. Turn the active driver (off and) on prior to each examination to wake it up from standby mode.

3. Place the elastic belt on the MR patient table at liver level and position the patient in a supine position with head-first. Position and secure the passive driver as explained in the section *Driver setup for liver MRE*. Lateral placement is preferred over anterior placement but good contact between the driver face and the subject's abdomen is critical.

4. Direct the end of the passive driver tubing towards where it will connect to the tubing from the active driver. In some cases this may be at the back of the bore.

5. Fasten the belt tightly. Ask the subject if they can breathe normally with the belt; if not, adjust the belt. Inform them about expected examination duration, order of sequences, that the Elastography is performed at end-expiration, and that they will feel vibrations coming from the driver during the activation. Repeat the latter to the patient just before the MRE sequence to avoid them being startled.

6. Verify passive driver positioning in scout images in relation to the liver at end-expiration and other landmarks. Adjust the driver as necessary.

7. Run the MR Elastography sequence and acquire the images at end-expiration.

8. Load the results into the Viewing Task Card and review image quality as described in the section *Postprocessing and evaluation* (magnitude for breathing artifacts, wave images for good propagation along with depth penetration, and confidence mask for successful inversion). In case of insufficient quality, check driver positioning and repeat, using a modified protocol where appropriate, e.g., in case of iron overload.

9. Measure stiffness via ROI evaluation as described in the section *Postprocessing and evaluation*.

Driver setup for liver MRE

Positioning of the passive driver on the subject (Figure 1) is one of the most critical steps in an MRE examination. Optimal driver positioning ensures that the externally generated mechanical waves are transferred to the subject efficiently and thereby penetrate deep into the liver. This helps achieve the desired anatomical coverage and obtain stiffness measurements with high quality.

To enable the performance of reliable human liver MRE, the passive driver is placed on the upper abdomen centered at the fifth intercostal space but lateral to the midclavicular line as shown in Figure 1. While positioning the passive driver it is necessary to make sure that the driver's flat surface area is fully in contact with the body close to the liver.

To maintain the passive driver in one fixed position throughout the imaging session, it is necessary to immobilize it with a dedicated elastic belt firmly while ensuring the subjects' comfort to breathe normally. To improve contact between the subject and the passive driver it is advisable to use extra cushioning material such as a sponge or clothing materials (as shown in Figure 2) in between the passive driver and the belt to tightly hold the driver against the body. This enables mechanical waves to be delivered to the region of interest uniformly throughout the imaging session. Finally, it is important to ensure that the passive driver is connected tightly to the active driver via plastic tubing so that there is no air leakage. It may be advantageous to connect the remaining tubing only after the subject has been moved into the scanner.

After placing the driver, it is important to verify that the driver is positioned correctly, i.e., centered in H-F direction with respect to the liver. If collected at end expiration localizer images of sagittal and axial views like those in Figure 3 will show the placement of the driver. The indentation on the sagittal view indicates that the driver is placed at the center with respect to the liver. Similarly, the axial view will show the indentation anterior to the liver. If the position of the driver is not correct, then the driver must be adjusted with respect to these landmarks.

Sequence optimization and image acquisition

The Siemens Healthineers MRE product consists of two sequence options, a GRE based sequence with an optional rapid acquisition mode (see Figure 4) and a sequence based on single-shot spin-echo echo planar imaging (SE-EPI). Both sequences acquire 2D axial slices in the center of the liver at end-expiration with through-slice motion encoding and include a fractional encoding option to shorten TE (Figure 4). The SE-EPI MRE acquisition is more efficient and should be the default acquisition where possible. The primary benefit of SE-EPI is that multiple slices are acquired in a single 11–13 seconds breath-hold and the SE-EPI component makes the sequence more robust to susceptibility that occurs with liver iron loading or with higher field strengths. Fat saturation is very important for SE-EPI; SPAIR-strong is the preferred fat suppression setting for this sequence. GRE MRE requires multiple breath-holds (one per slice), however, in some situations such as where implants exist and lower radio frequency flip angles are necessary, or if referencing previous GRE MRE studies, it can be the sequence of choice. Standard imaging parameters for the two sequences are shown in Table 1 and the standard Siemens Healthineers protocol tree for

2 Demonstration of MRE setup and driver placement for liver imaging, using the dedicated elastic belt, plus cushioning material (arrow).
Watch the videos on https://www.magnetomworld.siemens-healthineers.com/clinical-corner/protocols/body-pelvis/mr-elastography

MR Elastography is shown in Figure 5. As previously mentioned, an MRE protocol can be added either at the beginning (pre-contrast) or the end (post-contrast) of a measurement program.

The mechanical excitation frequency is fixed at 60 Hz, and the amplitude of the active driver is typically set to 40%, which will work well, irrespective of body habitus, in 85% of the patients. If the current driver amplitude should lead to either too much or too little motion encoding, some control over the motion encoding strength is possible using the Gradient mode UI parameter, since the amplitude of the motion encoding gradient (MEG) will scale with it: It is lower for Normal and higher for Fast Gradient mode.

The active driver is activated ("triggered") via the sequence, and automatic breath-hold commands can be used. Make sure that both MRE and the localizer are acquired in end-expiration.

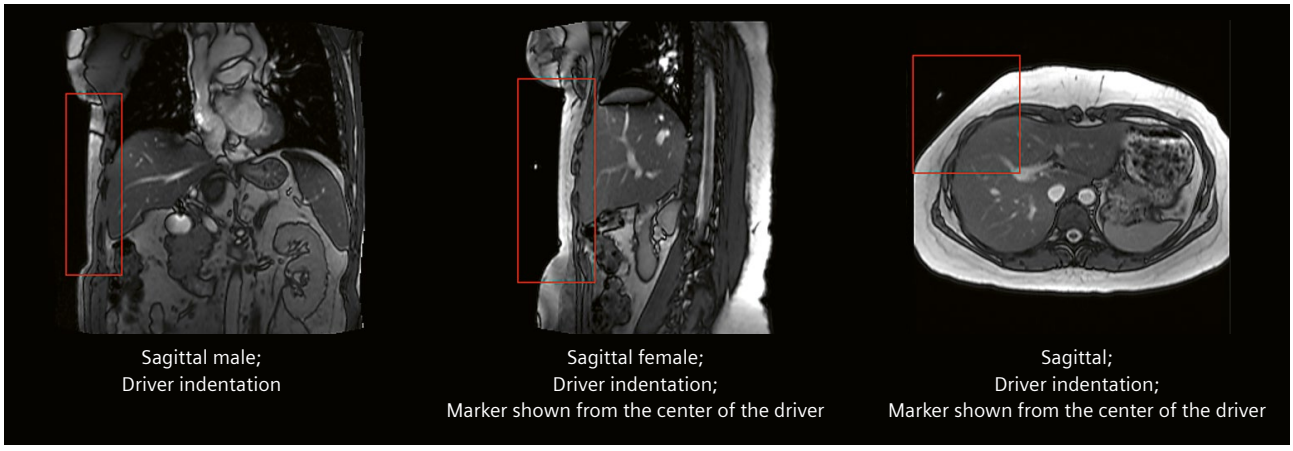

3 Localizers illustrating the driver placement for an optimized MRE liver examination. Positioning the driver center to the liver facilitates uniform propation of waves in the region of interest. (An MR visible fiducial has been added to the passive driver in this case showing the center of the passive driver in these images.)

4 Example parameter card for a GRE MRE protocol in Rapid mode (TR 25 instead of 50 ms, petrol highlight). Shortening the TE below the gap in the range bar (orange highlight) would activate fractional motion encoding (which may boost signal at the expense of sensitivity, but this is only recommended for cases with short T2*).

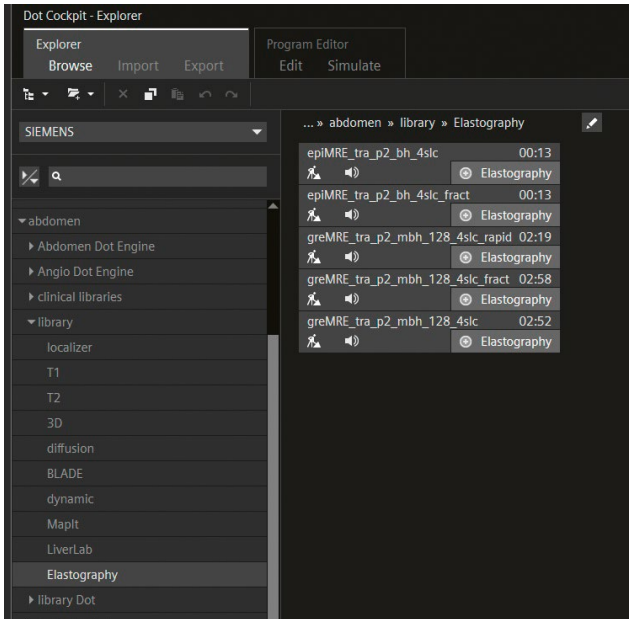

5 The Siemens Healthineers protocol tree for Elastography representing all MRE options: epiMRE with and without fractional encoding, and greMRE in its standard, rapid and fractional encoding configuration.

Parameter	SE-EPI MRE	GRE MRE
FOV	420 mm (x 100%)	420 mm x 70–100%
TR	1000–1200 ms	25[a] or 50 ms
TE	47 ms or lower[b]	21 ms or lower[b]
Slice thickness	8 mm, 25% gap	10 mm, no gap
Acquisition matrix	100 x 100%	128 x 80%
Bandwidth	2170 Hz/pixel	399 Hz/pixel
Gradient Mode	Normal, Fast[c]	Normal, Fast[c]
GRAPPA factor	2	2
GRAPPA reference lines	24 GRE/separate	12 integrated
Fat saturation	SPAIR – strong	none
Other key settings	Prescan Normalize, Adaptive Coil Combination	

Table 1: Typical sequence parameters for MRE.
[a] Selecting a TE of 25 ms will put the GRE MRE sequence into "Rapid" mode [14] (see Figure 4).
[b] Selecting TE lower than the gap in the sequence UI (see Figure 4) will cause the motion encoding gradients to be shortened to 65% of full ("fractional" encoding [15]); this is beneficial for short T2 / T2*, but will also reduce motion encoding, so it is only recommended for problem-solving.
[c] The gradient mode will influence the motion encoding via the MEG amplitude; start with Normal, and if there is not enough motion encoding, go to Fast.
Protocols (.exar1 files) are available for download at https://www.magnetomworld.siemens-healthineers.com/clinical-corner/protocols/body-pelvis/mr-elastography

Insert 2: Trouble shooting

No waves or inadequate waves in the liver (Figure 6)

1. Check tubing for disconnection and pneumatic pressure leakage. Make sure that the passive driver diaphragm (flat surface) is not damaged.
2. Make sure the passive driver has a good contact with the subject's body and is positioned correctly as shown in Figure 2.
3. Make sure the active driver is turned on and not in standby mode.

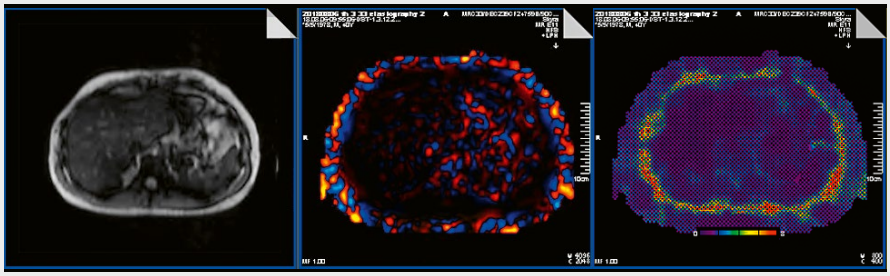

6 Example of a scan without mechanical vibration. The reason could be a disconnected pressure hose, or an active driver in standby mode.

No planar waves (Figure 7, Figure 8)

1. Adjust the driver position lateral to the center of Xiphoid as shown in Figure 1.
2. Check the localizer images as shown in Figure 3 to ensure the driver position is correct. If not adjust the driver position accordingly.
3. Additional care must be taken in imaging women and obese subjects in placing the driver laterally by moving the breast to have adequate planar waves in the liver.

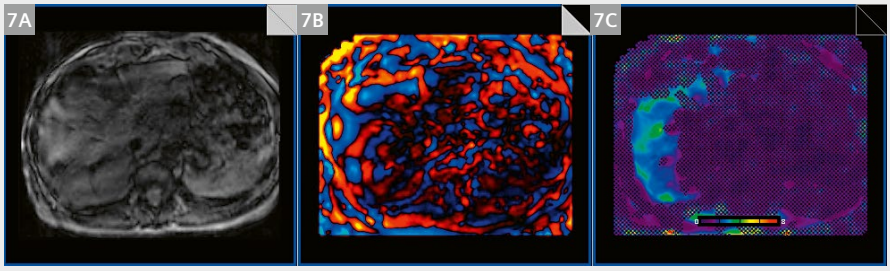

7 Volunteer example at 1.5T with bad placement of the passive driver. **(7A)** Magnitude, **(7B)** wave image with incoherent wave pattern, **(7C)** elastogram with 95% confidence markings.

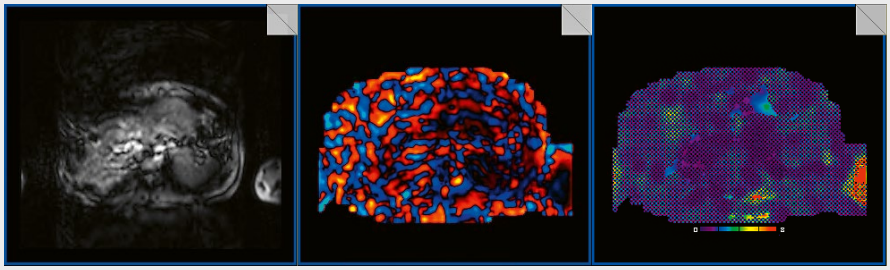

8 Example of a scan with erroneous driver triggering (Rapid GRE). The reason could be a wrongly set mechanical frequency on the active driver, or a wrongly configured trigger output (optical-to-electrical converter).

Signal loss through transverse relaxation (Figure 9)

The motion encoding gradient between excitation and acquisition in the sequence timing causes echo times to be comparatively long, e.g., ~20 ms for gradient-echo sequences and ~50 ms for SE-EPI sequences. Long echo times in turn make the sequences prone to signal loss if the transverse relaxation times (T2 or T2*) are short, which can be the case at 3T or with hepatic iron overload. Image acquisition parameters should be adjusted for these scenarios. The GRE based MR elastography technique does not perform well on iron overload liver; however, the SE-EPI based technique can be deployed with customized parameter settings [11] to obtain diagnostic quality images.

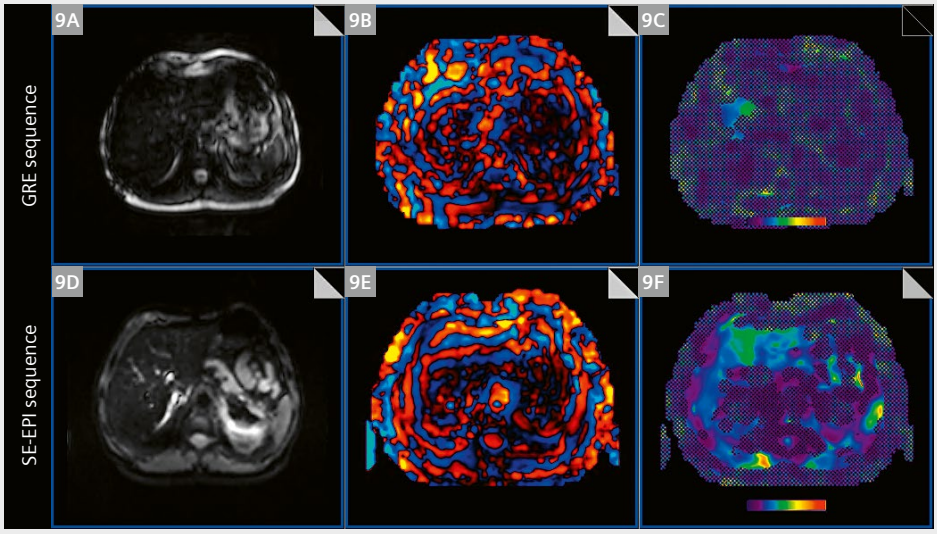

9 Volunteer example at 3T with R2* ~ 90 s-1, corresponding to a liver iron content of ~1.5 mg/g dry weight. **Top row**: GRE sequence, **bottom row**: SE-EPI sequence. **(9A, D)** magnitude, **(9B, E)** wave image, **(9C, F)** elastogram with 95% confidence markings.

Postprocessing and evaluation

The phase difference images are processed for the standard MRE option using an inline implementation of Resoundant's MMDI inversion algorithm to generate the stiffness maps called elastograms. Stiffness is calculated as the magnitude of the complex shear modulus [18]. The output further contains the original magnitude and phase difference images, and additional computed output: confidence map, stiffness map with confidence markings, and finally colored interpolated wave images. The confidence map is based on the wave quality, i.e., which includes wave signal-to-noise-ratio (SNR) wave amplitude and shape. Then, the stiffness map uses a 95% threshold of the confidence map (shown as unhatched area) to determine the regions to trust within the liver parenchyma and report the stiffness values. Figure 10 shows an example of output series obtained in one healthy volunteer.

The image quality of the data should be analyzed further to determine if any motion artifacts exist which are typically a result of improper breath-hold. The artifacts appear in the magnitude image as blurring or ghosting in the phase encoding direction. Additionally, the wave images (colored images of the output from the scanner) are also qualitatively analyzed to determine discernible waves propagating in the liver as connected wave fronts as shown in Figure 10.

The stiffness map is generated using a color scale from 0–8 kPa; a grayscale reading of 100 corresponds to 1 kPa. Note that all colorized maps are natively grayscale images displayed using a color lookup table; hence, they can be windowed, and ROI measurements can be made directly from them[1].

For repeatable measurements, a large region of interest is drawn in the liver parenchyma excluding the hatched region, avoiding the large vessels and at least 1 cm in from the edge of the liver. Note that the cross-hatched regions contain pixels of value zero, so they must not be included in ROI measurements. If in doubt, propagate ROIs to the stiffness map without cross-hatching. Make sure that the wave images show planar wave propagation in the selected region and avoid areas close to the liver edge and the left lobe. Divide ROI mean values by 100 to report the mean stiffness value in kPa. Hot spots in the stiffness maps that occur under the MRE driver or at the liver periphery are typically due to over driving or wave reflections respectively and should be avoided when drawing the ROIs. However, it is acceptable to include small artificial hot spots in the center region of the parenchyma as these may not change the mean stiffness value significantly. In Figure 10, it can be observed that planar waves penetrate throughout the liver and the stiffness map shows sufficient coverage of the liver to report the mean stiffness. Table 2 shows typical stiffness values used to stage liver fibrosis [19]; a meta-analysis [20] reported slightly different values. We advise the user to consult the scientific literature for latest studies which best match their clinical environment.

Stiffness values are generally independent of field strength. However, increased sensitivity to susceptibility effects such as iron overload cause signal loss in the liver parenchyma to be more prevalent at higher field strengths.

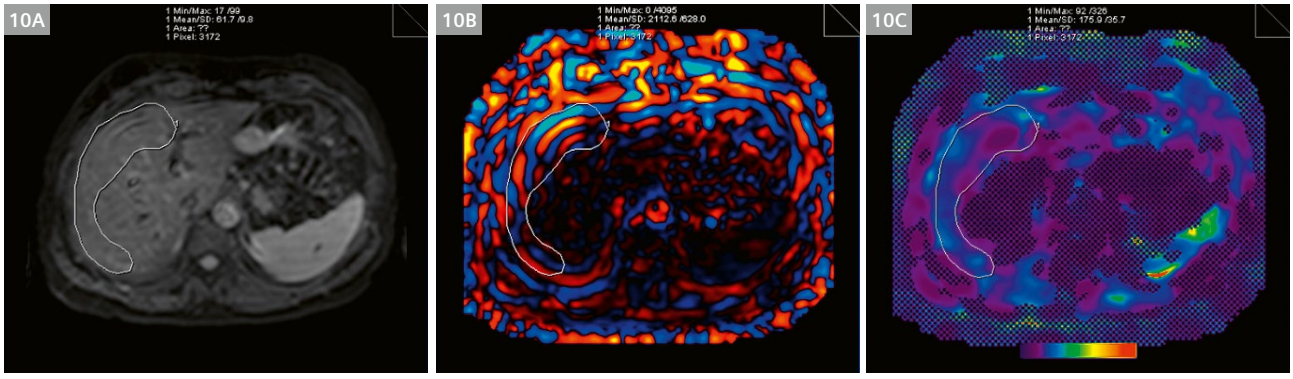

10 Scan results (SE-EPI) from a healthy volunteer. **(10A)** Magnitude, **(10B)** wave image, **(10C)** stiffness map with 95% confidence mask overlay; note the color bar indicating the color map distribution across the 0–8 kPa range. Planar wave propagation can be inferred from the uninterrupted wave pattern in the ROI. The manual free-hand ROI contours select regions of high wave quality while observing anatomical placement and the confidence mask.

[1]*Some PACS systems may not be able to retain these properties. Depending on syngo MR software version, there may be transfer/export settings to manage this.*

F0	F1	F2	F3	F4
3.00 ± 1.12 kPa	3.11 ± 0.82 kPa	3.87 ± 1.85 kPa	4.78 ± 1.89 kPa	6.52 ± 2.34 kPa

Table 2: Mean ± standard deviation values of MRE-derived liver stiffness for different fibrosis stages from 289 patients according to [19].

Insert 3: Setup and configuration

The hardware part of the MRE option is set up by a service engineer. Settings of the active driver can typically be configured once and remain unchanged thereafter. Details can be found in the operator manual [16]; some of them are given here for reference.

Figure 11 is a screenshot of the active driver's configuration page which can be accessed via a web browser and Ethernet connection, which may be a special research configuration[2]. The number of cycles per trigger is set to 3 for both GRE and SE-EPI MRE sequences as they are each designed to trigger the active driver every 50 ms. In pediatric patients[3] or in the 15% of adult patients with very large or very small body habitus, it can be beneficial to change the driver amplitude.

Note: If you have an older driver with earlier firmware (< version 2.0 as shown in the lower right-hand corner of the configuration screen), the driver frequency will need to be set to 60.1 Hz in order to sync correctly with the incoming triggers from the sequence. Additionally, the driver has a sleep timer configured in the lower part of the right-hand column on the configuration page. After the preset amount of time, the amplifier will go to sleep and no longer respond to triggers. To wake up the unit either depress the Trigger button on the configuration page or manually cycle the power on the unit. Without this sleep timer, damage to the driver can occur, greatly limiting its lifespan.

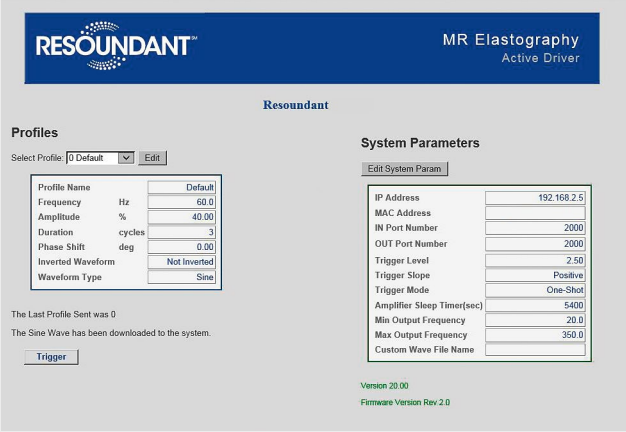

11 Screenshot showing the MRE active driver setting card (Resoundant Inc, Rochester, MN, USA) containing all necessary parameters for either MRE sequence at the proper frequency and amplitude.

[2]Please work with your MR Collaborations scientist and your service engineer if this special configuration is necessary at your site.
[3]MR scanning has not been established as safe for imaging fetuses and infants less than two years of age. The responsible physician must evaluate the benefits of the MR examination compared to those of other imaging procedures.

Summary and take away points

It was the intent of this article to give Siemens Healthineers MRE users, both new and experienced, guidance on how to consistently perform MRE with high-quality results. The content is weighted heavily on achieving a good patient setup with proper passive driver positioning. We have found that driver positioning can be highly variable in practice and is a major contributor to non-diagnostic MRE exams. Using the described workflow, however, it was shown that achieving measurable areas from 65% to 85% of liver coverage, our definition of a successful exam, is possible. Further, reproducibility of the results not only depends on patient setup and scanning workflow, but also on standardized image interpretation, quality checks, and ROI measurements. Therefore, the guidance provided includes these topics as well.

Once the MRE option is set up and configured correctly (see Insert 3), and the workflow for scanning, reading, and reporting is established, the procedure should be kept

unchanged to achieve low variability between examinations. In Insert 1 we summarize a best-practice workflow that includes some elements that may not be commonly considered. With its additional hardware and patient setup, the MRE acquisition has some inherent complexities not present in other MR imaging applications. Optimal wave propagation can depend on multiple factors ranging from hardware functionality to setup to exiting patient pathology. To address some of the more common scenarios we have provided a troubleshooting guide as Insert 2.

Finally, it should be noted that the current standard MRE solution is tailored to breath-hold liver applications by only acquiring a low number of slices and only encoding a single (through-slice) motion direction. This implicitly makes simplifying assumptions of in-plane, planar wave propagation without reflections. This also makes localized stiffness readings, e.g., by liver segment, less reliable. Thus, this "2D" standard solution cannot easily be transferred to other organs in the abdomen, or to other body regions. There exist prototypes with contiguous coverage of larger regions and "3D" motion encoding in all three spatial directions [12], as well as dedicated applications in other body regions [13].

References

1 Michalopoulos GK, DeFrances MC. Liver regeneration. Science. 1997;276(5309):60-6.
2 Bataller R, Brenner DA. Liver fibrosis. J Clin Invest. 2005;115(2):209-18. Erratum in: J Clin Invest. 2005;115(4):1100.
3 Sharma S, Khalili K, Nguyen GC. Non-invasive diagnosis of advanced fibrosis and cirrhosis. World J Gastroenterol. 2014;20(45):16820-30.
4 Wang XP, Wang Y, Ma H, Wang H, Yang DW, et al. Assessment of liver fibrosis with liver and spleen magnetic resonance elastography, serum markers in chronic liver disease. Quant Imaging Med Surg. 2020;10(6):1208-1222.
5 Tana MM, Muir AJ. Diagnosing Liver Fibrosis and Cirrhosis: Serum, Imaging, or Tissue? Clin Gastroenterol Hepatol. 2018;16(1):16-18.
6 Trout AT, Serai S, Mahley AD, Wang H, Zhang Y, Zhang B, Dillman JR. Liver Stiffness Measurements with MR Elastography: Agreement and Repeatability across Imaging Systems, Field Strengths, and Pulse Sequences. Radiology. 2016;281(3):793-804.
7 Venkatesh SK, Wang G, Lim SG, Wee A. Magnetic resonance elastography for the detection and staging of liver fibrosis in chronic hepatitis B. Eur Radiol.2014;24(1):70-8.
8 Hallinan JT, Alsaif HS, Wee A, Venkatesh SK. Magnetic resonance elastography of liver: influence of intravenous gadolinium administration on measured liver stiffness. Abdom Imaging. 2015;40(4):783-8.
9 Bolster Jr B, Jin N, Kannengiesser S, MR Elastography – Pearls and Pitfalls. MAGNETOM Flash (71) 2/2018:19-23.
10 QIBA Profile, Magnetic resonance elastography of the liver. Stage 2: consensus profile. Radiological Society of North America https://qibawiki.rsna.org/images/a/a5/MRE-QIBAProfile-2018-05-02 CONSENSUS.pdf (2018).
11 Barrera CA, Otero HJ, Hartung HD, Biko DM, Serai SD. Protocol optimization for cardiac and liver iron content assessment using MRI: What sequence should I use?, Clin Imaging, Volume 56, 2019, Pages 52-57. 2019;56:52-57.
12 Shi Y, Glaser KJ, Venkatesh SK, Ben-Abraham EI, Ehman RL. Feasibility of using 3D MR elastography to determine pancreatic stiffness in healthy volunteers. J Magn Reson Imaging. 2015;41(2):369-75.
13 Dong H, White RD, Kolipaka A. Advances and Future Direction of Magnetic Resonance Elastography. Top Magn Reson Imaging. 2018;27(5):363-384.
14 Chamarthi SK, Raterman B, Mazumder R, Michaels A, Oza VM, Hanje J, Bolster B, Jin N, White RD, Kolipaka A. Rapid acquisition technique for MR elastography of the liver. Magn Reson Imaging. 2014;32(6):679-83.
15 Rump J, Klatt D, Braun J, Warmuth C, Sack I. Fractional encoding of harmonic motions in MR elastography. Magn Reson Med. 2007;57(2):388-95.
16 Siemens Healthineers MR. Operator manual MR Elastography.
17 Resoundant Inc. Technical report. Available from https://www.resoundant.com/technical-report. [Accessed Feb 23, 2022].
18 Manduca A, Bayly PJ, Ehman RL, Kolipaka A, Royston TJ, Sack I, Sinkus R, Van Beers BE. MR elastography: Principles, guidelines, and terminology. Magn Reson Med. 2021;85(5):2377-2390.
19 Yin M, Glaser KJ, Talwalkar JA, Chen J, Manduca A, Ehman RL. Hepatic MR Elastography: Clinical Performance in a Series of 1377 Consecutive Examinations. Radiology. 2016;278(1):114-24.
20 Singh S, Venkatesh SK, Wang Z, Miller FH, Ehman RL, et al. Diagnostic performance of magnetic resonance elastography in staging liver fibrosis: a systematic review and meta-analysis of individual participant data. Clin Gastroenterol Hepatol. 2015;13(3):440-451.

Contact

Arunark Kolipaka, Ph.D., FAHA, FSCMR
Associate Professor & Technical Director,
Magnetic Resonance Imaging
The Ohio State University
Wexner Medical Center
Department of Radiology
395 West 12th Ave, 4th Floor
Columbus, OH 43210
USA
Phone: +1 614-366-0268
arunark.kolipaka@osumc.edu

Enhanced Myocardial PET-MR Imaging with MR-guided Motion-corrected PET Image Reconstruction

Camila Munoz[1], Sam Ellis[1], Stephan G. Nekolla[2], Karl P. Kunze[1,3], Radhouene Neji[1,3], Rene M. Botnar[1,4], Andrew J. Reader[1], Claudia Prieto[1,4]

[1]School of Biomedical Engineering and Imaging Sciences, King's College London, London, UK
[2]Nuklearmedizinische Klinik und Poliklinik, Technische Universität München, Munich, Germany
[3]MR Research Collaborations, Siemens Healthcare, Frimley, UK
[4]Escuela de Ingeniería, Pontificia Universidad Católica de Chile, Santiago, Chile

Abstract

Simultaneous PET-MR has shown promise for addressing several of the technical challenges that may degrade image quality in cardiac PET imaging, such as high noise levels, attenuation artifacts, and respiratory and cardiac-induced motion artifacts. While state-of-the-art PET image reconstruction techniques have addressed these issues separately, their combined effect has not been widely explored in cardiac PET-MR imaging. We have recently introduced a single cardiac PET-MR image reconstruction framework[1] which fully utilizes MR-derived information to allow both MR-based motion compensation and MR-based anatomical guidance within the reconstruction pipeline for improved simultaneous diagnostic cardiac PET-MR imaging.

We performed an initial validation of the proposed framework on fifteen cardiac ^{18}F-FDG PET-MR datasets and evaluated the resulting images by measuring myocardial contrast and noise, comparing our images to conventional PET image reconstruction methods. Results show that our framework results in sharper cardiac PET images, with increased contrast and reduced noise. In particular, myocardium-to-blood pool contrast increased by 143% on average ($p < 0.0001$) compared to conventional uncorrected non-guided PET images. Furthermore, anatomical guidance significantly reduced image noise compared to non-guided PET image reconstruction by 16.1% ($p < 0.0001$). These improvements have the potential to improve clinical interpretability and diagnosis based on cardiac PET-MR images.

Introduction

Cardiac imaging has been a key clinical application for both magnetic resonance (MR) and positron emission tomography (PET) imaging. Both imaging modalities can provide information about various aspects of cardiac disease, and therefore, the introduction of simultaneous PET-MR scanners was very promising for the comprehensive assessment of cardiovascular health from a single examination. Indeed, several studies focusing on the assessment of myocardial viability and inflammatory and infiltrative diseases, such as myocarditis and sarcoidosis, have demonstrated the benefit of the complementary functional and anatomical information provided by both imaging modalities in terms of improved prediction of patient outcomes and increased sensitivity for disease detection and treatment monitoring compared to each modality alone [1–3].

Simultaneous PET-MR imaging has also enabled the development of novel approaches to address several of the technical challenges that affect PET image quality. In order to produce clinically interpretable and quantitative cardiac PET images, an accurate attenuation correction is fundamental. In clinical practice, attenuation maps (μ-maps) are acquired under breath-hold before the actual PET acquisition, and although patients are instructed to hold their breath at the end-expiration position, lack of patient compliance or incomplete breath holds can result in μ-map errors and/or potential misalignment between the μ-map and the PET image position. This may lead to image artifacts that appear as reduced myocardial uptake and could be mistaken for myocardial defects [4]. Since the introduction of hybrid PET-MR systems, several specialized MR acquisition schemes have been proposed to enable free-breathing [5] or respiratory-resolved μ-maps [6], improving the correspondence between attenuation and emission data and reducing motion-induced artifacts.

Another important source of image degradation is respiratory and cardiac motion throughout PET data acqui-

[1]*Work in progress. The application is currently under development and is not for sale in the U.S. and in other countries. Its future availability cannot be ensured.*

sition, which may induce blurring and affect the detection and delineation of small lesions. Several approaches for MR-based PET motion compensation have been proposed in the literature, where dynamic MR images acquired with sufficient temporal resolution and tissue contrast are used to estimate the organ displacement due to physiological motion [7–9]. These techniques have shown promising results for improved PET image quality and improved correspondence between both imaging modalities, but a limitation of most of them is that the MR images simultaneously acquired with PET data are designed for motion estimation purposes only. The insufficient spatial resolution or appropriate tissue contrast of these MR images limits their use for diagnostic purposes, and hinders the full realization of the potential of truly simultaneous cardiac PET-MR.

Finally, the counts-limited nature of PET image acquisition causes noise in the reconstructed images. Conventional PET image reconstruction methods, such as maximum likelihood expectation maximization (MLEM) [10], are usually terminated at early iterations to prevent the onset of noise, resulting in bias due to underconvergence and therefore reducing the quantitative value of the reconstructed PET images. In the context of PET-MR imaging, anatomical information provided by the simultaneously acquired MR images can be used to guide the PET image reconstruction, enabling noise reduction and partial volume correction [11, 12]. These approaches have shown significant improvements in brain PET-MR imaging, however, their use in cardiac PET-MR applications has not been widely explored. This is because in order to enable accurate

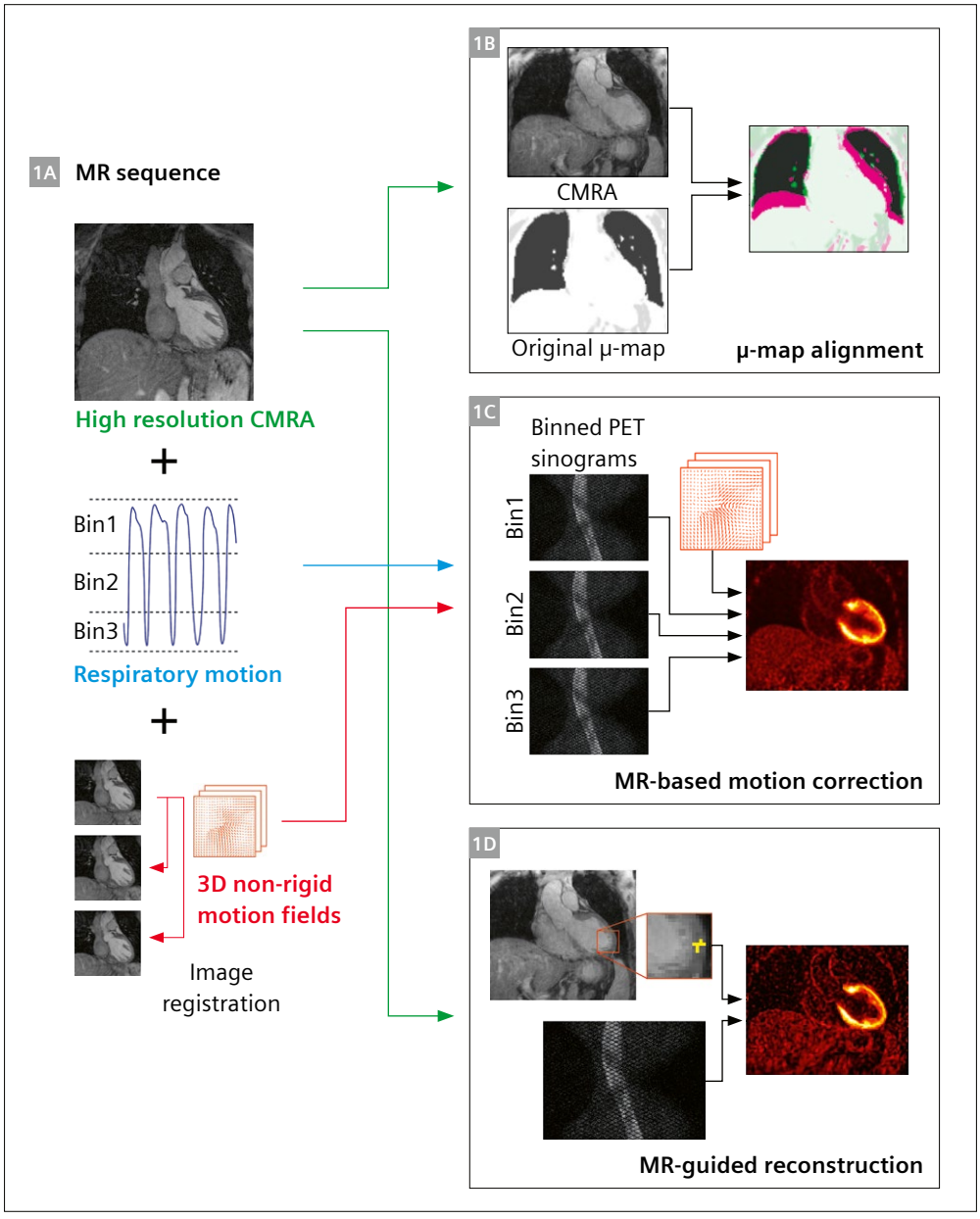

1 Overview of MR-based improvements for the proposed MR-guided motion compensated PET image reconstruction framework. **(1A)** The MR sequence provides a high-quality end-expiration coronary MR angiography (CMRA) image, and respiratory motion information, which can be used to improve the PET image reconstruction by **(1B)** aligning PET μ-maps to the free breathing end-expiration CMRA position, **(1C)** performing MR-based motion-correction, and **(1D)** performing MR-guided PET image reconstruction.

anatomical guidance from cardiac MR images, three-dimensional images with sufficient volumetric coverage and high tissue contrast that also provide information about physiological motion (so that they can be motion-aligned to the PET image position) are required. The acquisition of such images is challenging, as most clinically available cardiac MR protocols are based on acquiring stacks of 2D slices under repeated breath-holds.

We have recently proposed a novel framework[1] that exploits the advantages of hybrid cardiac PET-MR imaging to improve myocardial PET imaging, by integrating several elements of state-of-the-art PET image reconstruction [13]. For this, we previously developed a cardiac PET-MR imaging sequence for simultaneous diagnostic PET and coronary MR angiography (CMRA) [14]. This sequence provides both respiratory motion information and a whole-heart high-resolution CMRA image that allows for myocardial PET image reconstruction to be improved as follows:

(1) μ-maps are aligned to the end-expiration respiratory position using the CMRA images as reference, reducing attenuation-induced artifacts;
(2) MR-derived motion information is incorporated into a motion-corrected image reconstruction of PET data; reducing motion-induced blurring and
(3) high-contrast motion-corrected 3D CMRA images are used for anatomically guided PET image reconstruction, suppressing noise while preserving quantification performance (Fig. 1).

Here we present a brief summary of our technique, including some results from our initial clinical experience in patients with and without known cardiovascular disease, which demonstrate the benefits of the proposed MR-guided motion-corrected reconstruction framework for improved cardiac PET-MR imaging.

Methods

The integrated PET image reconstruction framework uses our cardiac PET-MR sequence introduced in [14] to produce high-quality whole-heart MR information. Following the aforementioned approach, a respiratory signal and a set of 3D MR images in various respiratory states are produced as an intermediate output in the MR reconstruction process. The respiratory signal can be used for binning the PET data into corresponding respiratory bins, and then a motion-compensated PET image reconstruction [15] can be performed using motion fields estimated from the set of 3D MR images, in a similar manner as for the MR image reconstruction. In order to minimize the effect of cardiac-induced motion, ~30% of the PET data corresponding to systole are discarded using the electrocardiogram signal as a reference. To improve the correspondence between the μ-map and the PET image position, the conventional breath-held μ-map is registered to the end-expiration CMRA image before PET image reconstruction. By using this method, the PET image reconstruction produces an end-expiration diastolic cardiac PET image.

In order to reduce noise, the high-resolution CMRA image is then used to perform a patient-specific anatomically-guided PET image reconstruction. Anatomical guidance groups voxels which are expected to have a similar PET intensity, for example due to being in close proximity and composed of the same tissue type and applies anisotropic smoothing between these voxels. In this work, we used a weighted quadratic penalty [16], wherein the *a priori* similarity between a PET voxel and each of its neighboring voxels is calculated from the CMRA image using a patch-based Gaussian similarity function. These similarity weights are incorporated into the PET image reconstructions using a modified maximum *a posteriori* expectation maximization (MAPEM) algorithm [17], with an automatically selected regularization strength [18]. Further technical details can be found in [13].

Study design

For our first validation study, two cohorts of patients were included. The first cohort included five oncology patients without known or suspected cardiovascular disease, who exhibited physiological myocardial uptake of ^{18}F-FDG. In absence of cardiac conditions, ^{18}F-FDG uptake is expected to be uniform throughout the myocardium. The second cohort included ten patients with symptomatic coronary artery disease, chronic total occlusion (CTO) of a relevant coronary artery and evidence of wall motion abnormalities. These patients underwent a clinical PET-MR examination protocol for the assessment of myocardial viability, which included conventional 2D late gadolinium enhanced (LGE) MR.

All fifteen acquisitions (patient average age 62.8 ± 12.5 years old, 11 male, 4 female) were performed in Biograph mMR systems (Siemens Healthcare, Erlangen, Germany). All subjects signed a written informed consent and the study was performed in concordance with the Declaration of Helsinki and approved by the corresponding Institutional Ethics Committee. Relevant imaging parameters for the CMRA acquisition include coronal orientation, resolution = 1 × 1 × 2 mm^3, field of view = 304 × 304 × 88-112 mm^3 covering the whole heart, with data acquired during the mid-diastolic quiescent period of the cardiac cycle. The average acquisition time for the CMRA sequence was 11.1 ± 2.2 minutes.

The proposed PET image reconstruction framework was implemented in MATLAB (Mathworks, Natick, MA, USA) using custom developed software [19]. Relevant PET reconstruction parameters include resolution modelling (4.3 mm full-width half maximum (FWHM)), voxel

size = 2.03 × 2.08 × 2.08 mm^3, and matrix size = 127 × 344 × 344. Note that all list-mode PET data were truncated to the scan duration of the CMRA sequence, to allow the use of the MR respiratory trace for PET data binning.

In order to assess the effect of the MR-guidance and MR-based motion correction separately we performed some comparative reconstructions. First, clinically representative reconstructions of the PET datasets were performed using MLEM [10]. These reconstructions did not include respiratory motion correction (no motion-correction, NMC), used the original breath-held μ-map and were run for clinically representative 63 iterations. We then run a reconstruction focusing on the motion-correction (MC) components of our proposed framework. For this, we included μ-map alignment, respiratory motion-correction and cardiac-gating (with data acquired during systole being rejected as described above). These reconstructions were run to convergence, i.e. 200 iterations.

Finally, a reconstruction with the complete proposed method was performed, incorporating aligned μ-maps, respiratory motion correction, cardiac-gating, and anatomi-

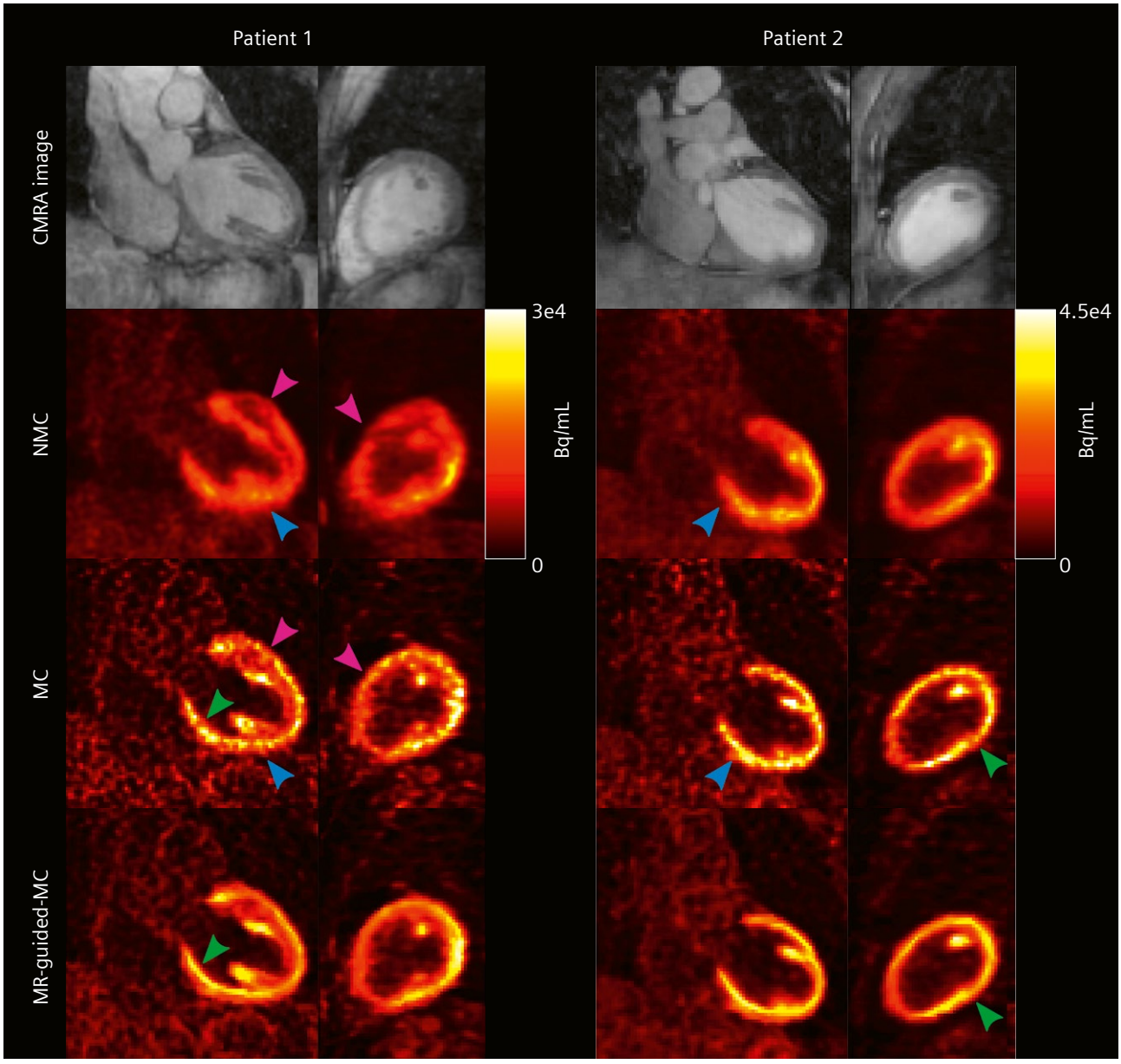

2 Comparative reconstruction methods for two patients from the first cohort (not known cardiac disease) alongside corresponding CMRA images. Aligning the scanner-provided u-map to the CMRA image removes a defect mimicking artifact in Patient 1 (magenta arrows), while applying motion compensation improves contrast and sharpness in the inferior myocardium (blue arrows). Combining motion compensation with MR-guided PET image reconstruction results in reduced noise and improved sharpness (green arrows).

cal guidance with automatic regularisation strength selection (MR-guided-MC).

All images were analysed in terms of noise and contrast. Contrast was measured as the contrast recovery coefficient (CRC) between the left-ventricular myocardium and blood pool, and noise was calculated as the standard deviation (SD) of voxels within the myocardium. These metrics were then compared between reconstruction methods with a paired 2-tailed Student *t*-test with $p < 0.05$ considered a statistically significant difference. Additionally, 17-segment analysis [20] was performed to assess the impact of the proposed method in quantification at a segment-level, and contrast between healthy myocardium and myocardial viability defects was computed from manually defined regions of interest in patients with transmural myocardial defects.

Results

Figure 2 demonstrate the differences between the reconstructed PET images for two representative patients from the first cohort, alongside the CMRA images used for MR-guidance. In Patient 1 we could observe a defect-mimicking artifact in the top of the myocardium (Fig 2, magenta arrows), due to a particularly poor alignment between the average free-breathing end-expiration position and the position of the breath-hold μ-map. The artifact was removed by aligning the μ-map using the proposed method, while deblurring of small structures such as the papillary muscles (Fig 2, blue arrows) was observed when applying motion compensation. Indeed, motion compensation resulted in an increased myocardium CRC for the MC images in all cases (Fig. 4). This increase in contrast arises from both the motion compensation deblurring and the convergence of the MLEM algorithm; where improved contrast represents convergence towards true regional means. However, an increased noise could also be observed in both the reconstructed images and the measured myocardial SD (Fig. 4). Such noise increase arises from the convergence of the MLEM algorithm, but also since reducing counts from the PET data (by rejecting systolic data) results in a lower signal-to-noise-ratio. Finally, by

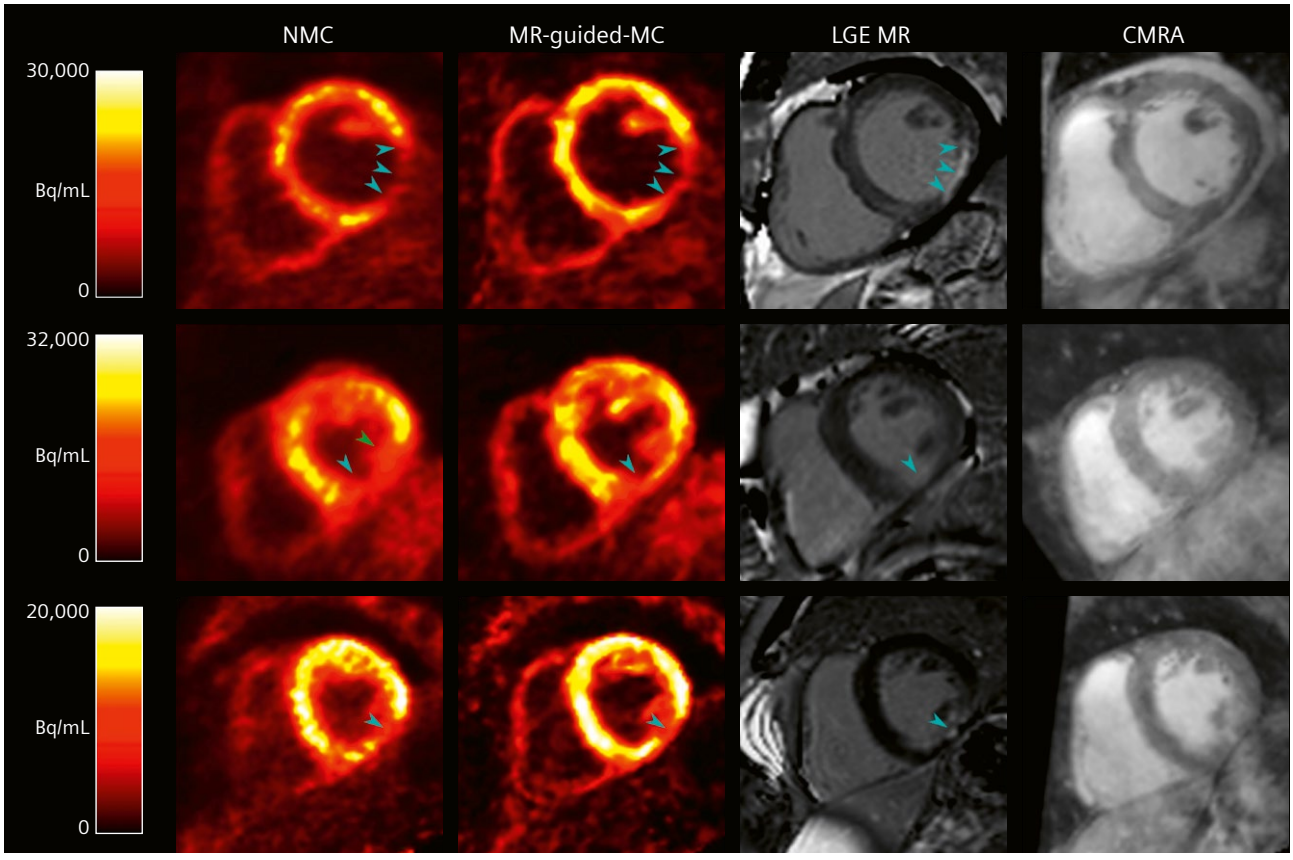

3 Example short-axis view of the reconstructed ^{18}F-FDG PET images for three selected patients with cardiac disease, alongside simultaneously acquired CMRA images and corresponding conventional late-gadolinium enhancement (LGE) MR images, showing the extent of myocardial scarring. The proposed method improves image quality while maintaining the appearance of ^{18}F-FDG hypo-intense defects (cyan arrows). In some cases, the uncorrected PET images falsely depict the defect as more extensive than it actually is (green arrow, row 2). Note that LGE images are shown only for comparison and did not provide any information for the guided PET reconstructions, which instead used high-resolution CMRA images.

including MR-guidance in the respiratory motion-corrected cardiac-gated PET reconstruction, the noise is reduced while preserving edges and small details.

Similar trends were observed for the patients with cardiac disease. Figure 3 shows example PET images for three representative patients, including images reconstructed with the conventional method (NMC), and with the proposed MR-guided-MC method, alongside reference LGE MR images highlighting regions of myocardial scar and the corresponding CMRA image used for MR-based motion correction and guidance. The previously described improvements in terms of noise and contrast are apparent, and the depiction of myocardial defects (hypo-intense regions, cyan arrows) is preserved, coinciding with the hyper-intense regions in the LGE MR images.

Violin plots showing myocardium-to-blood CRC and myocardium SD for all patients are shown in Figure 4. The MC significantly increases both CRC and SD compared to the conventional NMC method ($p < 0.0001$). Applying the proposed MR-guided-MC method results in a similar or slightly higher increase of CRC, while the increase in noise levels is significantly reduced ($p < 0.0001$).

When measuring transmural defects in five of the patients with cardiac disease, we found that the proposed MR-guided-MC method increases the CRC by 18.6% and their contrast-to-noise ratio by 47.7% on average compared to the conventional NMC reconstruction, indicating that the MR guidance information is sufficiently localized to maintain relevant patterns of uptake while successfully reducing noise.

Furthermore, 17-segment analysis indicates that all heart segments show an increased uptake with the proposed method (reflecting improved quantification) which ranges from ~15% increase at the apical segments to over 60% increase towards the basal anterior segments (Fig. 5). This variety in the uptake increase may be due to both the nonrigid nature of the motion of the heart and the variability in respiratory patterns across different patients.

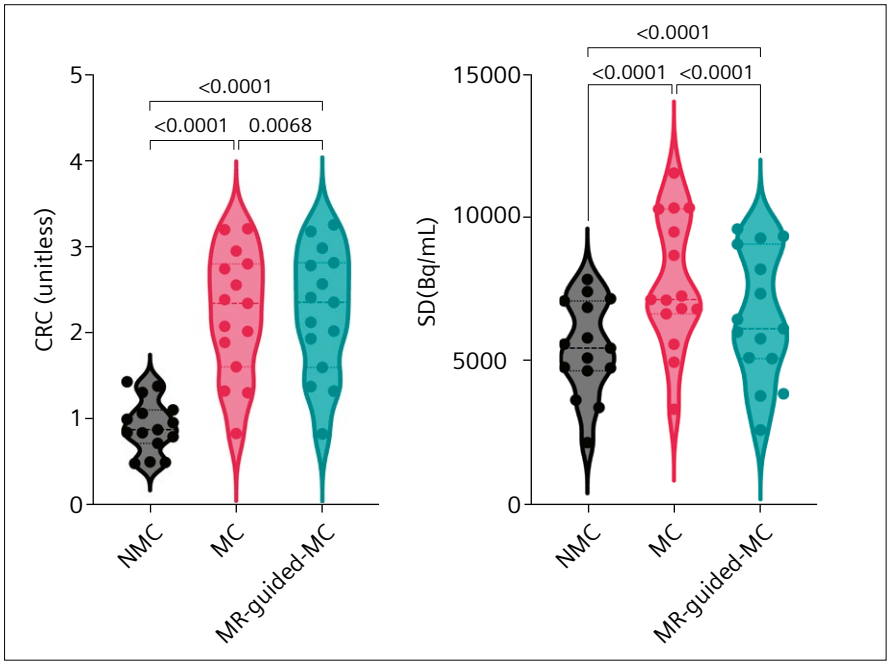

4 Violin plots showing statistical analysis for the comparative methods in terms of contrast recovery coefficient (CRC) between myocardium and blood pool and myocardium standard deviation (SD) for all patients.

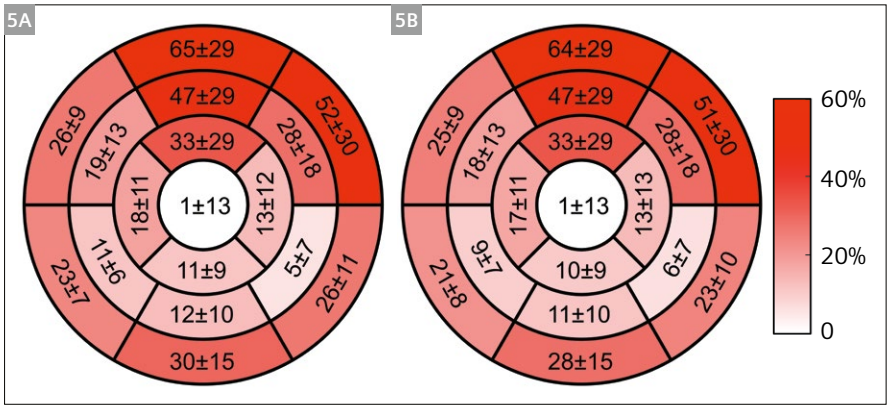

5 17 segment analysis showing the relative difference in PET uptake values between **(5A)** MC and NMC reconstructions, and **(5B)** the proposed MR-guided-MC method and NMC images. While an overall increase of ~17 ± 9% was observed for both MC and MR-guided-MC methods, some areas of the left ventricle myocardium show a significantly larger increase than others, with an ~15% increase at the apical segments to over 60% increase in the basal anterior segment.

Summary

Simultaneous PET-MR has shown potential for improving PET image quality by using MR information to address various degrading factors. In separate research works, MR-based motion compensation and MR-guided reconstruction have been demonstrated to improve PET image quality. In this article, we have described a recently introduced framework that integrates these developments into a single PET-MR framework that produces high quality, diagnostic CMRA images alongside improved ^{18}F-FDG cardiac PET images. This integrated PET image reconstruction framework improves image quality by including MR-based μ-map alignment, respiratory motion correction and cardiac-gating and MR-based guidance of PET data.

The framework was evaluated in terms of contrast and noise and compared to a conventional and a motion-compensated PET image reconstruction. The proposed method produced the highest contrast of all the methods, and significantly reduced image noise compared to the reference reconstruction that incorporated the motion compensation components of the framework without MR-guidance. In addition, applying the proposed framework to ^{18}F-FDG PET data from cardiac patients demonstrated that the visual appearance of clinically relevant features, such as hypo-intense defects, are preserved. These improvements have the potential to improve clinical interpretability and diagnosis based on cardiac PET-MR.

Acknowledgments

This work was supported by the following grants:
(1) EPSRC EP/P032311/1, EP/P007619/1, EP/P001009/1;
and (2) BHF programme grant RG/20/1/34802.

References

1 Rischpler C, Siebermair J, Kessler L, Quick HH, Umutlu L, Rassaf T, et al. Cardiac PET/MRI: Current clinical status and future perspectives. Semin Nucl Med. 2020;50:260–9.
2 Vitadello T, Kunze KP, Nekolla SG, Langwieser N, Bradaric C, Weis F, et al. Hybrid PET/MR imaging for the prediction of left ventricular recovery after percutaneous revascularisation of coronary chronic total occlusions.
Eur J Nucl Med Mol Imaging. 2020;47(13):3074-3083.
3 Wicks EC, Menezes LJ, Barnes A, Mohiddin SA, Sekhri N, Porter JC, et al. Diagnostic accuracy and prognostic value of simultaneous hybrid 18F-fluorodeoxyglucose positron emission tomography/magnetic resonance imaging in cardiac sarcoidosis.
Eur Hear J Cardiovasc Imaging. 2018;19:757–67.
4 Ouyang J, Li Q, El Fakhri G. Magnetic resonance-based motion correction for positron emission tomography imaging.
Semin Nucl Med. 2013;43:60–7.
5 Robson PM, Dweck MR, Trivieri MG, Abgral R, Karakatsanis NA, Contreras J, et al. Coronary artery PET/MR imaging: Feasibility, limitations, and solutions.
JACC Cardiovasc Imaging. 2017 Oct 1;10(10):1103–12.
6 Kolbitsch C, Neji R, Fenchel M, Mallia A, Marsden P, Schaeffter T. Respiratory-resolved MR-based attenuation correction for motion-compensated cardiac PET-MR.
Phys Med Biol. 2018 Jun 27;63(13):135008.
7 Manber R, Thielemans K, Hutton B, Barnes A, Ourselin S, Arridge S, et al. Practical PET respiratory motion correction in clinical PET/MR.
J Nucl Med. 2015;56:890–6.
8 Küstner T, Schwartz M, Martirosian P, Gatidis S, Seith F, Gilliam C, et al. MR-based respiratory and cardiac motion correction for PET imaging. Med Image Anal. 2017 Dec 1;42:129–44.
9 Kolbitsch C, Neji R, Fenchel M, Schuh A, Mallia A, Marsden P, et al. Joint cardiac and respiratory motion estimation for motion-corrected cardiac PET-MR. Phys Med Biol. 2019;64:15007.
10 Shepp LA, Vardi Y. Maximum likelihood reconstruction for emission tomography. IEEE Trans Med Imaging. 1982;1:113–22.
11 Schramm G, Holler M, Rezaei A, Vunckx K, Knoll F, Bredies K, et al. Evaluation of parallel level sets and Bowsher's method as segmentation-free anatomical priors for time-of-flight PET reconstruction.
IEEE Trans Med Imaging. 2018;37:590–603.
12 Bland J, Mehranian A, Belzunce MA, Ellis S, da Costa-Luis C, McGinnity CJ, et al. Intercomparison of MR-informed PET image reconstruction methods. Med Phys. 2019;46:5055–74.
13 Munoz C, Ellis S, Nekolla SG, Kunze KP, Vitadello T, Neji R, et al. MRI-Guided Motion-Corrected PET Image Reconstruction for Cardiac PET/MRI. J Nucl Med. 2021 Dec;62(12):1768–74.
14 Munoz C, Neji R, Cruz G, Mallia A, Jeljeli S, Reader AJ, et al. Motion-corrected simultaneous cardiac positron emission tomography and coronary MR angiography with high acquisition efficiency. Magn Reson Med. 2018;79(1):339–50.
15 Qiao F, Pan T, Clark JW, Mawlawi OR. A motion-incorporated reconstruction method for gated PET studies.
Phys Med Biol. 2006 Aug 7;51(15):3769–83.
16 Ellis S, Mallia A, McGinnity CJ, Cook GJR, Reader AJ. Multi-tracer guided PET image reconstruction.
IEEE Trans Radiat Plasma Med Sci. 2018;2:499–509.
17 De Pierro AR. A modified expectation maximization algorithm for penalized likelihood estimation in emission tomography.
IEEE Trans Med Imaging. 1995;14:132–7.
18 Reader AJ, Ellis S. Bootstrap-optimised regularised image reconstruction for emission tomography.
IEEE Trans Med Imaging. 2020;39:2163–75.
19 Belzunce MA, Reader AJ. Assessment of the impact of modeling axial compression on PET image reconstruction.
Med Phys. 2017;44:5172–86.
20 Cerqueira MD, Weissman NJ, Dilsizian V, Jacobs AK, Kaul S, Laskey WK, et al. Standardized Myocardial Segmentation and Nomenclature for Tomographic Imaging of the Heart.
Circulation. 2002 Jan 29;105(4):539–42.

Contact

Dr Camila Munoz
King's College London
School of Biomedical Engineering and Imaging Sciences
3rd Floor, Lambeth Wing
St Thomas' Hospital
London, SE1 7EH
UK
Tel.: +4402071888299
camila.munoz@kcl.ac.uk

MRI's Helium Footprint – And How to Make it Harder to Spot

Philipp Grätzel von Grätz, M.D.

Berlin, Germany

Helium is a finite resource. In fact, it is exceedingly rare on our planet, which is why efforts are underway to make helium-dependent industries more sustainable. Magnetic resonance imaging (MRI) is among these industries: One out of every seven litres of liquid helium consumed annually worldwide is used for cooling superconducting magnets in MRI machines. There are ways to get this figure down, both on the product and on the delivery side of the business. Achieving real helium sustainability for MRIs requires that several approaches be taken simultaneously.

Helium is what makes party balloons fly, and this is all that many people know about it. But while it is true that party balloons account for a relevant – albeit variable – share of the annual global helium consumption, there is much more to know about this inert, noble gas. Were you aware, for example, that helium is among the most abundant elements that exist? Bar hydrogen, it is actually the second most abundant one in the universe. The sun, for example, consists of 73 percent hydrogen and 23 percent helium, while other elements only account for the remaining 4 percent.

The global helium economy

So there is definitely no shortage of helium out there in space. But not every celestial body is a thermonuclear fusion reactor. The sun is. The Earth is not. Down on Earth, helium is extremely scarce. It is, in fact, one of the rarest naturally occurring elements. The majority of Earth's helium comes from natural radioactive processes, i.e., decaying heavy elements. This process is as slow as it sounds, which means that helium is a non-renewable, finite resource.

Where does helium come from? There is no such thing as helium-specific mining. Rather, helium is a by-product of natural gas mining. "The US has traditionally been the largest source of helium worldwide," says Andrew Wade, Helium Commodity Manager at Siemens Magnet Technology in Oxford, UK. In recent years, though, the helium supply from the US has dried up, and Wade has had to turn to other countries for procurement: "The biggest producers at the moment are Qatar and Algeria. There will also be some large gas fields opening in Siberia soon."

Helium is not only finite, it is also volatile: When a helium balloon pops, its helium escapes into the atmosphere, from where it cannot be retrieved. In other words:

1 Container compressor facility to retrieve helium from old MRI systems that undergo refurbishing.

2 Looking into the 20-foot-long container.

Unless recycled, any cuts into our planet's helium reserves will be final cuts. The end of Earth's helium supply is not imminent: At current rates of consumption, the global reserves might in fact last some three centuries. But end they will, and thus there is a strong case to improve sustainability in helium-dependent industries.

Magnetic resonance imaging and helium

What is helium currently used for? There are several industries that cannot do without helium at the moment. Helium is a shielding gas for welding and for laser processing in industrial manufacturing, especially in the aviation industry. The space industry, too, uses helium for pressurisation and purging. Helium is needed for producing semiconductors and optical fibres, which makes it indispensable for the IT and microelectronics industry. Appreciable quantities go into gas chromatography analytics and into producing the breathing mixture for deep-sea diving. Finally, helium serves as a cryogenic cooling liquid for superconductors. The latter may in fact be the single most important use of helium today, with the MRI industries accounting for the biggest share: "About 15 percent of the total global helium production is consumed by MRI," says Wade.

The MRI industry uses superconducting magnets to create strong and dynamic magnetic fields for modern-day MRI machines. Helium, which liquifies at about 4 K or −269° C, can create the low temperatures needed for supraconductivity. In essence, copper and niobium wires in MRI magnets are embedded in a bath of liquid helium. "The trick is stopping that helium from boiling," explains Wade. To do so, MRI machines use a cold head within a vacuum flask which recondenses any gas that arises. "The total amount of helium needed is different from MRI system to MRI system. As a rule of thumb, traditional MRI systems contain 1,500 litres of helium. About 2,000 litres are needed to get to a stable system. And after ten years, another 500 litres or so might have to be refilled. In the meantime, a well-managed magnet should not need any refilling."

Does it have to be that much?

If that sounds like a lot, that's because it is, especially given that the MRI industry is growing. "At the moment, the installed base increases at about 4,000 systems per year globally," estimates Wade. Under these conditions, the finite nature of helium means there is a need to act. There are three roads that can be taken toward better helium sustainability, and Siemens Healthineers is proceeding on all three of them.

"An important lever is trying to improve logistics and delivery," says Karlheinz Hörner, Director Magnetic Resonance Supply Chain Management at Siemens Healthineers in Erlangen, Germany. To get an MRI machine from the production site to the customer, whether by ship, by air cargo, or by lorry, is a challenging task. The problem is that as soon as the cooling is switched off for transport, the helium starts to evaporate. "Without cooling, we lose about 3% helium per day," says Hörner.

This is not a problem in the first couple of days, but it becomes a problem at a certain point: "We aim to ship any of our MRI machines to the customer within 20 days. The critical time frame is around 25 days, which is when 70 to 80% of the helium is lost." Once at the target destination, such a helium-drained magnet has to be re-cooled with liquid nitrogen and, depending on the amount of helium lost, potentially re-filled with liquid helium. Refilling can come with its own challenges, especially in remote

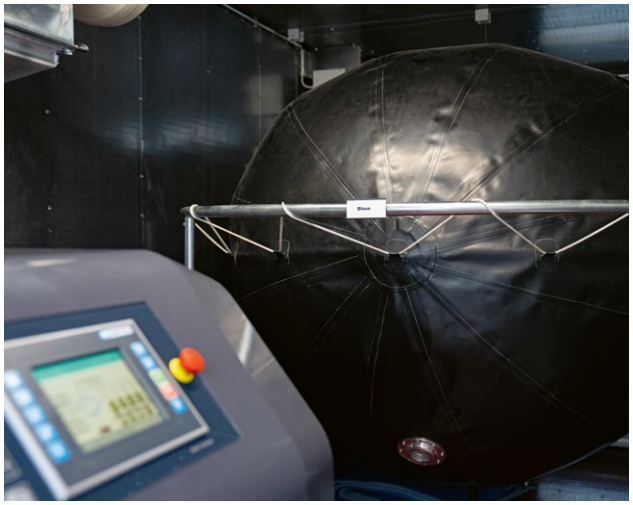

3 Helium bubble connected to a compressor that densifies helium up to a pressure of 200 bar.

4 Highly compressed recycling helium is filled into gas bottles and returned to gas vendors.

destinations. Helium is a diva. The COVID-19 crisis hasn't made life smoother for MRI shipping, either.

Helium cooling to go

In order to reduce helium losses during transport and to gain more overall flexibility, Siemens Healthineers started to introduce innovative cooling containers for long-distance MRI shipping from 2016 onwards. "There are 25 of these containers now – seven in Germany and the rest in China. This fleet will grow in the years to come," says Hörner. The cooling containers essentially mirror the MRI cooling on-site, in the hospital. There is a cooling unit at the front end of the container that keeps the MRI's cold head working all the way to customer. Avoiding breaks in the cooling chain means that no helium evaporates or needs to be refilled.

With MRI cooling containers, MRI machines can be shipped to remote countries without using air freight. This is why MRI cooling containers not only increase helium sustainability; avoiding air transport is also better for the climate. "This is especially relevant for India, where we had to use planes until recently. Australia and New Zealand have already told us that they won't accept MRI deliveries by air cargo at all anymore."

Cooling trucks are the siblings of cooling containers for shipping when it comes to overland transport by lorry. Cooling trucks are especially important in Brazil, where Siemens Healthineers operates a small factory for the local market. The cooling trucks are used to ship MRI machines to cities in the Amazon region, like Manaus, or to Recife and other cities on the north-eastern coast of South America. The benefits are the same as with cooling containers for cargo ships: No planes needed. Helium refilling avoided.

Helium recycling: from bench to balloon

A second important method of ensuring helium sustainability is recycling. This is done at the Siemens Healthineers facility in Forchheim, Germany, where old MRI systems undergo refurbishing. Originally, MRI refurbishing was done without helium retrieval. But this has changed in summer 2021, says Hörner: "We are now using a specifically designed, 20-foot-long container. It features a helium bubble which is connected to a compressor that densifies the collected helium up to a pressure of 200 bar." In the end, the highly compressed helium is filled into gas bottles, which gas vendors like Linde in turn sell to welders, divers, or indeed party balloon providers.

How much helium can be retrieved from a magnet that comes in for refurbishing depends on the type of MRI machine and on its overall condition. "Typically, MRI machines arrive at Forchheim with 25 to 30% of their original helium load," says Hörner. With 50 to 80 magnets finding their way back to Forchheim per year, this adds up to a substantial amount of recycled helium. Between July and September 2021 alone, nearly 20,000 litres of helium were retrieved with the help of the new container-compressor facility.

Rethinking MRI by draining the magnet

In addition to transport and logistics as well as recycling, there are the magnets themselves. This is where most can be gained in terms of helium sustainability, but it is also a technically demanding avenue to go. Over the years, the helium consumption of MRI machines has improved substantially, says Andrew Wade. During a ten-year lifecycle, an MRI system from the late 1980s required about 14,500 litres of helium in total. In a system produced in the early years of the 21st century, that value is down to around 3,100 litres on average. This translates into global statistics: "As an estimate, the MRI industry has managed to reduce overall helium consumption by around 25% during the last seven years – even though the installed base increased," Wade believes.

But 3,000 litres of helium per machine is by no means the upper limit of possible reductions. These days, Siemens Healthineers is pioneering an entirely new MRI platform that can be considered a moonshot from a helium sustainability perspective. Presented to the public at RSNA 2020, it is not the next evolutionary step towards less helium consumption. Rather, it marks the beginning of a totally new class of MRI systems that are radically different from their predecessors.

At the heart of the new platform is a newly designed magnet, the DryCool magnet. In the MAGNETOM Free.Max and MAGNETOM Free.Star systems, it comes with a field strength of 0.55T. The new magnet is much lighter and requires much less niobium-titanium wire, which means that cooling can be reduced to a minimum: The system contains no more than 0.7 litres of liquid helium under normal operation. Needless to say, this platform has the potential to change the world's helium sustainability equations completely. MRI's helium footprint, which was once as conspicuous as a dinosaur track, may soon become much harder to spot.

Further reading

Keeping a Hot System Cool by system architect Stephan Biber available from https://www.magnetomworld.siemens-healthineers.com/hot-topics/lower-field-mri

Meet Siemens Healthineers

Siemens Healthineers: Our brand name embodies the pioneering spirit and engineering expertise that is unique in the healthcare industry. The people working for Siemens Healthineers are totally committed to the company they work for, and are passionate about their technology. In this section we introduce you to colleagues from all over the world – people who put their hearts into what they do.

Dominik Nickel, Ph.D.

Dominik Nickel began his academic career in 1999 as a student at the Technical University of Darmstadt, Germany. He completed his physics degree in 2003, which also included a period studying abroad at Trinity College Dublin in Ireland. On finishing his undergraduate studies, Dominik embarked on his Ph.D. in theoretical nuclear physics in 2003, which he was awarded by the Technical University of Darmstadt in 2007. Dominik joined Siemens Healthineers in 2010, after postdoctoral scholarships at the Center for Theoretical Physics, MIT, Cambridge and the Institute for Nuclear Theory, UW, Seattle, both in the USA. Dominik is an application developer and principal key expert working on sequence and reconstruction techniques with focus on abdominal imaging.

Erlangen, Germany

How did you first come into contact with MRI?
Compared to many colleagues, this was quite late. Originally, I was pursuing an academic career in theoretical physics. During my second postdoc in the USA, I decided to look for a job in Erlangen where my wife was already working. It is hard to say how much luck was involved, but eventually I got a position in application development in MR at Siemens Healthineers. My first actual contact with an MR scanner was on entering the factory.

What is the most fascinating aspect of MRI?
That it is so broad. From an application idea to its clinical use, many different aspects play a role. The hardware, MR physics, implementation, clinical workflow, clinical expertise, ... Most applications rely on teamwork with many people contributing to different aspects.

What are the biggest challenges in your job?
There are a lot of ideas for improving sequences and signal processing. At first glance, many may even look similar. It is challenging to assess the potential of an idea and decide what to implement. Since many ideas do not work out, it is also challenging to know when to give up on an idea and move on to the next one.

What do you think are the most important developments in MRI and healthcare?
Tough question. Of course deep learning reconstruction is a big topic for me. In particular, I find the acceleration of bread-and-butter applications most impressive, because many new developments focus on particular use cases. Trying to look ahead, conventional hardware feels somewhat converged, partly due to limitations imposed by patient safety. Compared to other modalities, MR is still challenging when it comes to robustness and standardization. Here I would hope for further developments. That also includes the workflow. Lower field strengths have now also become clinical reality. There should be development to explore this further.

What would you do if you could spend a month doing whatever you wanted?
Travel with my family. Usually I like being at home, but after two years of restrictions due to the COVID-19 pandemic, I would love to go on bigger trips.

The entire editorial staff at University College London (UCL), UK, and at Siemens Healthineers extends their appreciation to all the radiologists, technologists, physicists, experts, and scholars who donate their time and energy – without payment – in order to share their expertise with the readers of MAGNETOM Flash.

MAGNETOM Flash – Imprint

Publisher:
Siemens Healthcare GmbH
Magnetic Resonance,
Karl-Schall-Str. 6, D-91052 Erlangen, Germany

Editor-in-chief:
Antje Hellwich
(antje.hellwich@siemens-healthineers.com)

Guest Editor:
Daniel Alexander, Ph.D.
Professor of Imaging Science
Department of Computer Science
Faculty of Engineering Science
University College London (UCL)
Gower Street, London, WC1E 6BT
d.alexander@ucl.ac.uk

Editorial Board:
Jane Kilkenny; Nadine Leclair, M.D.;
Heiko Meyer, Ph.D.; Rebecca Ramb, Ph.D.;
Wellesley Were

Review Board:
André Fischer, Ph.D.; Daniel Fischer;
Giulia Ginami, Ph.D.; Tobias Kober, Ph.D.;
Felix Müller-Witt; Gregor Thörmer, Ph.D.

Copy Editing:
Sheila Regan, Jen Metcalf, UNIWORKS,
www.uni-works.org
(with special thanks to Kylie Martin)

Layout:
Agentur Baumgärtner,
Friedrichstr. 4, D-90762 Fürth, Germany

Production:
Norbert Moser,
Siemens Healthcare GmbH

Printer:
Schmidl & Rotaplan Druck GmbH,
Hofer Str. 1, D-93057 Regensburg, Germany

We welcome your questions and comments about the editorial content of MAGNETOM Flash. Please contact us at magnetomworld.team@siemens-healthineers.com

Manuscripts as well as suggestions, proposals and information are always welcome; they are carefully examined and submitted to the editorial board for attention. MAGNETOM Flash is not responsible for loss, damage, or any other injury to unsolicited manuscripts or other materials. We reserve the right to edit for clarity, accuracy, and space. Include your name, address, and phone number and send to the editors, address above.

MAGNETOM Flash is also available online:

www.siemens-healthineers.com/magnetom-world

Not for distribution in the US

On account of certain regional limitations of sales rights and service availability, we cannot guarantee that all products included in this brochure are available through the Siemens sales organization worldwide. Availability and packaging may vary by country and is subject to change without prior notice. Some/All of the features and products described herein may not be available in the United States.

The information in this document contains general technical descriptions of specifications and options as well as standard and optional features which do not always have to be present in individual cases, and which may not be commercially available in all countries.

Due to regulatory reasons their future availability cannot be guaranteed. Please contact your local Siemens organization for further details.

Siemens reserves the right to modify the design, packaging, specifications, and options described herein without prior notice. Please contact your local Siemens sales representative for the most current information.

Note: Any technical data contained in this document may vary within defined tolerances. Original images always lose a certain amount of detail when reproduced.

Siemens Healthineers Headquarters
Siemens Healthcare GmbH
Henkestr. 127
91052 Erlangen, Germany
Phone: +49 9131 84-0
siemens-healthineers.com

Published by Siemens Healthcare GmbH · Order No. A91MR-1000-150C-7600 · Printed in Germany · 11607 0422 ·